The Olympian Symposium 2026

The Evolution of Interstellar Medium Across Cosmic Times

POSTERS BOOK

18 – 22 May, 2026
Mediterranean Village
Paralia Katerini
Olympus Riviera, Greece

OLYMPIAN
SYMPOSIUM

The Olympian Symposium 2026
The Evolution of Interstellar Medium Across Cosmic Times
`https://olympiansymposium.org/`

Monday 18 May – Friday 22 May, 2026
Paralia Katerini, Olympus Riviera, Greece
Mediterranean Village Hotel

Cover image: JWST image of the Tarantula Nebula (NIRCam Image)
Credits: NASA, ESA, CSA, STScI, Webb ERO Production Team

之江实验室
ZHEJIANG LAB

Intelligent Computing
A SCIENCE PARTNER JOURNAL

DEPARTMENT OF
ASTROPHYSICS, ASTRONOMY
& MECHANICS
SCHOOL OF PHYSICS
ARISTOTLE UNIVERSITY OF THESSALONIKI

REGIONAL
UNIT OF
PIERIA
REGION OF CENTRAL MACEDONIA

List of Posters

Arai, Reiji	54	Non-parametric continuum determination in a 3D datacube using a low-rank and sparse matrix decomposition
Arora, Raghav	37	Magnetic fields as gravitational aids in galaxies
Arriagada Torres, Pablo	30	The resolved star formation of starbursts at cosmic noon
Böhm, Lennart	1	Connecting Filamentary Accretion to Feedback at $\sim$100 AU Scales in W33 Main
Bisbas, Thomas	55	RAYTHEIA: A high-performance ray-tracing algorithm for three-dimensional direction-dependent equations in astronomical simulations
Busch, Michael	20	OH as a Tracer of “CO-Dark" Gas in the Interstellar Medium Near and Far
Chen, Szu-Ting	38	An Empirical Determination of Cosmic-Ray Propagation in NGC 1333 across Multiple Scales
Dhrubojyoti, Sengupta	9	Seeing Through the ISM: Recovering Intrinsic X-ray Emission in Metal-Poor Dwarf Galaxies
Dignan, Anna	47	Multiwavelength Tracers of Massive Star Formation Rates in Nearby Galaxies
Dutkowska, Katarzyna	56	Rethinking Molecular Diagnostics in Extreme Environments: Insights from Astrochemical Modeling
Fadul, Abubakar	57	Post-Processing Hydrodynamical Simulations: A Pipeline for Astrochemical Evolution in Molecular Clouds
Faerber, Timothy	2	Expansion Signatures in 35 HII Regions traced by SOFIA [CII] Emission
Garland, James	3	Stirring the Pot: Spiral-Arm-Induced Star Formation and ISM Enrichment in NGC 628
Grasha, Kathryn	48	Anchoring the Extragalactic Chemical Abundance Scale
Greif, Christine	58	CAT - Contour Analysis Tool: An Interactive Tool for Background and Morphology Analysis
Gupta, Akash	59	Chemical modeling of high-mass star-forming regions: A post-processing study of MHD simulations
Herard-Demanche, Thomas	31	A Cosmic City in Formation: an extreme proto-cluster at $z > 7$
Immer, Katharina	4	Disruption of a massive molecular cloud by a supernova in the Galactic Centre
Jarvis, Emma	5	The Ionized Interstellar Medium in M33: A Resolved View of HII Regions and Diffuse Ionized Gas
Jiang, Xuejian	60	PDFchem modeling of large-scale carbon distribution in Orion A
Johnson, Madisen	21	Molecular Hydrogen Across Environments: From Local Star-Forming Clouds to the Early Universe
Kaiser, Leonard	39	A modeling perspective on galactic Faraday rotation observations

Kobak, Agnieszka	22	The puzzle of the methanol maser rings - physical properties and molecular gas emission tracers
Kobayashi, Masato	10	Molecular Cloud Formation in Low-Metallicity ISM and Its Role in Galactic Star Formation
Lam, Natalie	11	The Evolution of the Mass-Metallicity and Fundamental Metallicity Relation at $z > 2$ Based on Unprecedented High-redshift Metallicity Calibrations and Sample Sizes
Lau, Cheryl	6	Modelling semi-confined supernovae in turbulent Giant Molecular Clouds
Lim, Jeremy	23	Cluster Mergers - not AGN Feeback - Mitigates Gas Cooling and Star Formation in Cluster Central Galaxies
Linden, Sean	32	Merger INduced starbursts and the Gas Lifecycle Examination with ALMA
Liu, Mengting	49	First High-Sensitivity OH Measurements toward a Pulsar
Lundqvist, Emma	33	Ionization structure in Lyman continuum leaking galaxies
Madden, Suzanne	16	Resolving Multiphase Gas and Dust in Low-Metallicity ISM: SOFIA [CII] and [OIII] Mapping in the Large Magellanic Cloud (LMC+)
Matijevic, Luka	34	The influence of the environment on the morphology and ISM properties of the lopsided galaxy NGC 2276
Meng-Zhe, Yang	40	The JCMT BISTRO Survey: Unveiling the Magnetic Fields around Galactic Center
Meng-Zhe, Yang	41	The JCMT BISTRO Survey: Magnetic Fields in the Massive Star-Forming Region Onsala 2
Michiyama, Tomonari	35	Cloud-Cloud Collisions Induce Filament-Mediated Super Star Cluster Formation in the Antennae Overlap Region: Evidence from ALMA and JWST
Mishra, Divya	42	Mapping the Magnetic Field of M83 using Optical Imaging Polarimetry
Mouli Ghosh, Esan	7	Stellar feedback in the massive star-forming region W43
Nagashima, Yuzuki	24	Environmental Variations in the GMC-scale 13CO/C18O Abundance Ratio in NGC 1068
Nianias, James	25	Outflows from Low-Luminosity Galaxies in the Early Universe
Nigou, Emma	50	Turning JWST/MIRI backgrounds into a survey of diffuse molecular hydrogen
Nordlander, Thomas	26	Evidence of a supernova at the low mass end in the early Universe
Pantoni, Lara	66	IMEGIN Large Program: mapping the millimeter dust properties and the ISM lifecycle in nearby galaxies
Peltonen, Joshua	27	Bridging the Gap in the New Era of Star Formation
Poosch, Hans Christian	61	Unraveling Galactic Filament Networks: A Graph-Theoretic Approach
Ranjan, Adarsh	12	Unveiling Metal Mixing in a Grand-Design Spiral: A UV-optical multiphase spatially resolved study of M83
Rodriguez, Maria Jimena	13	Star formation in a metal-poor environment: the case of NGC 602

Sampson Olalde, Georgina	14	Disentangling Heating Mechanisms in the Interstellar Medium of Extremely Metal-Deficient Galaxies
Schilke, Peter	8	Mechanical and radiative feedback in high-mass cluster forming regions - an ALMAGAL study
Scibelli, Samantha	17	Complex Aromatic Chemistry Detected at the Dawn of Star and Planet Formation
Seifried, Daniel	43	MHD simulations of molecular clouds and synthetic dust polarisation maps: What can we learn from it?
Sho, Ebihara	28	Nitrogen enhancement of GN-z11 due to the pollution from supermassive stars
Siwakoti, Utsav	36	A JWST MIRI-MRS Map of the Nucleus of the Nearby Starburst Galaxy NGC 253
Smith, Rowan	44	Simulating how galactic forces and magnetism affect how stars form in the ISM
Soler, Juan	51	The neutral atomic shell of the extended Orion nebula (EON)
Stanton, Reagan	45	The Multiphase Magnetic Fields of the Dwarf Galaxy IC10
Sudeshna, Patra	15	Is a Universal Conversion Factor Valid Across All Metallicitiy? Variation of Dense Gas Mass–Luminosity Conversion Factor Across the Milky Way
Sulzenauer, Nikolaus	52	Cosmic fireworks mark the 1st billion years: the extreme interstellar medium conditions of giant elliptical galaxies in formation
Uday Nagdeo, Ameya	62	Fluctuation dynamos in the supersonic turbulence at $Pm \geq 1$
Wakefield, Ben	53	Investigating a bright, compact and isolated region of high-mass star formation with the JCMT
Wang, Youxin	18	Hot core chemistry in the outer Galaxy: impact of metallicity on the formation of complex organic molecules
Whitaker, Katherine	29	New Probes of Massive Galaxy Formation at High Redshift
Whitworth, David	46	Magnetic regulation of ISM phases and star formation: The B-n relationship
Williamson, Victoria	63	Turbulence in the HI-H_2 Boundary Layer
Yanchulova, Petia	19	Interstellar Dust Extinction in Nearby Galaxies
Zhang, Tianwei	64	Spectuner-D1: Efficient spectral line fitting of interstellar molecules using deep reinforcement learning
Zimmerman, Birka	65	Cores in Massive Clumps: Building a Bridge Between Simulations and Synthetic Observations

Non-parametric continuum determination in a 3D datacube using a low-rank and sparse matrix decomposition

Reiji Arai (Shizuoka U./NAOJ), Toshiki Saito (Shizuoka U./NAOJ), Akio Taniguchi (KIT),
Nanase Harada, and Kouichiro Nakanishi (NAOJ/SOKENDAI)

Introduction

Remarkable advancements in radio facilities allow us to detect a greater number of molecular emission and absorption lines. Some sources have so few line-free channels that **determination of a continuum level is not trivial** (e.g. Ando et al. 2017). It is still challenging to accurately separate and analyze each component.

In this study, we aim

- Developing a method that **determine the continuum level non-parametrically** based on the 3D structure of the data.
- To achieve this, we apply **a low-rank and sparse matrix decomposition technique.**

In this poster, we present the results of decomposition and discussion for them.

Data

We used a 3D datacube from an ALMA Large Program, **ALCHEMI (Martín et al. 2021) survey targeted the starburst galaxy NGC253**. We focused on a only single Band 3 spectral window in this study. For our analysis, we reshaped 3D datacube (v, *x*, *y*) into a 2D matrix (pixels, v).

Method

A low-rank and sparse matrix decomposition based on the **GoDec algorithm** (Zhou & Tao 2011). It can decompose a matrix into a Low-rank matrix that can be express easily and a Sparse matrix whose almost elements are zero. **For example,** the algorithm can be applied to separate the surveillance camera video into its background (Low-rank) and walking people (Sparse). (*Figure 1: **surveillance camera video***)

Result

In this analysis, we modeled **the continuum as Low-rank** and **emission lines as Sparse** based on their 3D structure. The data was successfully decomposed into the two components. Unlike previous methods, our new method does not require a priori assumptions and **can decompose the data non-parametrically.** (*Figure 1: **1 Channel Slice***).

As a result of the decomposition

- The method can **also separate absorption lines** as a sparse component.
- The low-rank component contains some features that are not smooth (*Figure 1: **1 Spectrum***).

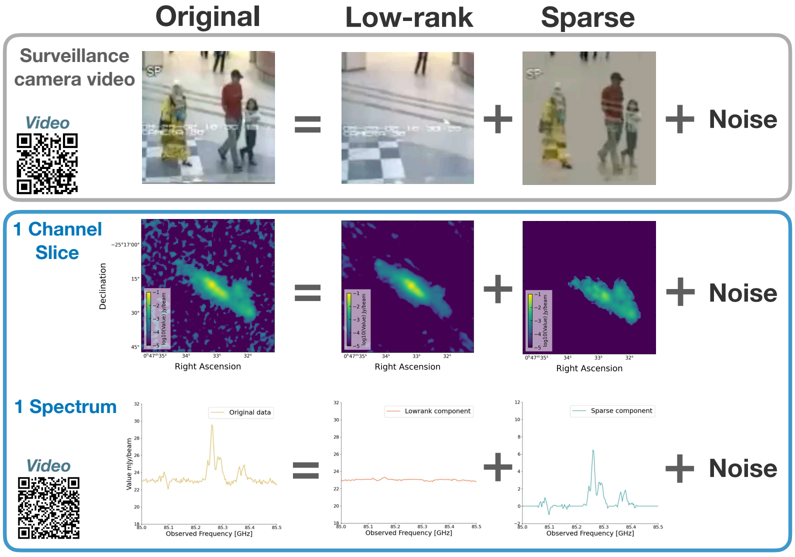

***Figure 1**:*
- *An example of the decomposition (Zhou&Tao 2011) (**upper**),*
- *Results of decomposition:*
  - *1 channel sliced maps (**middle**)*
  - *spectra of each component (**lower**) .*

Discussion

We compared our method with **STATCONT** (Sánchez-Monge et al. 2018) using integrated intensity maps of a c-C3H2 line that are made by each method.

- The scatter points are distributed close to the 1 to 1 line. It shows **consistency with the STATCONT**.
- However, some outliers (**Magenta**) come from the center region where continuum is very bright. We think that **low line-to-continuum contrast makes separation difficult.**

The advantages of our method;

- Assuming only a Low-rank structure for the continuum. So, Our new method **can determine the continuum level non-parametrically** without some assumption for its shape.
- It can be applied to observational data that has continuum shape not as simple as e.g., single power law from **upcoming facilities such as the ALMA-Wideband Sensitivity Upgrade.**

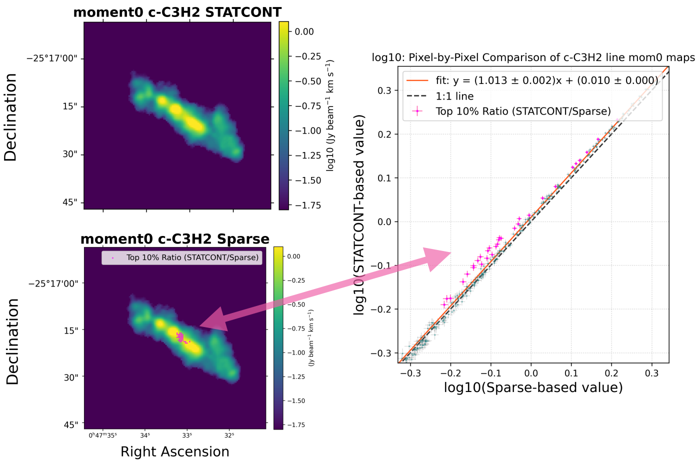

***Figure 2**: Moment0 map of c-C3H2 lines; Upper left: STATCONT, Lower left: Sparse component), and a pixel-by-pixel scatter (Right)*

Future Works

- We aim **to minimize the attribution of some emission lines to the low-rank component** by applying smoothing or related techniques.
- Apply this decomposition method to other part of ALCHEMI spectral data and data from other facilites such like JWST/NIRSPEC and VLT/MUSE, and future facilitie.

References & Acknowledgements

- *Ando et al. 2017, ApJ, 849, 2;*
- *Martín et al. 2021, A&A, 656, 46;*
- *Sánchez-Monge et al. 2018, A&A, 609, 101*
- *Zhou & Tao, 2011, Proceedings of the 28th International Conference on Machine Learning, 35, 33–40*

This work was supported in part by the Japan Foundation for Promotion of Astronomy

Magnetic fields as gravitational aids in disc galaxies

Raghav Arora[1], Oscar Agertz[1], Christoph Federrath[2], Mark Krumholz[2]

Magnetic fields

- Galaxies are magnetised with fields in equipartition with thermal, turbulent components [1].

Credits: NASA/SOFIA; NASA/JPL-Caltech/Roma Tre Univ.

Fig: NGC1068 with overlaid magnetic fields.

Gravitational instability

- Canonical expectation: **Thermal**, **magnetic pressure** and rotation against **gravity** [2].

$$\mathrm{Q_{eff}} = \frac{\kappa\sqrt{(\boldsymbol{c_s}^2 + \boldsymbol{v_a}^2)}}{\pi \boldsymbol{G\Sigma}} \begin{cases} \mathrm{Q_{eff}} \gtrsim 1 & \text{; Stabilisation} \\ \mathrm{Q_{eff}} \lesssim 1 & \text{;Destabilisation} \end{cases}$$

Q. Do magnetic fields simply stabilize, as expected?

Isolated Galaxy Simulations

No! Magnetic fields destabilise inner galactic regions

Parameters: $\mathrm{Q_{eff}} \approx 1$, $\beta = P_{thermal}/P_{magnetic}\ \epsilon\ \{\infty(hydro), 10, \boxed{1}, 0.1\}$

Observed strengths

increasing initial magnetisation

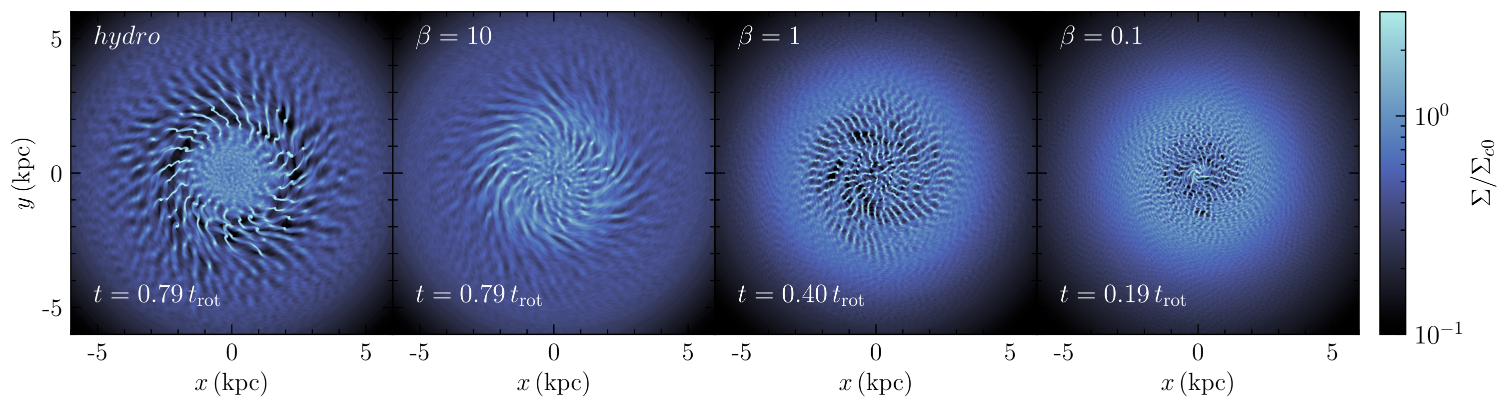

To destabilize or not?

- They destabilise beyond a critical strength: $\boldsymbol{\beta_c}$
- $\boldsymbol{\beta_c}$ increases with radius, or background shear.
- In qualitative agreement with the MagnetoJeans instability [3].

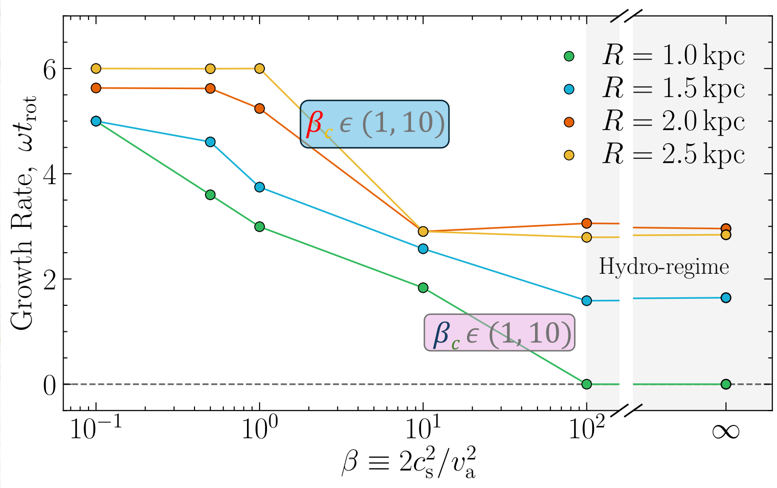

increasing initial magnetisation

References

[1] Beck, R. (2016) Magnetic fields in spiral galaxies. *Astron Astrophys Rev* **24**, 4.

[2] Toomre, A. (1964, May). On the gravitational stability of a disk of stars. ApJ 139, 1217–1238

[3] Kim & Ostriker (2001). Amplification, Saturation, And Q Thresholds For Runaway: Growth Of Self-Gravitating Structures In Models of Magnetized Galactic Gas Discs ApJ 559 : 70-95,

[1]Lund Observatory, Division of Astrophysics, Department of Physics, Lund University, SE-221 00 Lund, Sweden
[2]Research School of Astronomy and Astrophysics, Australian National University, Canberra, ACT 2611, Australia

Raghav Arora
raghav.arora@fysik.lu.se

RAYTHEIA: A high-performance ray-tracing algorithm for three-dimensional direction-dependent equations in astronomical simulations

Zhengping Zhu[1], Thomas G. Bisbas[1], Xuefei Tang[1], Brandt A.L. Gaches[2], Tianwei Zhang[1], and Huaxi Chen[1]
[1]Research Center for Computational Earth and Space Science, Zhejiang Laboratory, Hangzhou 311100, China
[2]Faculty of Physics, University of Duisburg-Essen, Lotharstraße 1, 47057 Duisburg, Germany

Abstract

We present RAYTHEIA, a high-performance reverse ray-tracing algorithm designed to efficiently solve 3D direction-dependent equations in astronomical simulations. It uses a dual-grid framework in which the native simulation mesh -serving as the source grid (SG) for ray emission- and an adaptive mesh refinement (AMR) Cartesian contribution grid (CG) are constructed for efficient ray-walking and contribution accumulation. The core of the algorithm integrates a leaf-only linear-octree data structure to reduce memory overhead, the digital differential analyzer (DDA) traversal method to efficiently determine the ray-walking path, Morton Code indexing to fast leaf cell lookup during traversal, the slab method to analytically compute the path length, and domain decomposition for the parallization. Integrated RAYTHEIA with the 3D-PDR code, we model PDR chemistry in a turbulent, star-forming cloud at an unprecedented resolution of 512^3 grid cells. We further demonstrate RAYTHEIA by producing high-resolution synthetic emission maps of key diagnostic lines of a star-forming region capturing physical effects such as [O I] 63 μm self-absorption and measuring the [C I]-bright but CO-dark molecular gas.

Framework of RAYTHEIA

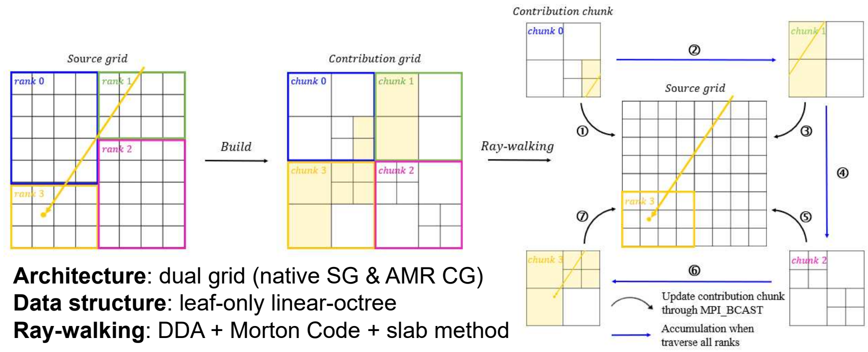

Architecture: dual grid (native SG & AMR CG)
Data structure: leaf-only linear-octree
Ray-walking: DDA + Morton Code + slab method

Fig.1. Two-dimensional schematic of RAYTHEIA framework. **Left**: the source grid (SG), which can retain the native simulation discretization and defines ray-emitting element locations. **Middle**: the contribution grid (CG), an AMR Cartesian grid built from the SG, provides a traversal-friendly representation for ray-walking and contribution accumulation. **Right**: the direction-dependent integral for the yellow ray from rank 3 is computed via a chunk-to-chunk strategy—contribution chunks are sequentially broadcast (black arrows), traversed to evaluate intersected-cell contributions (yellow shading), and accumulated into the total integral, with buffers reused for subsequent chunks (blue arrows). The framework is parallelized through distributed-memory domain decomposition, partitioning the domain into spatial chunks assigned to separate MPI ranks (colored rectangles).

Results with unprecedented 512^3 resolution

Column density

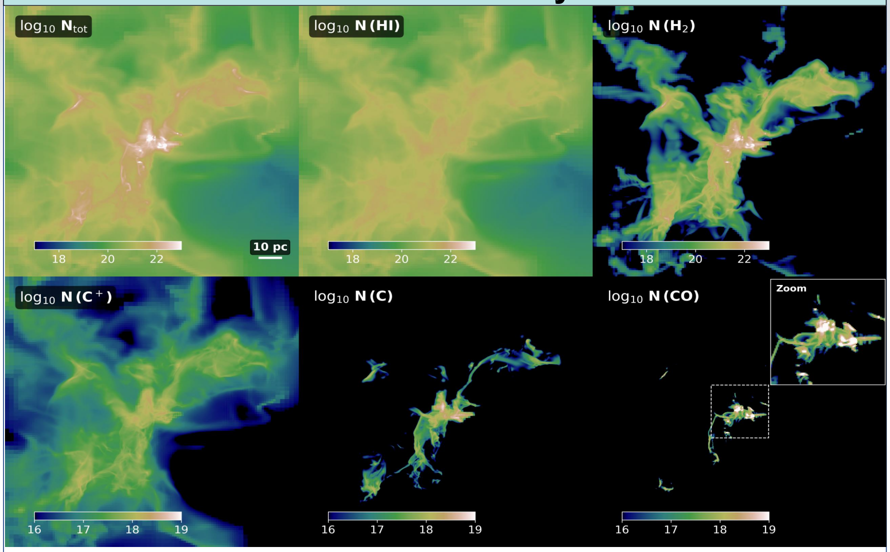

Fig.2. Column density plots of the star-forming region taken from SILCC-Zoom (Seifried et al. 2017).

Integrated maps and self-absorption

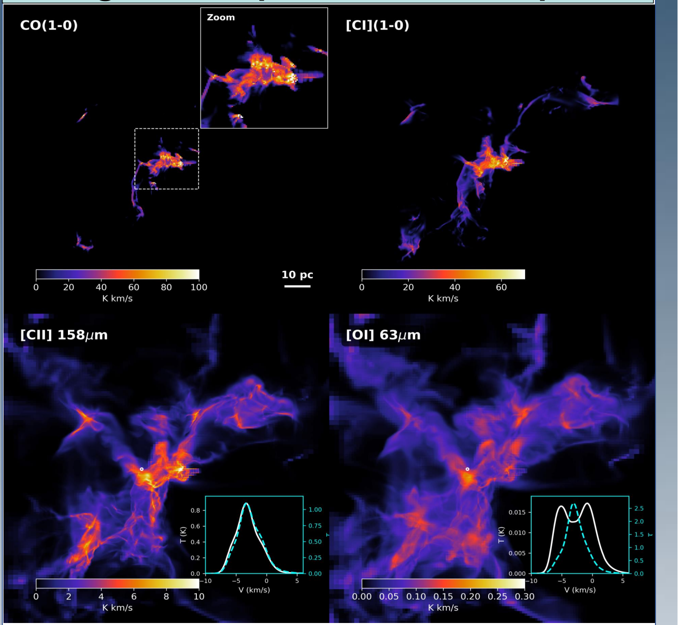

Fig.3. Velocity-integrated emission maps. The top inset shows a close-up of the central region in CO (1-0). The bottom insets show brightness temperature and optical depth spectra for the white-circled region.

CO-dark molecular gas

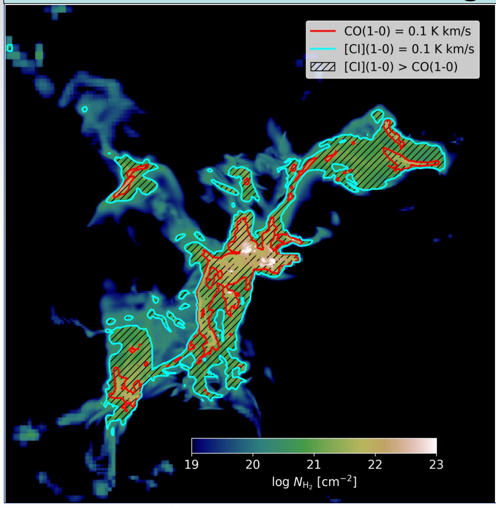

Fig.4. H_2 column density map with contours showing the adopted 0.1 K km s^{-1} detection limit for CO (1-0) (red) and [C I] (1-0) (cyan). The hatched region marks gas where the [C I] (1-0) intensity exceeds CO (1-0). This corresponds to CO-dark gas where [C I] (1-0) is bright (outside the CO-bright region).

Contact:
Zhengping Zhu (zhuzhp@zhejianglab.edu.cn)
Thomas G Bisbas (tbisbas@zhejianglab.edu.cn)

之江实验室
ZHEJIANG LAB

W33 Main

A NEARBY, EVOLVED HUB-FILAMENT SYSTEM
IN THE GODZILLA NEBULA

How far can **accretion flows** through a **hub-filament system** survive after the onset of **massive-star feedback?**

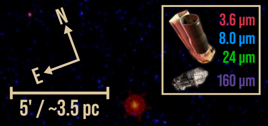

ACCRETION VS. FEEDBACK

VLA observations of NH_3 at ~8700 au, combined with GBT data, trace the **dense molecular gas kinematics.**

We test whether **coherent accretion flows** connect pc-scale **filaments** to the inner **hub**.

VLT/KMOS and VLA recombination lines trace **ionized gas** shaped by massive-star **feedback**.

Our ALMA Cycle 12 observations will test how far hub-feeding survives feedback toward **core scales**.

W33 MAIN QUICK FACTS

Distance	~ 2.4 kpc	Immer+2013,2014
Mass	~ 4000 $M_\odot$	Immer+2013,2014
Bolometric luminosity	~ 449 000 $L_\odot$	Immer+2013,2014
Evolutionary stages	From hot cores to HC & UC HII regions	Wood&Churchwell 1989 Armante+2024

The hub is fed by flows within 1 pc.

Ammonia traces well-organized molecular filaments converging towards a central hub.

XCLASS (Möller+2017) fits reveal **continuous accretion flows from the inner ~1 pc**, while sub-hubs appear to intercept inflow farther out.

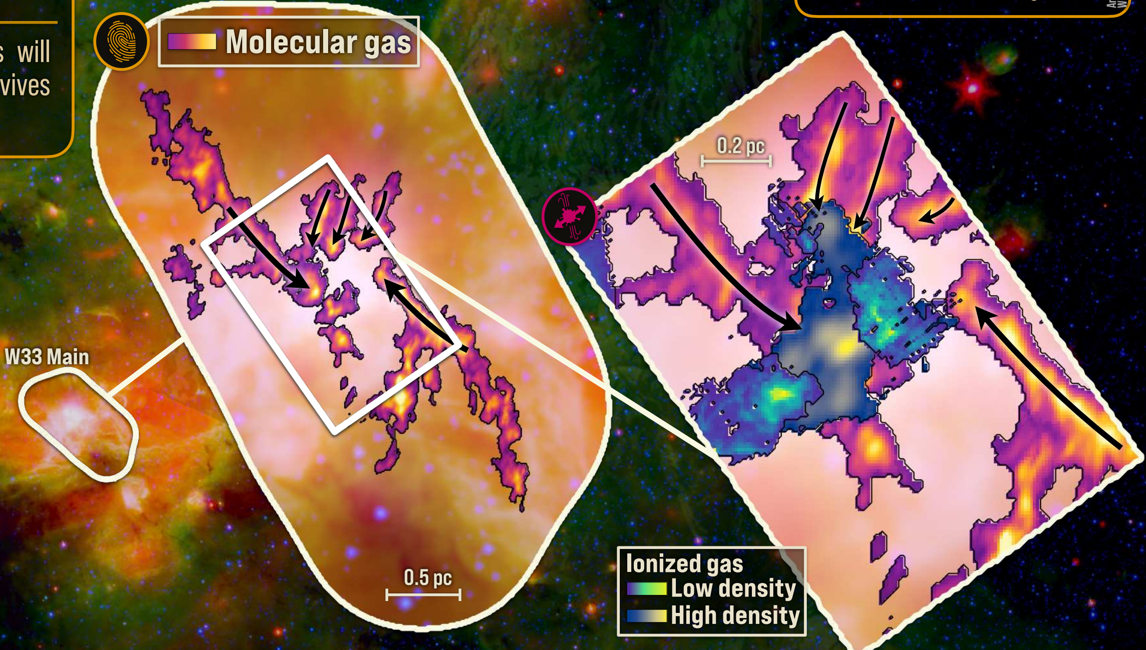

The accretion-feedback interface lies within 0.1 pc.

Feedback escapes anisotropically through low-density channels **instead of disrupting the dense filamentary reservoir** – a champagne flow-like morphology.

Filaments keep their morphology but are heated toward the hub.

The molecular filaments remain morphologically intact into the hub, but XCLASS fits reveal strong heating from ~20 K to ~100 K within the inner ~0.5 pc.

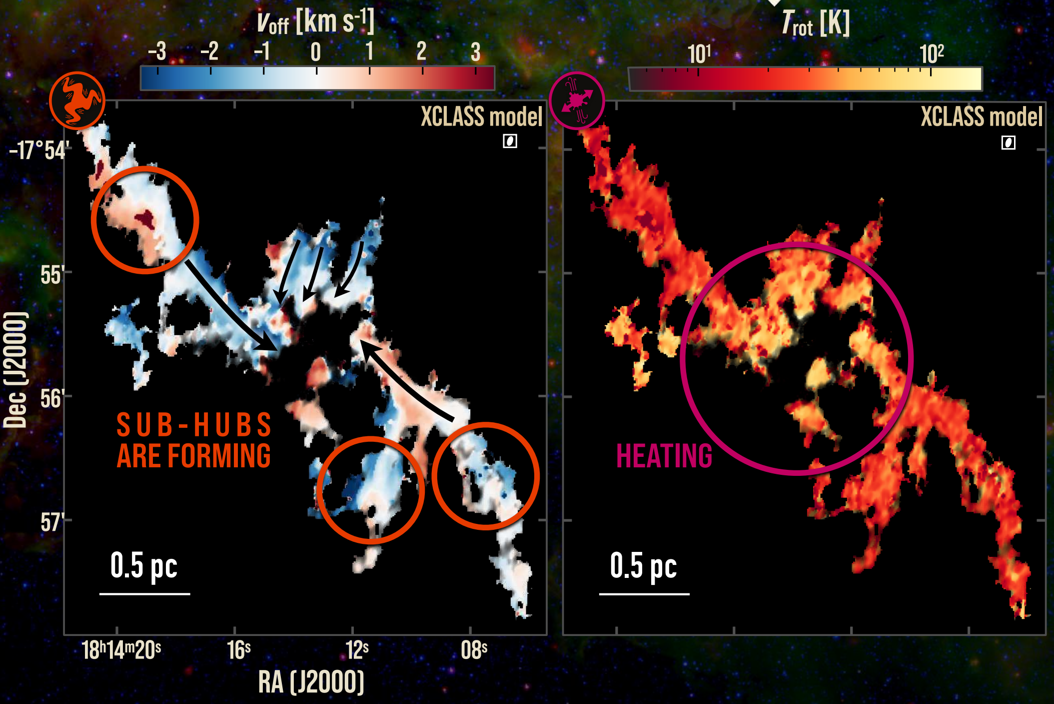

ESO
IMPRS
Lennart Böhm
lennart.boehm@eso.org

Accretion flows still feed the hub while ionized feedback escapes perpendicular to the inflow axis. Our high-resolution follow-up will test how far this feeding survives toward core scales.

18cm OH as a tracer of Dark Molecular Gas Near and Far: First Results from the GBT Survey of OH in M31

Michael P. Busch (Jansky Fellow, NRAO)
mpbusch@nrao.edu

(Scan for your next Sudoku book!)

Molecular Gas in the Galaxy

Molecular gas is an important component of the interstellar medium (ISM) to measure for several reasons:

- Star formation rates depend on the total mass of molecular gas
- Chemistry of Photodissociation Regions (PDRs)
- Missing baryons have implications for cosmology
- Tracing galactic structure

Carbon-Monoxide (CO) is used as a conventional tracer for molecular gas because molecular hydrogen, the most abundant molecule, is non-emitting in cold molecular environments of the general ISM. CO is bright and abundant.

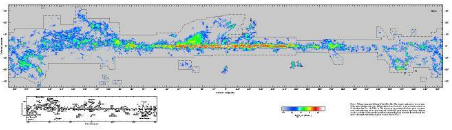

What is 'Dark' Molecular Gas?

Dark Molecular Gas is inferred from observational hints that CO (molecular) and HI (atomic) lines are not tracing the total gas content as traced by dust emission.

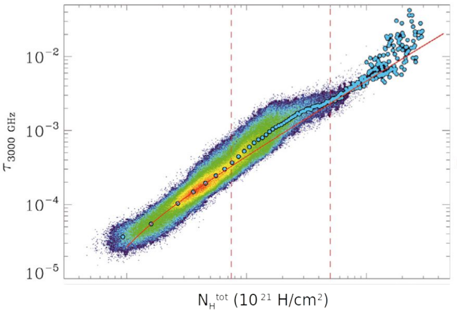

Planck Collaboration: *Planck* XIX, 2011

PDR Schematic

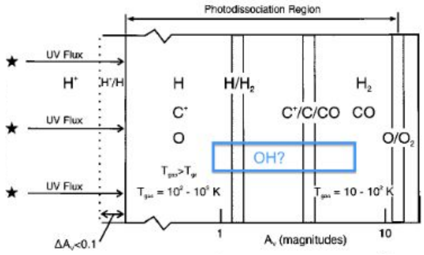

Figure Adapted from Li 2015, who adapted it from Tielens 2005.

Dark molecular gas (or "CO-dark" gas) is expected from theoretical models which show that CO may not exist in environments of **low column density**, where the CO molecule may not be sufficiently shielded from ambient interstellar flux and thus photodissociation occurs.

Additionally, there may not be sufficient volume density to excite the CO molecules collisionally in diffuse environments, and both mechanisms are most likely at play in understanding the dark molecular gas.

Observing Dark Molecular Gas with OH

In Busch et al 2021, we showed that OH traced an abundant amount of molecular gas not seen by CO in the form of a diffuse disk. In Busch 2024, we detected quasi-thermal OH from the outskirts of the Andromeda galaxy at an R ~ 13 kpc.

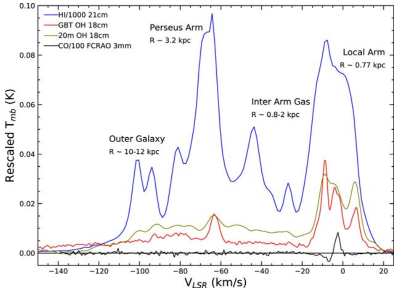

Busch et al. 2021 – Thick Disk of Dark Molecular Gas In the Outer Galaxy

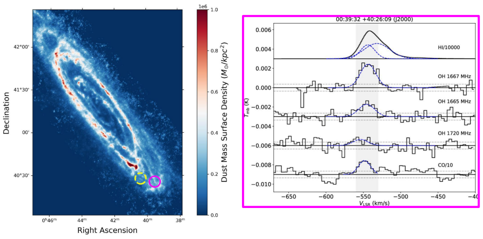

Left: The dust surface density of M31, yellow circle. Right: HI, OH 1665, 1667 and 1720 MHz and CO (Dame 1998).
Busch 2024 - Detection of quasi-thermal ("normal") OH emission in another Galaxy.

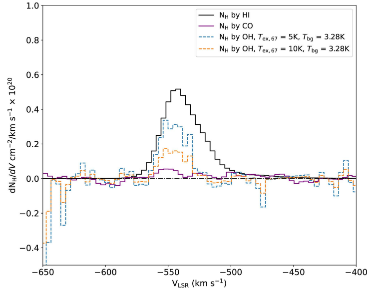

All gas tracers transformed to physical units (hydrogen nuclei column density). OH appears to trace 2x more than CO at this location.

Survey Design of the M31 Northern Molecular

We designed the follow-up survey of M31 to cover the northern molecular ring of M31, which is completely CO-bright gas. The reason for this is to compare the OH and CO directly when both are detected on galactic scales to calibrate the CO-to-H2 conversion factor using OH as a secondary tracer of H2. In addition we will be able to constrain the amount of gas in each aperture using new dust maps from HST's PHAT survey (Gordon et al. 2016).

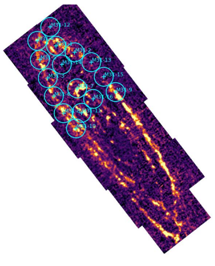

M31 – CO Nieten Map

GBT/GBO, NRAO/AUI

Initial Results: Spectra of OH and CO

We have reduced the preliminary OH 1667 MHz spectra and compared them to the smoothed CO data (IRAM 30m). We observe OH in every position that has CO bright gas. We infer that these positions are rich of molecular gas and in the molecular ring of M31.

We will be comparing kinematics, mass inferred by both tracers soon.

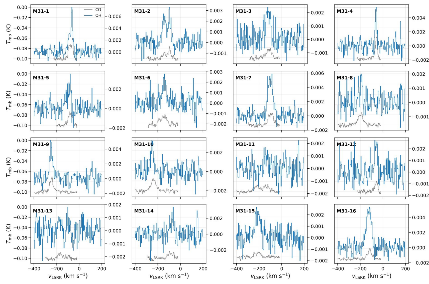

CO Spectra (black), and OH 1667 MHz spectra of M31 positions. (Preliminary)

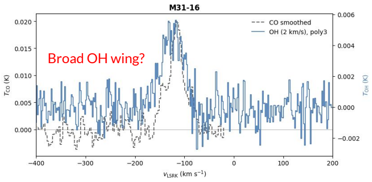

Zoom in on M31-16 comparing the OH and CO towards this position.

Conclusions & Future Work

We have shown that **OH appears to trace the Dark Molecular Gas** with sensitive radio observations (RMS ~ 3mK). With differences between CO and OH emission being explained as a consequence of excitation conditions and radiative trapping, as shown by both volume and column density.

New surveys of OH in M31 and M33 are planned in order to sample the extent of the dark molecular gas in the local group. Phased array feed technology will make mapping this faint signal much more viable, while ngVLA and SKA will observe OH in absorption across the sky. We will be observing more of M31 in the future.

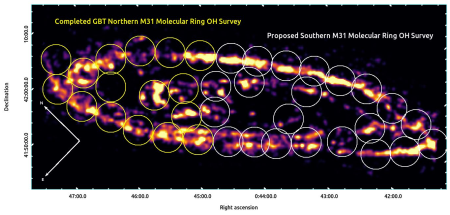

References

Allen, R. J., Hogg, D., & Engelke, P. 2015, ApJ,149, 123
Busch, M. P, Allen, R. J., Engelke, P., Hogg, D., Neufeld, D., & Wolfire, M, 2019, ApJ, 883, 158
Busch, M. P, Engelke, P., Allen, R. J., Hogg 2021 *ApJ* 914 72
Busch, M. P. 2024 *ApJ* 967, 148
Dame, T. et al. 1993 *ApJ*, 418, 730
Engelke, P., & Allen, R. J. 2019, ApJ, 874, 49
Gordon, K. D., et al. *ApJ*, 826, 104
Grenier, I. A., Casandjian, J.-M., & Terrier, R. 2005, Sci, 307, 1292
Hollenbach, D. J. & Tielens, A. G. G. M., 1999 Rev. Mod. Phys. 71, 173
Neufeld, D., Kaufman, M., Goldsmith, P., Hollenbach, D., & Plume, R. 2002, ApJ, 580, 278
Nieten, Ch., et al. 2006 A&A 453, 459-475
Wolfire, M. G., Hollenbach, D., & McKee, C. F. 2010, ApJ, 716

SFRS & PHANGS: Multiwavelength Tracers of Massive Star Formation Rates in Nearby Galaxies

PhD Candidate at University of Virginia, Charlottesville
wzb3eb@virginia.edu

Anna Dignan[1], **Eric Murphy**[2], **Cosima Eibensteiner**[2], **Adam Leroy**[3], and the
Star Formation in Radio Survey (SFRS) & PHANGS (Physics at High Angular Resolution in Nearby Galaxies) Teams
[1]University of Virginia, Charlottesville, VA [2]National Radio Astronomy Observatory, Charlottesville, VA [3]The Ohio State University, Columbus, OH

Context

Massive stars play a critical role in the formation and evolution of galaxies and planets, as well as the chemical enrichment of the ***interstellar medium (ISM).*** Therefore, knowing where and how massive stars form is a crucial part of understanding the planetary systems, galaxies, and molecular gas that make up the Universe.

Measuring SF rates is essential for studying galaxy formation and evolution; however, the various tracers used to do so probe different timescales and can suffer from complications. Here, I attempt to disentangle the discrepancies among tracers using observations from the SF in Radio (SFRS) and Physics at High Angular Resolution in Nearby GalaxieS (PHANGS) surveys.

Observations

SFRS

VLA: 3–33 GHz radio continuum

33 GHz (Murphy+2012, 2018)

3 and 15 GHz (Linden+2020)

13 Galaxies

PHANGS

ALMA: CO (J=2–1) (Leroy+2021)

JWST/MIRI: 21 µm (Lee+2023)

MUSE/VLT: H recomb. lines (Emsellem+2022)

VLA: 2.85″ ~185 pc → **ALMA:** 1.65″ ~85 pc

Example galaxy: NGC 4254

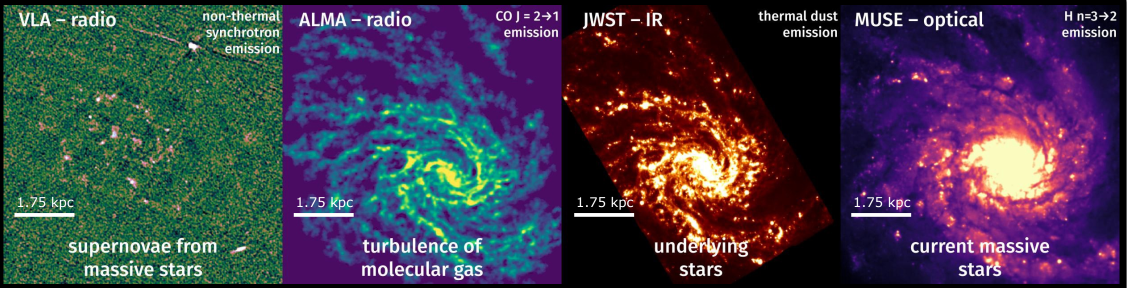

VLA: α^{NT}, 33 GHz SF rates
13/13 galaxies

SFE

ALMA: M_{mol}, I_{CO}, line widths
13/13 galaxies

JWST: 21 µm SF rates
12/13 galaxies

MUSE: BPT diagram, Hα SF rates
5/13 galaxies

How does supernova feedback regulate SF?

Do **steeper α^{NT}** (older supernova remnants) correspond with **broader line widths** (more turbulence)?

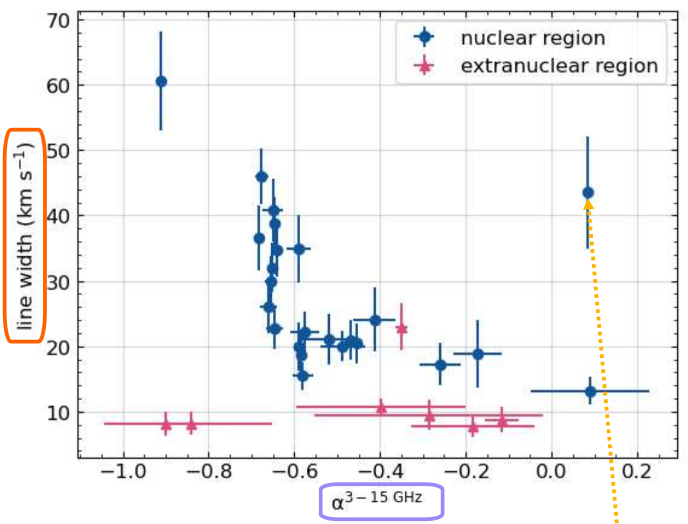

Next up: do **broader line widths** (more turbulence) correspond with **lower SF efficiencies?**

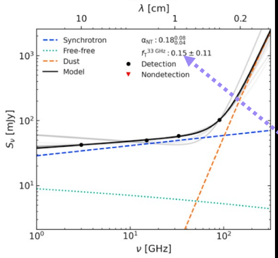

NGC 4579: known outlier due to AGN (Murphy+2018, Dignan+2025)

f_T^{33GHz}: ingredient for calculating 33 GHz SF rates

How do different SF rate indicators compare?

Are **radio, infrared,** and **optical SF rates** consistent with each other, especially in galaxy centers?

Coming soon: Hα SF rates and BPT diagram (do **shallower α^{NT}** i.e. younger supernova remnants correspond with **stronger shocks?**)

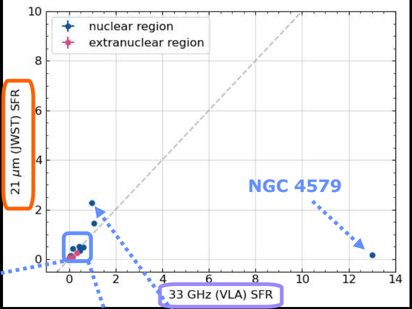

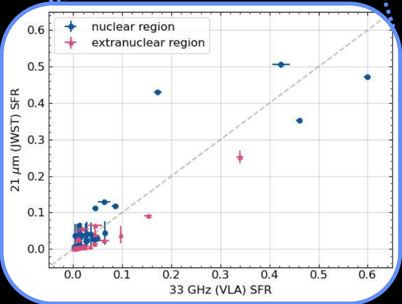

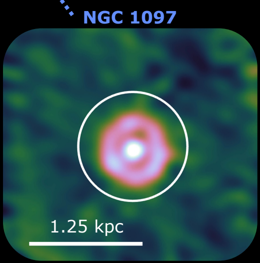

Example galaxy (NGC 0628): WISE Band 1 stellar mass map derived from z0MGS (Leroy+2019)

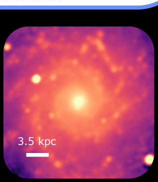

Next up: do **higher stellar masses** (more underlying stars) correspond with **lower SF rates?**

References

1 E. J. Murphy et al 2012, *ApJ* **761** 97 DOI: 10.1088/0004-637X/761/2/97
2 E. Murphy et al 2018, *ApJS* **234** 24, DOI: 10.3847/1538-4365/aa99d7
3 S. T. Linden et al 2020, *ApJS* **248** 25, DOI: 10.3847/1538-4365/ab8a4d
4 A. K. Leroy et al 2021, *ApJS* **257** 43, DOI: 10.3847/1538-4365/ac17f3
5 J. C. Lee et al 2023, *ApJL* **944** L17, DOI: 10.3847/2041-8213/acaaae
6 E. Emsellem et al 2022, *A&A* **659** A141, DOI: 10.1051/0004-6361/202141727
7 A. Dignan et al 2025, *ApJ* **988** 216 DOI: 10.3847/1538-4357/ade436
8 A. K. Leroy et al 2019, 2019 *ApJS* **244** 24 DOI: 10.3847/1538-4365/ab3925

RETHINKING MOLECULAR DIAGNOSTICS IN EXTREME ENVIRONMENTS

INSIGHTS FROM ASTROCHEMICAL MODELING

Katarzyna Dutkowska[1], Bin Jia (贾彬)[1], Gijs Vermariën[1], Mathilde Bouvier[1], Serena Viti[1, 2, 3]

[1]Leiden Observatory, Leiden University, The Netherlands
[2]TRA 'Matter'/Argelander-Institut für Astronomie, University of Bonn, Bonn, Germany
[3]Department of Physics and Astronomy, University College London, Gower Street, London, UK

TOOL: UCLCHEM
(gas-grain chemical code)

GOAL: Explore chemistry under extreme physical conditions

- T warm (> 50 K)
- n_H dense (> 10^3 cm^{-3})
- ζ strong (≳ 10^{-16} s^{-1})
- G_0 strong (≳ 10 Habing)
- v_s slow to fast (≳ 5 km s^{-1})

REGIONS: Galactic Center
and nearby starbursts

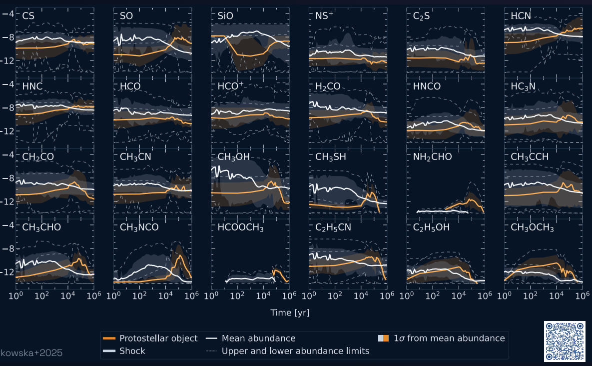

Dutkowska+2025

Gas-phase abundances

←Time-averaged abundances of **24 species** under **Galactic Center**-like conditions

- Integrated molecular signatures can obscure environmental complexity
- Combining multiple tracers may help disentangle the dominant physical processes

Interpreting molecular abundances requires accounting for the coupled effects of physical processes

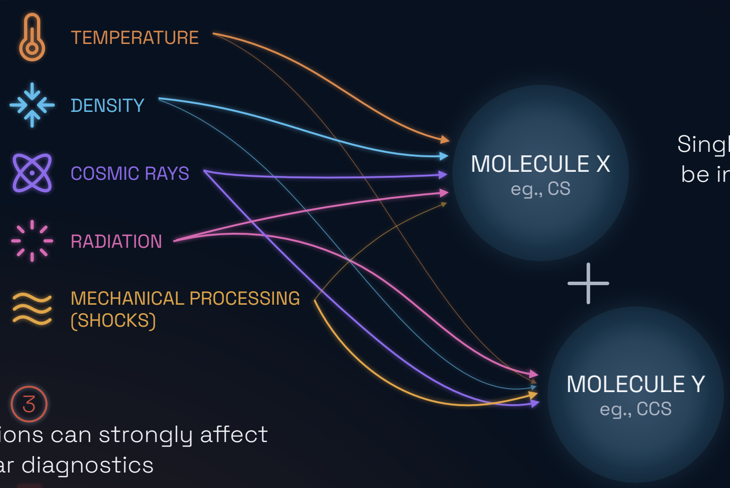

① Single-species diagnostics may be insufficient to constrain the underlying physics

③ Chemical assumptions can strongly affect molecular diagnostics

- **HCO⁺** is widely used as a tracer of dense gas and ionization in extreme environments
- Recent models[3,4] show that its abundance can vary by several orders of magnitude depending on the adopted **chemical network** and local physical conditions
- Removal of the destruction channel **C + HCO⁺ → CO + CH⁺** is linked to the strongest abundance enhancements
- Similar network-dependent effects may influence other commonly used molecular tracers

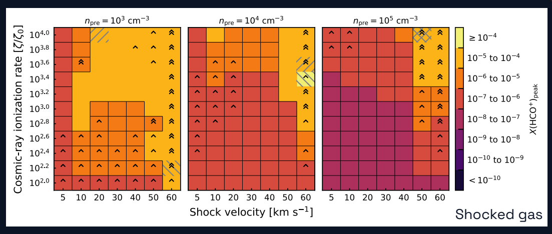

Dutkowska, Jia+2026 submitted

⩓ 1 ≤ $\Delta_{UMIST22/UMIST12}$ < 2 dex // Global maximum in UMIST12
^ $\Delta_{UMIST22/UMIST12}$ > 2 dex \\ Global maximum in UMIST22

② Combining multiple tracers helps disentangle competing physical processes

- **CS** and **CCS** were observationally associated with the same quiescent GMC gas component in the center of **NGC 253**[1]
- Chemical models[2] suggest that the two species may not trace the same gas, while the CS/CCS ratio can help separate starburst- and shock-dominated scenarios
- Interpreting the observed ratios may therefore require combining multiple tracers and diagnostics

Shock-dominated

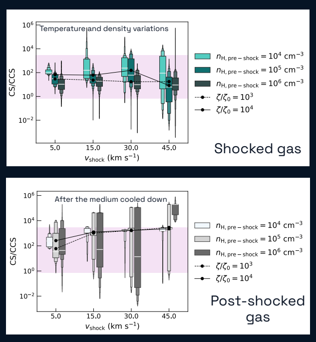

Bouvier, Dutkowska+in prep.

Starburst-dominated

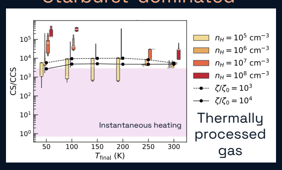

Bouvier, Dutkowska+in prep.

Key takeaways

- Similar molecular signatures can emerge under very different environmental conditions
- Individual tracers may probe distinct gas components within the same region
- Predicted abundances of common tracers such as HCO⁺ can depend strongly on the adopted chemical network

Contact me:

kmdutkowska.carrd.co
dutkowska@strw.leidenuniv.nl

References: [1] Bouvier+2024 [2] Bouvier, Dutkowska+in prep. [3] Dutkowska+2025 [4] Dutkowska, Jia+2026 submitted
UCLCHEM: Holdship+2017 (uclchem.github.io)

Nitrogen enhancement of GN-z11 due to the pollution from supermassive stars

Sho Ebihara
UTokyo / University of Manchseter D1

Abstract

GN-z11 shows high log(N/O)>-0.25, and supermassive stars' (SMS) stellar wind is suggested as the possible origin of nitrogen (Isobe+23). Using the galaxy formation simulation, we added SMS pollution and tested whether SMS can realize a GN-z11-like nitrogen-rich galaxy. We assumed that SMS formed at the galaxy center, formed the ionized bubble, polluted the inside, and emitted emission lines. From star formation history, we assumed the central SMS weighed $10^{3-5}\ \mathrm{M}_\odot$. Mixing SMS ejecta with galactic gas by changing the pollution fraction, we found that 10—30 % pollution can reproduce a GN-z11-like galaxy. This pollution fraction occurs when SMS forms a Strömgren sphere at a gas density of $10^{4-5}\ \mathrm{cm}^{-3}$.

Introduction: GN-z11 is N/O-enhanced

GN-z11 shows log(N/O)>-0.25, which is higher than that of local galaxies, log(N/O)<-0.8 (Fig. 1).

GN-z11's chemical abundance is biased from the abundance of CCSN's ejecta, toward the abundance produced by the CNO cycle equilibrium state. (Fig. 1)

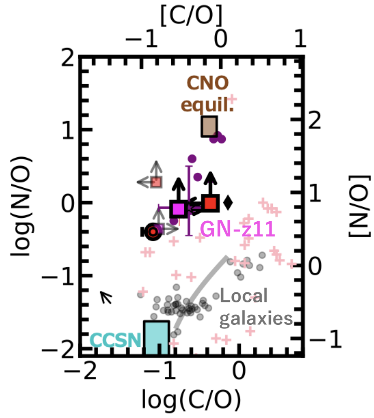

Fig.1: Chemical abundance ratio of GN-z11, local galaxies, CNO-cycle's equilibrium state, and core-collapse supernovae. (Isobe+23)

Introduction: possible origins of high N/O

- Wolf-Rayet stars (WR)
- Supermassive stars (SMS, $>10^4\ \mathrm{M}_\odot$)
- Tidal disruption events (TDE)

By using a one-zone model, Isobe+23 suggested these stellar events can produce GN-z11-like nitrogen-rich abundance (Fig. 2).
⇨Testing SMS pollution by more realistic galaxy simulation is a new approach.

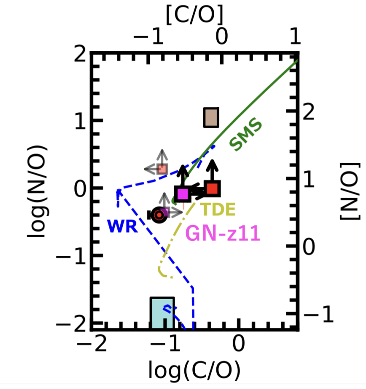

Fig.2: Possible chemical abundance ratio produced by WR, SMS, and TDE. (Isobe+23)

Method ~adding SMS to the simulation~

We used the N-body/SPH code ASURA (Saitoh+09) and the chemical evolution library CELib (Saitoh+17).

We assumed that SMSs are located at the center of globular clusters through runaway collisions (Fujii+24).

We also assumed that (1) the central SMS formed an ionized sphere, (2) the SMS polluted inside the sphere, and (3) we observed the emission lines from the sphere.

The next step is… to estimate the mass of the central SMS and the size of the ionized bubble.

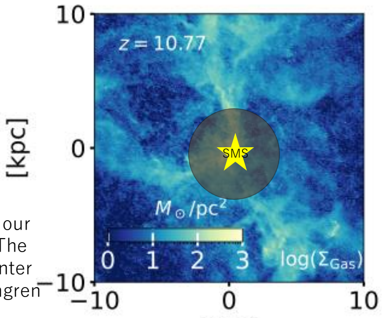

Ebihara+26

Fig.3: The concept picture of our SMS formation assumption. The SMS formed at the galaxy center and pollutes inside the Strömgren sphere it made, resulting in emission lines.

Result ~How does the central SMS weigh?~

From Fujii+24, $3-5\ \%$ of the system's star formation rate (SFR) is transferred to SMS mass accretion. We found that the SFR around the galaxy center ($<10\ \mathrm{pc}$) is $0.3-30\ \mathrm{M}_\odot\ \mathrm{yr}^{-1}$. Thus,

Mass accretion rate: $3-5\ \%$ of $0.3-3\times10^1\ \mathrm{M}_\odot\ \mathrm{yr}^{-1}$⇨ 9.0×10^{-3}–$1.5\ \mathrm{M}_\odot\ \mathrm{yr}^{-1}$.

In contrast, according to Vink+18, the SMS's mass loss follows:
$$\log \dot{M} = -9.13 + 2.1\log(M_{\mathrm{SMS}}/\mathrm{M}_\odot) + 0.74\log(Z/Z_\odot)\ [\mathrm{M}_\odot\ \mathrm{yr}^{-1}],$$

where adopted our galaxy's metallicity $Z=0.1\,Z_\odot$.

SMS reaches its maximum mass when mass accretion and mass loss rate are balanced. Under our accretion rate range, 9.0×10^{-3}–$1.5\ \mathrm{M}_\odot\ \mathrm{yr}^{-1}$, our SMS grows to $10^{3-5}\ \mathrm{M}_\odot$ (see Fig. 4).

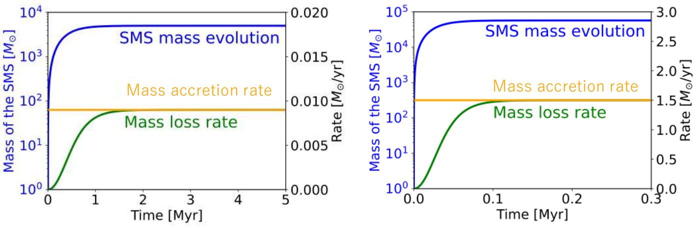

Fig.4: The SMS mass evolution under the constant mass accretion rate, $9.0\times10^{-3}\ \mathrm{M}_\odot\ \mathrm{yr}^{-1}$ (left) and $1.5\mathrm{M}_\odot\ \mathrm{yr}^{-1}$(right). (Ebihara+26)

Result ~SMS changes chemical abundance~

Fig.5: The chemical abundance change if SMS ejecta were mixed with our galaxy's gas at z=10.77 (the blue triangle). The grey triangle shows our simulated galaxy's abundance between z=10.6 and z=10.77. The blue and yellow shaded region is GN-z11 by Isobe+25 for $n_e=10^3$ and $10^5\ \mathrm{cm}^{-3}$, respectively.

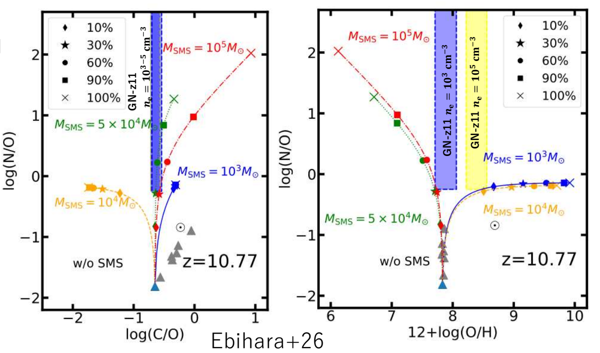

Ebihara+26

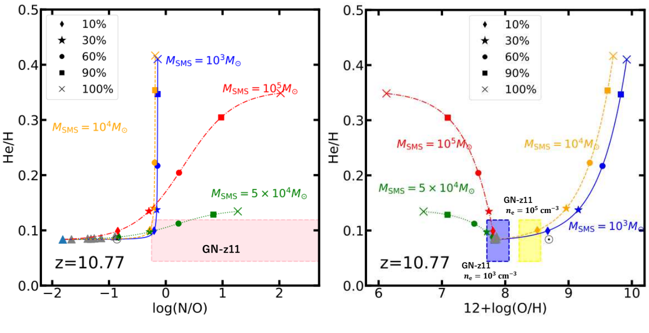

Nagele+23 calculated ejecta from $10^{3-5}\ \mathrm{M}_\odot$ SMSs. We mixed the ejecta into our result by changing the pollution fraction ($f_{\mathrm{SMS}}=\frac{M_{\mathrm{ej}}}{M_{\mathrm{ej}}+M_{\mathrm{gas}}}$) (Fig. 5). ($M_{\mathrm{ej}}$: Mass of ejecta, M_{gas}: Mass of galactic gas)

To determine the realistic pollution fraction, we assumed the size of an ionized bubble. We assumed gas number density $10^3, 10^4$ and $10^5\ \mathrm{cm}^{-3}$ and calculated enclosed gas mass and pollution fraction (f_{SMS}) of SMS (Table 1).

Table 1	n_{H} [cm^{-3}]	Strömgren radius [pc]	Enclosed gas mass [$\mathrm{M}_\odot$]	Pollution fraction[%]
Low density model	10^3	16.4	4.59×10^5	0.99
Middle density model	10^4	3.54	4.59×10^4	9.09
High density model	10^5	7.63×10^{-1}	4.59×10^3	50

From Fig. 5, the pollution fraction of ~ 30% is most suitable.
⇨ $10^{4-5}\ \mathrm{cm}^{-3}$ gas density is most desirable.

Summary

- GN-z11 is nitrogen-rich, and supermassive stars (SMS) are possible polluters.
- Using a galactic simulation, we incorporated SMS pollution into galactic chemical evolution.
- We assumed that SMS formed at the galaxy center, formed the ionized bubble, polluted the inside, and emitted emission lines.
- From star formation history, we assumed the central SMS weighed $10^{3-5}\ \mathrm{M}_\odot$. Mixing SMS ejecta with galactic gas by changing the pollution fraction,
- We found that 10—30 % of the pollution can reproduce a GN-z11-like galaxy. Such a pollution fraction occurs when SMS forms a Strömgren sphere at a gas density of $10^{4-5}\ \mathrm{cm}^{-3}$.

Post-Processing Hydrodynamical Simulations: A Pipeline for Astrochemical Evolution in Molecular Clouds

abubakar.fadul@uni-due.de

Abubakar Fadul & Brandt Gaches | Faculty of Physics, University of Duisburg-Essen, Lotharstraße 1, 47057 Duisburg, Germany

Introduction

A molecular cloud consists of gases and dust, from which stars and planets are formed. Modelling the chemistry of molecular clouds is crucial to understand their evolution. However, due to the computational cost of 3D simulations, most of the models restrict the chemistry to a certain amount of species. In this work, we present a Julia-based post-processing pipeline with gas-phase chemistry (and ice-phase chemistry planned), which allows us to compute chemical abundances from hydrodynamical simulation outputs, while reducing the computational cost.

Methodology

The chemical evolution of a reaction network can be described by a set of coupled ordinary differential equations (ODEs). Given the physical conditions and the reaction network, the abundance of each species evolves according to its formation and destruction rates:

$$\frac{\mathrm{d}n_i}{\mathrm{d}t} = \sum_{j\in F_i}\left(k_j \prod_{r\in R_j} n_{r(j)}\right) - \sum_{j\in D_i}\left(k_j \prod_{r\in R_j} n_{r(j)}\right)$$

where n_i is the abundance of the i^{th} species, F_i is the set of all reactions that produce species i, k_j is the rate coefficient of the j^{th} reaction, R_j is the Reactants involved in reaction j, D_i is the set of reactions that destroy species i, and $n_r(j)$ is the number density of reactant r in reaction j. This produces a coupled system of Ordinary Differential Equations, solved numerically in Julia using DifferentialEquations.jl

Results

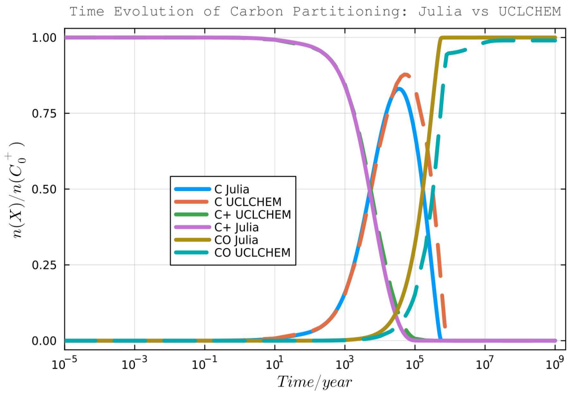

Figure 1. Fractional abundances of C^+, C, and CO relative to the initial ionized carbon abundance as a function of time. The chemical evolution shows the conversion of C^+ into C and subsequently into CO. Solid lines represent the Julia model, while dashed lines show UCLCHEM results for same physical conditions.

We benchmarked the Julia against UCLCHEM using a reduced 33-species chemical network under warm moderately shielded molecular gas ($n_H = 10^4$ cm^{-3}, $A_V = 1$ mag, T = 300 K, $\zeta = 1.31\times10^{-17}$ s^{-1} , and $G_0 = 1.7$). The Julia implementation reproduces the overall chemical behavior of UCLCHEM while achieving an order-of-magnitude improvement in computational performance for the same physical conditions and chemical network.

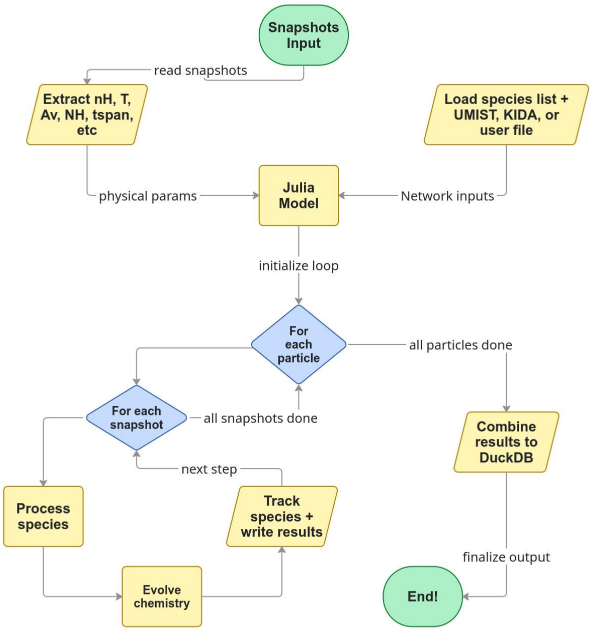

Figure 2. Flowchart of the Julia pipeline. The model first extracts the relevant physical conditions from the simulation snapshots and loads the desired chemical database. For Every Particle across all snapshots, the Model Evolutions the Chemistry, tracks through species time, and records the results. After all particles are processed, the results are written into a single DuckDB database for future analysis.

Conclusion

- The benchmark confirms that the Julia implementation preserves the overall chemical behavior
- The improved computational efficiency makes the Julia framework suitable for larger chemical networks
- Current simulations include gas-phase chemistry only; future work will include ice-phase chemistry

References

- Holdship, J., et al. (2017). "UCLCHEM: A Gas-Grain Chemical Code for Clouds, Cores, and C-Shocks." *The Astronomical Journal*, 154(2), 38.
- Bezanson, J., Edelman, A., Karpinski, S., & Shah, V. B. (2017). Julia: A fresh approach to numerical computing. SIAM review, 59(1), 65-98.

Deutsche Forschungsgemeinschaft
German Research Foundation

UNIVERSITÄT DUISBURG ESSEN
Offen im Denken

PHYSIK

Expansion Signatures in 35 H II Regions traced by SOFIA [C II] Emission

Timothy Faerber, L. D. Anderson, M. Luisi, L. Bonne, N. Schneider, V. Ossenkopf-Okada, A. G. G. M. Tielens, R. Simon, and M. Rollig

Center for Gravitational Waves and Cosmology, West Virginia University | Prepared for The Olympian Symposium 2026

35 H II regions in the SOFIA [C II] sample

12 Expansion candidates from PV diagrams

12.2 km/s Mean expansion velocity of the candidates

9/12 Expansion candidates with bubble morphologies

Abstract

We analyze expansion in 35 Galactic H II regions observed in [C II] 158 μm with SOFIA. Using moment maps and PV diagrams, 12 (~34%) show expansion, with a mean velocity of ~12.2 km s^{-1}. Bubble-like regions expand more often than irregular ones. Blueshifted expansion dominates (8 solely blueshifted, 1 redshifted, 3 both), indicating geometric or observational bias. Spherical models support expansion in 8 of 12 candidates; dynamical ages are 10–100× shorter than ionizing star lifetimes. Fourteen regions (~40%) are [C II] bubbles, including 9 expansion candidates. Thermal pressure likely drives expansion in M43; stellar winds dominate M17, M42, RCW 120, and RCW 79.

Research Summary

- 35 SOFIA [C II] H II region PDR maps analyzed for expansion via PV diagrams and residual modeling.
- 12/35 show expansion; 9/12 are bubble-like [C II] shells.
- Mean expansion velocity: 12.2 km/s; blueshifted detections dominate.
- M17, M42, RCW 120, and RCW 79 favor stellar winds; M43 favors thermal expansion.

Scan for Faerber et al. 2025

Figure 1 | HII Region Expansion Diagram

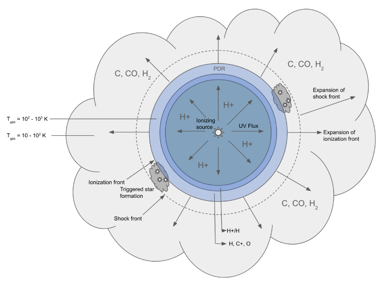

Schematic of an expanding H II region showing an ionization front driving a shell where star formation may be triggered. The ionization front is extremely thin (~10^{-3} pc) compared to the ~1 pc region size, so the figure is not to scale. While real H II regions have complex substructure and shocks, we adopt this simplified model to interpret our observations.

Figure 2 | Representative PV Detections

Two representative position-velocity cuts through M17. The left panels are PV diagrams taken along the red axis in the right panels.

One axis (top panels) shows only blueshifted expansion; the other (bottom panels) reveals both red- and blueshifted shells.

This process was repeated for each H II region in the sample at 16 different angles intersecting the WISE-defined center of each region and extending beyond the PDR in each direction (or as far as emission was as observed).

The ellipses were fitted by eye for each PV diagram. The results for the 12 expansion candidates are shown in Table 1.

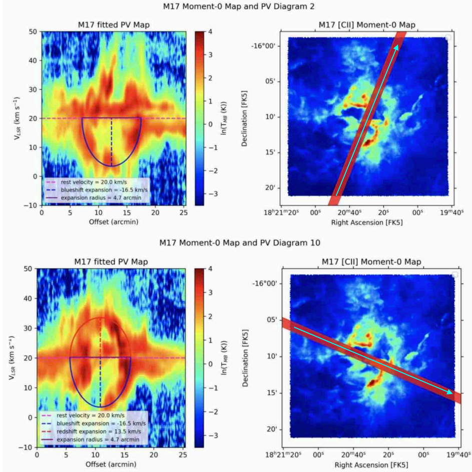

Figure 3 | PV Expansion Asymmetry

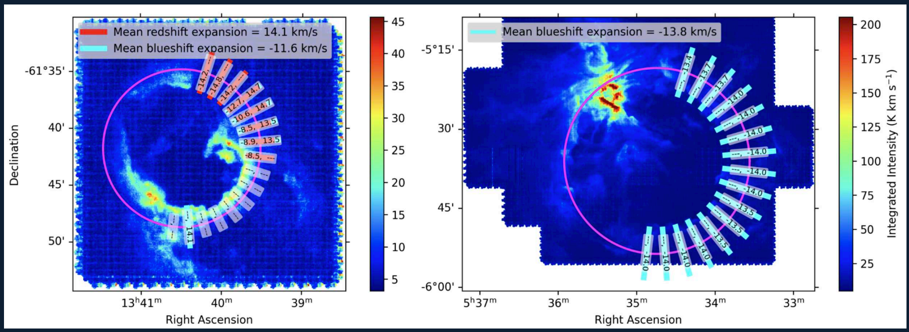

RCW 79: nine of 16 axes show expansion (one blue, four red, four both) within a range of -14.8 km/s to 14.7 km/s

M42 (Orion): all 16 axes show only blueshfited expansion within a range of -14.0 km/s to -13.4 km/s

Figure 4 | Velocity Residual Map: RCW 120

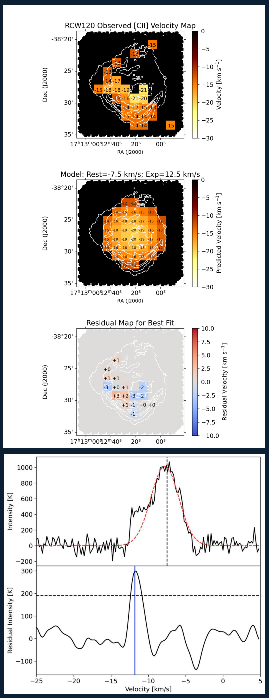

Top: Observed (top), modeled (middle), and residual (bottom) velocity maps for RCW 120. The best-fit shell reproduces the large-scale blueshifted structure and isolates localized non-uniformities. This process was repeated for M17, M42, M43, NESSIE-Aa, NGC 7538, RCW 36, RCW 79, and W40.

Bottom: Example spectrum taken from bin in velocity maps. A Gaussian profile is fitted to the main [CII] component at the rest velocity of the H II region and then subtracted from the raw spectrum (top). The residual emission (bottom) allows us to estimate the line-of-sight velocity of the gas in that bin.

Table 1 | Expansion Candidate Global Parameters

Region	Bubble	Redshift Expansion		Blueshift Expansion		Max. Theoretical Expansion		Ionizing Source(s)	t_source	t_dynamic
		PV Diagrams [km/s]	Velocity Maps [km/s]	PV Diagrams [km/s]	Velocity Maps [km/s]	Thermal Expansion [km/s]	Stellar Wind [km/s]		[Myr]	[Myr]
G083+936	Y	12.6 ± 0.6	-	8.9 ± 0.5	-	-	-	-	-	0.01
G316+796	Y	13.0 ± 0.4	-	-	-	-	-	-	-	0.16
M17	Y	13.2 ± 0.2	10.0 ± 0.8	17.5 ± 1.5	14.0 ± 0.4	10.59	57.03	O4V-O4V	~2.5	0.15
M42 (Orion)	Y	-	-	13.8 ± 0.2	12.0 ± 0.6	10.39	34.41	O7V	~5	0.12
M43	Y	-	-	3.6 ± 1.5	7.0 ± 2.5	9.65	-	B0.5V	~10	0.04
N19	N	-	-	8.3 ± 0.2	-	-	-	-	-	0.47
NESSIE-Aa	Y	-	-	16.4*	10.0 ± 1.1	-	-	-	-	0.10
NGC 7538	Y	-	-	14.6 ± 1.6	11.0 ± 1.3	10.39	-	O7V	~5	0.11
RCW 120	Y	-	-	15.3 ± 0.6	12.5 ± 1.0	10.29	28.43	O8V	~6	0.14
RCW 36	N	-	-	-	-	10.34	14.33	O8V-O9V	~7	0.13
RCW 79	Y	14.1 ± 0.5	14.5 ± 0.5	11.6 ± 2.6	18.0 ± 0.2	10.59	41.50	O3V-O5V	~2.5	0.86
W40	N (Bipolar)	-	-	12.0 ± 0.4	13.0 ± 0.5	-	-	-	-	0.04

*For NESSIE-Aa, expansion was only seen across one of the explored PV axes. Errors were estimated from the standard deviation of the values derived across all axes, so there are no associated errors on PV-derived values for NESSIE-Aa.

Acknowledgements

TF and LDA acknowledge support from Universities Space Research Association grant “H II Region Dynamics Revealed by [C II] Emission” #09-0520.

Timothy Faerber; Ph.D. Candidate, West Virginia University

Stirring the Pot
Spiral-Arm-Induced Star Formation and ISM Enrichment in NGC 628

James Garland
james.garland@mail.utoronto.ca
Laurie Rousseau-Nepton
David A. Dunlap Department of Astronomy & Astrophysics
UNIVERSITY OF TORONTO

Spiral Arms and Gas Enrichment

Spiral arms are the primary sites of star formation in disk galaxies, concentrating gas compression and stellar feedback to shape the structure and chemical enrichment of the ISM. The origin and nature of spiral arms remain unsettled, but **gas-phase metallicity** may preserve subtle azimuthal signatures of arm-driven enrichment and mixing at the **0.01-0.1 dex** level. Two classes of spiral arm models predict different metallicity patterns:

Dynamic spiral arms
Arms co-rotate with the disk, so gas flows into the arms from both sides, yielding **little or no azimuthal offset** in metallicity.

Quasi-stationary spiral density waves
Gas flows across the arms, producing downstream enrichment and an azimuthal gradient that **reverses sign at corotation**.

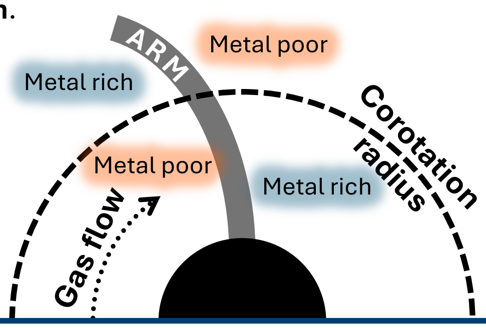

Exploring NGC 628 with SIGNALS

The Star formation, Ionized Gas, and Nebular Abundances Legacy Survey (**SIGNALS**) observed **4285 emission-line regions** in the face-on grand design spiral galaxy NGC 628.

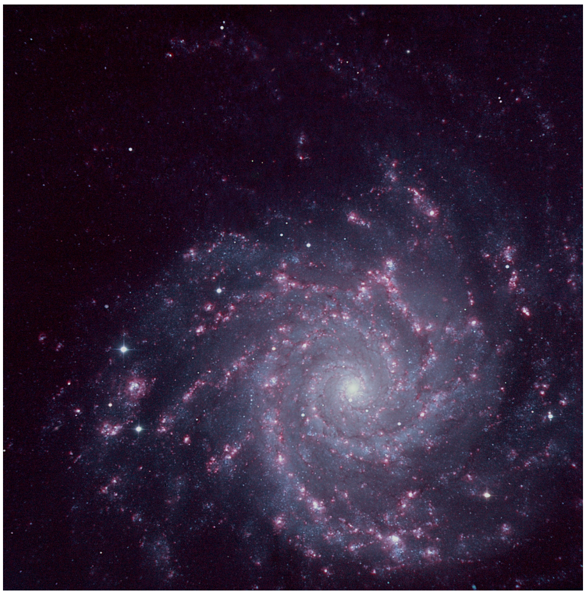

SIGNALS image of NGC 628.

The survey's **high spatial (35 pc) resolution** yields a catalog of H II regions with well-constrained line intensities and physical properties. This enables precise metallicity estimation across the disk using **strong-line calibrations** and **Bayesian photoionization model grid fitting**.

Morphological Classification

We use a **machine learning model** trained on morphological classifications by citizen scientists to obtain a **probabilistic map** of spiral arm strength. The gradient of this map identifies the direction toward peak arm likelihood, allowing each H II region to be assigned an **arm-relative** leading or trailing position.

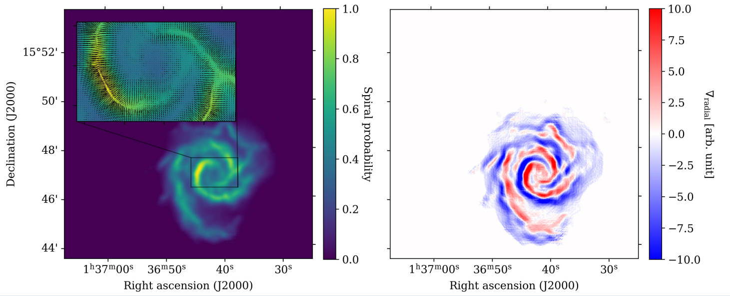

Evidence for Spiral-Induced Enrichment?

Strong line metallicities show trends in leading vs trailing edges of arms with varied **radial dependencies**.

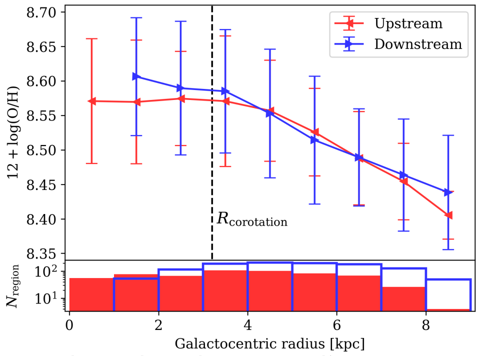

Radially-dependent abundance gradients across arms may be **consistent with spiral density wave theory**.

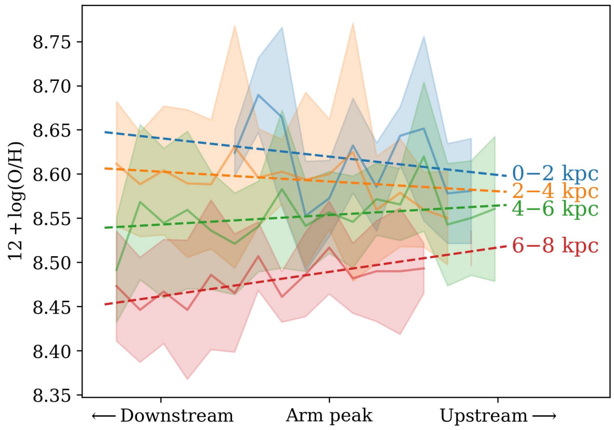

Future Work

Detected azimuthal abundance trends are subtle and may be affected by **metallicity calibration**, **residual radial metallicity gradients**, and **resolution effects**.

Testing these systematics will enable extension to **population-scale IFU surveys**, building a census of how azimuthal ISM structure depends on **galaxy structure**, **star formation**, and **environment**.

Stellar Feedback in the Mini-Starburst Region W43 Main Traced by [C II] 158 μm Emission

Esan Mouli Ghosh[1], **Floris van der Tak**[1,2], **John Bally**[3] **and Alexander Tielens**[4]

1) Kapteyn Astronomical Institute, University of Groningen 2) Netherlands Institute for Space Research (SRON) 3) Department of Astrophysical and Planetary Science, University of Colorado Boulder 4) Astronomy Department, University of Maryland

ESAN MOULI GHOSH

eghosh@astro.rug.nl

Introduction

Stellar feedback from massive stars injects energy and momentum into the ISM, with radiation and winds driving HII regions, expanding shells and complex kinematic structures. W43, a luminous massive star-forming complex at ~5.5 kpc near the junction of the Galactic bar and the Scutum-Centaurus spiral arm, is an ideal Galactic "mini-starburst" laboratory. The far-infrared [C II] 158 μm line traces UV-illuminated gas across photodissociation regions (PDRs), diffuse clouds, and the outer envelopes of molecular clouds.

Observations

We use high spectral-resolution SOFIA upGREAT FEEDBACK [C II] 158 μm observations (14.1″ beam) complemented by multi-wavelength tracers: APEX ^{12}CO(J=3–2) and ^{13}CO(J=3–2) (18″ beam), IRAM ^{13}CO(J=2–1) and C^{18}O(J=2–1) (11.7″ beam), Spitzer 8 μm (2" beam), and Herschel PACS (70μm, 160μm) and SPIRE (250μm–500μm) (5" to 35" beam) dust maps.

Morphology

- Two limb-brightened shells observed towards east and west side of WR-OB cluster, redshifted and blueshifted respectively.
- A bright core and ridge observed in [CII] where the two bubbles and the molecular Z-shaped filament overlap along the LOS.
- The west bubble (7.5 pc x 4 pc) is prominent in 8 μm, 70 μm, 160 μm, and [C II] velocity channels between 70-110 km s^{-1}.
- The east bubble (4.6 pc x 7 pc) is fainter in 8μm but traced by [C II] emission from 90–120 km s^{-1}.

This suggests a bipolar geometry. A persistent 90–95 km s^{-1} gap is observed in [CII] emission. Presence of [C^{18}O] in this velocity range implies absorption by a foreground molecular cloud component

Kinematics

- Position-Velocity diagrams across various regions show complex velocity structures from 70 to 125 km s^{-1} in [CII] emission.
- Ellipse-like structures in PV space are consistent with expanding bubbles. The west bubble is observed in ^{12}CO and ^{13}CO as well.
- The east bubble and west bubble have an average expansion velocity of 15 ± 2 km s^{-1} and 17 ± 2 km s^{-1} respectively.
- There is a background gradient in the systemic velocity of ~20 km/s over 35 pc in the south-west to north-east direction.

Left : RGB plot of [C II] from V$_{LSR}$ = 85–90 km s^{-1} (blue), 95–100 km s^{-1} (green) and 105–110 km s^{-1} (red). Right: Spitzer 8 μm image overlayed with a schematic diagram of W43 complex

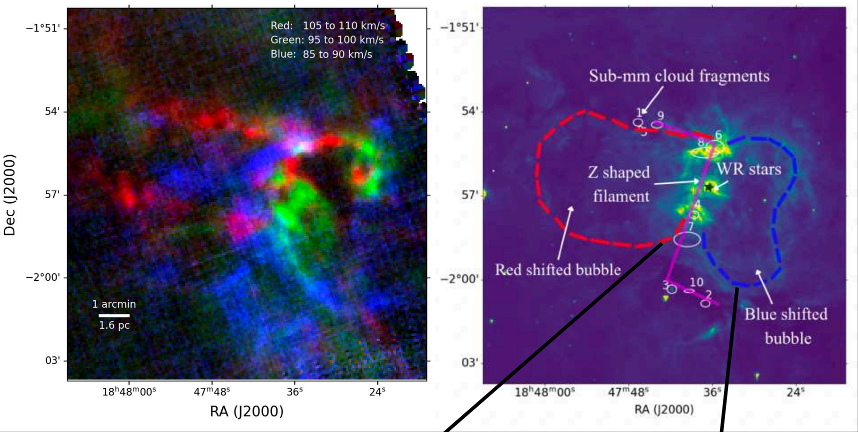

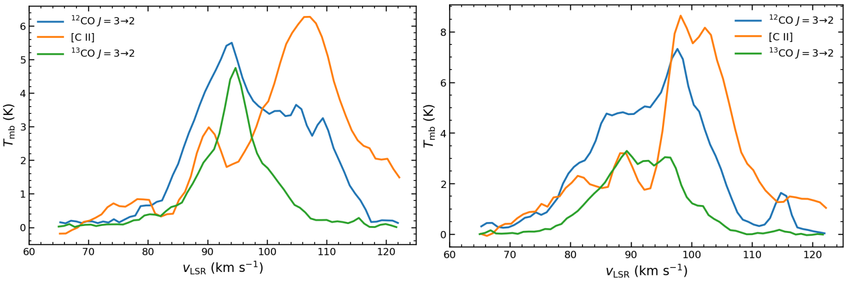

Average [CII], ^{12}CO J=3-2 and ^{13}CO J=3-2 spectra towards east bubble (left) and west bubble (right)

PV diagrams of east (left) and west (right) bubble in ^{12}CO, [CII] and ^{13}CO along with integrated intensity maps and corresponding PV cuts

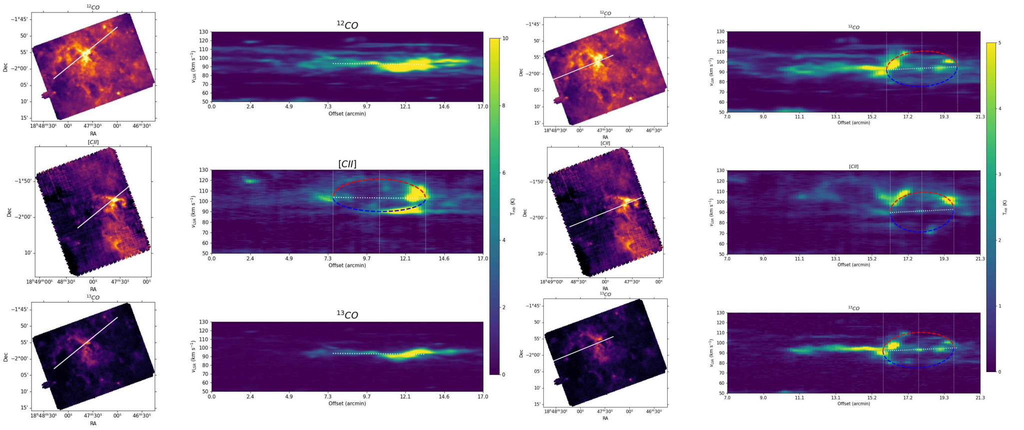

Column Densities and Masses

(Preliminary)

- Dust SED fitting of Herschel Hi-GAL 70–350 μm was carried out. Column densities in dense sub-mm cores (identified by Motte et al 2003) reach above N(H)=1×10^{24} cm^{-2}. Average column density in the east and west bubble are N(H)=5.5×10^{22} cm^{-2} and N(H)=5.9×10^{22} cm^{-2} respectively. The dust temperatures are 27 K and 28 K. Masses of the entire shell are calculated to be 4500 M$_\odot$ and 6800 M$_\odot$
- [^{13}C II] hyperfine emission is detected towards west bubble and will be used to constrain [^{12}C II] column density as well.
- RADEX modelling gives a model-dependent C^{+} column lower than the total dust-derived column.

Energetics

- W43 contains 1 WN7 Wolf–Rayet star and two O-type supergiants, powering the HII region with a total IR luminosity of ~3.5×10^{6} L$_\odot$ and emitting 10^{51} LyC photons s^{-1}
- The east and west bubble have KE of 1.2×10^{49} erg and 1.3×10^{49} erg respectively.

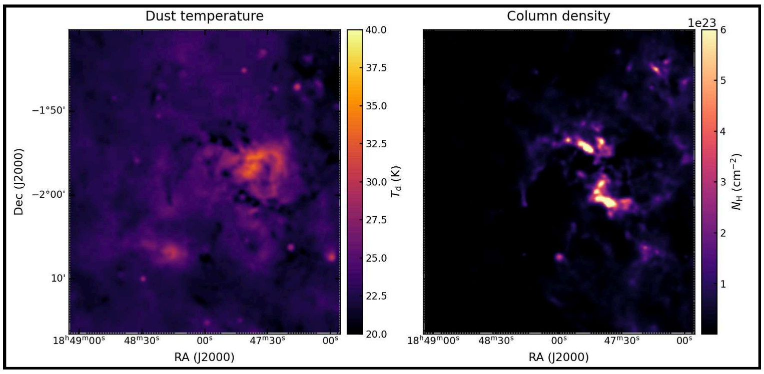

Remarks

- KE of bubbles in W43 are much higher than that of the Orion Veil (2.5×10^{48} erg) and comparable to RCW49 (4×10^{49} erg) which is also powered by WR stars.
- Studying W43 provides a nearby template for feedback in extreme, starburst-like environments that would be observable in nearby galaxies.

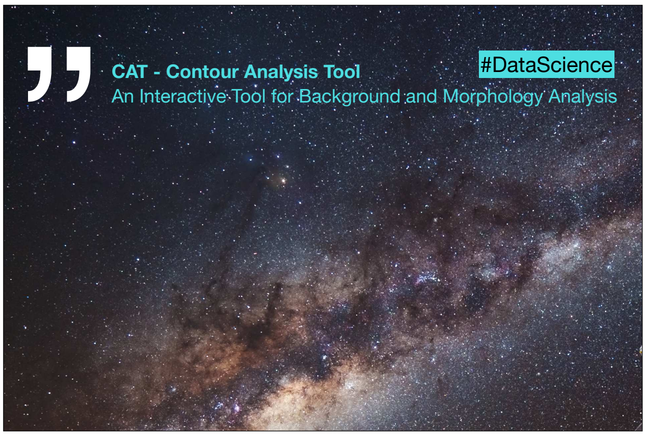
CAT - Contour Analysis Tool
An Interactive Tool for Background and Morphology Analysis
#DataScience

1


#DataScience

2

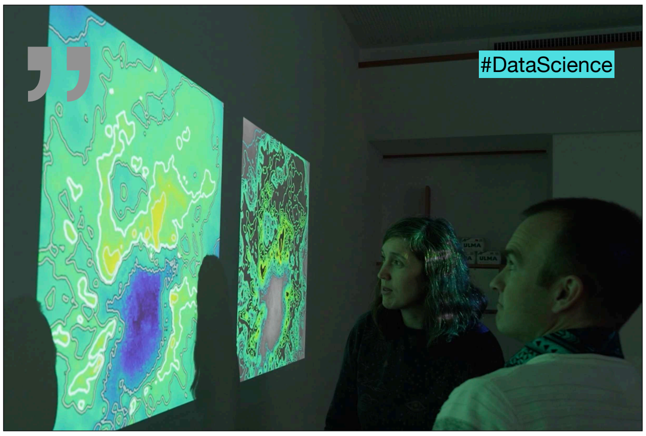
#DataScience

3

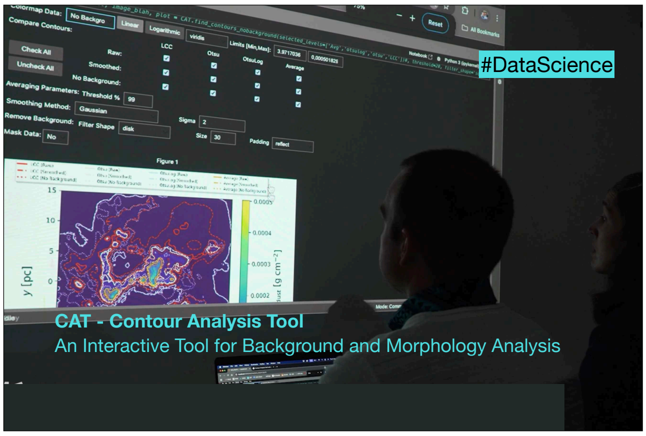
#DataScience
Check All
Uncheck All
Raw:
Smoothed:
No Background:
Averaging Parameters: Threshold %
Smoothing Method: Gaussian
Remove Background: Filter Shape disk
Mask Data: No
Sigma 2
Size 30
Padding reflect
Figure 1
y [pc]
CAT - Contour Analysis Tool
An Interactive Tool for Background and Morphology Analysis

4

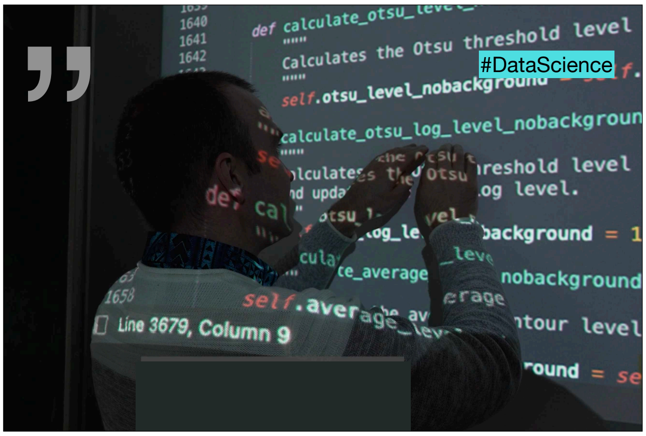
#DataScience
def calculate_otsu_level
Calculates the Otsu threshold level
self.otsu_level_nobackground
calculate_otsu_log_level_nobackgroun
Line 3679, Column 9

5

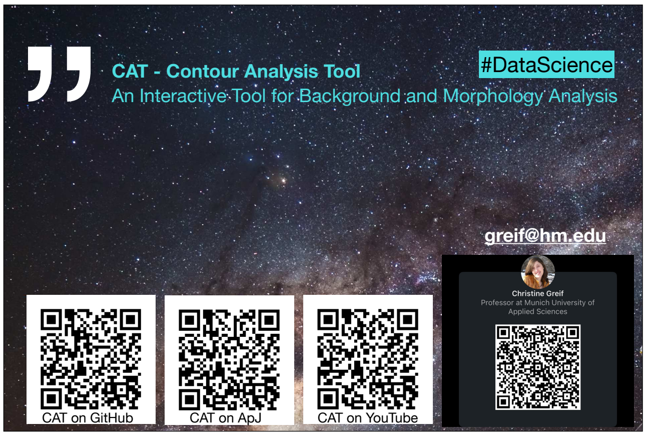
CAT - Contour Analysis Tool
An Interactive Tool for Background and Morphology Analysis
#DataScience
greif@hm.edu
CAT on GitHub
CAT on ApJ
CAT on YouTube
Christine Greif
Professor at Munich University of Applied Sciences

6

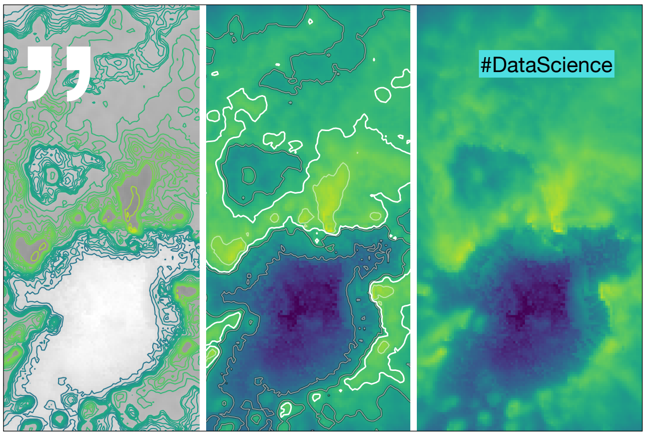
#DataScience

7

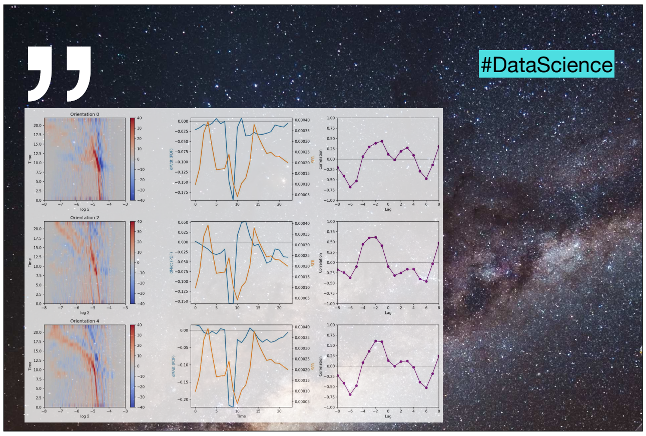
#DataScience
Orientation 0
Orientation 2
Orientation 4
Time
Lag

8

CHEMICAL EVOLUTION OF HIGH-MASS STAR-FORMING REGIONS

An MHD Simulation Post-Processing Approach

Akash Gupta[1], Peter Schilke[1], Valentine Wakelam[2], Birka Zimmermann[1], Stefanie Walch-Gassner[1]
1: I. Physics Institute, University of Cologne, Germany 2: Laboratoire d'Astrophysique de Bordeaux, Bordeaux, France

High-Mass Star-Forming Regions (HMSFRs) and Chemistry: Massive star formation is not well understood due to their rapid evolution and highly embedded nature. The commonly accepted evolution sequence is: Molecular Clouds (MCs)→Cold Cores→Hot Molecular Cores (HMCs)→HII Regions (Beuther et. al. 2007). HMCs are hot (T~100K), dense ($n_H \sim 10^6$ cm^{-3}), have no UV heating and are shielded from external UV field→ Complex Organic Molecules (COMs) formed on grains sublimate > detection of CH_3OH, H2CO, CH_3OCH_3, etc. (Herbst & van Dishoeck 2009).

Why post-processing MHD Simulations?: Most of the chemical models use stationary models only considering temperature evolution (e.g., Garrod et. al. 2008) but do not consider mass transport and chemical history of the gas. We use Lagrangian Tracer Particles from an MHD simulation (Zimmermann et. al. 2025) and post-process the simulation with the NAUTILUS three-phase model (Ruaud et. al. 2016), thus, modeling chemistry from cold cores stages to evolved hot cores stages.

Chemical Memory of the gas: CH_3OH/CO and N_2H^+/CO gas-phase ratios

CH_3OH/CO

In cold, high-density regions CO freezes out on grains and with no gas-phase reactions at low temperatures this ratio is also very low. On ices, CO goes under successive hydrogenation and forms CH_3OH and other COMs, so when temperature rises, they come into gas-phase, and we see higher CH_3OH/CO ratios.

This ratio is highly dependent on the history of the gas, as we see a large spread in the ratio even when they are at the same temperatures (see Fig. 1) which reflects the different chemical histories of these particles.

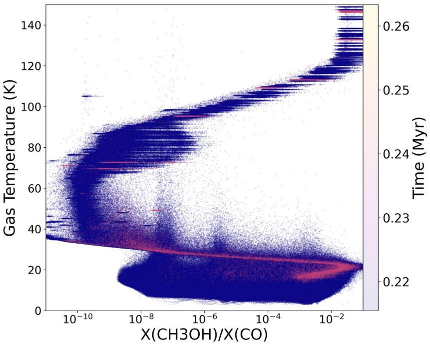

Fig.1: CH_3OH/CO abundance ratio with gas temperature for all tracer particles color coded with evolution time.

N_2H^+/ CO: Dense Gas Tracer

N_2H^+ is abundant where the electron fraction is low, and CO is frozen out on the ices, so this ratio can trace dense gas, and the observed ratio is found to be: 1:900 (Pety et al. (2017)).

We find the peak ratio varying from 10^{-4}-10^{-2} for low temperature and dense regions (see Fig. 2). As the density increases, this ratio increases but falls sharply as the temperature also begins to rise. It effectively tracks the 'cumulative cold-time' of the gas parcels, something that provides a more detailed view of core evolution.

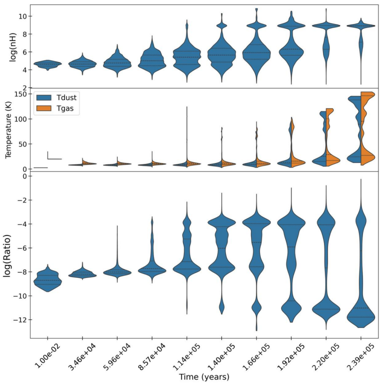

Fig.2: Top: number density, Mid: Gas and Dust Temperature, Bottom: N_2H^+ /CO abundance ratio; distribution of all particles at each time step of simulation.

Effect of Initial Conditions on long term chemical evolution

- Most of the chemical calculations start with atomic initial abundances in an already dense gas, which is not realistic. In this work: we first run our chemical model in MCs in a pre-collapse type run on various constant temperatures.
- n_H: Spitzer type contraction from 100cm^{-3} to n_H(initial, MHD), T: {5,10,15,20}K → run NAUTILUS with atomic abundances → obtained species abundances now input for post-processing step: for all tracer particles.

Results: 1.) Strong signatures of initial conditions in chemistry even at the end of post-processing due to ice-phase chemistry. The observed hot core abundances thus retain a chemical memory of this pre-collapse condition. **2.)** Chemical reservoirs for different molecules change as initial temperature in MCs increases and above 12K, CO_2 is dominant reservoir for C and O: CO_2 forms at expense of H_2O (see Fig. 3). **3.)** More COMs at 15K, 20K due to higher mobility of molecules on grains, their production diminish again at 25K, since CO freeze-out is suppressed.

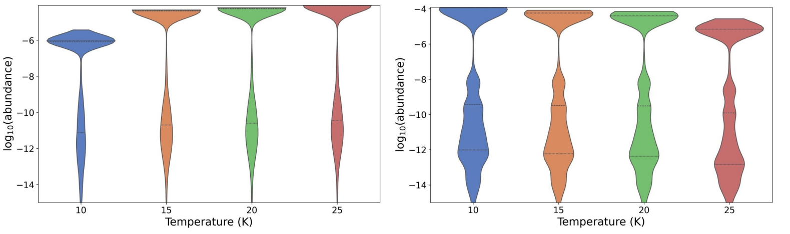

Fig.3: CO_2 & H_2O abundances after post-processing starting with various initial conditions

Summary

- Chemistry is rarely in equilibrium, and we need to follow the temporal evolution of density and temperatures to realistically compare to observations.
- Molecular ratios like CH_3OH/CO, N_2H^+/CO acts as clocks tracing the chemical history.
- Chemical reservoirs change for elements as we change the initial conditions of the gas which will form stars.
- Based on chemistry during star formation we may be able to use some species as tracer of initial physical conditions. Gupta et. al. (in prep.)

References: Beuther, H., Churchwell, E. B., McKee, C. F., & Tan, J. C. 2007, in Protostars and Planets V, ed. B. Reipurth, D. Jewitt, & K. Keil, 165; Herbst, E. & van Dishoeck, E. F. 2009, ARA&A, 47, 427; Cernicharo, J., Marcelino, N., Roueff, E., et al. 2012, ApJ, 759, L43; Zimmermann, B., Walch, S., Clarke, S. D., Wünsch, R., & Klepitko, A. 2025, MNRAS; Pety, J., Guzmán, V. V., Orkisz, J. H., et al. 2017, A&A, 599, A98; Ruaud, M., Wakelam, V., & Hersant, F. 2016, MNRAS, 459, 3756; Garrod, R. T., Widicus Weaver, S. L., & Herbst, E. 2008, ApJ, 682, 283

The Birth of a Cosmic Metropolis?

Thomas Herard-Demanche
with Rychard Bouwens, Sander Schouws, Jackie Hodge et al.
Leiden Observatory, Leiden University

"Where galaxies grow up fast"

Protoclusters (PCs), the progenitors of present-day galaxy clusters, trace the densest regions of the early Universe and provide key laboratories for studying accelerated galaxy growth. Simulations predict that PCs may host 30–50% of cosmic star formation at z≳7 and their physical volume expands significantly towards high redshift [1].

The combined power of JWST and ALMA has recently enabled efficient spectroscopic confirmation of high-redshift PCs, including dust-obscured members inaccessible to UV surveys.

Recent examples include A2744-z7p9OD at z=7.88 [2] as well as MACS0416-OD-z8p5 at z=8.5 [3], with 23 and 9 confirmed members respectively.

"Are we peaking at something extreme?"

REBELS-12 is one of the 40 galaxies targeted with the Reionization Era Bright Emission Line Survey (REBELS). From this ALMA large program, R12 was detected in both $[CII]_{158\mu m}$ and dust continuum at z=7.35. Its emission is double-peaked in [CII], hinting at a merger, with a UV-bright component also detected in $[OIII]_{88\mu m}$ and a UV-dark component detected in [CII] only [4].

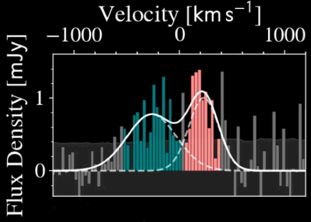

Additionally, a serendipitous [CII] detection was made at the same redshift revealing an HST-dark companion just 58 pkpc away [5], hinting at a potentially overdense region.

NIRSpec/IFU follow-up of R12 revealed an ISM enriched to 0.35 $Z_\odot$, placing R12 amongst the most massive and metal-rich sources found at z>6 [6].

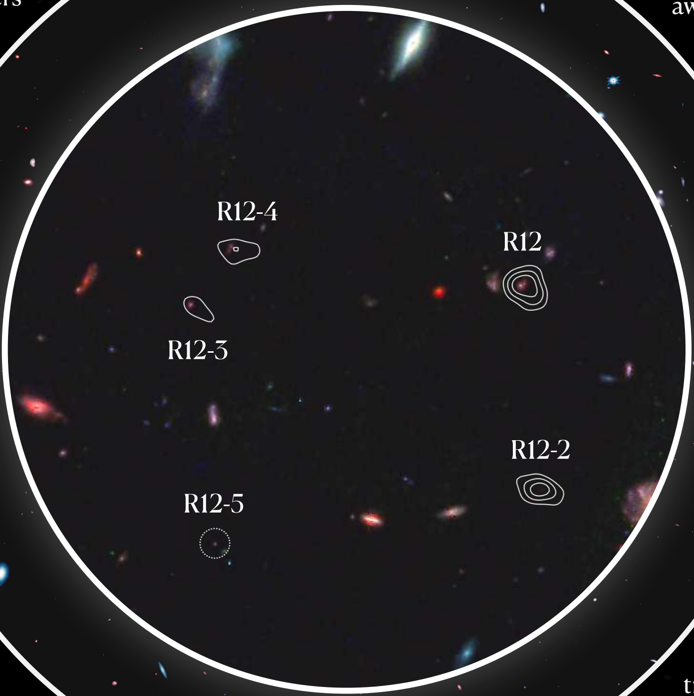

"OFF THE CHARTS!"

JWST/NIRCam grism observations with GO-6480 (PI: Schouws) uncovered three additional [OIII]5007 emitters within Δz<0.005 of R12, with two of them also detected in [CII] in the ALMA data.

SED modelling using JWST/NIRCam photometry shows that the R12-PC members are ~10× more massive than other PC members at similar redshifts, with $\log(M_\star/M_\odot)\sim9.5$. Furthermore, their [CII]-inferred SFRs place them nearly 1 dex above the *observed* main sequence at z~7.

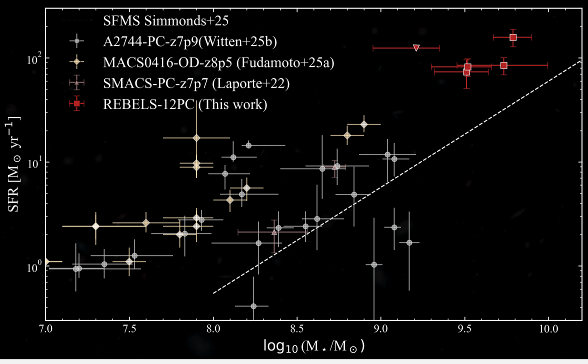

"Doe normaal, dan doe je al gek genoeg"

Mapping the R12-PC members' stellar masses to halo masses [7] gives log(Mh)~12.3 — above the track for Coma-like clusters [8]. But forward-tracking [9] tells a more subtle story: R12-PC has a ~90% chance of reaching log(M200)=14 by z~0.

Extreme then, but likely a normal cluster in the end.

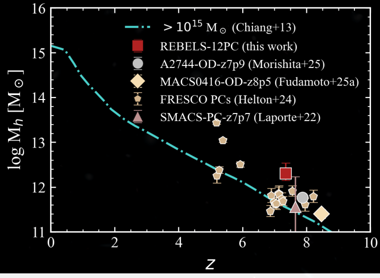

REBELS12-PC is one of the most compact spectroscopically confirmed protocluster cores currently known at z>7, and likely the most extreme, containing five confirmed members within only 108 kpc.

Its galaxies are unusually massive, chemically evolved, and intensely star-forming, showing merger activity and heavy dust-obscuration. While this system is extreme at high-z, it likely evolves into a normal cluster by z~0, nonetheless providing us with a rare glimpse into the earliest stages of dense cosmic structure formation.

References:

[1] Chiang+17, [2] Witten+25, [3] Fudamoto+25, Algera+24, [5] Fudamoto+21, [6] Rowland+25, [7] Behroozi+19, [8] Chiang+13, [9] Witten+26, in prep.

The M0.8-0.2 Ring

A coherent expanding shell too energetic for a single supernova?

Katharina Immer
Mairi Nonhebel
Ashley Barnes
+ ACES collaboration

Background three colour image
Green: 8 µm Spitzer GLIMPSE survey (Churchwell et al. 2009)
Yellow: 24 µm Spitzer MIPSGAL survey (Carey et al. 2009)
Red: 20 cm emission observed by MeerKAT (Heywood et al. 2019, 2022)

Why is this interesting?

Expanding molecular shells trace energetic feedback. The observed energetics challenge a standard supernova origin.

The M0.8-0.2 Ring may trace one of the most energetic recent feedback events in the CMZ.

Multiwavelength view of the Ring

Coherent ring-like morphology across molecular, dust and radio continuum tracers

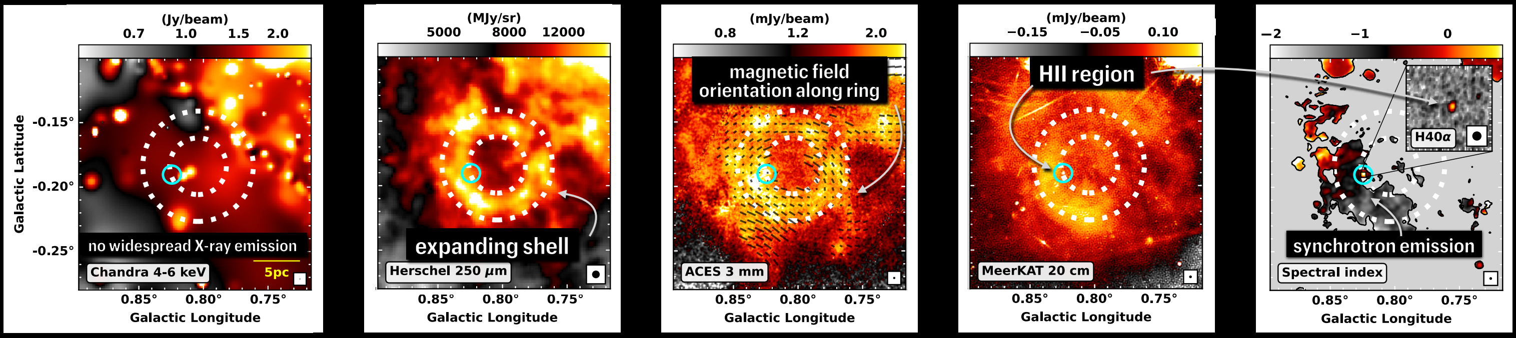

Evidence for expansion

Blue- and red-shifted components consistent with shell expansion

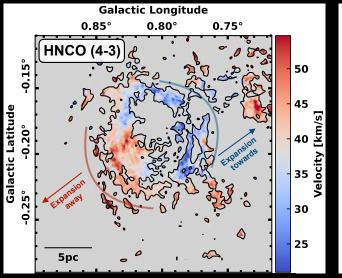

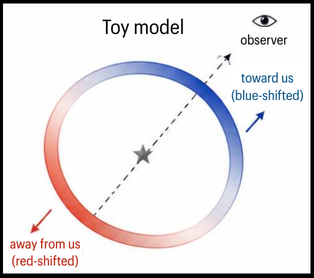

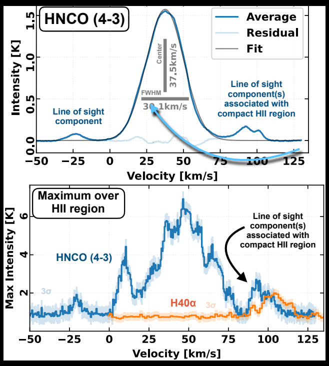

M0.8-0.2 in a nutshell

Radius: 6 pc

Systemic velocity: 37.5 km/s

Expansion speed: 15 km/s

Age: 0.4 Myr

Gas mass: ~10^6 $M_\odot$

Kinetic energy: ~10^{51} erg

What caused the Ring?

	Scenario	Explains	Main Issue
✗	Projection effect	Multiple velocity components	Ring coherent in space, velocity and polarisation
⚠	Cloud collision	Geometry	Velocity mismatch with inflowing gas
✗	Stellar feedback	HII region present	Insufficient energy and velocity offset
⚠	Supernova	Synchrotron signature	>100% coupling efficiency requires clustering of SNe
✓	Hypernova	Energetics + morphology	Rare event

Possible hypernova remnant in the Galactic Centre

Standard feedback scenarios cannot explain the observed energetics. An unusually powerful explosion is favoured.

ACES data papers are out:
Longmore et al. 2025 (overview); Ginsburg et al. 2025 (continuum); Walker et al. 2025 (narrow SPWs); Lu et al. 2025 (intermediate SPWs); Hsieh et al. 2025 (broad SPWs)

Nonhebel et al.
2024, A&A, 691, A70

THE IONIZED INTERSTELLAR MEDIUM IN M33: A RESOLVED VIEW OF HII REGIONS AND DIFFUSE IONIZED GAS

Emma Jarvis, Laurie Rousseau-Nepton
University of Toronto

David A. Dunlap Department of
Astronomy & Astrophysics
UNIVERSITY OF TORONTO

INTRODUCTION

Massive stars ionize surrounding gas and create H II regions. Studying large samples of H II regions provides information on star formation mechanisms, stellar feedback and galaxy evolution in different galactic environments. We present a new catalog of >4,000 H II region candidates in M33 (Jarvis et al. 2026, in prep).

OBSERVATIONS

- We present integral field spectroscopy observations of the spiral galaxy M33
    - Spatial resolution ~3pc
- These observations are part of the **Star formation, Ionized Gas, and Nebular Abundances Legacy Survey** (SIGNALS)
- Instrument: the imaging Fourier transform spectrometer **SITELLE** which has high spatial resolution (0.8”) and large field of view (11’x11’).

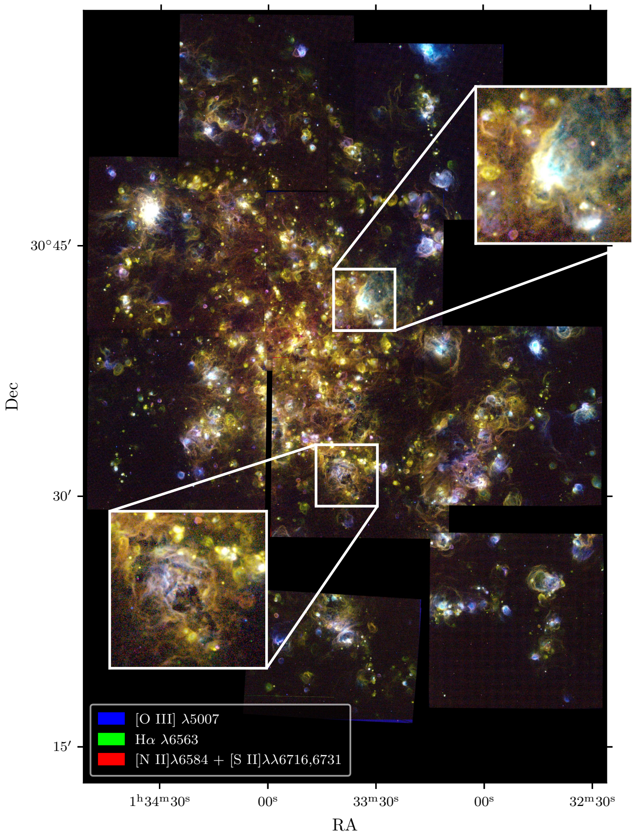

Fig 1. Three-colour mosaic of nine SITELLE fields mapping the ionized has emission in M33.

RESOLUTION EFFECTS

- We degrade the maps to simulate observations of M33 at further distances
- The HII region luminosity and size distribution is strongly impacted by spatial resolution

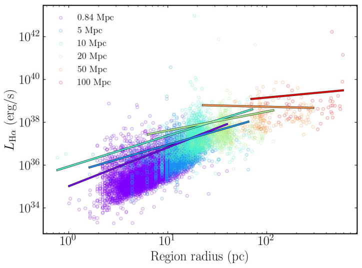

Fig 6. Luminosity vs radius of HII regions identified for various map resolutions.

HII REGION IDENTIFICATION

1. We identify emission regions as peaks in the Hα+[OIII] map

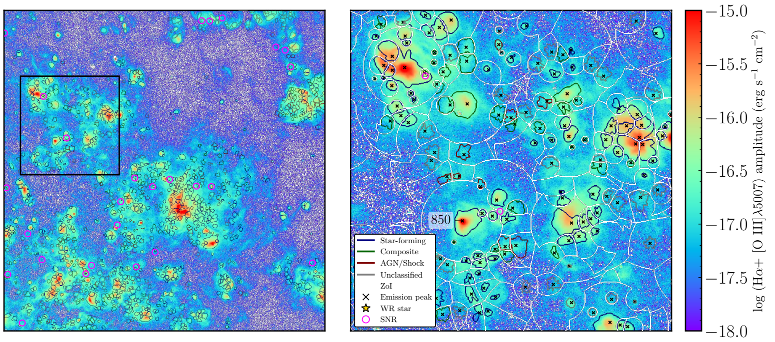

Fig. 2. Hα+OIII map for one SITELLE field of M33 with emission peaks and HII region boundaries identified.

2. The boundary of each region is defined using the Hα+ [OIII] amplitude profile in each azimuthal direction.

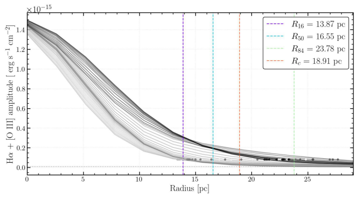

Fig 3. 1D ray profiles extending from the peak for region #850.

3. Within each boundary, we fit an integrated flux for every line

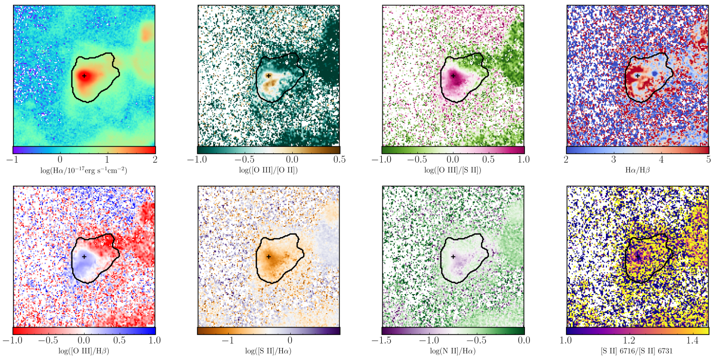

Fig 4. Various line ratio maps for region #850.

HII REGION CATALOG

We include many observed and derived physical HII region properties in the catalog:

- Integrated fluxes:
    - Hα, Hβ, [SII], [NII], [OIII], [OII]
- Ionization parameter
- Electron density
- Gas-phase metallicities
- Region size
- Hα luminosity
- Galactocentric radius

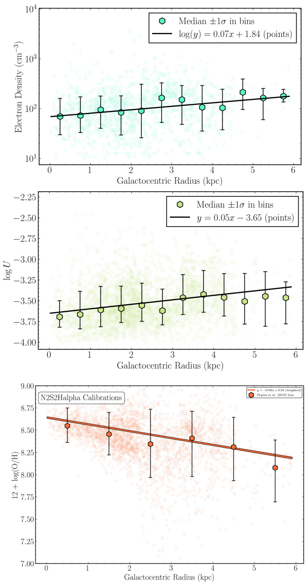

Fig 5. Radial gradients of HII region properties

PDFCHEM Modeling of Large-Scale Carbon Distribution in Orion A

Xuejian Jiang (蒋雪健), **Zhejiang Lab**
Co-Is: Thomas Bisbas, Sihan Jiao, Di Li & Donghui Quan et al.
(jiangxuejian@zhejianglab.org)

Abstract

- **Motivation**: To understand the carbon (C^+, C and CO) properties in Orion A (a molecular cloud/filament undergoing active star-formation), and compare observations with theoretical estimates.
- **Method**: We provide a new and fast algorithm PDFCHEM[1,2], which calculates the average abundances and brightness temperatures of species, using column density distributions (N_H-PDF). We adopt a grid of FUV intensities (χ/χ_0 ~ 10^{-1} to 10^5 Milky Way value) and a standard cosmic-ray ionization rate (ζ_{CR} ~ 2×10^{-16} s^{-1}) in our 1D simulations. We apply the method to **>1000 *N*-PDFs in Orion A with 2500 PDR simulations.**
- **Existing observations**: >300 YSOs in Orion A; High-quality hydrogen column density map[3] (data from JCMT/SCUBA-2, Herschel & Planck); Archival CO and [CII] data[4]. These can help constrain our PDFCHEM results.

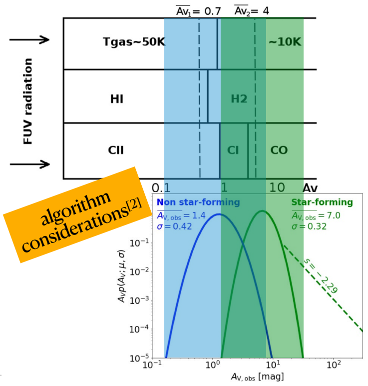

algorithm considerations[2]

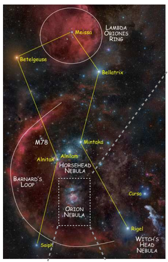

Orion A

- giant molecular cloud,
- ~10^5 $M_\odot$ mass,
- ~1400 light-years away, most active star-forming region in the Sun's local neighbourhood.

Hydrogen column density map[3]

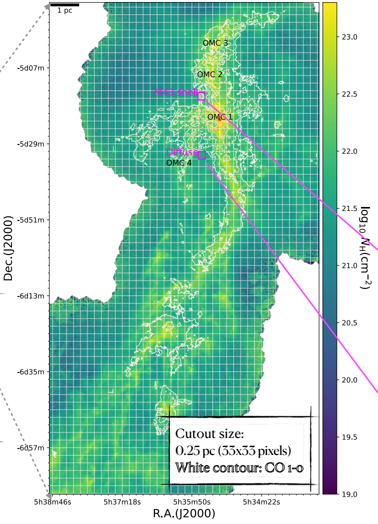

Cutout size:
0.25 pc (33x33 pixels)
White contour: CO 1-0

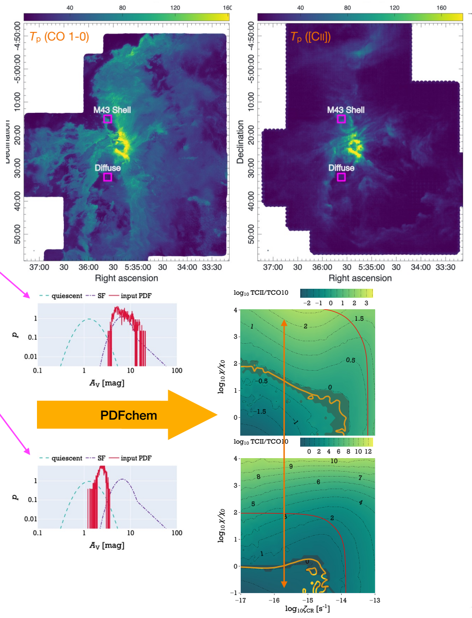

Data and Method

- **3D-PDR** Simulations of grids of FUV and CR.
- Input: N_H-PDF from each cutout is taken as a weight of Av distribution.
- PDFchem calculates average abundances and emissions.
- Line ratio of **[CII]/CO 1-0** from observations are used to constraint models.
- Best fits of FUV and species maps are derived.
- Using Sliding-window method to keep resolution

Results and Conclusions

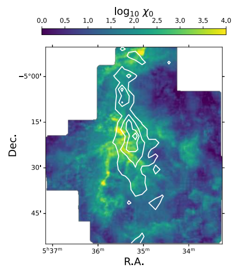

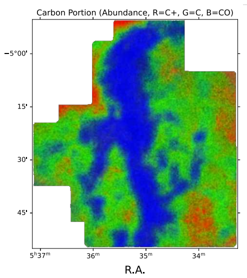

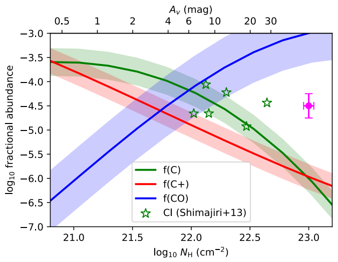

In ISM studies, [CII] and [CI] are helpful to compliment CO data for a more accurate H_2 mass estimate.

References

[1] Bisbas et al. 2019MNRAS.485.3097B
[2] Bisbas et al. 2023MNRAS.519..729B
[3] Jiao et al. 2022SCPMA..6599511J
[4] Kong et al. 2018ApJS..236…25K
[5] Padovani et al. 2018A&A…614A.111P
[6] Tobin et al. 2020ApJ…890..130T

- Derived FUV map matches the YSOs distribution (white contour)
- Derived C^+, C & CO abundance map — more CO along filament, more C^+ & C in outer region
- Our modeled C abundance is consistent with observations. C can be high in lower N_H (<10^{22} cm^{-2})

PDFchem is open-source:
github.com/Jiangxuejian/PDFchem

PDFchem is useful for observations!

- ✓ Takes seconds to run
- ✓ Support observational PDFs
- ✓ Interactive input/output
- ✓ Pure Python & cloud computing

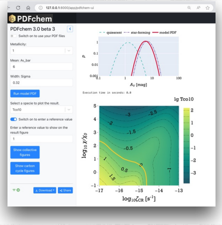

We have developed a AI agent for 3D-PDR!
github.com/Jiangxuejian/3D-PDR-agent

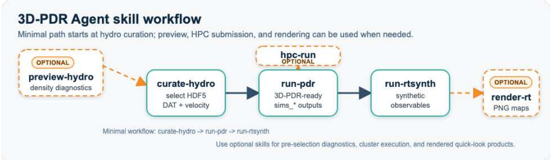

3D-PDR Agent skill workflow

Minimal path starts at hydro curation; preview, HPC submission, and rendering can be used when needed.

Minimal workflow: curate-hydro -> run-pdr -> run-rtsynth

Use optional skills for pre-selection diagnostics, cluster execution, and rendered quick-look products.

Madisen Johnson
3rd Year PhD Candidate
madisenmjohnson@gmail.com

Radiation Field Dependence of Milky Way H_2 Formation

Madisen Johnson[1], Blakesley Burkhart[1,2], Shmuel Bialy[3], Uri Malamud[3], and Benjamin Godard[4,5]

[1] Rutgers University, [2] Flatiron Computational Center of Astrophysics, [3] Technion – Israel Institute of Technology, [4] Observatoire de Paris, [5] Laboratoire de Physique de l' Ecole Normale Superieure

Motivation

Nearly all observational estimates of the H_2 formation rate and rate coefficient in the Milky Way assume chemical equilibrium — that formation and dissociation are in balance everywhere (Jura 1974, Wolfire et al. 2008). A key obstacle is that the formation rate depends on both the local gas conditions and G_0. Existing rate calibrations are typically derived at a single G_0, making them inapplicable to regions with different radiation environments without recalibration. **We address this by building an analytic formation rate function that works at any G_0, enabling non-equilibrium rate measurements across the Milky Way from column density observations alone.**

$$\dot{\Sigma}_F^{(\mathrm{obs})} = \bar{m} k_0 N_{21}^{\alpha} N(\mathrm{H}) = 0.14\ f_{\mathrm{H}} N_{21}^{1+\alpha}\ \mathrm{M}_\odot\ \mathrm{pc}^{-2}\ \mathrm{Myr}^{-1}$$

$$\dot{\Sigma}_D^{(\mathrm{obs})} = \frac{4\pi p_{\mathrm{diss}} \bar{m}}{1-p_{\mathrm{diss}}}\, \mathcal{I}_{\mathrm{tot}} \left(\frac{\tau_{\mathrm{tot}}}{1-\mathrm{e}^{-\tau_{\mathrm{tot}}}}\right) = 0.30\ \mathcal{I}_5 \left(\frac{N_{21}}{1-\mathrm{e}^{-1.9 N_{21}}}\right)\ \mathrm{M}_\odot\ \mathrm{pc}^{-2}\ \mathrm{Myr}^{-1}$$

Planck Dust + GALFA HI → H_2 formation rate

FIMS/Spear I_{UV} → H_2 destruction rate

Simulations

We use RAMSES (Teyssier et al. 2002) to simulate a 200 pc turbulent, solar metallicity ISM box at 128^3 resolution. We run 8 simulations varying only G_0 from 0.1 to 6.4, isolating the radiation field's effect of H_2 formation. Gas thermochemistry includes photoelectric heating, radiative cooling, and a hydrogen cooling network with H_2 self-shielding and dust shielding. Synthetic observables (N_H, N_{HI} $\langle Rn \rangle_{eff}$) are extracted along all three principal axes, yielding ~49,000 sightlines per G_0.

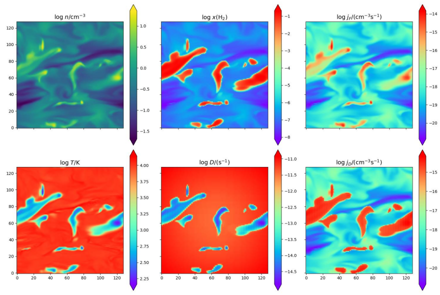

Two Regimes

The $\langle Rn \rangle_{eff}$-N relationship exhibits two physically distinct regimes:
Diffuse (WNM) : Formation rate scales linearly with column density – optically thin gas where every added column simply means more atoms exposed to the same UV field.

Dense (CNM + molecular): Self-shielding and dust absorption suppress photodissociation, enabling efficient grain-surface formation. The rate rises steeply with column density.

There is a smooth, sharp transition between the two regimes and the dense regime saturates at the fully molecular limit.

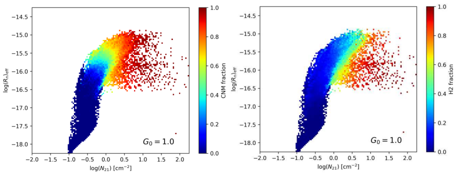

Building the Model: One Parameter

We model the effective H_2 formation rate surface density as a smooth transition between diffuse (WNM) and dense/molecular regimes at each G_0 value :

$$\Sigma_{\mathrm{form}}(N_H, G_0) = (1-S)\, A_{\mathrm{diff}} N_{21}^2 + S\, A_{\mathrm{dense}} N_{21}^{\alpha+1} \left[1 + \left(\frac{N_H}{N_{\mathrm{sat}}}\right)^q\right]^{-1/q}$$

With transition function:

$$S(N_H, G_0) = \left[1 + \left(\frac{N_H}{N_{\mathrm{break}}(G_0)}\right)^{-s}\right]^{-1}$$

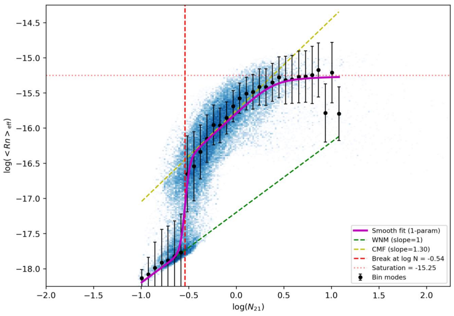

When investigating the fits, many variables were constant across all G_0 values and only one parameter – the transition column N_{break} – varies with G_0. This transition column follows a single linear relation:

$$N_{break} = 2.7 \times 10^{20} G_0^{1.07} cm^{-2}$$

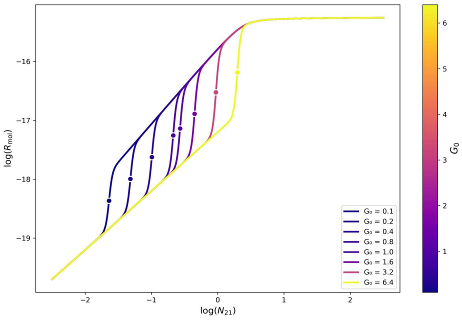

Enables the H_2 formation rate to be estimated directly from existing observations of total column density and inferred ISRF strength G_0.

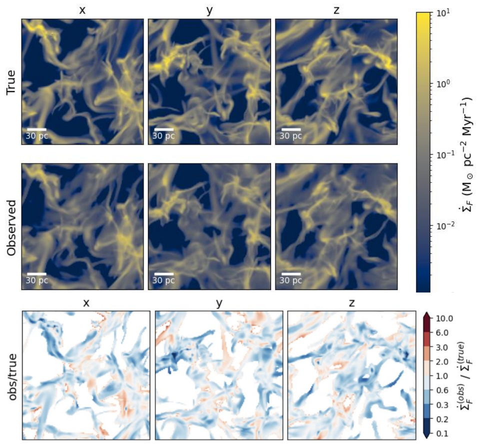

Application to the Eos Cloud

We apply our function to the newly discovered Eos molecular cloud (Burkhart et al. 2025) – the nearest molecular cloud at 94 pc, 99% CO dark. Using GALFA-HI, Planck dust, and FIMS/SPEAR FUV observations, we map the H_2 formation and destruction rates across the cloud at multiple values of G_0.

However, results using a preliminary version of *LightCube* (a 3D map of the local ISRF; Bish et al. *in prep*), allows us to estimate that the G_0 of the Eos Cloud is approximately 0.8.

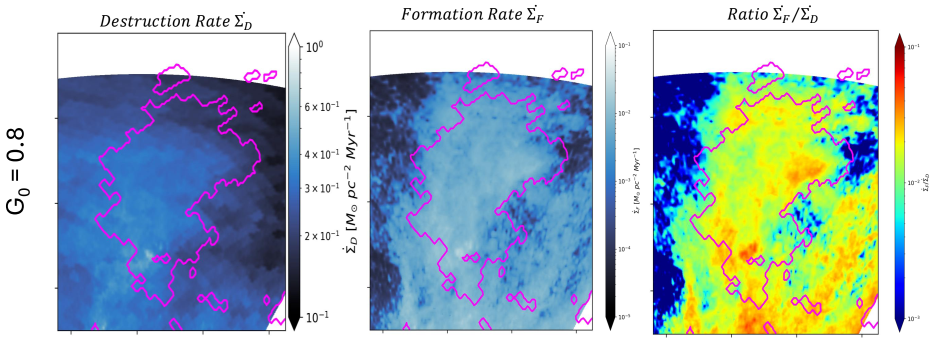

References

Jura 1974, ApJ, 191
Wolfire et al. 2008, ApJ, 680
Bialy et al. 2025, ApJ, 982, 24
Bialy & Sternberg 2019, ApJ, 881, 160
Teyssier 2002, A&A, 385
Burkhart et al. 2025, Nature Astronomy, 9, 1064
Planck Collaboration 2014, A&A, 571, A11
Peek et al. 2018, ApJS, 234, 2
Edelstein et al. 2006, ApJL, 644, L159
Jo et al. 2017, ApJS, 231, 21

Acknowledgements

Thank you to my numerous mentors and collaborators who have given me the tools and their time to learn how to explore all kinds of ideas.

I would also like to thank the organizers of the Olympian Symposium who have given me the opportunity to present my current work.

A Modeling Perspective on Galactic Faraday Rotation Observations

Leonard Kaiser
I. Physikalisches Institut
Universität zu Köln
kaiser@ph1.uni-koeln.de

We use data from the SILCC IX [1] simulations of the ISM in disk galaxies to investigate the structure of the magnetic field and its influence on observations of Faraday rotation [5].

Magnetic Field Structure

intricate field structure, coupled with the density

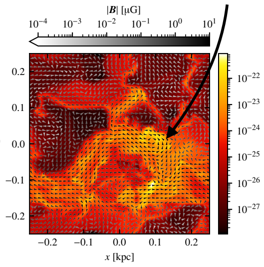

Fig.: Magnetic field B and mass density ρ in a slice through a SILCC IX simulation [1].

I. Correlation length

typical autocorrelation length: $L_{\mathscr{A}} \sim 40\,\mathrm{pc}$, close to other studies [2]

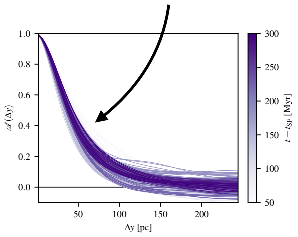

Fig.: Autocorrelation $\mathscr{A}(\Delta y) \sim \langle B_y(y)\,B_y(y+\Delta y)\rangle$ of the magnetic field along the y direction. Each line depicts one time step.

II. Stars influence the field structure

star-formation induced turbulence decreases the field coherence

field coherence drops in hotter, more ionised media

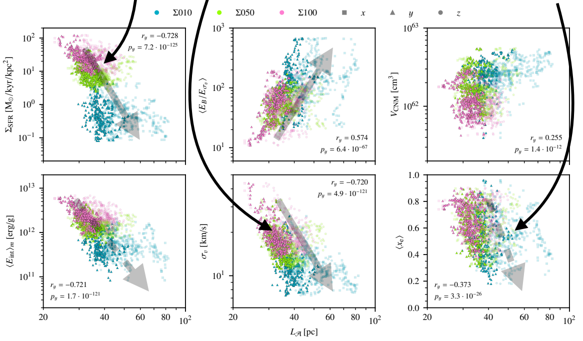

Fig.: Star formation rate and quantities of the ISM against the autocorrelation length of $B_{\parallel}$ for simulations with differing gas surface densities Σ in $M_{\odot}/\mathrm{pc}^2$. Shown are the star formation rate surface density, the average magnetic per turbulent energy, the volume of the cold neutral medium, the internal energy of the gas, the velocity dispersion, and the ionisation degree.

III. Scale comparison

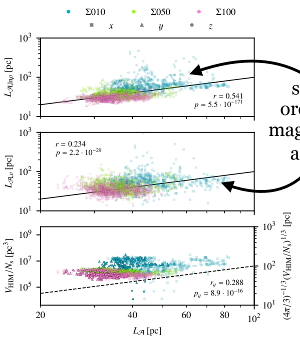

same order of magnitude as $L_{\mathscr{A}}$

Fig.: Length scales against the autocorrelation length of $B_{\parallel}$. Shown are the autocorrelation lengths of density and velocity, as well as the volume of the HIM per number of star clusters active in EUV.

I. RM distribution

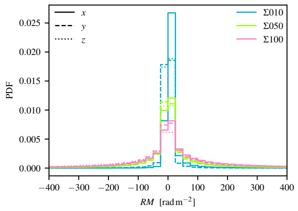

Fig.: Histograms of rotation measures integrated 500 pc across simulations with differing gas surface densities Σ in $M_{\odot}/\mathrm{pc}^2$.

- We observe a RM distribution comparable to other simulation work [3].
- Compared to observations [4], our distribution is more strongly peaked.
- The distribution is slightly skewed [4].

Rotation Measure

|RM| is enhanced around bright star clusters

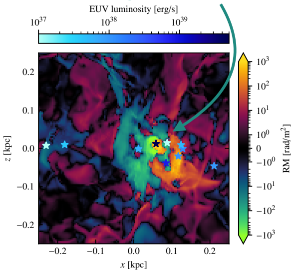

Fig.: Rotation measure integrated 500 pc across a SILCC IX simulation [1]. The markers represent star clusters with color indicating their brightness in the extreme ultraviolet.

III. Reconstructing B

B estimate using constant $\hat{N}_e$ is spread due to the variation of true n_e

B estimate with known N_e is more precise

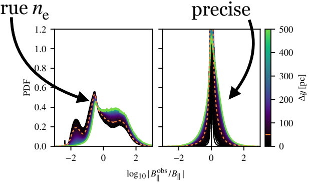

- Electron column density data is required for a reliable estimate of the magnetic field from Faraday rotation.
- Still, the relative error is $\mathcal{O}(10)$.

Fig.: Distributions of ratios between the magnetic field estimated from RM, $B_{\parallel}^{\mathrm{obs}}$, and the true field at different integration lengths Δy. *Left:* Estimate using a constant electron column density $\hat{N}_e$. *Right:* Estimate using the true electron column density N_e.

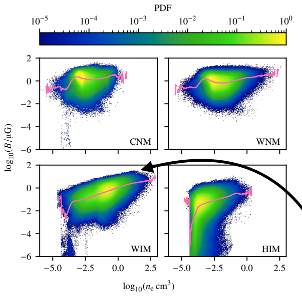

- A slight overestimation of the magnetic field arises due to the correlation between magnetic field and electron density in the ionised media.

strong correlation in the WIM

Fig.: Correlation between the magnetic field and electron density in different phases of the ISM.

II. Contribution to RM

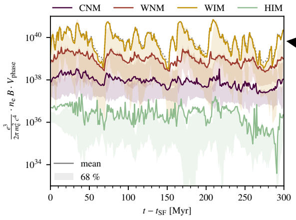

WIM contributes most to RM

Fig.: Estimated contribution of the different ISM phases to RM. Plotted is the product of the average $n_e B$ with the volume of gas in the phase.

WIM reaches the highest n_e

similar maximum B in all phases

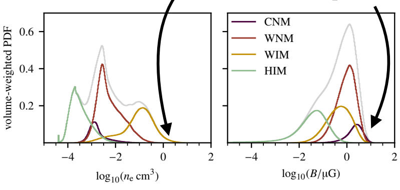

Fig.: Distribution of electron number density and magnetic field strength in the different phases of the ISM.

Conclusion

- The parallel magnetic field has a correlation length $L_{\mathscr{A}} \sim 40\,\mathrm{pc}$, influenced by the star formation rate.
- To reconstruct the magnetic field from RM within a factor of $\mathcal{O}(10)$, knowledge of the electron density is needed.
- The WIM contributes most to RM.

References

[1] Brugaletta et al. *MNRAS* 543, 4286 (2025)
[2] Hollins et al. *ApJ* 850, 4 (2017)
[3] Bracco et al. *A&A* 663, A37 (2022)
[4] Dhakal & Seta *MNRAS* 544, 2698 (2025)
[5] Kaiser, Seifried et al. (in prep.)

SFB 1601

UNIVERSITY OF COLOGNE

The origin of CH3OH maser rings in high-mass star-forming regions

Agnieszka Kobak

NICOLAUS COPERNICUS UNIVERSITY IN TORUŃ
Faculty of Physics, Astronomy and Informatics

G23.657-0.127 was discovered as a 6.7 GHz methanol maser source in the Toruń survey (Szymczak et al. 2000). Later, interferometric observations with the European VLBI Network (EVN) revealed a nearly circular maser ring with a radius of 405 AU and a width of 95 AU at a distance of 3.19 kpc (Bartkiewicz et al. 2009). The ring morphology suggests a connection with the accretion disk, but the proper motion studies indicate expansion (Bartkiewicz et al. 2020). To resolve the dust and gas at similar spatial scales, we observed this source and four more with similar ring-like methanol maser morphology, with the Atacama Large Millimeter/Submillimeter Array (ALMA).

The continuum band 6 ALMA observations with a high angular resolution of 25 mas reveal a central point continuum source and a ring structure.

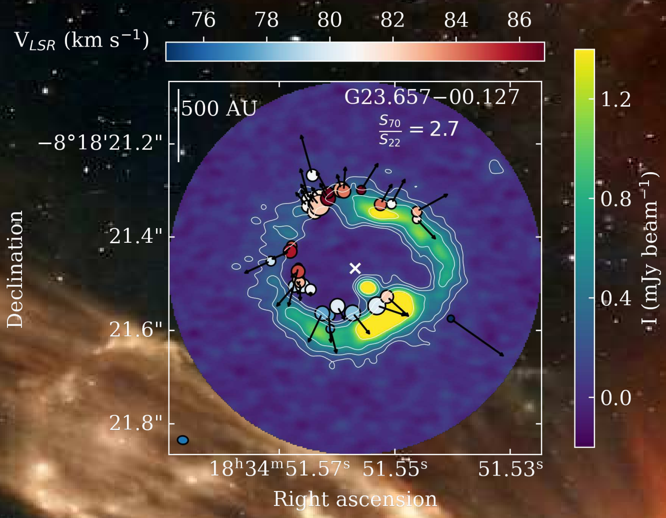

The 6.7 GHz methanol masers coincide with the 1.3 mm ring continuum emission.
The outer edge of the ring is located at a distance of ~260 mas (830 AU) from the center (marked with a white cross). The ring has a width of 80 mas (255 AU). The point continuum source near the center of the ring is unresolved. A Gaussian fit to the spatial distribution of the point emission yields the size of the beam (19x28 mas, 60x90 AU).

The SiO (5-4) emission fills the inner cavity of the ring and the peak of SiO coincide with 1.3 mm continuum point source.

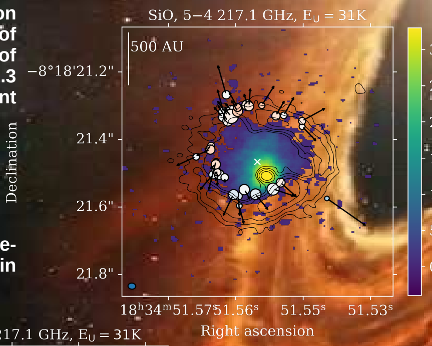

Red-shifted and blue-shifted outflows drain from the point source.

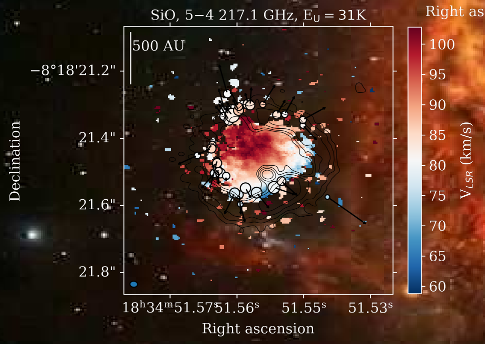

Combined high-resolution data with low-resolution data from ALMAGAL show large-scale blue-shifted outflow cone.

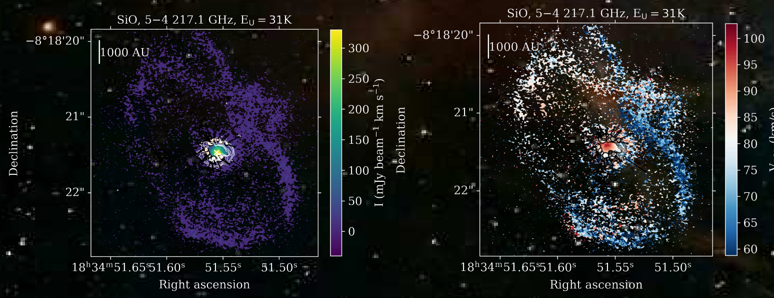

The moment 0 map of spectral lines, e.g., CH_3OH, H_2CO, CH_3CN, also show a ring structure coincident with the continuum emission and 6.7 GHz masers.

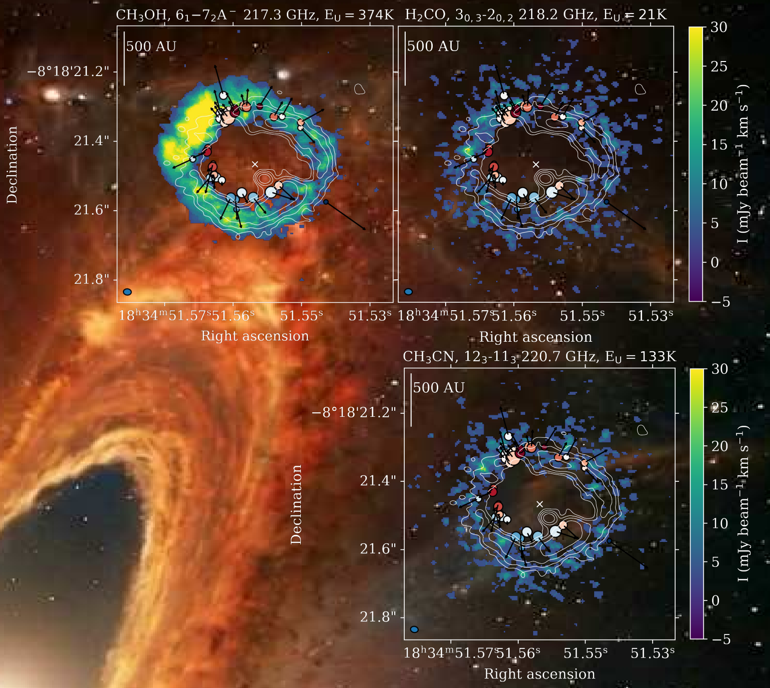

The moment 1 maps of spectral lines, e.g., CH_3OH, H_2CO, CH_3CN, show red-shifted and blue-shifted parts of the gaseous ring, which kinematically cover with velocities of 6.7 GHz CH_3OH maser spots.

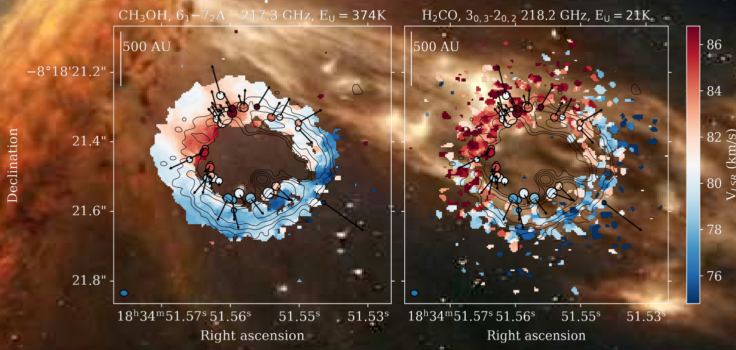

Four different sources with observed 6.7 GHz methanol maser ring-like morphology. No visible, resolved dusty disc for ALMA observations. Additionally the coincidence between radio maser and 1.3 mm continuum emission seems to be related with age of source.
Bigger S_{70}/S_{22} → younger source → bigger offset.

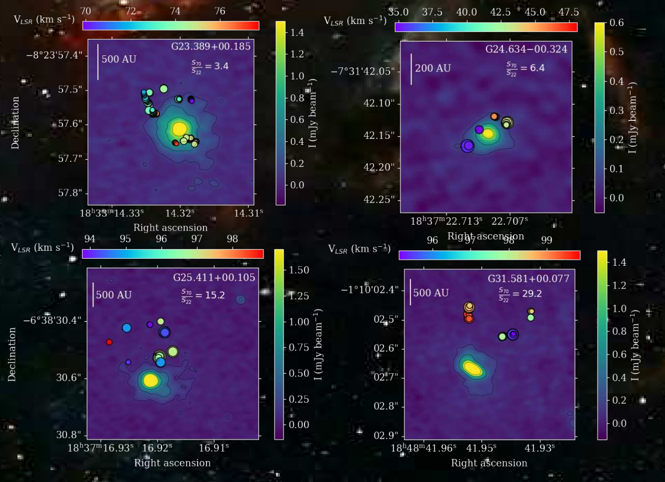

Molecular Cloud Formation in Low-Metallicity ISM and Its Role in Galactic Star Formation

Masato I.N. Kobayashi (Japan National Institute for Fusion Science, kobayashi.masato@nifs.ac.jp)
Kengo Tomida, Kazuyuki Omukai (Tohoku Univ.), Tsuyoshi Inoue (Konan Univ.), Kazuki Tokuda (Kagawa Univ.), Kazunari Iwasaki, Rin Yamada, Natsuko Izumi (NAOJ), Kei E. I. Tanaka (Science Tokyo)

The Olympian Symposium 2026, 2026 May 18-22 @ Paralia Katerini, Greece

Introduction

- ✓ The ISM is ubiquitously bubble-structured (e.g., PHANGS-JWST, Williams et al. 2024)
- ✓ Molecular clouds are compressed many times by supernovae during cloud lifetime, especially in star-burst env. (e.g., McKee & Ostriker 1977, Inoue & Inutsuka. 2008, Inutsuka et al. 2015, Padoan et al. 2016, Kobayashi et al. 2017, 2018, Chevance et al. 2020, Rathjen et al. 2023, Bazzi et al. 2026 in press)

→ In the past Universe (=low metallicity env.), how do molecular clouds form?

Previous works and this work

Colliding HI flow simulations and theories

Iwasaki et al. 2019

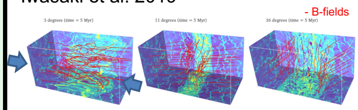

- ○ 40pc (flow direction) x 20 pc x 20 pc
  20 km s^{-1} + 20 km s^{-1}
- ○ Basic chemical network:
  H^+, H, H_2, He^+, He, C^+, O, CO
  (Nelson & Langer 1997; Inoue & Inutsuka 2012)
- ○ B-field regulate cloud formation

< 15 deg: HI(WNM) → HI(CNM) → **Molecular cloud**
> 15 deg: HI(WNM) → HI(CNM)

$$\frac{B_\perp^2}{8\pi} = \rho_0 V_0^2 \longrightarrow \sin\theta'_{\rm cr} \sim 0.3\left(\frac{\epsilon}{0.1}\right)\left(\frac{\langle n_0\rangle}{5\ {\rm cm^{-3}}}\right)^{1/2}\left(\frac{V_0}{20\ {\rm km\ s^{-1}}}\right)\left(\frac{B_0}{5\ \mu{\rm G}}\right)^{-1} \quad \sim 15\ {\rm deg}$$

Inoue & Omukai 2015, Bialy & Sternberg 2019

- ○ Thermal instability occurs at Z > 10^{-3} $Z_\odot$ by CII and OI fine-structure lines
- ○ However without B-fields. What happens with B-fields?

Interesting metallicty?

Delgado Mena 2019 (Gaia + follow-up spectroscopy)

Majority of stars in the Milky Way galaxy have 1 – 10^{-1} $Z_\odot$

This work: high-resolution low-metallicity sim. with B-fields

- ✓ Code: Athena++ (Stone et al. 2020)
- ✓ HI (WNM) head-on collisions: 0.57 cm^{-3}, 20 km s^{-1} (Kolmogorov perturbation seeded)
- ✓ Photo-electric heating, Lyα, OI, CII, CO (Newly implemented metallicity-dependent cooling curves based on Koyama & Inutsuka 2002 / Sutherland & Dopita 1993)
- ✓ Size: 20pc (flow direction) x 10 pc x 10 pc
- ✓ Resolution: 0.02 pc high enough to resolve the growth of thermal instability
- ✓ Metallicity: 1.0 $Z_\odot$, 0.5 $Z_\odot$, 0.2 $Z_\odot$ similar to Milky Way, LMC, and SMC
- ✓ B-fields: 1uG tilted against flows 0, 15, and 30 deg

Results

3D structures and turbulence of clouds

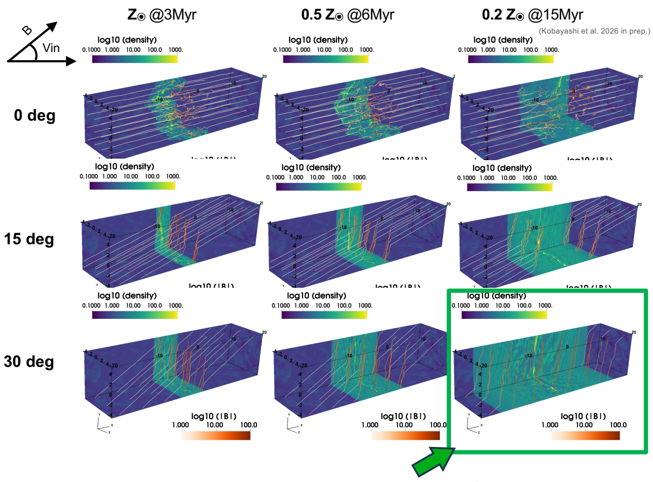

- ○ **Tilted B-fields suppress the formation of CNM / molecular clouds**
- ○ **Clouds become less turbulent (x 0.5) in lower metallicity env.**
  (Observational support in the outskirt MW and SMC: ohno et al. 2023, Lin et al. 2025)

@ Solar metall (**lower** temperature / less Pthermal)

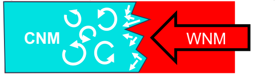

@ Lower metal (**higher** temperature / higher Pthermal)

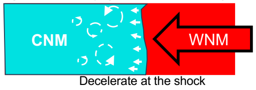

Cloud formation conditions

- ○ CNM fraction reduces in lower metallicity environment

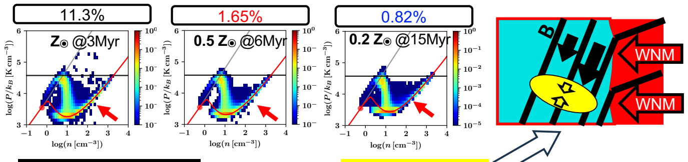

- ○ **Shear along B-fields** dominates over thermal instability
- ○ Competition: thermal instability & shear
  - ❑ Cooling timescale

$$\tau_{\rm cool} = \frac{e(n_1, T_1)}{n_1^2 \Lambda(T_1)}$$

post shock density: $n_1 \sim n_0\sqrt{\frac{\rho_0 V_{\rm inflow}^2}{(B\sin\theta)^2/8\pi}}$

  - ❑ Shear timescale

$$\tau_{\rm shear} = \frac{\lambda_{\rm max}}{\left\langle \left| \frac{\mathbf{v}(\mathbf{r}+\lambda_{\rm max,\perp}/2) - \mathbf{v}(\mathbf{r}-\lambda_{\rm max,\perp}/2)}{|\lambda_{\rm max}|} \cdot \frac{\mathbf{B}(\mathbf{r})}{|\mathbf{B}(\mathbf{r})|} \right| \right\rangle}$$

Ex.) 0.2 $Z_\odot$ (Kobayashi et al. 2026 in prep.)

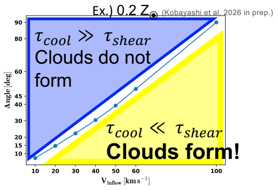

Proposed galaxy evolution scenario

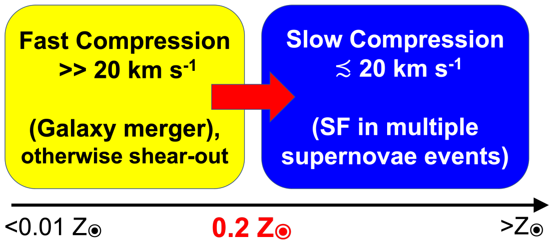

High P_{ram}, bursting SF

Fast Compression >> 20 km s^{-1}

(Galaxy merger), otherwise shear-out

Low P_{ram}, slow SF

Slow Compression ≲ 20 km s^{-1}

(SF in multiple supernovae events)

<0.01 $Z_\odot$ **0.2 $Z_\odot$** >$Z_\odot$

Key take-home messages

When < 0.2 $Z_\odot$, molecular clouds form only in fast-compression conditions.

(1) When galaxies were young with < 0.2 $Z_\odot$, star formation was limited to a bursty mode by mergers, cold accretion etc.

(2) Once galaxies exceeded > 0.2 $Z_\odot$, a slow mode of star formation started (e.g., chains of supernovae compressions).

The Evolution of the Mass-Metallicity and Fundamental Metallicity Relations at $z \gtrsim 2$

Based on Unprecedented High-Redshift Metallicity Calibrations and Sample Sizes

Natalie Lam[1], L. Clarke[1], A. E. Shapley[1], R. L. Sanders[2], M. W. Topping[3], G. B. Brammer[4,5], N. A. Reddy[6], S. Karthikeyan[1]
[1]UCLA, [2]University of Kentucky, [3]Steward Observatory, [4]DAWN, [5]Niels Bohr Institute, [6]UC Riverside

Introduction

- Galaxy evolution is governed by the baryon cycle (e.g., gas inflow/outflow, star formation, stellar/supernova feedback).
- The **mass–metallicity relation (MZR)** traces chemical enrichment across cosmic time.
- Observations show that early galaxies are more metal-poor at fixed stellar mass.
- Incorporating **star formation rate (SFR)** reduces the scatter in the MZR at z ~ 0, reflecting the **fundamental metallicity relation (FMR)**.
- FMR encodes self-regulation processes linking star formation, gas accretion, and feedback.
- A key open question is whether these regulatory processes are already established in galaxies at high redshifts.

Methods

- Large sample of 601 galaxies from JADES at 1.4 < z < 7.
- Representative sample of the star-forming galaxy population above $10^{8.5}$ $M_\odot$.

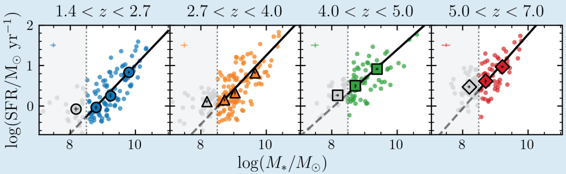

* *Star-forming main sequence (SFMS) from Clarke+2025*[1]

- Updated high-z strong-line metallicity calibrations from Sanders+2025.[2]
- High S/N stacked spectra enable robust measurements of gas-phase metallicity.
- Composite spectra constructed in fine bins of: redshift, stellar mass, and offset from the SFMS

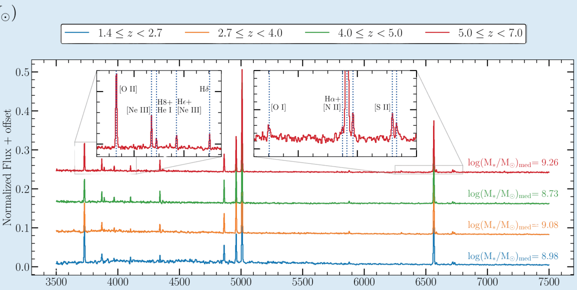

Example composite spectra from Clarke+2026[3]

Evolution of the MZR

- MZR slope γ stays constant between 1.4 < z < 5.0 at $\gamma \sim 0.21$ and steepens to $\gamma \sim 0.41$ between 5 < z < 7.
- Normalization Z_9 decreases smoothly between z ~ 0 and z ~ 3.24 with $d\log(\mathrm{O/H})/dz = -0.10 \pm 0.02$. Mild evolution between z ~ 3.24 and z ~ 4.40.
- At 5 < z < 7, high-mass end matches up with the z ~ 4 MZRs. Low-mass end matches literature on lower-mass systems.

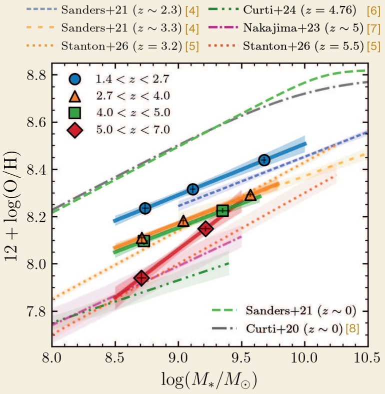

stack	γ	Z_9
$1.4 < z < 2.7$	0.22 ± 0.03	8.29 ± 0.02
$2.7 < z < 4.0$	0.21 ± 0.03	8.17 ± 0.01
$4.0 < z < 5.0$	0.21 ± 0.04	8.15 ± 0.01
$5.0 < z < 7.0$	0.41 ± 0.09	8.06 ± 0.02

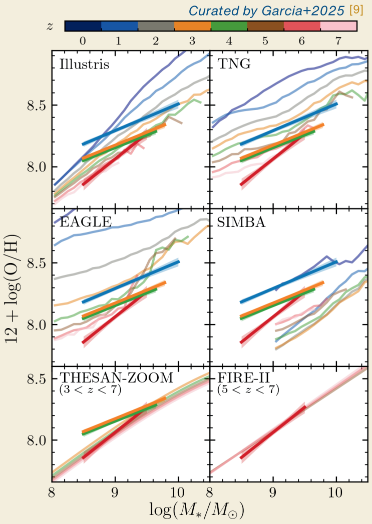

Comparing to z ~ 0 FMR

- High-z stacks are systematically offset to lower metallicity than local FMR at fixed stellar mass.
- High-z stacks lie on a power law-like locus.

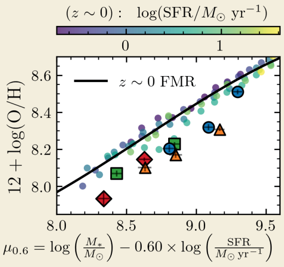

Residuals around the MZR and SFMS

- At z ~ 5, anti-correlation between MZR residual $\Delta\log(\mathrm{O/H})$ and SFMS residual $\Delta\log(\mathrm{SFR}/M_\odot\,\mathrm{yr}^{-1})$ exists. Regulatory
- Typical dependence of $\Delta\mathrm{O/H} \propto \Delta\mathrm{SFR}^{-0.1}$ is weaker than in the local universe.
- Tentative anti-correlation above 10^9 $M_\odot$ at 5 < z < 7. Lack of anti-correlation below 10^9 $M_\odot$ suggests turbulent processes dominate in low-mass systems at z > 5.

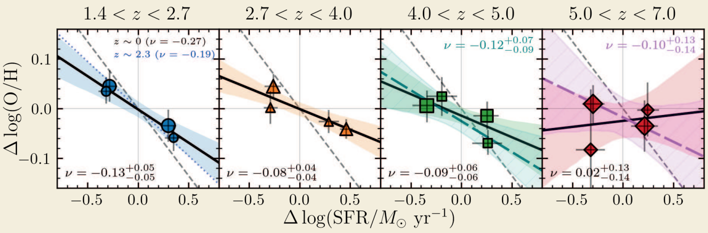

Discussion

- By z ~ 5, a weak FMR emerges, though with milder coupling between metallicity and SFR than observed locally.
- Potentially due to mismatched timescales between metal enrichment and highly variable bursty star formation and feedback-driven outflows.
- At z > 5, this regulatory relationship is tentatively seen in massive galaxies but may break down at lower stellar masses, suggesting different evolutionary pathways across galaxy mass.
- Simulations capture either MZR slope or metallicity normalization, but struggle to account for both simultaneously.
- Current sample sizes are insufficient to constrain evolutionary models.

Future Work

To rigorously study the MZR and FMR at z > 4, a factor of 2–3 increase in spectroscopic sample sizes is needed, spanning a broader range of stellar masses and ensuring representativeness of the full galaxy population.

[1] Clarke, L., Shapley, A. E., Lam, N., et al. 2025, arXiv e-prints, 2510.06681
[2] Sanders, R. L., Shapley, A. E., Topping, M. W., et al. 2025, arXiv e-prints, 2508.10099
[3] Clarke, L., Lam, N., Shapley, A. E., et al. 2026, ApJL, 1002, L15
[4] Sanders, R. L., Shapley, A. E., Jones, T., et al. 2021, ApJ, 914, 19
[5] Stanton, T. M., Cullen, F., Carnall, A. C., et al. 2026, MNRAS, 547, stag449
[6] Curti, M., Maiolino, R., Curtis-Lake, E., et al. 2024, A&A, 684, A75
[7] Nakajima, K., Ouchi, M., Isobe, Y., et al. 2023, ApJS, 269, 33
[8] Curti, M., Mannucci, F., Cresci, G., & Maiolino, R. 2020, MNRAS, 491, 944
[9] Garcia, A. M., Torrey, P., Ellison, S. L., et al. 2025, MNRAS, 536, 119

Natalie Lam
NSF Graduate Research Fellow
natalielamwy@astro.ucla.edu
www.natalielamwy.com

Supernova feedback in porous photoionized Giant Molecular Clouds

Cheryl S. C. Lau [1], Ian A. Bonnell [2], Yueh-Ning Lee [1,3]

1 National Center for Theoretical Sciences (Physics division), National Taiwan University, TW
2 School of Physics and Astronomy, University of St Andrews, UK
3 Center of Astronomy and Gravitation, National Taiwan Normal University, TW

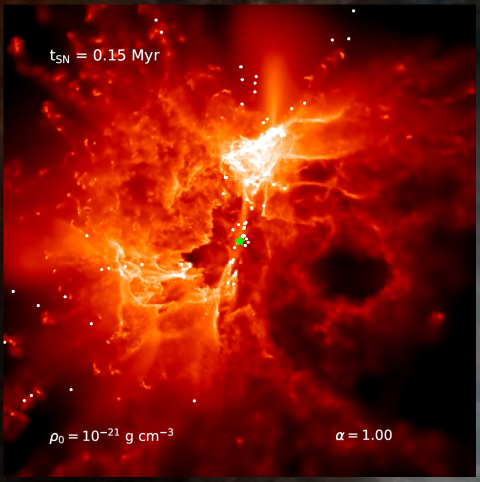

Introduction

Supernovae (SNe) regulate star formation by expelling gas from the Giant Molecular Clouds (GMCs) and sustaining turbulence in the ISM. On larger scales, they are also responsible for driving outflows from the galactic discs into the halo.

Current galaxy simulations often rely on sub-grid models to incorporate stellar feedback. Many of these models are computed in 1-D, which assume spherical symmetry.

However, GMC simulations reveal that SN blowouts can be highly asymmetrical, especially when the environment has been modified by early feedback, i.e. ionizing radiation and stellar winds (Lucas+ 2020).

Pre-SN feedback can carve cavities and channels in the GMCs, allowing SN energy to "vent" out of the porous cloud without damaging the dense star-forming regions. SNe thus deviate from being spherical.

Aim: To examine the impact of SNe exploding within ionization-driven cavities of different structures and morphologies.

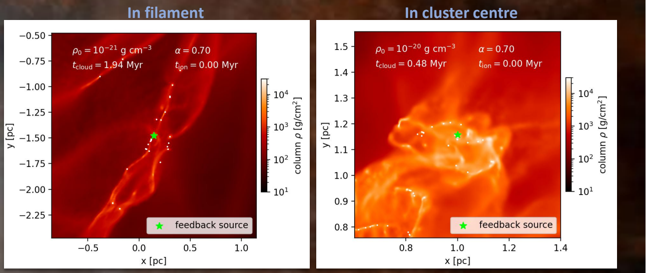

Numerical methods

GMCs are simulated with Smoothed Particle Hydrodynamics (SPH) code Phantom (Price + 2018). Photoionization is added by coupling SPH to Monte Carlo Radiative Transfer (MCRT) grid code CMacIonize (Vandenbroucke+ 2018, Petkova+ 2021, Lau+ 2025a); SNe are injected as 10^{51} erg of kinetic energy.

① Compact environment

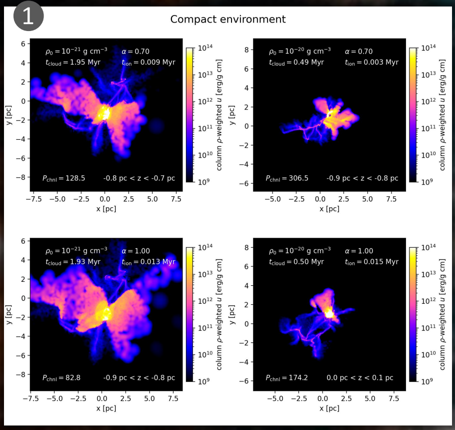

② Dispersed environment

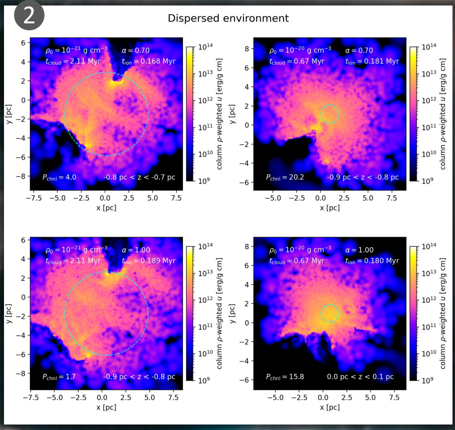

The Simulations

We first evolve H II regions in GMCs with varied densities and gravitational boundness. The ionizing sources either lie along a filament or within a cluster.

① During the early times, the ionized gas show distinctive channel structures – low-density paths that connect the embedded regions inside the GMCs towards to outer ISM.

② At later times, the GMCs are largely dispersed due to expansion of H II regions. Cavities become much bigger and less clumpy.

The ionizing source in each snapshot is then detonated as SN, and we compare the properties of their outflows.

Results

Kinetic Energy and Momentum

- SNe deposit the majority of their energies and momentum when the shocks collide with cavity walls, hence SNe in GMCs retain more kinetic energy at smaller distances compared to spherical blasts in uniform medium (yellow).
- At ≤ 10 pc, the evolutions of ① (red) and ② (blue) differ significantly. But **beyond 20 pc, they become increasingly similar to each other.**

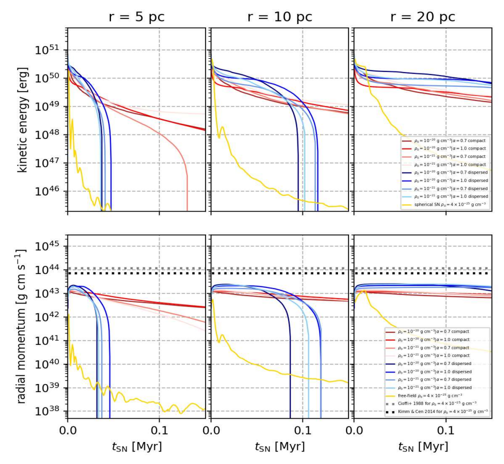

Outflow velocity

- Maximum outflow velocities in both ① (left) and ② (right) agree with the predictions computed with the semi-confined SN analytical model presented in Lau+ (2025b), as opposed to the spherical blast (free-field) model.
- Velocities after 0.1 Myr in ① and ② are highly similar, possibly indicating that SN outflow properties **at late-times are rather independent of the porosity of its parent GMC**.

① Compact environment (r_{detect} = 10 pc)

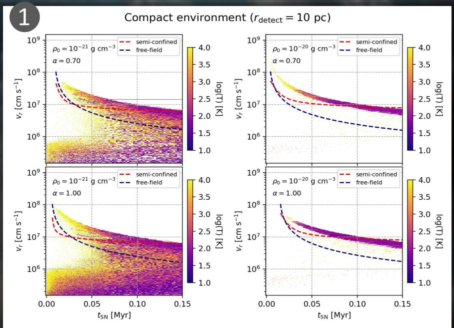

② Dispersed environment (r_{detect} = 20 pc)

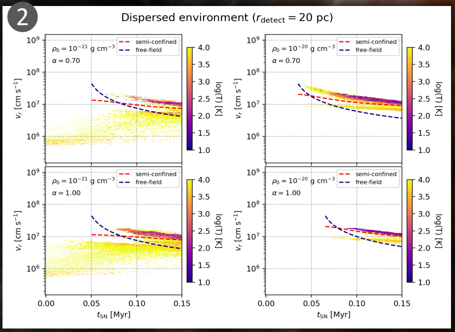

Conclusion

It may be better to treat SNe in GMCs or any clumpy ISM as partially-confined explosions rather than as spherical blasts. However, on larger spatial and temporal scales, the amount of deviations appear consistent across a broad range of GMC porosities. Implementing the "channelling effect" into SN sub-grid models could be less complex than previously thought.

Lau C. S. C., Bonnell I. A., 2025, MNRAS, 540, 1124
Lau C. S. C., Petkova M. A., Bonnell I. A., 2025, MNRAS, 538, 1461
Lucas W. E., Bonnell I. A., Dale J. E., 2020, MNRAS, 493, 4700
Petkova M. A., Vandenbroucke B., Bonnell I. A., Kruijssen J. M. D., 2021, MNRAS, 507, 858
Price D. J., et al., 2018, PASA, 35, e031
Vandenbroucke B., Wood K., 2018, Astron. Comput., 23, 40

Cluster Mergers – not AGN Feedback – Mitigates Gas Cooling and Star Formation in Cluster Central Galaxies

Jeremy Lim, Arsen Levitskiy, Yuxuan Zeng (HKU), Jeremy Sanders (MPe), Youichi Ohyama (ASIAA), & Megan Donahue (Michigan State U.)

Feedback – whether associated with an AGN or star formation, or both – is deemed necessary to mitigate the accumulation and/or cooling of gas that would otherwise fuel a higher rate of star formation in galaxies. The most widely-cited exemplar of AGN feedback is jets from cluster central galaxies: these jets are seen to disperse, and is presumed to (re-)heat, the intracluster medium (ICM) at cluster cores. The mechanical energy thus deposited is deemed to closely balance cooling of the ICM, which would otherwise cool at rates of up to 100s – 1000s $M_\odot$/yr. Instead, re-heating from these jets lowers the cooling rate by an order of magnitude.

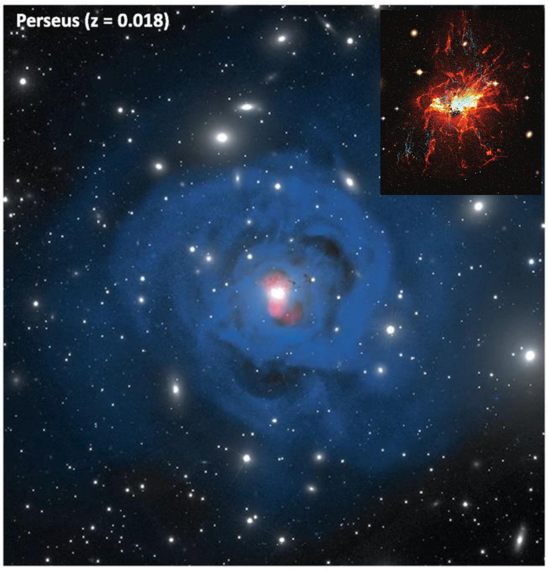

Inner region of the Perseus Cluster (from Hlavacek-Larrondo et al. 2024): optical image in white, X-ray image in blue tracing the ICM, and radio image in red tracing opposing jets from an AGN in the cluster central galaxy (NGC 1275). The radio jets have blown cavities in the ICM; other prominent cavities in the ICM are filled with weaker radio emission from earlier episodes of AGN activity. Insert shows region immediately around the cluster central galaxy (from Lim et al. 2019). Red/white traces optical line-emitting gas, betraying a net amount of ICM cooling, and blue traces numerous star clusters that have formed from this gas.

To better understand the relationship between ICM thermodynamics, gas cooling, and star formation in cluster central galaxies, we have studied all three aspects in detail among the 25 clusters observed in the Cluster Lensing and Supernova survey with Hubble (*CLASH*) program. 12 of these clusters host cluster central galaxies displaying optical line-emitting gas and recent (if not ongoing) star formation.

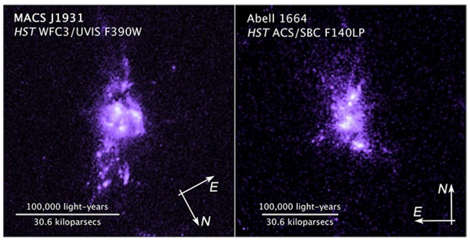

UV emission tracing newly-formed stars associated with the central galaxies of two clusters observed in the *CLASH* program. Notice that the star-forming regions span over 30 kpc.

We find different ICM thermodynamical profiles among clusters hosting star-forming and non-star-forming cluster central galaxies (Brightest Cluster Galaxies; BCGs), such only clusters having the lowest core entropies host star-forming BCGs. These also are the clusters in which their BCGs display the most powerful radio jets.

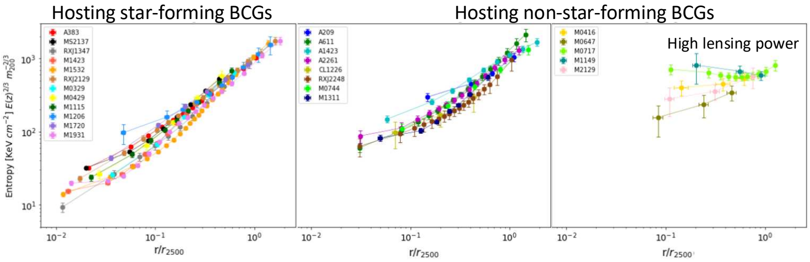
Hosting star-forming BCGs

Hosting non-star-forming BCGs

High lensing power

The morphology of the X-ray-emitting ICM on large scales reflects the degree to which a cluster is dynamically disturbed on a global scale. To check their individual level of disturbance, we evaluated how well the centers of different X-ray isophotes agree (alignment), the coincide between the X-ray isophote centers and the global X-ray center (symmetry), and the projected distance between the BCG center and the global X-ray center (Offset). We find that clusters cannot simply be classified as disturbed or relaxed; rather, they span a continuous range of disturbance states. Because the only process able to disturb clusters on a global scale is a merger with another cluster, we conclude that the *CLASH* (and by extension all) clusters are at ***different stages of dynamical relaxation following a merger***.

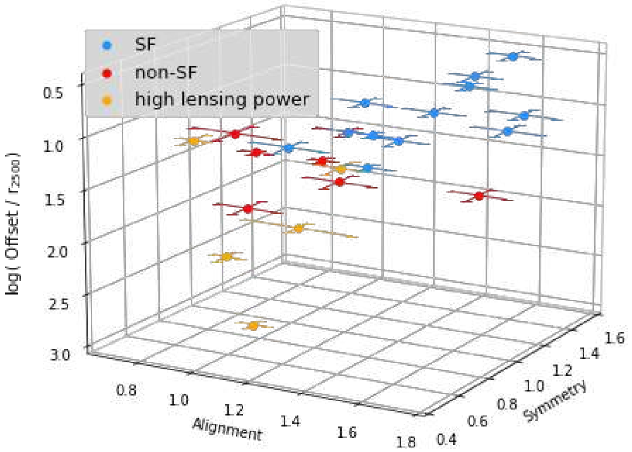

Inferences of ICM cooling rates of 100s – 1000s $M_\odot$/yr are based on a critical assumption: that clusters have cooled over a Hubble time (~10^{10} Gyr). Cosmological simulations indicate that it can take many Gyr for clusters to dynamically relax following a merger, as shown on the right (from Chen et al. 2026); the results presented above suggest that vigorous ICM cooling resumes only after clusters have sufficiently relaxed. If, among clusters hosting star-forming BCGs, vigorous ICM cooling has only resumed recently (say over the past $\lesssim 1$ Gyr), then the ICM cooling-rate would be up to an order of magnitude or more lower – in which case jets from AGNs in BCGs are no longer required to regulate (i.e., closely balance) ICM cooling.

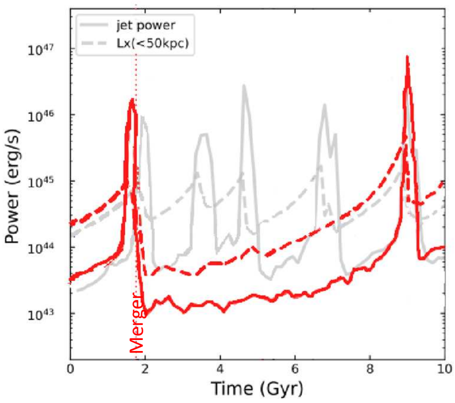

Merger INduced Starbursts and the Gas Lifecycle Examination

PI: Sean T. Linden

Co-PIs: Y. Song, C. Eibensteiner, M. Sanchez-Garcia, S. Aalto, E. Treister, H. Inami, A. Evans

ABSTRACT

While ALMA continues to revolutionize our understanding of the lifecycle of star formation in nearby galaxies, there remains a critical lack of dedicated large surveys targeting stellar nurseries in extreme starburst environments. In the local Universe, galaxy mergers drive starbursts by compressing gas into galactic centers, producing uniquely high gas densities, elevated turbulent energy densities, and extreme specific star formation rates. Here, we present the first results from a new Cycle 12 ALMA Large Program: The Merger INduced starbursts and Gas Lifecycle Examination (MINGLE). With CO(2-1) observations at ~70 pc resolution, we will measure the luminosity, mass, and kinematics of individual giant molecular clouds across 22 mid-stage (41 nuclei) luminous infrared galaxies (LIRGs). Combined with matched-resolution HST Pa-beta observations, we can characterize the physical processes which drive extreme star formation and feedback in these dynamically evolving systems.

INTRODUCTION

During merger events, compressive tides and turbulence are most impactful from first pericentric passage to final coalescence, fueling energetic star formation activity in the ISM with high molecular gas fractions and high specific star formation rates; conditions analogous to observations of high-redshift galaxies (Renaud et al. 2015, 2019, 2022). Case studies of individual major mergers, such as the Antennae galaxies, reveal that giant molecular clouds (GMCs) appear to evolve differently in extreme starburst environments (Brunetti et al. 2021, He et al. 2023).

The ALMA-MINGLE survey is a Cycle 12 Large Program designed to study 22 mid-stage merging LIRGs using ALMA and HST observations. The survey will provide the first systematic assessment of GMC luminosities, masses, and kinematics at ~70 pc scales to understand the physical processes driving star formation and feedback in extreme environments.

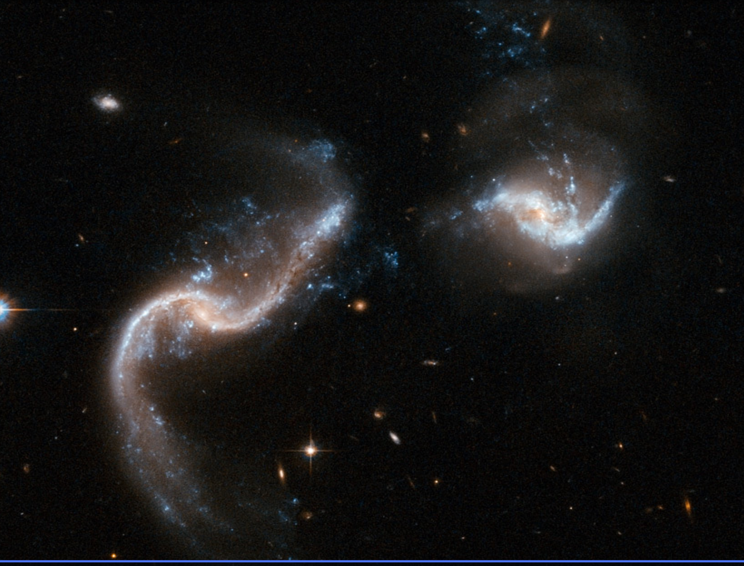

WEBSITE

RESULTS

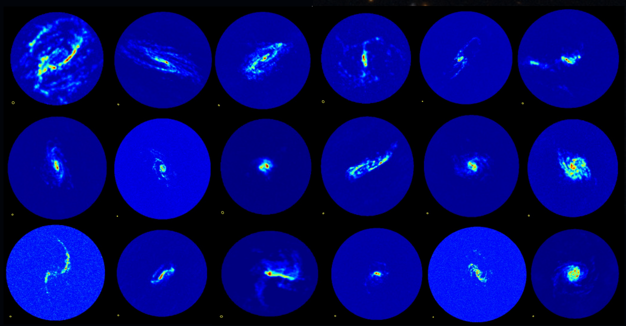

Fig. 1: **TM2 Moment-8 maps of CO (2-1) emission in 15/22 LIRGs observed in the MINGLE survey.**

MINGLE observations of CO (2-1) emission are taken at both GMC-scale (TM1) and kpc-scale (TM2) resolution. The combination of high spatial (~70 pc) and spectral (~2 km/s) resolution allow us to resolve the cloud-scale kinematics, turbulence, and star-forming structures across these dynamically evolving systems. As of May 2026, observations for all 22 LIRGs in both TM1 and TM2 are now completed.

Initial imaging demonstrates the ability to recover spatially resolved GMC populations and map ISM physical conditions across merger environments (see Figure 1). These data will enable comparisons with predictions from pc-scale hydrodynamic merger simulations of star formation and feedback across cosmic time

NEXT STEPS

The next phase of the MINGLE survey will be to apply a grid-based analysis to map GMC properties and star-forming regions throughout the sample. This technique has been developed for mergers in the Great Observatories All-Sky LIRG Survey (Armus et al. 2009, Saravia et al. 2025 - Figure 2). Importantly, relative to lower–resolution observations MINGLE will resolve the complex line profiles of individual GMCs (Figure 3).

Our immediate science goals and the future science enabled with this Cycle 12 ALMA Large Program complement the legacy that surveys such as the Physics at High Angular resolution in Nearby GalaxieS (PHANGS – Leroy et al. 2025) are delivering for non-interacting galaxies. Without high-resolution ALMA observations of the cold molecular gas, we are missing a vital component in the study of birth clouds, the lifecycle of the cool ISM, and the relationship between turbulence and star formation in mergers.

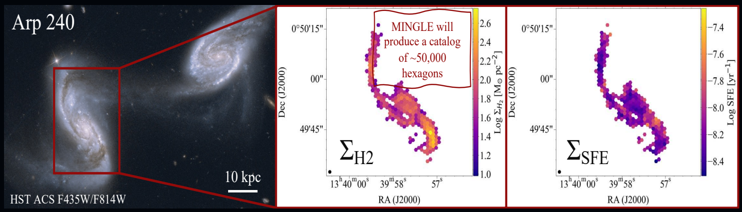

Fig. 2: **Grid-based analysis of Arp 240 presented in Saravia et al. (2025).**

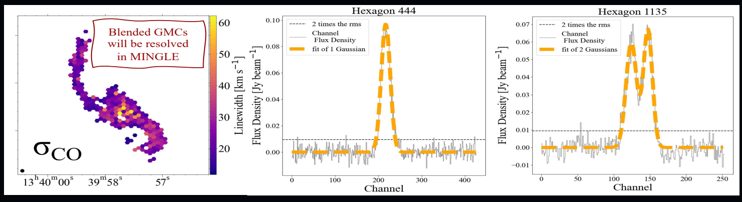

Fig. 3: **With high spectral resolution MINGLE will resolve the line profiles of blended GMCs which cannot be done with existing data.**

REFERENCES: Armus, L.+2009 PASP, 121, 559; Brunetti,N.+2021 MNRAS 500, 4730; He,H.+2023 ApJ 950, 56; Leroy,A.+2021 ApJ 257, 43, +2025; Renaud,F.+2015 MNRAS 446, 2038; Renaud,F.+2019 A&A 621A, 104; Renaud,F.+2022 MNRAS 516, 4922; Saravia, A+2025 ApJ, 979, 217

First High-Sensitivity OH Measurements toward a Pulsar

Mengting Liu, D. Li, J. Dawson, M. Busch, D. Rybarczyk, G. Hobbs, D. Quan, C. Tsai, T. Bisbas

Contact: liumengting@nao.cas.cn

Research Center for Computational Earth and Space Science, Zhejiang Laboratory

We present the **first high-sensitivity, high-velocity-resolution** observations of **the 1665 and 1667 MHz OH main lines toward a pulsar**, **PSR J1644−4559** (*l*=339.193°, *b*= −0.195°), using **Murriyang, CSIRO's Parkes Radio Telescope.**

Motivation

Why OH?

- OH traces molecular gas across both **dense and diffuse** environments , including **CO-dark gas** where CO emission is weak or absent.

Why Pulsars?

- **Sub-arcsecond angular size** background sources with pencil beam measurements (0.03″ for PSR J1644−4559).
- **Simultaneous on-pulse and off-pulse spectra** during one rotational period without repointing the telescope.

The Gap:

Before this work, **only three pulsars** had been observed in OH absorption or pulsar-stimulated emission, with OH properties **poorly constrained by limited optical depth sensitivity** ($\sigma_\tau > 0.01$) and **velocity resolution** ($\mathrm{d}v > 0.44$ km /s) [1–3].

Observations

Parkes Telescope: the ultra-wideband low-frequency receiver

Pulsar phase-resolved spectroscopy technique @1665 & 1667 MHz

Velocity resolution: dv~ 0.088 km/s

Achieved Sensitivity (T_{int} ~71.6 hours):

Optical depth rms: σ_τ ~4×10^{-3}

Brightness temperature rms for the pulsar-off spectra: σ_{T_b}~3 mK

Results from the pulsar-off OH spectra

1. **Support a CO-dark Molecular Gas Reservoir in the Outer Galaxy [4]:** tentative detection of **broad OH emission at outer-Galaxy velocities** (~ 4 to 30 km/s) in both main lines, **coincident with HI but lack ^{12}CO emission** with N(H_2) ~ 2.3×10^{21} cm^{-2} and integrated line ratio ~0.4 (LTE value: 9/5). No comparable broad component in the inner Galaxy.
2. **Existence of Warm (T_{ex}> 19.8 K) or Clumpy OH Gas in the Local Galaxy:** detection of OH emission in the pulsar-off spectra at local-Galaxy velocities (~ −20 to 4 km/s) without corresponding pulsar absorption.

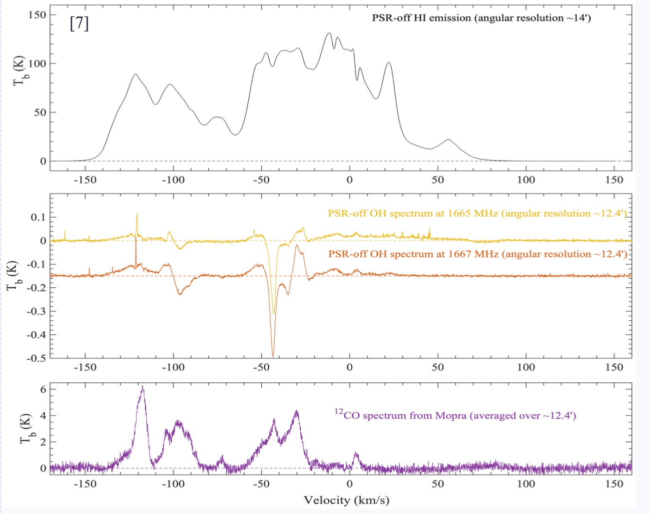

Scientific Impact

Pulsar phase-resolved spectroscopy, by probing an effectively pencil-beam line of sight, reveals intrinsic spectral-line structures and enables most accurate characterization of molecular gas conditions.

Radiative Transfer

$$T_\mathrm{b}^{\mathrm{ON}}(v) = (T_\mathrm{ex} - T_\mathrm{bg})\left(1 - e^{-\tau_1(v)}\right)$$
$$-T_\mathrm{psr}\left(1 - e^{-\tau(v)}\right) + T_\mathrm{psr} + T_\mathrm{bg},$$
$$T_\mathrm{b}^{\mathrm{OFF}}(v) = (T_\mathrm{ex} - T_\mathrm{bg})\left(1 - e^{-\tau_1(v)}\right) + T_\mathrm{bg}.$$

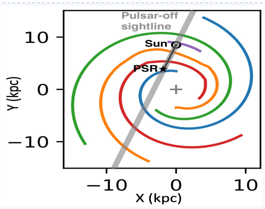

Results from the OH optical depth spectra toward the pulsar:

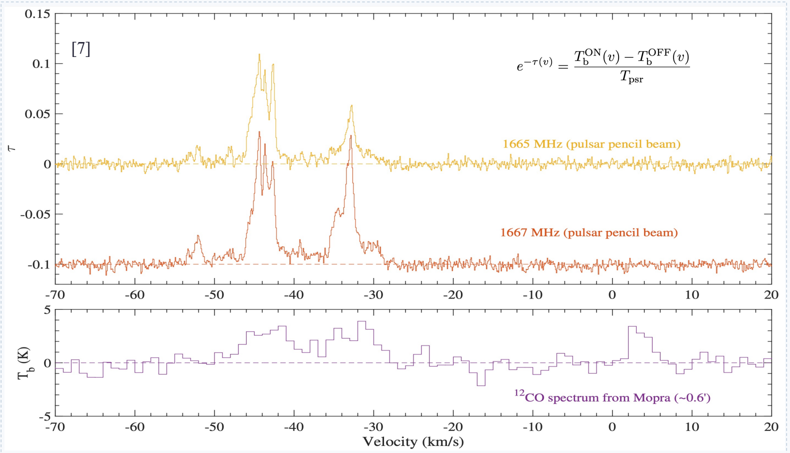

1. **Identify 13 OH absorption components (−54 to −28 km/s):** OH column densities of (0.04 – 8.3)×10^{14} cm^{-2}. **Resolved** 2 previously known features into **7 narrow components** (τ_0 ~ 0.01–0.03); **Revealed 6 new low-optical-depth components** (τ_0 ~ 0.007–0.03), characteristic of more diffuse OH gas detectable in the galactic plane **only through high-sensitivity observations**.

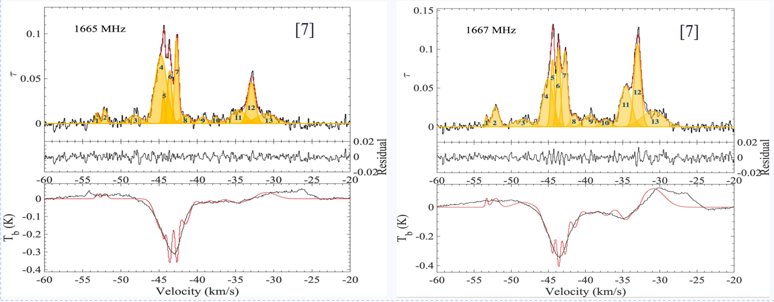

2. **Non-LTE excitation properties for OH gas:** 64% of components **deviate from the LTE** 1667/1665 optical depth ratio of 1.8 and 79% of components exhibit **excitation temperature differences** within **±2 K.** For components with |Tex(1665)−Tex(1667)| > 2 K, **the 1667 MHz transition** tends to show **higher excitation temperature**. The **1667/1665 optical depth ratio decreases toward smaller Galactocentric radii.**

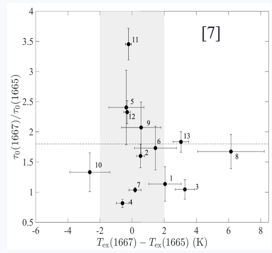

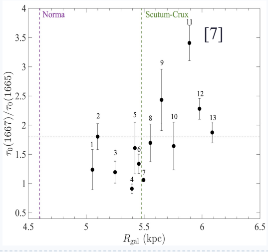

3. **Direct evidence for clumpy sub-beam structure in OH-bearing gas:** At v ~ −43 km/s, the **pulsar pencil beam resolves 4 narrow components** (FWHM 0.4–1.8 km/s), whereas the **beam-averaged pulsar-off spectra against the HII region** (G339.109−00.233 located behind the pulsar) shows **a single broad feature** (FWHM ~ 3.5 km/s).

4. **OH optical depth line blending remains significant at angular resolution of several tens of arcseconds:** **optical depth linewidths** measured **toward the pulsar** (0.4–3.5 km/s with a median of 1.1 km/s), **systematically narrower** than those measured with **the interferometers toward resolved extended continuum sources** [5,6].

5. **Turbulence properties and implications : resolved components** (v ~ −43 km/s) exhibit **subsonic to transonic internal motions relative to the CNM sound speed.** Treating the broad, **unresolved feature** as a single component (FWHM ~3.5 km/s) **overestimates** the **turbulent velocity dispersion** by **factors of 2–20**. Broad features reflect inter-cloud bulk motions, not supersonic internal turbulence which is consistent with **the two-phase ISM model** [7].

References

1. Stanimirovic et al. 2003, ApJ, 592, 953; **2.** Weisberg et al. 2005, Science, 309, 106; **3.** Minter et al. 2008, ApJ, 677, 373; **4.** Busch et al. 2021, ApJ, 914, 72; **5.** Hafner et al. 2023, PASA, 40, e015; **6.** Rugel et al. 2018, A&A, 618, A159; **7.** Liu et al. 2026 submitted.

Ionization Structure in Lyman Continuum Leaking Galaxies

Emma Lundqvist[1], Göran Östlin[1], Arjan Bik[1], Jens Melinder[1]

[1]Department of Astronomy, Stockholm University

emma.lundqvist@astro.su.se

1 LyC-leakers during the EoR

During the epoch of reionization (EoR), Lyman continuum (LyC) radiation, capable of ionizing hydrogen, escaped from star-forming galaxies to ionize the surrounding intergalactic medium (IGM). The exact means of this LyC-escape is still unknown.

Two scenarios exist: **a)** The extreme scenario where the number of ionizing photons exceed the number of neutral hydrogen atoms (density bounded nebula), **b)** Neutral hydrogen still remains in the ISM (radiation bounded nebula), but feedback and turbulence have created low-opacity and high-ionization channels through which the radiation escapes. This is also known as the picket-fence model, where LyC-detection is highly dependent on the line-of-sight direction to the galaxy [1].

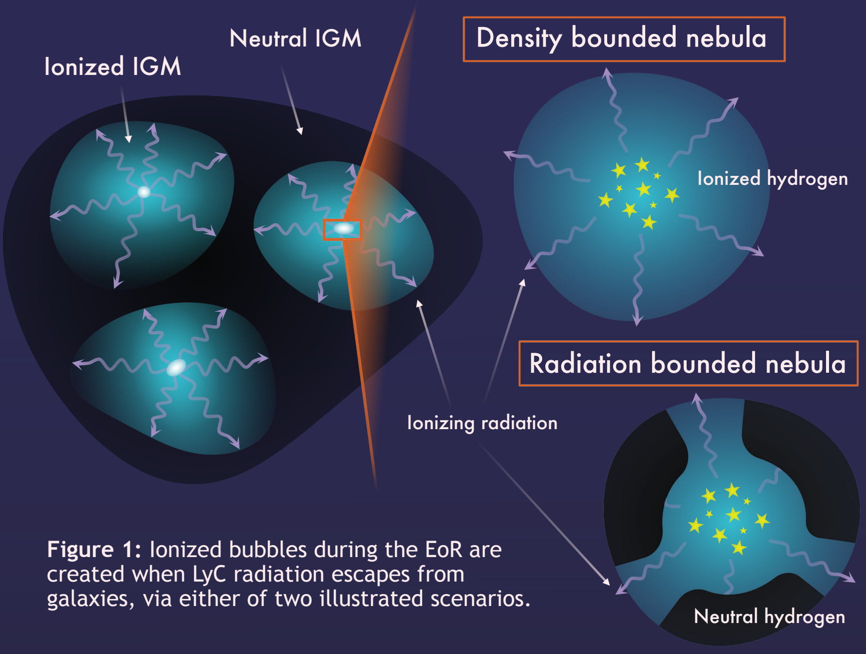

Figure 1: Ionized bubbles during the EoR are created when LyC radiation escapes from galaxies, via either of two illustrated scenarios.

2 VLT/MUSE observations

In this study, 14 star-forming galaxies were observed with VLT/MUSE, using AO [2], with ten of them being LyC-leakers [3, 4, 5]. With redshifts of $z \sim 0.3$, the targets are local analogs to star-forming galaxies during the EoR. The observed wavelengths of the integral field unit data stretch from 4650 - 9300 Å.

3 Results - [OIII]/[OII] maps

Using the spatially resolved spectroscopic data, we calculate the integrated flux of emission lines. To trace the ionization structure of the galaxies, we compare two lines of the same element and different ionization levels. Here, the ratio of the [OIII] λ5007 Å line to the [OII] λ3727 Å doublet (O_{32}) is used for this purpose. A high O_{32}-ratio has been shown to indicate a high LyC escape fraction, f_{esc} [6]. Fig. 2 shows the O_{32} maps of three of the galaxies in the sample.

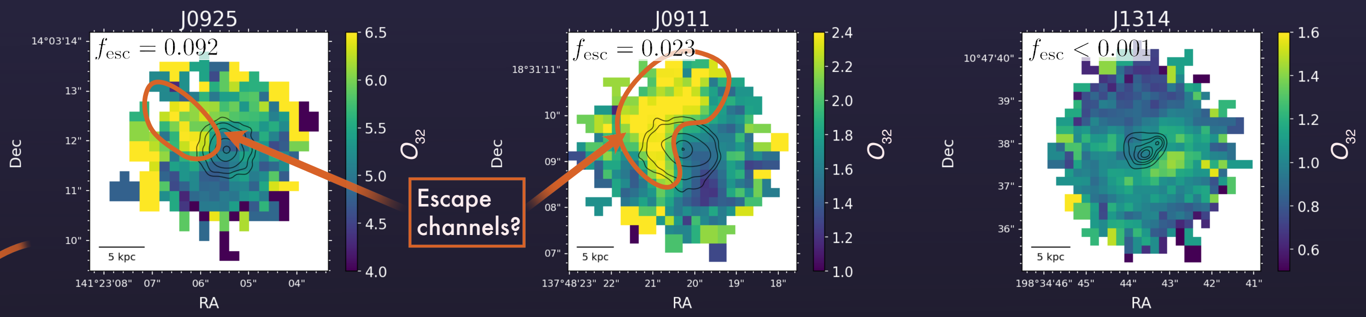

Figure 2: O_{32} maps for three of the observed galaxies. The leftmost and middle galaxies have a measured LyC escape, and both ISM:s exhibit a complex ionization structure with possible escape channels. The rightmost galaxy is a likely non-leaker with no clear ionization structure. The black contours show photometric data from the Hubble Space Telescope (WFC3/UVIS F547M) [7].

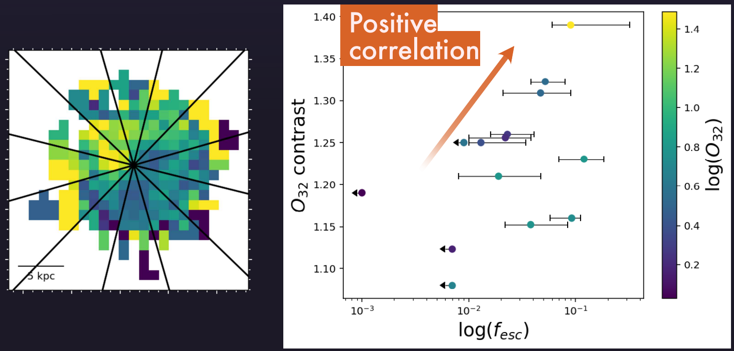

Figure 3: Left: An example how a galaxy (J0925) is divided into wedges. **Right:** A scatter plot of the O_{32} contrast to the LyC escape fraction for the whole sample, color coded by the mean O_{32}-value for each galaxy.

4 Ionization structure tracing f_{esc}

To investigate if the picket-fence model is a likely mechanism for LyC escape, we examined the ionization structure of the 14 galaxies. The galaxies were divided into wedges, simulating escape channels. A correlation was found between the O_{32}-contrast (the highest O_{32}-value in a wedge normalized by the galaxy mean) and the escape fraction f_{esc}. Fig. 3 shows an example with twelve wedges per galaxy. The correlation is statistically significant, with $p \sim 0.02$ and Kendall-τ ~ 0.47, lending weight to the picket-fence scenario.

References: [1] Zackrisson et al. 2013, ApJ, 777, 39 [2] Bacon et al. 2017, A&A, 608, A1 [3] Flury et al. 2022a, ApJS, 260, 1 [4] Izotov et al. 2018, MNRAS, 478, 4851 [5] Izotov et al. 2016, Nature, 529, 178 [6] Flury et al. 2022b, ApJ, 930, 126 [7] Le Reste et al. 2025 ApJS, 280, 27

Gas and Dust in Low-Metallicity ISM: SOFIA [CII] and [OIII] Observations in the Large Magellanic Cloud (LMC^+)

Suzanne C. Madden[1], **Christian Fischer**[2,3] **Léo Belloir**[1] & the **LMC^+ Consortium**

[1]CEA, Univ. Paris-Saclay,, CNRS, Gif-sur-Yvette, France
[2]Deutsches SOFIA Institut, Univ. Stuttgart, Stuttgart, Germany
[3]IRAM Saint-Martin d'Hères, France

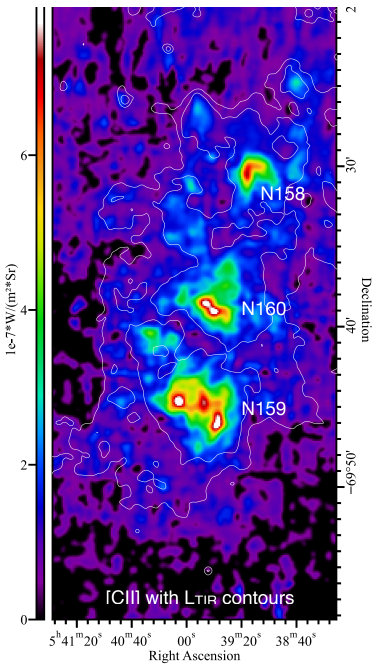

Introduction

We have mapped a large area (610pc x 260pc) of the southern molecular ridge in the closest low metallicity galaxy, the Large Magellanic Cloud (Z= 0.5Zo) in the 158 µm [CII] and 88 µm [OIII] lines at 2.5 pc resolution using the FIFI-LS spectrometer on the airborne platform, SOFIA *(Fischer et al 2025).* These observations allow studies of the major heating and cooling mechanisms in and around the massive star-forming regions, N158, N159 and N160. Photoelectric heating efficiency in relation to grain properties is studied *(Belloir et al 2026)* using Herschel & Spitzer maps & applying the hierarchical Bayesian SED model, HerBIE (*Galliano 2018).*

Key Questions

- How do local conditions influence the H^+ - H^0 - H_2 and the C^+ - C^0 - CO transitions and star formation in low-metallicity environments?
- How do the properties and structure of ISM phases transition from dense star-forming regions to more diffuse, low-A_V environments?
- What local factors favor the presence of CO-dark vs. CO-bright H_2 gas?
- How does the photoelectric heating efficiency vary in low metallicity environments and relate to local physical conditions?

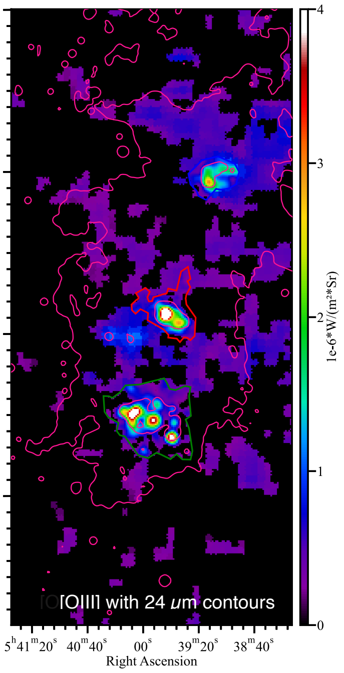

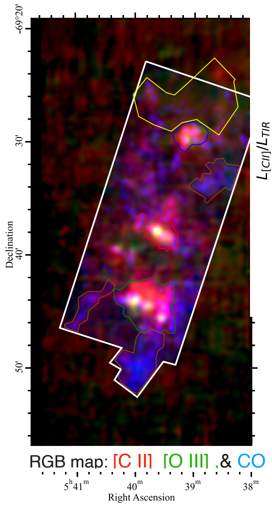

RGB map: [C II] [O III] ,& CO

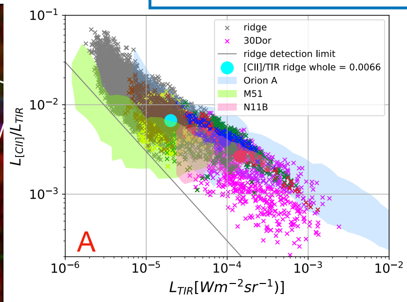

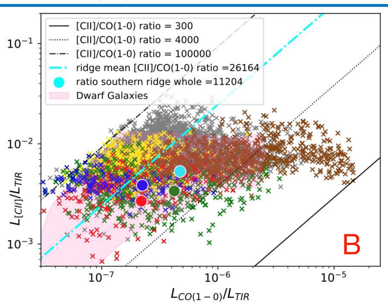

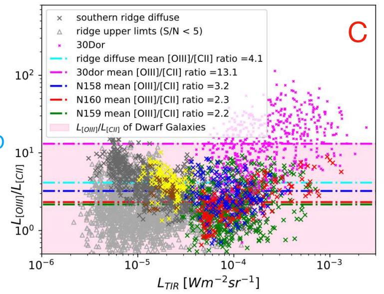

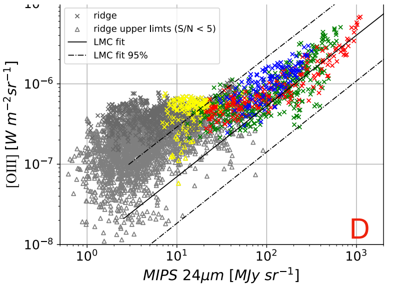

Line ratio Analysis (left plots)

A) $L_{[CII]}/L_{TIR}$ vs L_{TIR} (regions color coded in the RGB map, left); we add: 30Doradus (*Chevance + 2020*); Orion A (*Pabst +2021*); M51 (*Pineda+2018*); N11B (*Lebouteiller+2012*).

B) $L_{[CII]}/L_{TIR}$ vs L_{CO}/L_{TIR}. In pink: Dwarf Galaxy Survey range (*Madden +2020*).

C) $L_{[OIII]}/L_{[CII]}$ vs L_{TIR} for the three bright star formation regions (color coded in the RGB map, left; grey regions are outside the three star forming regions).

D) [OIII] vs MIPS 24*µm* in the three star formation regions. The fitted linear relation (solid black) & 95% confidence interval (dashed lines) from *Lambert-Huyghe + (2022)*.

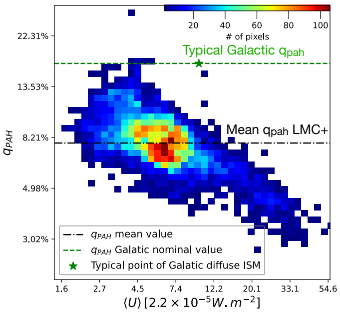

(*Left*) Fraction of small grains (<1.5 nm) vs. mean interstellar radiation field <U>.

$$\epsilon_{PE} \equiv \frac{L_{obs}([CII]) - L_{ion}([CII]) - L_{mol}([CII])}{L_{PAH}}$$

(*right*) PE heating efficiency (ε_{pe}) vs q_{PAH}. Blue histogram & map: takes into account phase decomposition; Red does not.

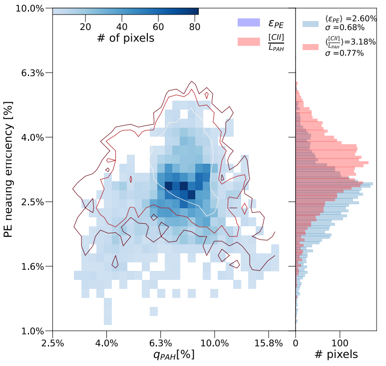

Map of q_{PAH} with [CII] contours.

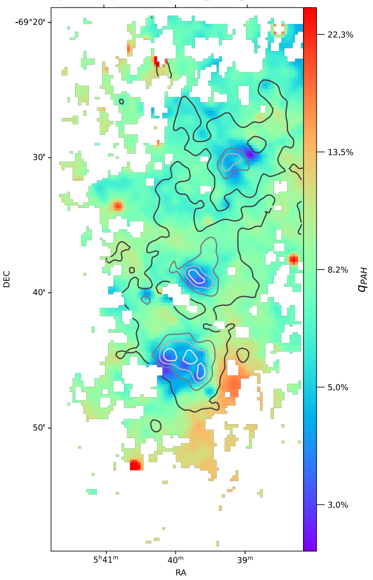

Conclusions

- Importance of [CII] as a cooling line relative to L_{TIR} increases with decreasing L_{TIR}.
- [OIII] is typically brighter than [CIII] throughout map; $L_{TIR}/L_{[OIII]}$ > 10 in extended, diffuse regions.
  => Hints to porous, clumpy ISM; UV light propagates well beyond the [HII] regions.
- CO emission is spatially limited and patchy compared to [CII]; $L_{[CII]}/L_{CO}$ is very high.
- High $L_{[CII]}/L_{CO}$ prefers regions with low L_{CO} => implications for important CO-dark molecular gas?
- Correlation between abundance of small a-C(:H) grains, the carriers of the PE effect, and starlight intensity => destruction of carriers by intense stellar radiation.
- $L_{[CII]}/L_{PAH}$ is a good proxy for PE efficiency; correcting for phases gives better estimate ($\varepsilon_{pe\sim15\%}$ lower)

The influence of the environment on the morphology and ISM properties of the lopsided galaxy NGC 2276

Luka Matijević[1], Antonino Marasco[2], Neven Tomičić[1]

[1]*University of Zagreb, Faculty of Science, Department of Physics, Zagreb, Croatia* | [2]*INAF Padova Astronomical Observatory, Padova, Italy*

Introduction

NGC 2300 group is a galaxy group consisting of 8 members [1], of which the two most massive are NGC 2300, and NGC 2276.

NGC 2276 displays a disturbed morphology at various wavelengths, including the **longest radio continuum tail** observed in a group galaxy [2]. Its asymmetric shape and unusually high star formation (SF) rate for its stellar mass (**~0.75 dex** above the main sequence of SF [3]) are caused by environmental forces. Those forces are suspected to be **tidal interaction** with its neighbor NGC 2300 [4] (Fig. 1), as well as **ram pressure** (RP) caused by its movement through the intergalactic medium (IGM) [5].

RP and tidal interaction have different imprints on the galactic morphology, with the former affecting just the gaseous component [6], while the latter affects both the gaseous and stellar component [7].

We present results from a multifrequency analysis of this galaxy by showing how those forces influence its various small- and large-scale properties.

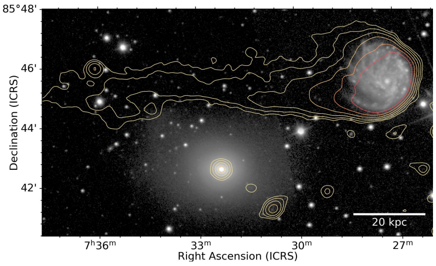

Figure 1. LOFAR's HBA 144 MHz continuum emission contours ($6\times2^{n}\times$RMS, RMS = 120 μJy, PSF FWHM = 11.9 $\times$8.2 asec^2) plotted on top of Palomar's ZTF g-band image of NGC 2300 group center. **Matijević+26 in prep**

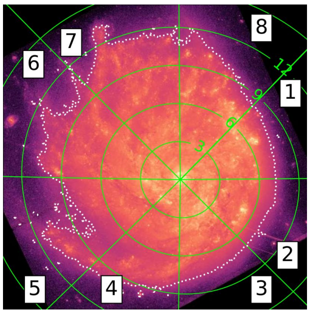

Figure 2. HST UVIS WFC3 F555W image divided into 8 sectors. The concentric ellipses show regions with constant galactocentric distance of 3, 6, 9, 12, and 15 kpc. [8]

Methods

- **Morphological Analysis:** Utilized photometric maps of NGC 2276 spanning near-ultraviolet (NUV) to near-infrared (NIR) wavelengths to analyze **radial profiles** on opposite sides, aiming to determine which of two effects is more prominent in shaping the galaxy's morphology.
- **Star Formation History (SFH)**: Extended wavelength coverage to include far-ultraviolet (FUV) to mid-infrared (MIR) and applied **fully spatially resolved** (sub-kpc) **spectral energy distribution** (SED) fitting using Bagpipes [9] to obtain the complete SFH.
- **Interstellar Medium (ISM) Diagnostics:** Analyzed and constrained the effects of the two forces on the disturbed ISM by applying **emission line diagnostics** through Baldwin, Phillips & Terlevich (BPT) [10] diagrams, utilizing integral field unit (IFU) data from the Calar Alto observatory and WEAVE LIFU.

Results

- Maps from Hubble Space Telescope (HST) and Spitzer NIR divided into 8 sectors (Fig. 2)
- Color-proxy radial profiles reveal the galaxy becoming **increasingly red** on its leading side (Sectors 1&2)

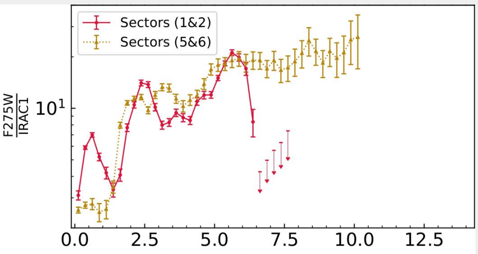

Figure 3. Color-radial profile of the leading and trailing side expressed as a ratio of F275W and IRAC 1. [8]

- The trailing side (Sectors 5&6) exhibits a slightly bluer shift → **ram pressure** is likely the **primary** morphological disturber

- Based on the SFH maps, stars with an age **≳1.1 Gyrs** are distributed almost perfectly **symmetrically** within the galaxy
- The distribution of **younger stars** is found to be **highly asymmetric**
- The most definitive evidence to date of **negligible tidal interaction** within this system

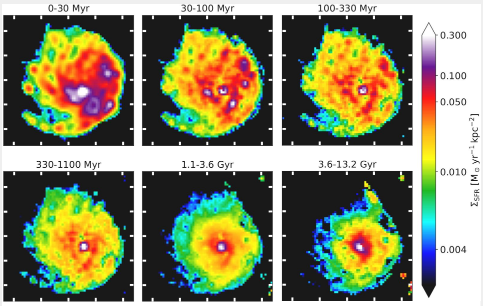

Figure 4. Σ_{SFR} as a function of position in the galaxy for different epochs corresponding to the six main age bins, derived as a Bagpipes posterior. **Matijević+26 in prep**

- 2D maps of BPT diagrams - Calar Alto observatory (top) and new WEAVE LIFU observations (bottom)
- Majority of the galaxy is covered by **HII regions**
- [OI] and [SII] excess on the southern side and the western tip of the galactic disk

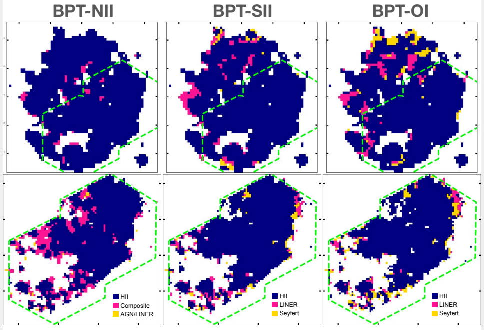

Figure 5. BPT diagrams of NGC 2276 extracted from Calar Alto IFU (top row), and WEAVE LIFU (bottom row). **Matijević+26 in prep**

- Calar Alto dataset additionally identifies [OI] and [SII] excess on the northern and eastern sides → mixing of the IGM and ISM, specifically driven by ram pressure (possibility of an ionized gas tail) [11]

Conclusions

We are mostly sure that this galaxy is affected solely by ram pressure with the following evidence: 1) By investigating the color radial profiles we found that the younger stars are more compressed on the leading side, and more extended on the trailing side, while the older stars remain stable; 2) detailed analysis through dedicated SFH shows that older stars are more symmetrically distributed, while the younger ones show a clear east-west asymmetry; 3) There is a possible evidence of an [OI] excess on the north and east sides (usually found in the ram-pressure stripped tails), however this claim needs to be investigated more thoroughly.

References

[1] Fadda D., et al., 2023, ApJ, 957, 83.
[2] Roberts I.D., et al., 2024, A&A, 689, A22.
[3] Tomičić N., et al., 2018, ApJL, 869, L38.
[4] Davis D.S., et al., 1997, AJ, 114, 613.
[5] Rasmussen J., et al., 2006, MNRAS, 370, 453.
[6] Gunn J.E., Gott J.R., 1972, ApJ, 176, 1.
[7] Toomre A., Toomre J., 1972, ApJ, 178, 623.
[8] Matijević L., et al., 2026, A&A, 707, A40.
[9] Carnall A.C., et al., 2018, MNRAS, 480, 4379.
[10] Baldwin J.A., et al., 1981, PASP, 93, 5.
[11] Tomičić N., et al., 2021, ApJ, 922, 131.

Acknowledgements

This work was supported by the Croatian Science Foundation under the project number HRZZ-MOBDOK-2023-8006.
This work was supported by the European Union – NextGenerationEU through National Recovery and Resilience Plan 2021-2026.
Institutional grant of University of Zagreb Faculty of Science PMF-YOUTHCONF-2026-03 & ProPubFO.

Croatian Science Foundation

Funded by the European Union
NextGenerationEU

Contact information

lmatijevic@phy.hr

The JCMT BISTRO Survey: Unveiling the Magnetic Fields around Galactic Center

Meng-Zhe Yang (NTHU) , Shih-Ping Lai (NTHU), Janik Karoly (UCL), and BISTRO team

Introduction and Motivation

The **Central Molecular Zone (CMZ)** hosts dense molecular clouds with extreme conditions near the Galactic Center, where star formation efficiency is significantly lower than in typical Galactic clouds.

Magnetic fields may provide additional support against gravitational collapse; we therefore investigate the magnetic field strength and energy balance in the **circumnuclear disk (CND)**, **20 km/s cloud (20MC)**, and **50 km/s cloud (50MC)**.

Data	Tracer	Angular Resolution
JCMT SCUBA2/POL2	450, 850μm	9.6", 14.6"
NRO	$C^{18}O$ (1–0)	15"
Herschel Hi-GAL	160, 250, 350, 500μm	12″, 18″, 25″, 36″

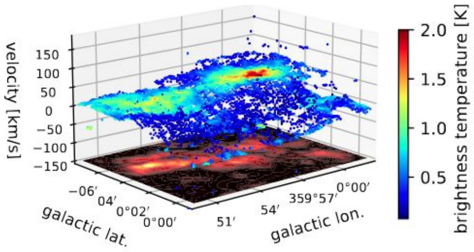

CND, 20MC, 50MC are **close in the sky** but clearly **separated in PPV space**.

Scientific Questions

Q1: Are magnetic fields dynamically dominant in Galactic Center clouds?

Q2: Are unusually strong background magnetic fields present in the CMZ?

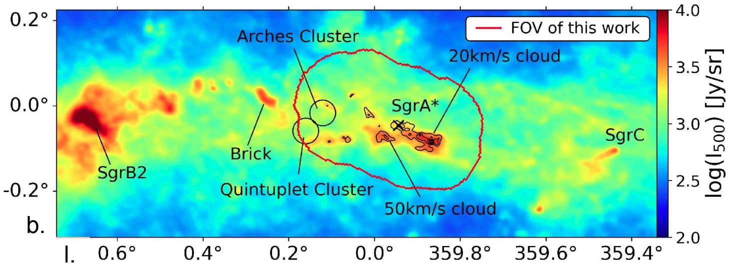

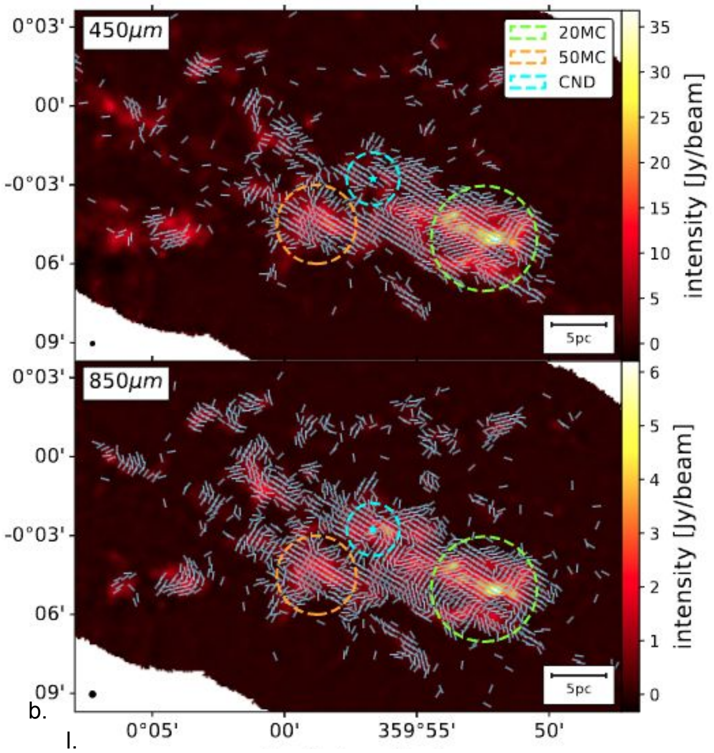

Magnetic Field Strength and Energy Budgets

$$B_{POS} = Q'\sqrt{4\pi\rho}\,\frac{\sigma_\nu}{\sigma_\theta}$$

(Davis 1951; Chandrasekhar & Fermi 1953)

ρ : mass density
σv: non-thermal velocity dispersion
σθ: angular dispersion

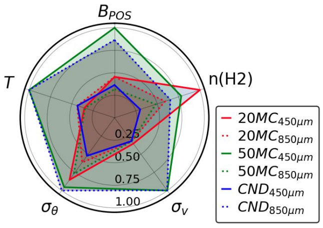

	BPOS [μG]		Btot [μG]	
	450μm	850μm	450μm	850μm
20MC	1.0	0.7	1.3	0.9
50MC	1.0	0.8	1.2	1.0
CND	2.2	1.9	2.8	2.5

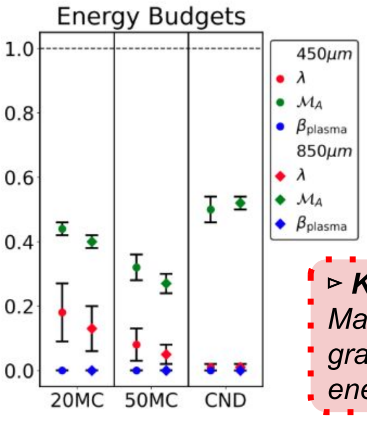

Mass-to-Flux Ratio, λ
λ < 1 (magnetic dominated)
Alfven Mach Number, M_A
M_A < 1 (magnetic dominated)
Plasma Beta, β_{plasma}
β_{plasma} < 1 (magnetic dominated)

▹ ***Key Results (Q1)***
Magnetic fields dominate over gravity, turbulent and thermal energies in all regions.

Field Strength and Density Relation

Crutcher et al. (2010) proposed that the B-n relation can be described as:

$$B_{max}(n) = \begin{cases} B_0 & , n < n_0 \\ B_0\left(\frac{n}{n_0}\right)^\kappa & , n > n_0 \end{cases}$$

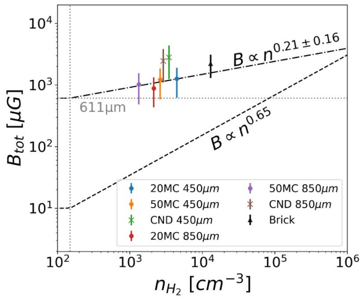

	Crutcher et al. (2010)	This work
B0	10 μG	611 μG
κ	0.65	0.21

▹ ***Key Results (Q2)***
The CMZ exhibits a flatter B-n relation and unusually strong background magnetic fields compared to typical Galactic molecular clouds.

The inner CMZ hosts dynamically important magnetic fields and may contain unusually strong background magnetic fields prior to significant cloud compression.

The JCMT BISTRO Survey: Exploring the Magnetic Fields in the Massive Star-Forming Region Onsala 2

Meng-Zhe Yang (NTHU), Hao-Yuan Duan (TAM), Shih-Ping Lai (NTHU), and BISTRO team

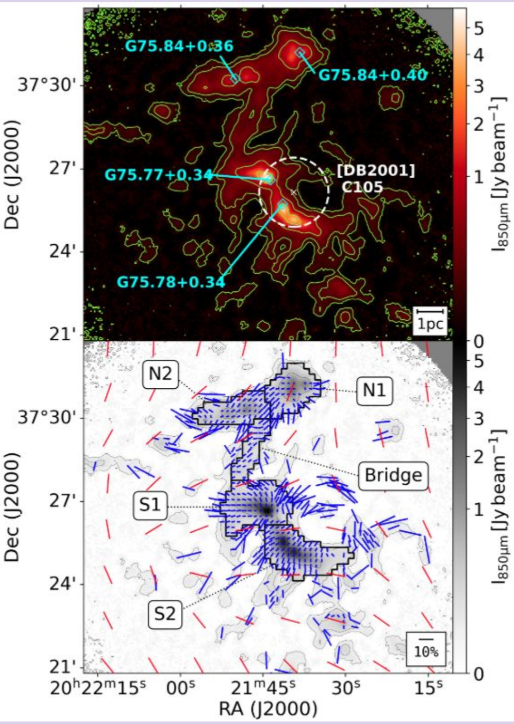

Introduction and Motivation

Star formation is regulated by magnetic fields, turbulence, and gravity. Onsala 2 in the Cygnus X complex hosts multiple HII regions, making it an ideal target for studying magnetic fields in massive star formation. By comparing magnetic fields across different scales, we investigate how dense structures affect magnetic field morphology.

Data	Tracer	Angular Resolution
JCMT BISTRO	850μm polarization	~14”
JCMT HARP	^{13}CO (3–2), C^{18}O (3–2)	~15”
Herschel PACS/SPIRE	70–500μm continuum	~5”.7–36”.6
Planck	353GHz polarization	~4.8’

Scientific Questions

Q1. What is the dynamical importance of magnetic fields in Onsala 2?

Q2. How do magnetic field properties vary with spatial scale and local environment in Onsala 2?

Magnetic Field Strength and Energy Budgets

$$B_{POS} = Q' \sqrt{4\pi\rho}\, \frac{\sigma_\nu}{\sigma_\theta}$$

(Davis 1951; Chandrasekhar & Fermi 1953)

ρ : mass density
σv: non-thermal velocity dispersion
σθ: angular dispersion

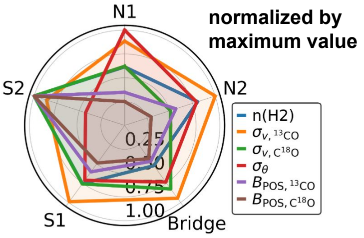

[μG]	$B_{POS,13CO}$	$B_{POS,C18O}$
N1	42.2	29.6
N2	68.7	34.7
Bridge	56.6	51.0
S1	73.2	57.7
S2	121.5	118.4

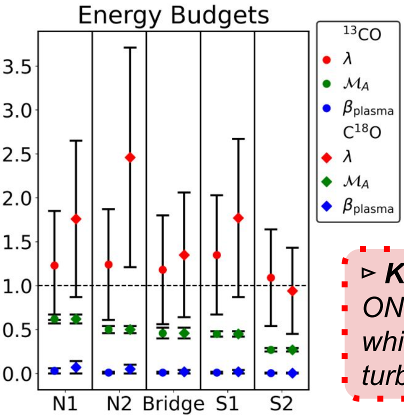

Mass-to-Flux Ratio, λ
λ > 1 (gravity dominated)
Alfven Mach Number, M_A
M_A < 1 (magnetic dominated)
Plasma Beta, β_{plasma}
β_{plasma} < 1 (magnetic dominated)

> ▹ ***Key Results (Q1)***
> *ON2 clumps are gravity-dominated, while magnetic energy exceeds turbulent and thermal components.*

Grain Alignment Efficiency

Dust polarization traces magnetic fields, while the grain alignment efficiency is quantified by fitting the relation between p_{undeb} and σ_{QU} (Pattle et al. 2019)

$$p' = \sqrt{\frac{\pi}{2}} \left(\frac{I}{\sigma_{QU}}\right)^{-1} \mathcal{L}_{\frac{1}{2}} \left[-\frac{p_{\sigma_{QU}}^2}{2} \left(\frac{I}{\sigma_{QU}}\right)^{2(1-\alpha)} \right]$$

α→0 indicates a better grain alignment efficiency.

> ▹ ***Key Results (Q2)***
> *Grain alignment efficiency increases closer to HII regions , affecting polarization diagnostics, especially in S1 and S2.*

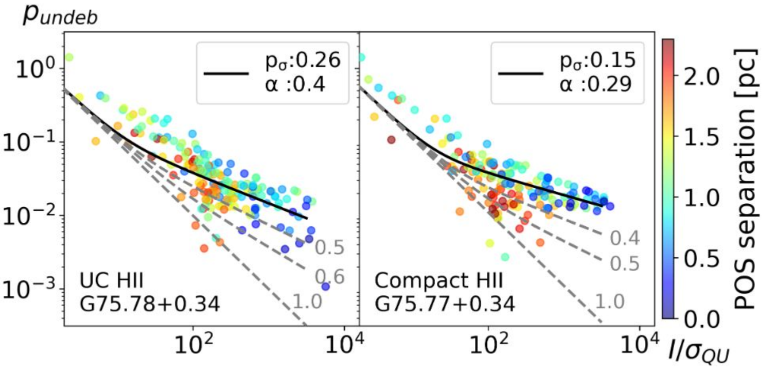

Magnetic Fields vs. Gravity Across Scales

> ▹ ***Key Results (Q2)***
> *The relative orientation between magnetic fields and gravity depends on global gravity.*

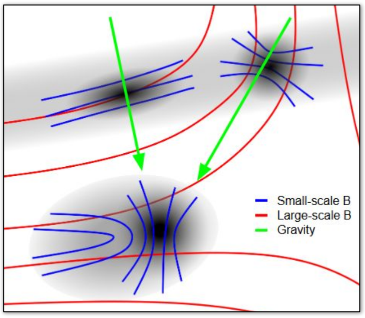

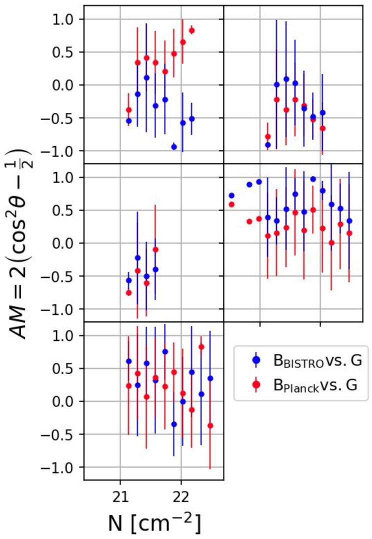

Take Home Message

ON2 appears to be a gravity-dominated yet magnetically regulated massive star-forming region, where magnetic field structures are influenced by the global gravitational field, while dust polarization properties vary with distance to HII regions.

Cloud–Cloud Collisions Induce Filament-Mediated Super Star Cluster Formation in the Antennae Overlap Region: Evidence from ALMA and JWST

Paper Link

Tomonari Michiyama (Shunan University)

et al., 2026, ApJ, 999, 119

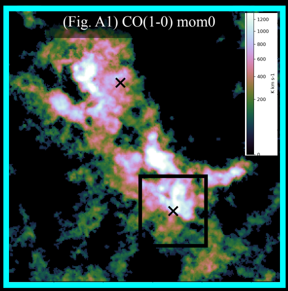

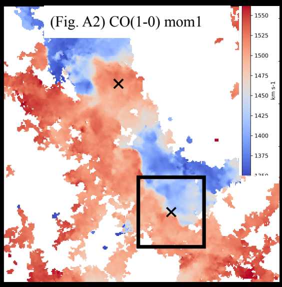

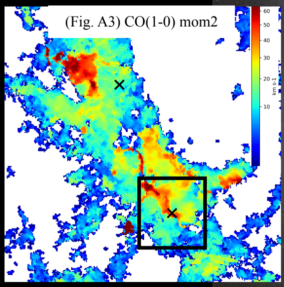

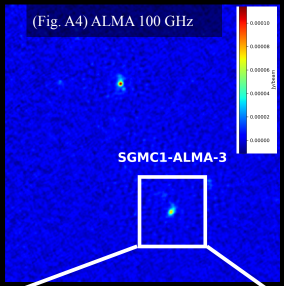

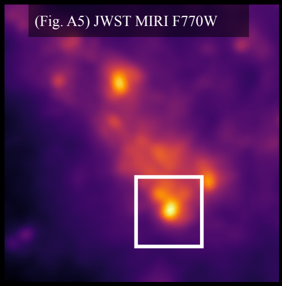

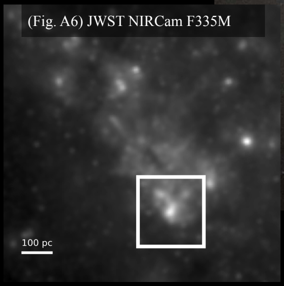

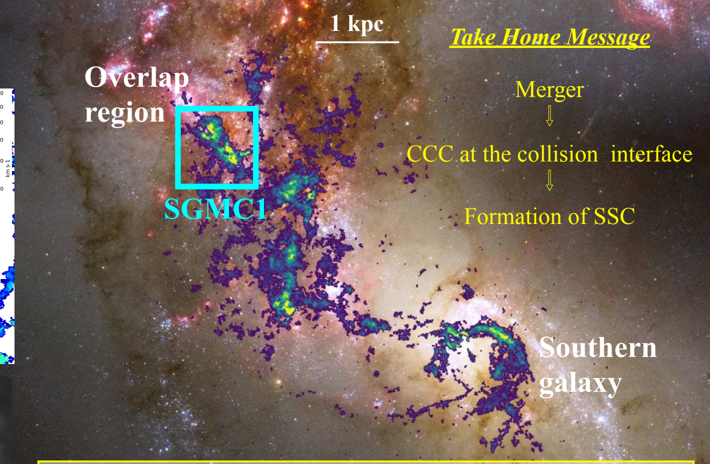

Take Home Message

Merger
⇩
CCC at the collision interface
⇩
Formation of SSC

DATA

ALMA: CO(1–0) 0.12″ (14.1 pc), a velocity resolution of 2.54 km/s
JWST: NIRCam F335M and MIRI F770W, polycyclic aromatic hydrocarbons (PAHs)
HST-based SSC catalog: from Whitmore et al. (2010)

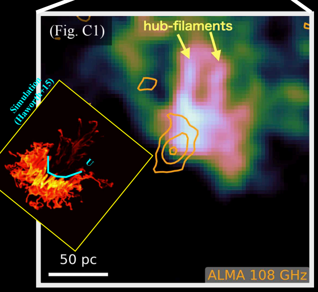

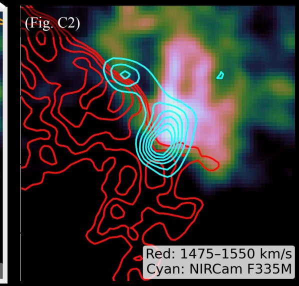

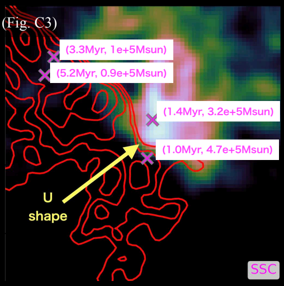

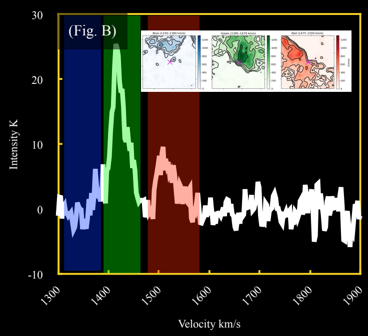

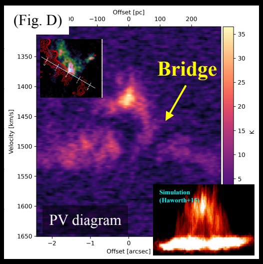

1. ***SGMC1-ALMA-3***

We focus on the SGMC1 region, originally identified by Wilson et al. (2000). Within SGMC1, Whitmore et al. (2014) identified a radio emission peak with SSC candidates, designated “SGMC1-ALMA-3.” Figures A1–A6 present our new ALMA CO(1–0) zoom-in view, 100 GHz continuum map, and JWST NIR–MIR images. At the 100 GHz peak of SGMC1-ALMA-3, the CO(1–0) emission shows two distinct velocity components: main (green; 1395–1470 km/s) and a redshifted one (1475–1550 km/s) (Fig. B). As shown in Fig. C, the 100 GHz continuum emission is located at the interface between these two components. The main component exhibits a hub–filament structure, while the redshifted one forms a “U”-shaped morphology. In addition, the position–velocity (PV) diagram extracted along the redshifted filament shows a bridge-like feature connecting the two components (Fig. D). These morphological and kinematic signatures are consistent with the cloud–cloud collision (CCC) scenario (see Fukui et al. 2021 for a review).

2. ***DISCUSSION***

- **Evidence for Cloud–Cloud Collision (CCC)**
  - A U-shaped structure at the interface suggests compression by ram pressure.
  - The estimated ram pressure is $P_{\rm ram}/k_{\rm B} \approx 1.5 \times 10^9$ K cm^{-3} ($P_{\rm ram} = \rho v^2,\ \rho = \frac{M}{\frac{4}{3}\pi R^3}$), which is enough to make U-shape.
- **Nature of 100 GHz Continuum Emission**
  2D Gaussian fitting yields a flux density of 300 μJy at 100 GHz.
  The flat spectral index rule out synchrotron or thermal dust emission.
  → This attributed to free–free emission from ionized gas.
- **Ionizing Photon Rate and Stellar Mass**
  The estimated ionizing photon rate is $Q(H^0) = 2.5 \times 10^{52}$ s^{-1}.
  → This implies that approximately 5–10% of the mass of the nearby SSC consists of young massive stars, which are likely the source of the observed free–free emission. This result agrees well with Starburst99 models.
- **Infrared Morphology and Sequential Star Formation**
  - F335M and F770W trace PAH emissions along the filament edge
  - Older SSCs lie downstream (northeast), beyond the PAH-emitting region.
  → Suggests sequential star formation propagation, likely triggered by CCC.

3. ***SUMMARY***

- High-resolution ALMA CO(1-0) observations of SGMC1-ALMA-3 reveal three key features that are naturally explained by a CCC model: a “U”-shaped structure within a large filament, a hub–filament morphology, and a bridge-like feature in the PV diagram.
- We present direct observational evidence that cloud–cloud collisions triggered by galaxy mergers drive super star cluster formation.

REF. Fukui et al. (2021), PASJ, 73, S1; Haworth et al. (2015), MNRAS, 454, 1634; Whitmore et al. (2010), AJ, 140, 75; Whitmore et al. (2014), ApJ, 795, 156; Wilson et al. (2000), ApJ, 542, 120;

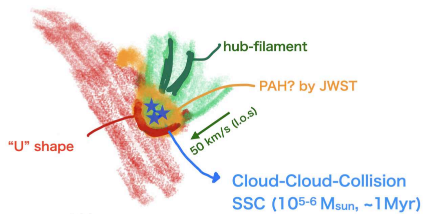

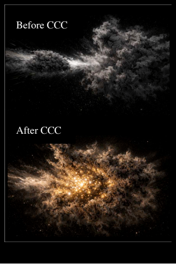

4. MACHINE LEARNING FRAMEWORK FOR FUTURE STUDIES

4.1 Spectral-shape classification

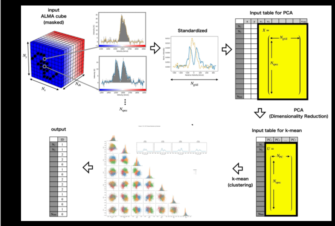

4.2 Three-dimensional component separation in position-position-velocity space

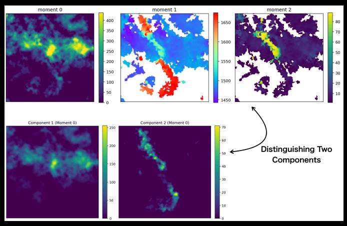

This figure illustrates a machine-learning framework for analyzing ALMA spectral cubes. Each spatial pixel spectrum is standardized, reduced with PCA, and classified using k-means clustering to generate a spatial component map. The right panels show that the method can separate two distinct gas components hidden within the same molecular structure. In the Antennae Galaxies, regions with large apparent velocity dispersion often exhibit multi-component spectra, indicating that the broad line widths arise from overlapping velocity components along the line of sight rather than intrinsically broad emission.

Mapping the Magnetic Fields of M83 using Optical Imaging Polarimetry

D.Mishra[1,2], L.Wang[1,2], F.Patat[3], L.Hu[4], et al.

[1]Department of Physics and Astronomy, Texas A&M University; [2]George P. and Cynthia Woods Mitchell Institute for Fundamental Physics & Astronomy, Texas A&M University; [3]European Organisation for Astronomical Research in the Southern Hemisphere (ESO); [4]McWilliams Center for Cosmology, Department of Physics, Carnegie Mellon University

Magnetic Fields in the Multi-phase ISM of Spiral Galaxies

Magnetic fields are significant component of the ISM in the spiral galaxies, influencing the total pressure balance, molecular cloud collapse, and cosmic ray propagation [1, 2]. Despite their importance, multi-phase magnetic field structure in external galaxies remains poorly constrained observationally. Multi-wavelength polarimetry traces magnetic fields in physically distinct ISM layers. Observations of M51 showed FIR and radio polarization trace different field structures, particularly in spiral arm environments [3].

VLT Optical Polarimetry – Observation & Results

We present VLT/FORS2 V-band optical polarimetry of M83 and compare the magnetic field morphology with existing SOFIA HAWC+ 154µm [4] and VLA+Effelsberg 6cm polarization [5].

Figure 1 (Top Right) shows the optical polarization vectors (binned by (11,11) factor) overlaid on spitzer $8\mu m$ image [6]. The vectors closely follow the spiral arm dust lanes across the galaxy, tracing the large-scale magnetic field morphology, thus, demonstrating the capability of optical polarimetry to map coherent field structure

Multi-Wavelength Polarimetry Comparison

Polarization angle (PA) difference histograms for optical, 90 degree rotated IR and radio polarization across the full galaxy (top) and spiral arms only (bottom), indicate that optical–IR angle difference distribution shows the strongest systematic offset.

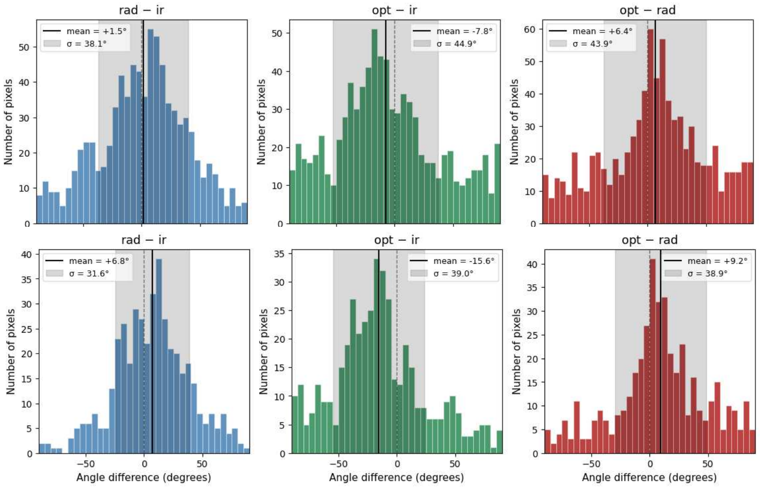

We performed Kolmogorov–Smirnov (K–S) test on the different PA difference pairs. Our results show that in the spiral arm environments, IR polarization varies significantly from both optical and radio, while optical and radio remain mutually consistent.

K-S Test Pair	Global	Spiral Arm
rad − IR vs opt − IR	KS=0.157, p=3.2e−09	KS=0.335, p=4.8e−22
rad − IR vs opt − rad	KS=0.075, p=0.019	KS=0.078, p=0.141
opt − IR vs opt − rad	KS=0.217, p=1.9e−17	KS=0.374, p=1.6e−27

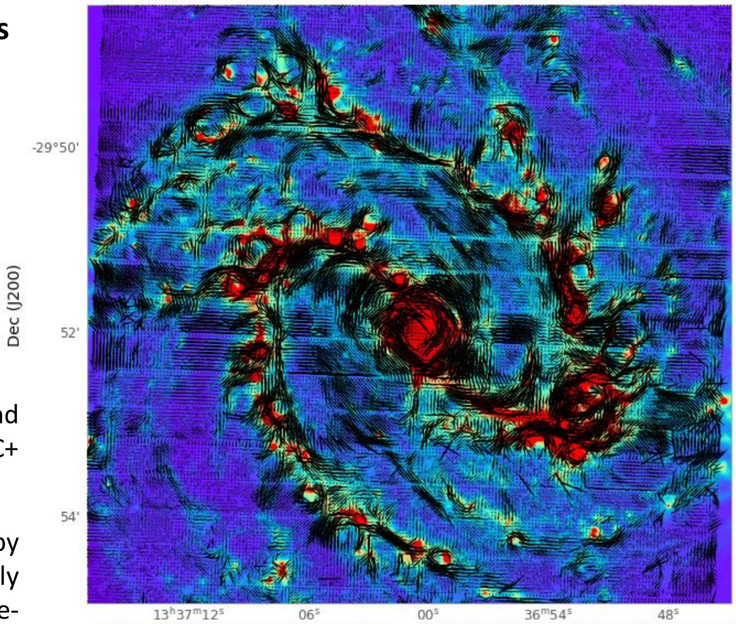

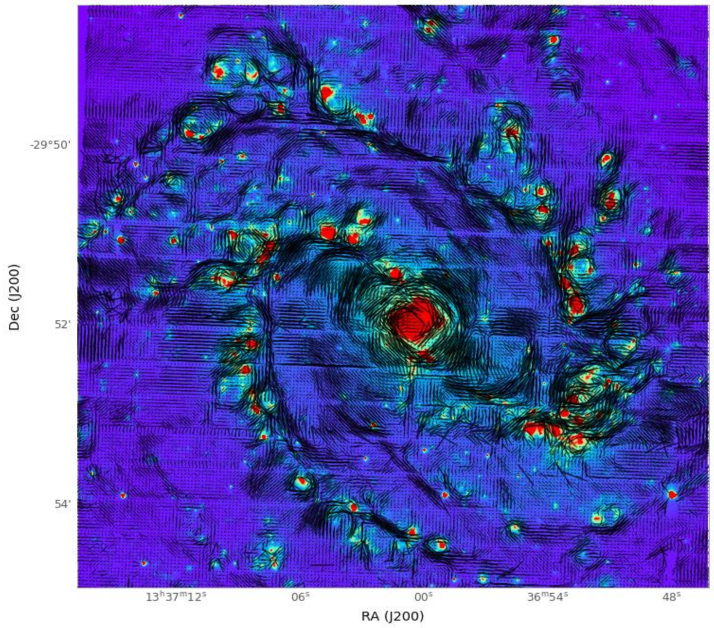

Figure 2 (Bottom Right) shows optical polarization vectors overlaid on H-alpha Image [6]. The vectors show systematic deflections and increased disorder around bright HII complexes, consistent with local magnetic field disruption by stellar feedback and expanding HII shells

Summary

- Optical polarization vectors trace dust lanes across M83.
- Field deflections around HII regions consistent with stellar feedback disrupting local field geometry
- IR polarization is statistically distinct from both optical and radio polarization in spiral arms, suggesting it traces a different or more localized magnetic-field component.
- Optical and radio polarization remain comparatively consistent within spiral arms, suggesting they trace a common ordered large-scale magnetic field.

References : [1] Beck 2015, A&ARv, 24, 4, [2] Hennebelle & Inutsuka 2019, [3] Borlaff et al. 2021, ApJ, 921, 128, [4] Rodriguez et al. 2022, ApJ 936, 1, [5] Frick. et al., 2016, AAP, 585, A21, [6] Dale et al. 2009, ApJ, 703, 517

FLUCTUATION DYNAMOS IN SUPERSONIC TURBULENCE AT $\mathrm{Pm} \gtrsim 1$

AMEYA UDAY NAGDEO[1,2], SHARANYA SUR[1,2] AND BHARGAV VAIDYA[3]
[1]Indian Institute of Astrophysics, Bengaluru [2]Pondicherry University, Puducherry [3]IIT-Indore, Simrol
Email: ameya.nagdeo@iiap.res.in

Introduction

Magnetic fields are a fundamental component of nearly all astrophysical systems, from stars and galaxies to the intracluster medium. Their ubiquity and persistence are widely attributed to dynamo processes, which amplify and sustain magnetic fields over cosmic timescales. Among these, the *Fluctuation Dynamo* plays a key role in turbulent environments, where it harnesses energy from 3D random/turbulent motions to efficiently amplify weak seed fields to dynamically significant strengths on timescales shorter than the lifetimes of such systems. In this study, we explore the Fluctuation Dynamo in supersonic turbulence with rms Mach number $\mathcal{M}_{\rm rms} \approx \mathbf{11}$, focusing on magnetic Prandtl numbers $\mathrm{Pm} = \mathrm{Rm}/\mathrm{Re} = \nu/\eta \geq 1$ cases explored up to $\mathrm{Pm} = 10$.

Forced Turbulence Module

PLUTO (Mignone et al. 2007) is a finite volume/finite difference shock-capturing MHD solver code designed to integrate a system of conservation laws.

$$\frac{\partial \rho}{\partial t} + \nabla \cdot (\rho \boldsymbol{U}) = 0,$$

$$\frac{\partial (\rho \boldsymbol{U})}{\partial t} + \nabla \cdot (\rho \boldsymbol{U} \otimes \boldsymbol{U} - \boldsymbol{B} \otimes \boldsymbol{B}) + \nabla P^* = \nabla \cdot (2\nu\rho \boldsymbol{S}) + \rho \boldsymbol{F},$$

$$\frac{\partial \boldsymbol{B}}{\partial t} = \nabla \times (\boldsymbol{U} \times \boldsymbol{B}) + \eta \nabla^2 \boldsymbol{B},$$

here $S_{ij} = (1/2)[U_{i,j} + U_{j,i} - (2/3)\delta_{ij}\partial_k U_k]$ is the traceless rate of strain tensor.

- We developed a driven turbulence module for the term $\boldsymbol{F}$, which is the turbulent acceleration field modelled using the Ornstein-Uhlenbeck (OU) process with a finite time correlation (Eswaran and Pope 1988; Gillespie 1996; Federrath et al. 2010) given by,

$$F(K; t+\Delta t) = F(K; t)e^{-\frac{\Delta t}{\tau}} + \sqrt{\sigma_{OU}^2 \times \left(1 - e^{-\frac{2\Delta t}{\tau}}\right)} \times n$$

- Acceleration field decomposed using a projection operator into solenoidal $\mathcal{P}_{ij}^{\perp}$ and compressive $\mathcal{P}_{ij}^{\parallel}$ components in Fourier space,

$$\mathcal{P}_{ij}^{\zeta}(\boldsymbol{k}) = \zeta \mathcal{P}_{ij}^{\perp} + (1-\zeta)\mathcal{P}_{ij}^{\parallel}$$

$\zeta \in [0, 1]$ controls the degree of the contributions of each component.

Magnetic to Kinetic Energy Ratio

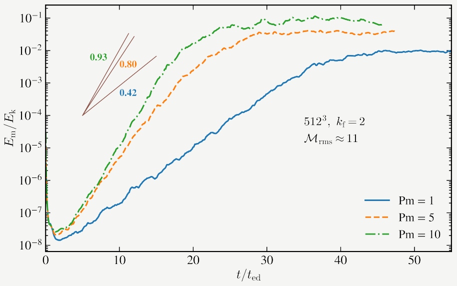

Higher Pm values produce faster exponential growth and higher saturation levels.

Numerical Implementation

- **Domain:** Periodic cubic box ($L = 1$) resolved at 512^3.
- **Thermodynamics:** Isothermal equation of state with sound speed $c_s = 1$.
- **Initial State:** Density $\rho = 1$, fluid at rest ($\boldsymbol{U} = 0$), and zero net flux seed field ($\boldsymbol{B}_{\rm init}$) at plasma $\beta = 10^6$.
- **Turbulent Forcing:** Purely solenoidal ($\zeta = 1$) applied at an average wavenumber $k_{\rm f}L/2\pi = 2$ (forcing scale $\ell_{\rm f} = 2\pi/k_{\rm f}$).
- **Mach Number:** Forcing amplitude is dynamically tuned to maintain a steady-state RMS Mach number $\mathcal{M}_{\rm rms} \approx 11$.
- **Dynamo Regime:** We explore magnetic Prandtl numbers $\mathrm{Pm} \geq 1$ by increasing viscosity (ν) to progressively lower the fluid Reynolds number (Re).

Table 1: Key parameters of simulations used in this study.

Run	Pm	$\mathrm{Re} = u\,\ell_{\rm f}/\nu$	$\langle E_{\rm m}/E_{\rm k}\rangle_{\rm sat}$	$\langle r_p\rangle_{\rm sat}$
Pm1	1	6600	$(9.0 \pm 0.4) \times 10^{-3}$	0.53 ± 0.02
Pm5	5	1320	$(3.5 \pm 0.2) \times 10^{-2}$	0.45 ± 0.01
Pm10	10	660	$(8.1 \pm 0.2) \times 10^{-2}$	0.34 ± 0.01

Stretching Versus Compression

The evolution equation of the magnetic energy in terms of local advection, stretching ξ_s, compression ξ_c and dissipation terms is,

$$\frac{\partial}{\partial t}\left(\frac{|\boldsymbol{B}|^2}{2}\right) = \underbrace{+S_{ij}B_iB_j}_{\xi_s} \underbrace{-\frac{2}{3}|\boldsymbol{B}|^2(\nabla \cdot \boldsymbol{U})}_{\xi_c} - \boldsymbol{U} \cdot \frac{1}{2}\nabla|\boldsymbol{B}|^2 - \eta \boldsymbol{B} \cdot (\nabla \times \boldsymbol{J})$$

Table 2: Time-averaged values of $\xi_{\rm s}$ and $\xi_{\rm c}$ obtained from the PDFs of stretching and compression terms in the above equation in the kinematic and saturated phases.

Run	Pm	$\xi_{\rm s}$		$\xi_{\rm c}$	
		Kin.	Sat.	Kin.	Sat.
Pm1	1	7.07 ± 0.31	2.33 ± 0.15	8.35 ± 0.23	1.77 ± 0.13
Pm5	5	4.57 ± 0.21	2.22 ± 0.07	4.48 ± 0.18	1.40 ± 0.12
Pm10	10	3.59 ± 0.16	1.62 ± 0.11	2.85 ± 0.21	0.56 ± 0.10

- In the kinematic phase, compression dominates for $\mathrm{Pm} = 1$, both terms are comparable for $\mathrm{Pm} = 5$, and stretching dominates for $\mathrm{Pm} = 10$.
- Stretching dominates over compression in the saturated phase for all Pm.
- Stretching and compression are suppressed in the saturated phase compared to the kinematic phase.

Conclusions

- In-plane magnetic fields are arranged in folds and strongly compressed at myriad locations, indicating field amplification by a combination of local stretching and compression.
- The growth rates in the kinematic phase and the saturation level of $E_{\rm m}/E_{\rm k}$ are strongly dependent on the Pm.
- The contribution of stretching and compression terms in the magnetic field equation varies with a change in Pm.
- Additionally, we have also studied the evolution of magnetic field - density correlation $\langle r_p\rangle$ decreasing with increasing Pm in the saturated stage. Reflecting the role of magnetic pressure forces in resisting the continued compression of the field lines due to supersonic turbulence.
- The solenoidal and compressive kinetic energy spectra show that, for $\mathrm{Pm} = 10$, higher viscosity suppresses small-scale velocity fluctuations more strongly in compressive than in solenoidal modes.

2D Slices

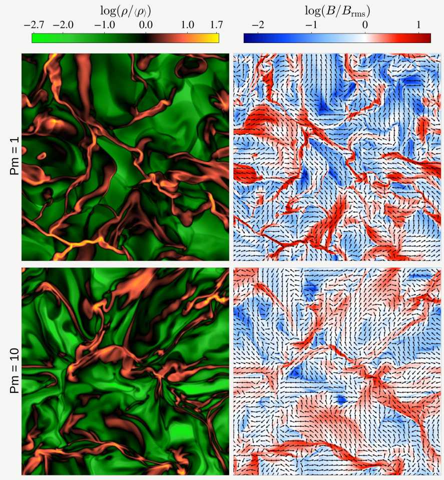

Faraday Rotation Measure

Assess the magnetic field coherence using synthetic RM measurements.

$$\mathrm{RM}(x_i, y_i, t) = \frac{K}{\mu m_p}\sum_{j=0}^{N-1}\left(\frac{L}{N}\right)\rho B_z\left(x_i, y_i, \frac{L}{N}j, t\right)$$

$$\bar{\sigma}_{\rm RM} = \sigma_{\rm RM}/\sigma_{\rm RM0}, \qquad \sigma_{\rm RM0} = \frac{K}{\mu m_p}\frac{(\rho B)_{\rm rms}}{\sqrt{3}}L\sqrt{\frac{2\pi}{k_{\rm f}L}}$$

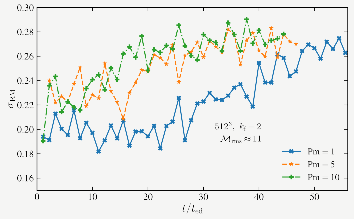

- In turbulent, gas-rich galaxies ($\bar{n}_{\rm e} \sim 1\,\mathrm{cm^{-3}}$) at high redshift ($z \sim 1$), fluctuation dynamos can amplify magnetic fields rapidly.
- Assume $u_{\rm rms} \sim 10\,\mathrm{km\,s^{-1}}$, $\ell_{\rm f} \sim 100\,\mathrm{pc} \Rightarrow t_{\rm ed} \sim 10^7\,\mathrm{yr}$ for a path length of $L = 1\,\mathrm{kpc}$ through the disc thickness.
- If the fluctuation dynamo saturates at a fraction $f \sim (0.1 - 0.2)$ of equipartition, $B_{\rm rms} = f\,B_{\rm eq} \approx (0.5 - 1)\,\mu\mathrm{G}$, giving $\sigma_{\rm RM0} \sim (74 - 150)\,\mathrm{rad\,m^{-2}}$ (Nagdeo, Sur, and Vaidya 2026).
- Thus, for $\bar{\sigma}_{\rm RM} \sim 0.3$, the Faraday RM dispersion, $\sigma_{\rm RM} \sim (\mathbf{22 - 45})\,\mathrm{rad\,m^{-2}}$. The value is comparable to RM excess values reported in the literature for MgII absorbers.

Future Work

However, the interstellar medium (ISM) is a multiphase system in reality. Therefore, we have developed an SNe-driven turbulence module in PLUTO (Mignone et al. 2007). In conjunction with radiative cooling, we are exploring the evolution of magnetic fields in periodic domains. Subsequently, we plan to investigate magnetic field evolution and profiles of magnetic fields and turbulent velocities, etc., within the stratified domain for various gas surface densities and surface SNe rates.

References

1. Nagdeo, A. U., Sur, S., & Vaidya, B. (2026). Fluctuation dynamos in supersonic turbulence at $\mathrm{Pm} \gtrsim 1$. The Astrophysical Journal, 998(2), 218. https://doi.org/10.3847/1538-4357/ae33bb
2. Nagdeo, A. U. & Sur, S. (2026). Evolution of Magnetic Fields in Supernovae Driven Turbulence (In Preparation).

DEPARTMENT OF PHYSICS
THE UNIVERSITY OF HONG KONG

Outflows from Low-Luminosity Galaxies in the Early Universe

Evidence for delayed SNe feedback

James Nianias[1], Jeremy Lim[1], Yik Lok Wong[2], Gordon Wong[1]

[1]Department of Physics, University of Hong Kong [2]University of Manchester

Motivation

Stellar feedback drives galactic outflows that regulate star formation and enrich the circumgalactic medium — but its **timing** is poorly constrained.

Core-collapse supernovae (SNe) are expected to dominate feedback after $\sim 5\,\mathrm{Myr}$, the main-sequence lifetime of the most massive stars.

The Lyα emission line is the most widely used outflow tracer at $z > 2$, but its resonant scattering makes profile interpretation model-dependent.

Key question: do Lyα profiles, metal emission lines, and metal absorption lines all paint a consistent picture of *strengthening feedback over the first* $\sim 10\,\mathrm{Myr}$?

Sample and Observations

Data: VLT/MUSE integral-field spectroscopy of **12 foreground galaxy clusters** from Richard et al. (2021), covering $\lambda = 4750$–$9300\,\text{Å}$.

Gravitational lensing boosts signal-to-noise, enabling detection of faint UV metal emission and absorption lines that would otherwise be undetectable.

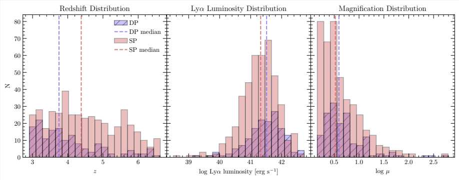

Left to right: Redshift distribution, lensing-corrected Lyα luminosity, and lensing magnification for the sample. Single-peaked (SP) and double-peaked (DP) sources are shown separately.

Sources:	576 Lyα emitters (421 SP, 155 DP)
Redshifts:	$2.9 < z < 6.7$
Clusters:	12 galaxy clusters (13 pointings)
Magnification:	up to $\mu \sim 100$
Spectral fitting:	asymmetric Gaussians + bootstrap

Diverse Lyα Morphologies

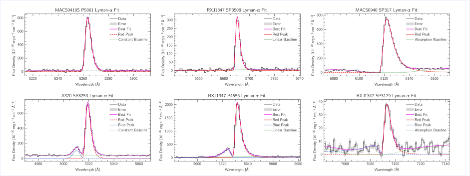

Six example Lyα profiles, ranging from (a–c) single-peaked to (d–f) double-peaked, with constant, linear, and damped-absorption baselines. The asymmetric Gaussian model is shown in red.

Evidence for Widespread Outflows

Three independent diagnostics point to outflows.

(i) Lyα Profiles Consistent with Outflows

In sources with measured systemic redshifts (from optically-thin C III] $\lambda\lambda1907, 1909$, He II $\lambda1640$, O III] $\lambda\lambda1661, 1666$ emission lines):

Single-peaked: Lyα redshifted relative to systemic in $\gtrsim 90\%$ of cases.

Double-peaked: the two peaks straddle the systemic in all but one case; red peak always dominant.

97% of sources show a red-skewed Lyα peak — the hallmark of outflowing gas.

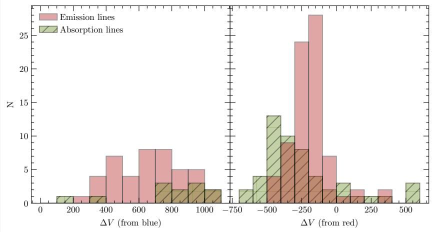

Velocity offsets of emission and absorption lines relative to the Lyα blue (left) and red (right) peaks. Absorption lines show larger offsets than optically-thin emission lines, consistent with the former tracing outflowing gas.

(ii) Blueshifted Metal Absorption Lines

Low- and high-ionization absorption lines (Si II $\lambda1260$, C II $\lambda1334$, Si IV $\lambda\lambda1394, 1403$) are detected in individual and stacked spectra and are **blueshifted in the majority of sources with measured systemic redshifts**.

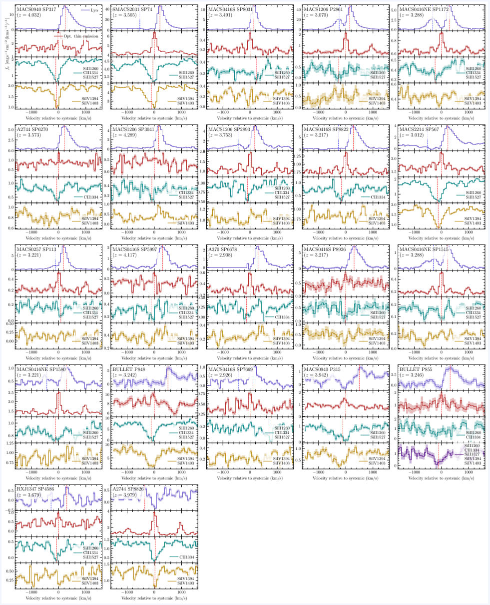

Comparison of the Lyα profile, stacked optically-thin emission, and stacked low- and high-ionization spectra for sources with both absorption detections and measured systemic redshifts. Dashed red lines mark the best-fit absorption centroid. Absorption centroids are blueshifted in all but a handful of cases.

Clumpy outflow geometry: EW ratios of Si II $\lambda1260$/Si II $\lambda1527$ and Si IV $\lambda\lambda1394, 1403$ doublets are consistent with absorption in *optically-thick clumps* with limited covering fraction — not a homogeneous medium.

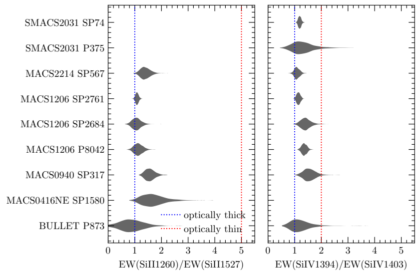

Monte Carlo EW ratio distributions for the Si II (left) and Si IV (right) doublets. The blue dashed line marks the optically-thick (clumpy) limit; red marks the optically-thin limit.

(iii) Lyα Width Encodes Outflow Velocity

Bayesian linear regression (LinMix) reveals a **significant positive correlation** ($P(\beta > 0) = 0.987$) between the absorption-line outflow velocity V_out and the Lyα intrinsic line dispersion $\sigma_{\mathrm{Ly}\alpha}$:

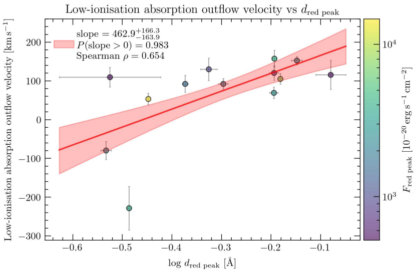

Outflow velocity from low-ionization absorption lines versus Lyα intrinsic dispersion. The LinMix regression is shown with its 68% posterior credible interval (shaded). Sources with broader Lyα profiles *genuinely drive faster outflows*.

This correlation cannot be explained by differences in ionization state alone. It implies that Lyα profile morphology encodes real kinematic information and that **narrower Lyα profiles indicate slower outflows**.

Delayed Supernova Feedback

Younger starbursts drive slower outflows.

Consistent with SNe onset within the first $\sim 10\,\mathrm{Myr}$.

He II $\lambda1640$ Anti-correlates with Lyα Width

He II $\lambda1640$ is a recombination line requiring photons with energies $> 54\,\mathrm{eV}$, produced almost exclusively by the most massive O type stars. Its equivalent width (EW) declines rapidly as stellar populations age.

We find a **highly significant anti-correlation** ($P(\beta < 0) \approx 0.9999$) between $\mathrm{EW}(\text{He II})$ and the Lyα intrinsic dispersion $\sigma_{\mathrm{Ly}\alpha}$:

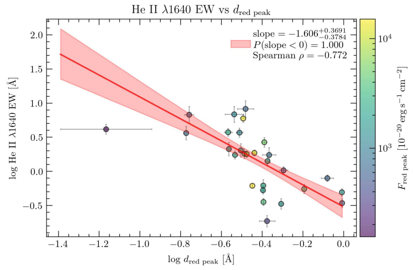

He II $\lambda1640$ rest-frame EW versus Lyα intrinsic dispersion $\sigma_{\mathrm{Ly}\alpha}$. SP sources in red; DP sources in blue. LinMix regression shown with 68% credible interval.

Consistent anti-correlations are found for:

He II $\lambda1640$ vs. Lyα **asymmetry** (significant)

He II $\lambda1640$ vs. Lyα **FWHM** (significant)

He II $\lambda1640$ vs. Lyα **blue–red peak separation** Δv_BR (DP sources only; significant)

C III] $\lambda\lambda1907, 1909$, O III] $\lambda\lambda1661, 1666$ vs. Lyα $\sigma_{\mathrm{Ly}\alpha}$ (qualitatively similar, weaker)

A **tentative direct correlation** between $\mathrm{EW}(\text{He II})$ and absorption-line outflow velocity V_out directly links the hardness of the ionizing radiation field to the outflow speed.

Stellar Age Interpretation

Comparison with **Gutkin et al. (2016)** photoionization model tracks at sub-solar metallicities ($Z/Z_\odot \sim 0.05$–0.2):

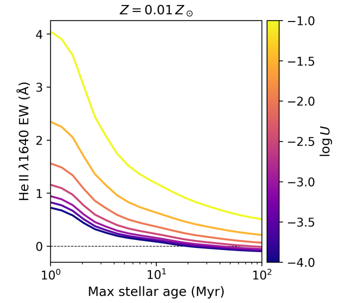

He II $\lambda1640$ EW vs. stellar population age from Gutkin et al. (2016) photoionization model tracks for a constant star formation history with metallicity $Z = 0.01Z_\odot$ and a range of ionization parameters. The He II $\lambda1640$ EW range is broadly consistent with what we find in our sample, and shows a steep drop within the first $\sim 5\,\mathrm{Myr}$, demonstrating the strong dependence of He II $\lambda1640$ EW on stellar age.

Sources with **strong** He II $\lambda1640$ emission → ages $\lesssim 10\,\mathrm{Myr}$; narrow Ly$\alpha$; **slow** outflows

Sources with **weak/absent** He II $\lambda1640$ → ages $\gtrsim 10\,\mathrm{Myr}$; broad Lyα; **fast** outflows

Key Conclusions

1. Lyα profiles and metal absorption lines provide consistent, independent evidence for **widespread clumpy, multiphase outflows** from high-z Lyα emitters.
2. Lyα intrinsic dispersion $\sigma_{\mathrm{Ly}\alpha}$ correlates positively with absorption-line outflow velocity — Lyα profiles encode **genuine kinematic information**.
3. He II $\lambda1640$ EW is **strongly anti-correlated** with $\sigma_{\mathrm{Ly}\alpha}$, asymmetry, FWHM, and peak separation.
4. He II $\lambda1640$ declines rapidly with stellar age, suggesting **younger starbursts drive slower outflows**.

Selected References

Richard et al. 2021, MNRAS, 501, 2090 (R21)
Leitherer et al. 1999, ApJS, 123, 3; 2014, ApJS, 212, 14
Stanway & Eldridge 2018, MNRAS, 479, 75
Gurung-López et al. 2019, MNRAS, 486, 1882; 2022, MNRAS, 510, 4525
Kelly 2007, ApJ, 665, 1489 (LinMix)
Verhamme et al. 2006, A&A, 460, 397
Woosley & Weaver 2002, RvMP, 74, 1015

nianias@hku.hk VLT/MUSE observations of 12 lensing clusters · 576 Lyman-α emitters at $2.9 < z < 6.7$ University of Hong Kong

HOW TO RECYCLE OBSERVATIONS

Turning JWST/MIRI backgrounds into a survey of diffuse molecular hydrogen

E. Nigou[1,2], B. Godard[1,2], P. Guillard[3], G. Pineau des Forêts[2,4], M. A. Miville-Deschênes[1 2], and P. Lesaffre[1 2]

[1] Laboratoire de Physique de l'École Normale Supérieure, ENS, Université PSL, CNRS, Sorbonne Université, 75005 Paris, France
[2] LUX, Observatoire de Paris, Université PSL, Sorbonne Université, CNRS, 75014 Paris, France
[3] Institut d'Astrophysique de Paris, Sorbonne Université, CNRS, 98 bis bd Arago, 75014 Paris, France
[4] Institut d'Astrophysique Spatiale, Université Paris-Saclay, CNRS, 91405 Orsay, France

CONTEXT

H2 in the diffuse ISM

Molecular hydrogen correlates with the **star formation rate** **[Lin+ 2019]** and initiates **interstellar chemistry** and the formation of complex species. It also plays an important role in **cooling** the gas, thus regulating both the thermal pressure of the diffuse gas and the relative phase distribution. **[Godard+ 2023]**

Rotationnaly excited H2 observations

- **UV absorption:** ~200 with FUSE, towards galactic and extra-galactic sources. **[Shull+ 2021, Wakker 2006]**
- **IR emission:** 6 detections with *Spitzer*, towards high galactic latitude clouds. **[Ingalls+ 2011]**

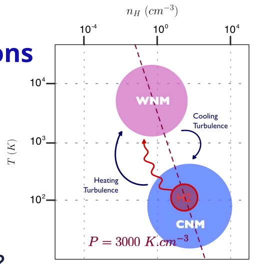

H2 in the diffuse medium.

Several unanswered questions

What is the H2 cooling rate?
How does it survive out of the cold medium?
what are its excitation mechanisms?

AN INNOVATIVE METHOD

MIRI/MRS data and observation strategy

The JWST database counts :

- **more than 16 000 available observations**
- ~4400 Mid-InfraRed Instrument (MIRI) observations
- almost **500 taken with the Medium Resolution Spectometer (MRS)**

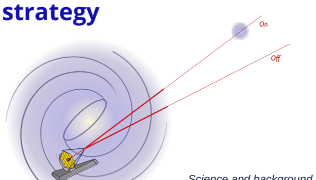

Science and background observations diagram.

The MRS produces **spectra from 5 to 28 μm**, allowing the detection of H2 pure rotational lines. All its science observations are associated with **off-pointing background observations**, whose lines of sight exclusively intersect **our galactic medium**.

We aim to rehabilitate 50% of the observation time to uncover rotationally excited H2 emission!

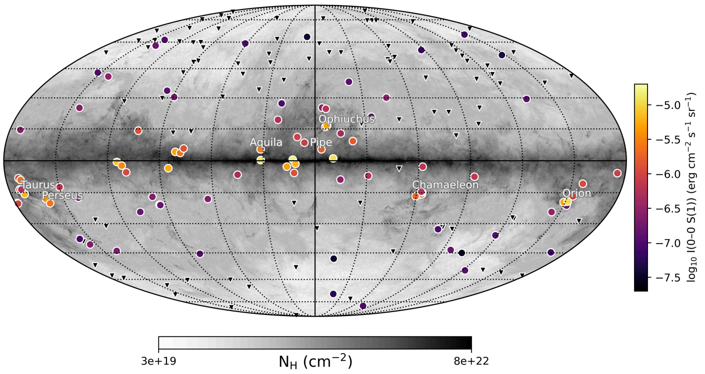

S(1) line detections throughout our galaxy. Background map obtained from ancillary data ***[Planck Collaboration+ 2024]****.*

The observational sample shows:

- **Widespread detection of rotationally excited diffuse H2** in our Galaxy.
- **Higher excitation for star-forming and denser regions**.

Diffuse medium selection

In order to gather information on the diffuse medium only, ancillary data of HI and dust **[Planck Collaboration+ 2014, HI4PI Collaboration+ 2016]** were used to design two criteria:

- On the line-of-sight-averaged **dust temperature**: $T_{\rm dust} < 25{\rm K}$
- On the **total hydrogen column density** perpendicular to the Galactic plane: $N_{\rm H}^{\perp} < 3 \times 10^{20} {\rm cm}^{-2}$

Rotational line detections

The final sample counts **233 backgrounds.**

H2 Lines	0-0 S(1)	0-0 S(2)	0-0 S(3)	0-0 S(4)	0-0 S(5)	0-0 S(6)	0-0 S(7)	0-0 S(8)
Number of detections	84	40	23	7	9	0	17	0

MORE INFORMATION

For more information on the MRS dataset and selection, the spectra processing and excitation measurements, see **Nigou+ 2026** (in press):

https://ui.adsabs.harvard.edu/abs/2026arXiv260326208N/abstract

ANALYSIS

Spatial properties

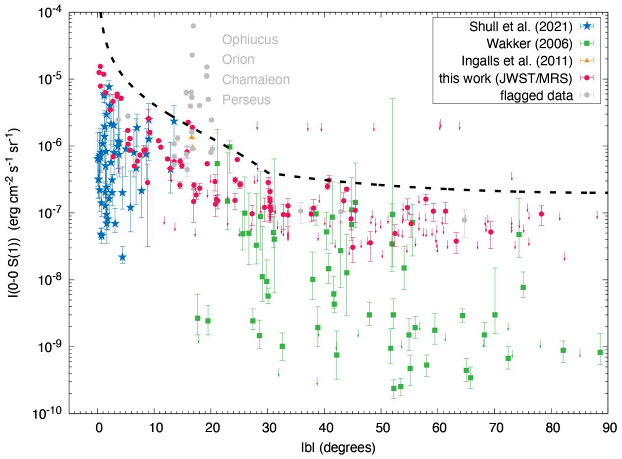

S(1) line intensities for different galactic latitudes. The dashed line is an analytical estimate of the maximum emission.

- **Detections at all latitudes**, up to 78°.
- Intensities in emission are higher than in absorption because of the **MRS sensibility limit**.
- A **simple geometric model** of our Galaxy (spherical Local Bubble + galactic medium slab), confirms that **the emission arises mainly from diffuse molecular gas**.:

$$I_{\rm max}(|b|) = \frac{C_1}{\max\left(\sin|b|,\, r\right)} + C_2 \left(\frac{1}{\sin|b|} - \frac{1}{\max\left(\sin|b|,\, r\right)} \right) \quad \text{with} \quad \begin{cases} r = 0.5 \\ C_1 = 2 \times 10^{-7} \ {\rm erg\,cm^{-2}\,s^{-1}\,sr^{-1}} \\ C_2 = 10^{-6} \ {\rm erg\,cm^{-2}\,s^{-1}\,sr^{-1}} \end{cases}$$

Cooling properties

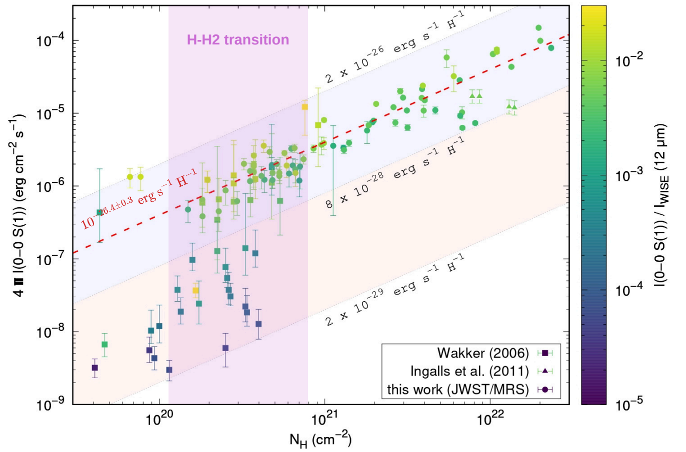

S(1) line flux vs total hydrogen column density, color-coded by the intensity ratio to the PAH surface brightness at 12 μm measured by WISE ***[Meisner & Finkbeiner 2014]****.*

- All measurements fall **past the H-H2 transition** → higher column densities.
- Newfound **constant cooling rate for the 0-0S(1) line**, with dispersion factor < 2:

$$\Lambda_{S(1)} = \frac{4\pi I(0-0\ S(1))}{N_{\rm H}} = 10^{-26.4\pm0.3}\ {\rm erg\ s^{-1}\ H^{-1}} \longrightarrow \text{20\% of the main carbon line cooling.}$$

HIGHLIGHTS

- **First detections of the S(4), S(5), and S(7) rotational lines** in the diffuse ISM.
- **Widespread detection of the S(1) line** (41% of the sample).
- The **large-scale galactic structure** of the diffuse gaz, consisting of a diffuse disk and a slightly denser local bubble, is **reflected by the S(1) line intensity** dependance on galactic latitude.
- Molecular hydrogen column densities fall **past the H–H2 transition** and between 10^{19} and 10^{22} ${\rm cm}^{-2}$, due to sensitivity limits.
- **New cooling law** for the diffuse ISM: $\Lambda_{S(1)} = 10^{-26.4\pm0.3}\ {\rm erg\ s^{-1}\ H^{-1}}$ It corresponds to **20% of the cooling rate of the [C II] 158 μm line** and **0.6% of the PAH surface brightness at 12 μm.**
- In just 3 years of JWST operating, the number of S(1) detections in emission is a third of the one obtained in absorption.
- The **excitation properties are similar** between the emission and absorption observations.

Evidence of a supernova at the low mass end in the early Universe

Thomas.Nordlander @ physics.uu.se **Uppsala University, Sweden**

An ECSN enriched second-generation star

Stars with masses above about $10\,\mathrm{M}_\odot$ tend to explode as core-collapse supernovae (CCSNe). Stars just less massive than this end their lives differently: They form compact O-Ne-Mg cores surrounded by a steep density gradient (Nomoto 1984, 1987). They may explode promptly through an electron capture mechanism as **electron-capture supernovae (ECSN)** - see figure on left.

ECSNe are necessary to explain the detailed isotopic chemical composition of the Sun (e.g., Wanajo et al. 2011, 2013a,b). They are used in many Galactic Chemical Evolution (GCE) models where they contribute light trans-iron elements, Z=28-40 (Hirai et al. 2018, Kobayashi et al. 2020).

Direct observational evidence for ECSNe is lacking. The Crab supernova is probably an ancient example (Nomoto et al. 1982). More recent examples like SN2018zd are all flawed and fail to give a consistent agreement with ECSN explosions and their progenitors (Hiramatsu et al. 2021, Callis et al. 2021, Cai et al. 2021, Van Dyk et al. 2023). We therefore lack a direct present-day confirmation of their explosion mechanism and chemical output.

The expected yields of an ECSN are very similar to the chemical composition of the extremely metal-poor red giant star SMSS J0843–1415 ([Fe/H] = -3.29) - see figure below.

It has strongly enhanced abundances of Zn, Sr, Y and Zr by 1-2 dex, with very high ratios of Zn/Cu and Sr/Fe. Abundances of iron-peak and lighter elements are similar to other halo stars at the same metallicity. These enhanced abundances in the light trans-iron elements Z=28-40 and lack of other s-process enhancement are consistent with enrichment from an ECSN, making it the first evidence of such an event in the early Universe.

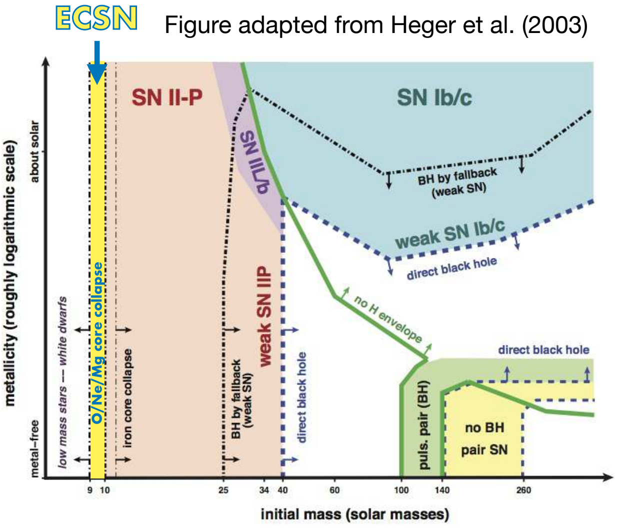

Figure adapted from Heger et al. (2003)

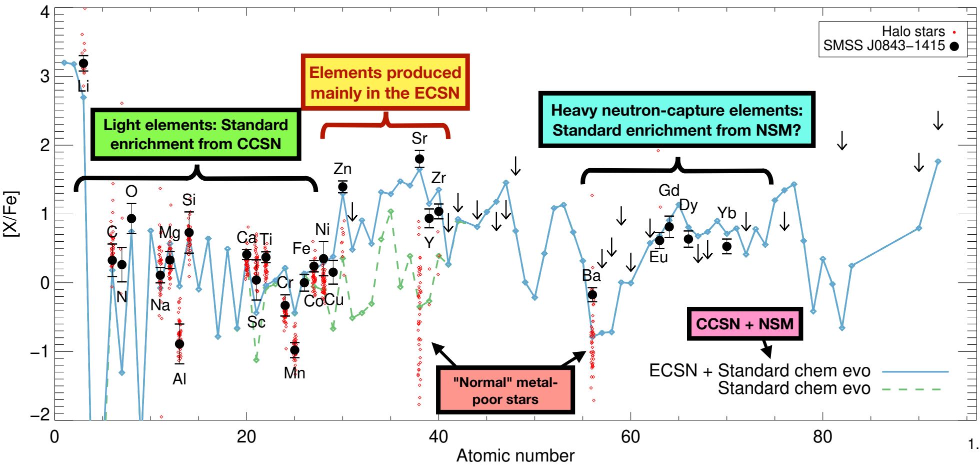

Pop III connection

We suggest an enrichment scenario where an 8-9 $\mathrm{M}_\odot$ metal-free first-generation (Pop III) star exploded as an ECSN in the early Universe. Such a star has a lifetime of about 30 Myr, far longer than more massive Pop III stars. The explosion is extremely weak, $< 10^{50}\,\mathrm{erg}$, and needed several Myr to dilute in the ISM to the levels observed in . By then, the ISM had already been enriched by Pop II CCSNe and neutron-star mergers, contributing both light and heavy elements.

This is the first observational evidence from second-generation stars that the Pop III initial mass function extended down to at least 9 solar masses.

Neutron-capture element enhancement

The heavy neutron-capture, r-process element, abundances are also enhanced. This star is therefore a mildly enriched, r-I star. ECSNe are not expected to produce heavy neutron-capture elements: is this coincidence, or new physics?

Enhanced r-process abundances are found in about 10 % of extremely metal-poor stars. The detailed abundances of these heavy elements match what is commonly seen in other metal-poor stars. There is therefore no evidence that it was created through an exotic process instead of as usual through binary neutron-star mergers (NSM). This enrichment is probably coincidental, unrelated to the ECSN.

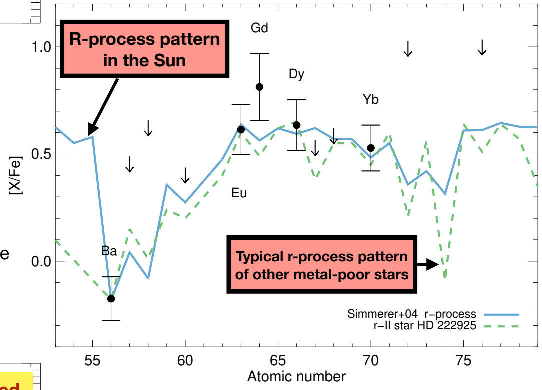

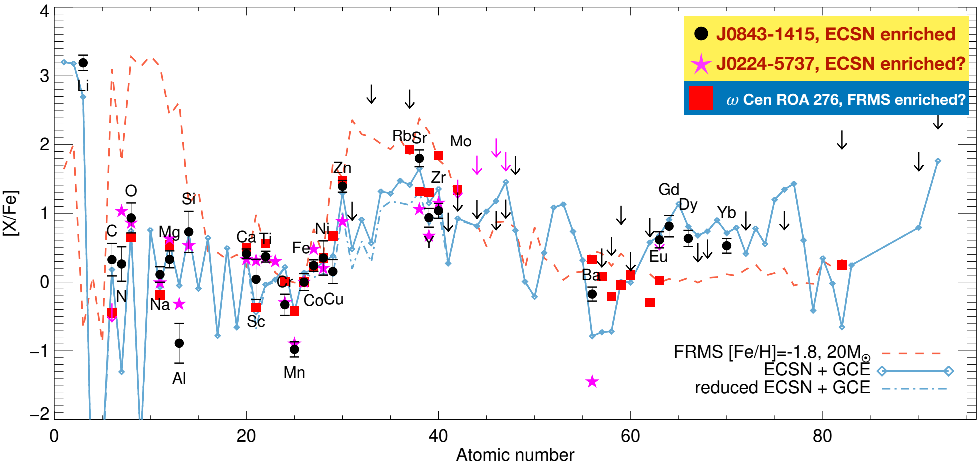

One of a kind?

Two more stars stars in the literature are enhanced by 1-2 dex in Zn, Sr, Y and Zr.

SMSS J0224-5737 ([Fe/H] = -3.8, Jacobson et al. 2015, Okada et al. 2025) is also a good match for enrichment from an ECSN. This star is not enhanced in r-process elements, implying that ECSNe really do not produce these heavy elements.

ω Cen ROA 276 ([Fe/H] = -1.3, Yong et al. 2017) is better explained by a fast-rotating massive star (FRMS). It is rich in Cu, Rb, Mo, and its heavy elements are more consistent with the s-process than the r-process.

References

Cai et al. 2021, A&A, 654, A157
Callis et al. 2021, arXiv.2109.12943
Hirai et al., 2018, ApJ, 855, 63
Kobayashi et al. 2020, ApJ, 900, 179
Hiramatsu et al. 2021, Nat Astron, 5, 903
Jacobson 2015, ApJ, 807, 171
Nomoto 1984, ApJ, 277, 791
Nomoto 1987, ApJ, 322, 206
Nomoto et al. 1982, Nature, 299, 803
Okada et al. 2026, ApJ, 997, 119
Van Dyk et al. 2023, MNRAS, 519, 471
Wanajo et al. 2011, ApJL, 726, L15
Wanajo et al. 2013a, ApJL, 767, L26
Wanajo et al. 2013b, ApJL, 774, L6
Yong et al. 2017, ApJ, 837, 176

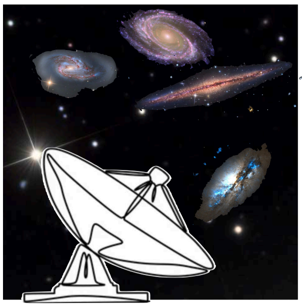

IMEGIN Large Program:

mapping the millimeter dust properties and the ISM lifecycle in nearby galaxies

author: Lara Pantoni[1,2,*] on behalf of NIKA2 collaboration

1 Université Paris-Saclay, CEA, 91191 Gif-sur-Yvette, France
2 Department of Physics and Astronomy, Universiteit Gent, 9000 Ghent, Belgium
* lara.pantoni@ugent.be

INTRODUCTION AND SCOPE

One of the key open questions in dust studies concerns the physical properties of grains at millimeter wavelengths.
Robust constraints on the dust opacity (κ) and its spectral slope (β) are critical for accurate dust mass estimates and for mapping dust-to-stellar, dust-to-gas, and dust-to-metal ratios, quantities that directly trace the chemical evolution of galaxies and the reservoirs available for star formation. Beyond the Milky Way, nearby galaxies offer access to a wide range of physical environments, albeit typically at kiloparsec-scale resolution.

GALAXY HIGHLIGHTS

Dust at large vertical distances in NGC 891

SCAN ME

At large vertical distances from the disk (>2 kpc), the mass fraction of small dust grains increases, reaching up to 20%.

➡ Dust grains from the disk may be shattered by SN-driven outflows and expelled into the galactic halo.

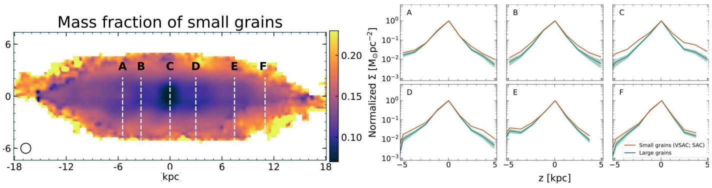

Katsioli et al. A&A 679, A7 (2023)

Dust in dwarf and starburst galaxies: NGC 2976 and NGC 2146

SCAN ME

1. In the low metallicity galaxy NGC 2976, β ~ 1.3 is shallower than in the starburst NGC 2146 (β ~ 1.7) and the dust mass is more than two orders of magnitude smaller.

2. Tight, super-linear correlations between Σ_{SFR} (Σ_{H2}) and the mm emission.

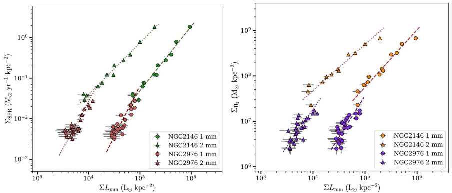

Ejlali et al. A&A, 693, A88 (2025)

β variations in the face-on spiral galaxy M 99

SCAN ME

1. β increases from ~1.6 in diffuse regions up to 2.5 in denser star-forming environments, reflecting dust grain evolution.

2. Fixed β models underestimate the dust mass of a factor ~ 2 on average, and systematically bias correlations with dust-to-stellar and dust-to-gas ratios.

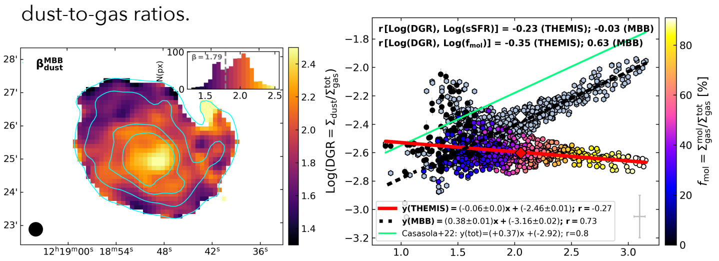

Pantoni et al. A&A, 709, A1 (2026)

THE PROGRAM

The IRAM 30m Guaranteed Time Large Program **Interpreting the Millimeter Emission of Galaxies with IRAM-NIKA2** (IMEGIN, PI: S. Madden) devoted ~200 h to mapping the mm continuum of **22 nearby galaxies** spanning a wide range of stellar masses, morphologies, and metallicities.

The IRAM 30m telescope (Sierra Nevada, Spain)

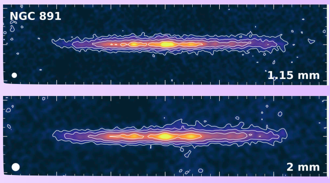

NIKA2 maps of NGC 891 (Katsioli et al. 2023)

THE SAMPLE

The sample was selected to lie within 30 Mpc and to benefit from high-quality NIR-to-FIR imaging for resolved SED modeling, complemented by matched-resolution UV, CO, and HI data.

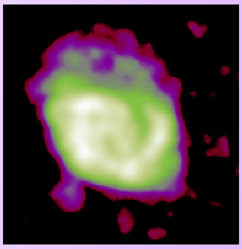

HI map of M99, VIVA VLA Atlas (Chung et al. 2009)

METHODS AND TOOLS

SCAN ME

The spatially-resolved SED of IMEGIN galaxies is modeled with the hierarchical Bayesian inference for dust emission (**HerBIE**) SED fitting code, coupled with the **THEMIS** dust model.

Spatially resolved SED modeling requires all input maps to be homogenized in angular resolution, pixel scale, orientation, and units. To meet these requirements we developed the Homogenization for IMEGIN Photometry (**HIP**) pipeline, which includes propagation of uncertainties through Monte Carlo method. HIP is available on **GitLab**! ⟶

SCAN ME

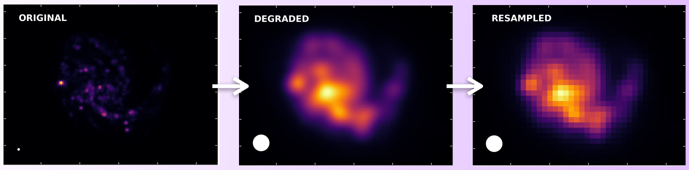

GALEX FUV map of M 99 degraded and resampled to match *Herschel*/SPIRE 500 µm with HIP (Pantoni et al. 2026)

The IMEGIN team is collecting additional high sensitivity data in the radio regime to better constrain galaxy SEDs (VLA accepted proposal "REIMEGING"; PI den Brok) and shed light onto the origin of the submm excess in low metallicity galaxies (GBT MUSTANG-2 accepted proposal "MESSING"; PI Ejlali). The team is engaged in other ongoing NIKA2 programs, such as "SEINFELD" (PI Galliano), focused on dwarf galaxies.

UNIVERSITY OF ALBERTA
peltonen@ualberta.ca

Introducing PxP:
A Population Synthesis Framework for Predicting YSO Properties

J. Peltonen[1], E. Rosolowsky[1], A. Ginsburg[2], R. Indebetouw[3,4], T. Richardson[2], and M. Jimena Rodriguez[5,6]

[1]University of Alberta, [2]University of Florida, [3]University of Virginia, [4]National Radio Astronomy Observatory, [5]Space Telescope Science Institute, [6]CONICET–UNLP

Motivation

-Young Stellar Objects (YSOs) are the most direct way to measure Star formation (SF)
-Requires **very high-resolution infrared** and **precise modelling**
-JWST is providing the infrared observations
-We designed a framework that can translate **JWST YSO observations into SF properties**

Models

-Richardson (2024) radiative transfer and **synthetic photometry** but no evolution
-Klassen (2012) **accretion histories**
-Connecting the two for single YSO leads to **degeneracy**
-Use populations to resolve degeneracy

Model Degeneracy with Single YSO

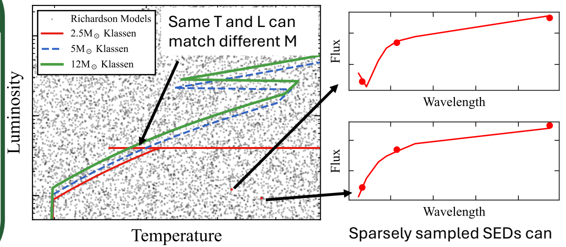

Same T and L can match different M

Sparsely sampled SEDs can be fit by multiple models

Generate Model Populations

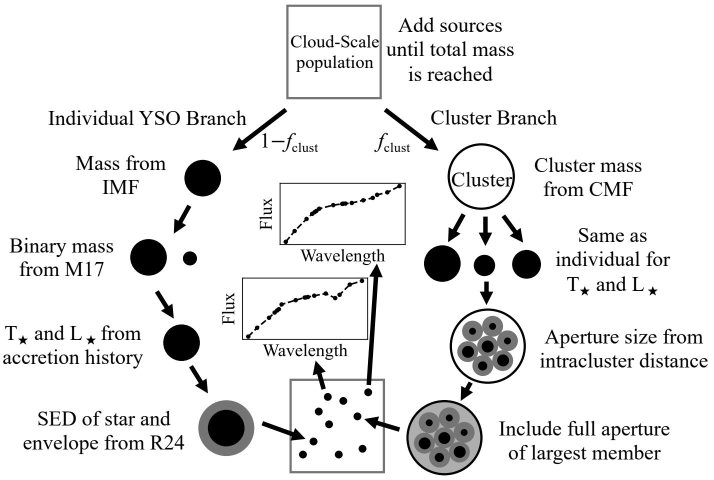

Cloud-Scale population

Add sources until total mass is reached

Individual YSO Branch

$1-f_{\mathrm{clust}}$

f_{clust}

Cluster Branch

Mass from IMF

Binary mass from M17

$T_\star$ and $L_\star$ from accretion history

SED of star and envelope from R24

Cluster

Cluster mass from CMF

Same as individual for $T_\star$ and $L_\star$

Aperture size from intracluster distance

Include full aperture of largest member

Transform Populations into Grids

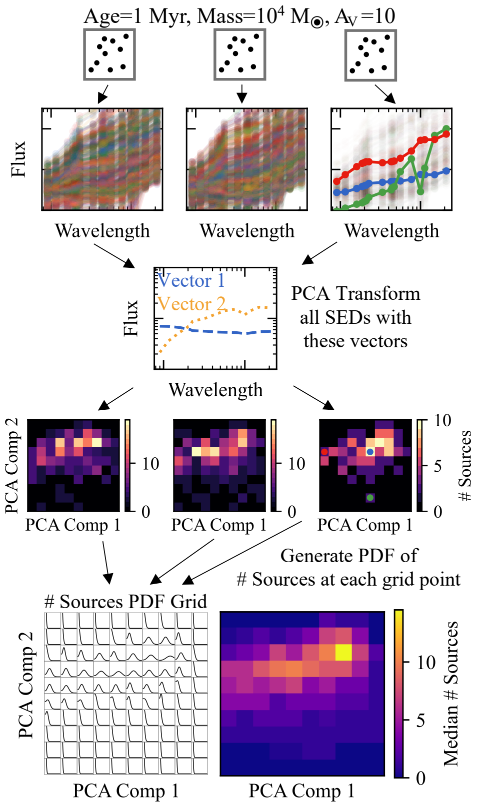

Age=1 Myr, Mass=10^4 $M_\odot$, A_V=10

PCA Transform all SEDs with these vectors

Generate PDF of # Sources at each grid point

PxP

-Generate YSO populations given the **total mass and age** of the population
-Populations are comprised of sources either single YSOs and unresolved clusters
-These populations contain **an SED for each of these sources**
-Using Principal Component Analysis (PCA) we reduce the populations **into 2D grids**
-By generating many populations with the same properties, we can create a statistical **grids of PDFs** of the expected number of sources at each grid point
-Then using **maximum likelihood fitting** we can determine a real populations properties by determining the **best fitting model grid**

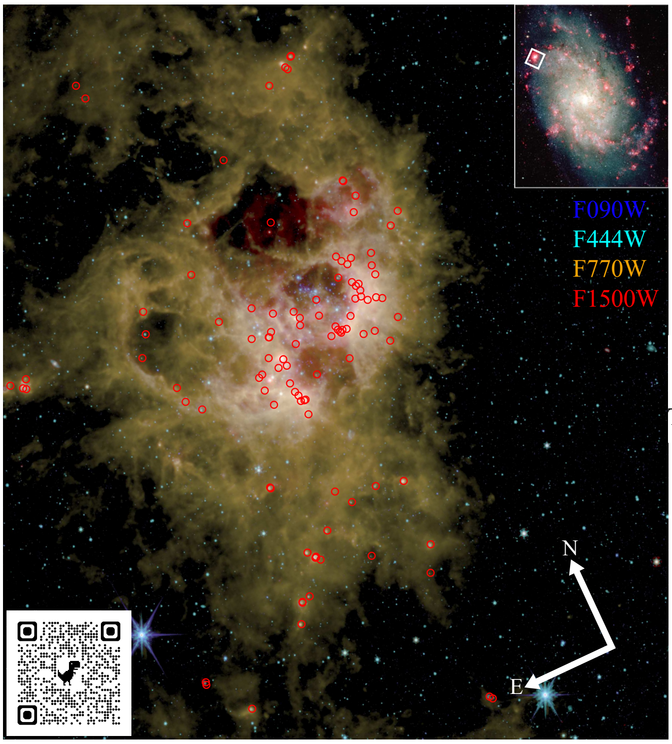

PCA Transform

NGC 604

-Identified YSOCs in NGC 604 in the same way as Peltonen (2024)
-Then apply the PCA transform to create a real grid of a YSO population
-The best fitting model grid has Mass: $(2.2 \pm 0.2)\times 10^4\ M_\odot$ and Age: 0.62 ± 0.01Myr
-This gives a direct star formation rate of $0.035 \pm 0.003\ M_\odot$/yr
-Consistent with the $0.016 \pm 0.02\ M_\odot$/yr predicted from Hα

Fit Real Population Grid to Model Grid

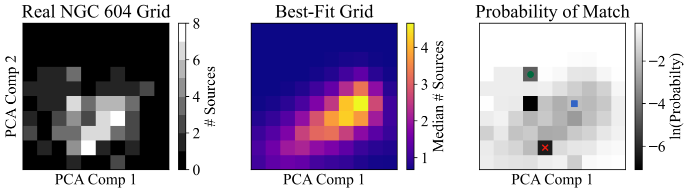
Real NGC 604 Grid
Best-Fit Grid
Probability of Match

Future Work

-Turn to local Milky Way clouds in the SESNA catalogue to determine their properties and constrain alternative star formation histories
-Directly measure star formation efficiency of molecular gas with YSOs as a function of GMC properties. Can we resolve the discrepancy between theory and observation seen in more distant targets (Leroy+2025)?

Unraveling Galactic Filament Networks: A Graph-Theoretic Approach[1]

H.-C. Poosch,[1,2] M. Behrendt,[3,2,1] and A. Burkert [2,1]
✉ hcpoosch@mpe.mpg.de

1 Max Planck Institute for Extraterrestrial Physics, Garching, Germany
2 Universitäts-Sternwarte, Ludwig-Maximilians-Universität München, Munich, Germany
3 Centre for Astrophysics and Planetary Science, Racah Institute of Physics, The Hebrew University, Jerusalem, Israel

MAX PLANCK INSTITUTE
FOR EXTRATERRESTRIAL PHYSICS

Existing methods measure what galaxies look like. We measure how their gas is wired. We treat the JWST-resolved filaments of three nearby spirals as networks and read their topology with graph theory, a new class of descriptor, complementary to traditional morphology.

ABSTRACT

JWST/MIRI 7.7 µm maps resolves the **warm ISM of nearby galaxies** into filamentary networks whose detailed topology, how filaments connect, branch and converge, has no objective, network-level descriptor. Using **DisPerSE**[2], we extract the networks, treat them as **weighted graphs**, and compute their **centrality measures**. Applied to three PHANGS–JWST[3] galaxies (NGC 628, IC 5332, and NGC 1087), the centrality diagrams reveal qualitatively different gas-network architectures. The framework provides a **new, objective, reproducible, network-level descriptor** of the gaseous interstellar medium, demonstrated here on three nearby spirals as a proof of concept.

IMPACT

A different observable.

Existing automated morphology measures describe the projected light distribution; Graph theory quantifies filament connectivity (which filaments are central or bottlenecks).
→ fundamentally different physical information

Network-level, not filament-level.

Existing filament tools characterize individual filaments; Graph centralities measure how those filaments connect, capturing structural information that no single-filament method can.

Per-node, continuous, multi-dimensional.

Every filament node has continuous closeness and betweenness values, yielding a 2D centrality diagram, a richer summary than any single-number morphological statistic.

ANALYSIS

The DisPerSE algorithm constructs a network of nodes (key structural points) and links (filamentary connections) over the gaseous ISM (Fig. 1, top row).

Classification metrics:

- **Closeness centrality**: average distance from a node to all other nodes → measure of distance from network center
- **Betweenness centrality**: number of connections passing through this node → measure of importance for network connectivity

Centrality Relations (Fig. 1, bottom row):

- **IC 5332:** multi-arm structure with varying lengths (A1): many parallel lines at different betweenness, arm splitting indicated by sudden jump in betweenness (vertical gray lines))
- **NGC 628:** two dominant arms of similar length (A2): two overlapping high-betweenness lines
- **NGC 1087:** mixture of other two cases with 3 main arms of different lengths (A3): 3 parallel lines at slightly different betweenness

All three galaxies exhibit a similar floor (B) at betweenness ≈ 0 - 0.05, corresponding to substructure.

	IC 5332	NGC 628	NGC 1087
Network Diameter / Physical Size	~3.75	~6.25	~2.5
Identified Features	multi-arm + splitting	2 dominant arms	3 arms + central feature
Inferred Morphology	flocculent	2-arm grand design	mixture

Table 1 Results for 3 different galaxies from the PHANGS-JWST Survey.

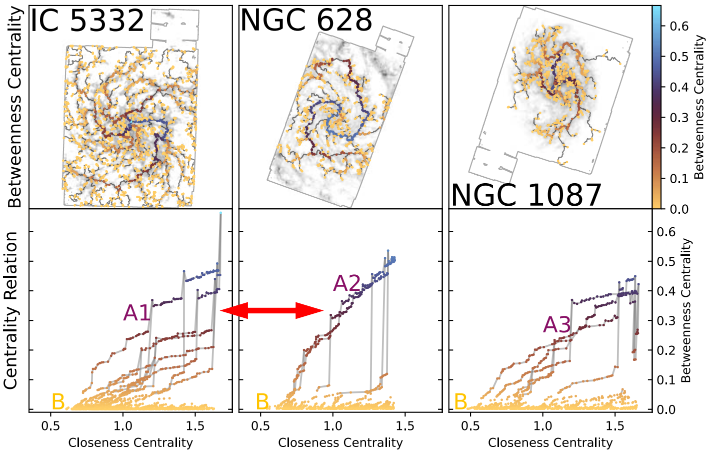

Figure 1 Results for 3 different galaxies from the PHANGS-JWST Survey.
Top row: extracted filament network overlaid on JWST-MIRI 7.7 µm maps; color = betweenness centrality (high = skeleton in blue/red, low = substructure in yellow)
Bottom row: closeness vs. betweenness centrality diagram; skeletal structure (A1-A3) differs between galaxies, similar substructure feature labeled as B

OUTLOOK

These metrics produce three distinct centrality fingerprints. Using observational and simulation data, we developed a graph-theory based mathematical model to interpret these properties. The method is to be validated against multiple observational angles by using mock observations of galaxy simulations
The approach yields a general classification framework that can be readily extended using graph theory tools.

[1] H.-C. Poosch et al. (in preparation)
[2] T. Sousbie 2011, MNRAS, 414, 350
[3] J. Lee et al. 2023, APJ, 994, 17L

Unveiling Metal Mixing in a Grand-Design Spiral:

A UV-Optical Multiphase Study of Young Star Clusters in M83

Adarsh Ranjan[1]; Bethan.L James[2]; Svea Hernandez[2]; R. Rickards Vaught[1]; Alessandra Aloisi[3]; Nimisha Kumari[2]; Peter Zeidler[2]
[1]Space Telescope Science Institute

1 STUDYING: Multiphase ISM around Young Star Clusters in M83

We study the multiphase ISM around young star clusters (YSCs) in the nearby, metal-rich, grand-design spiral galaxy M83. Our sample contains 18 YSCs with ages ~1-6 Myr, spanning galactocentric radius, $R/R_{25} \leq 0.56$.

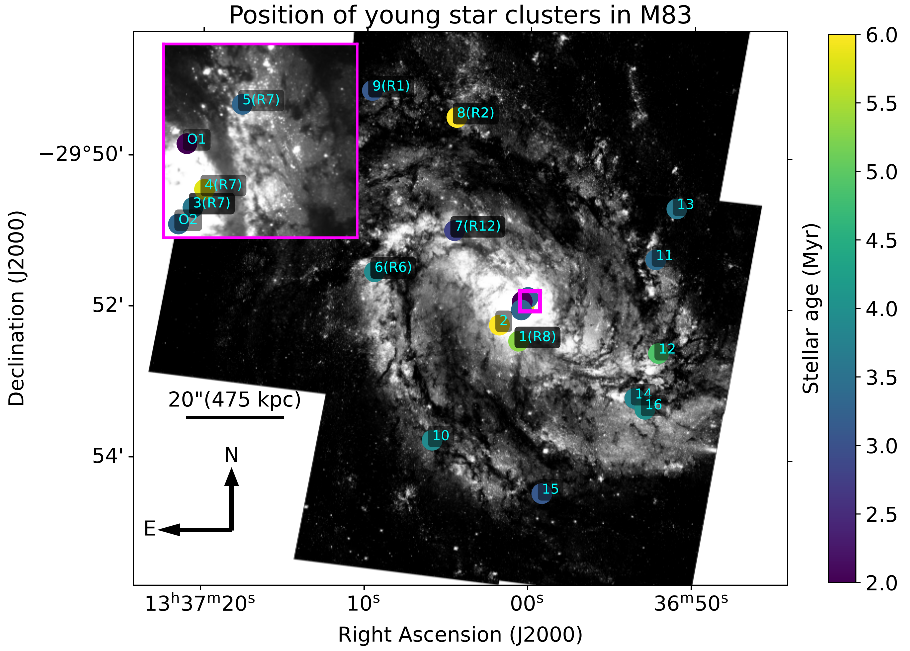

2 O3N2–T_e([S III]) RELATION

M83 is metal-rich and auroral lines are often weak or undetected. We adopt an empirical O3N2-T_e([S III]) relation to derive electron temperatures for ionized-gas abundances.

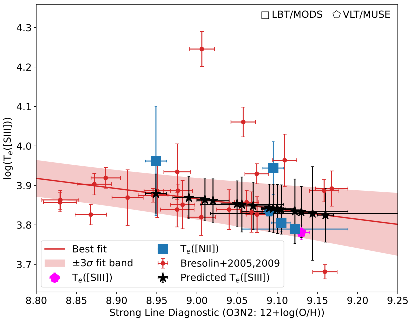

Consistent ionized-gas abundances even when auroral lines are weak.

Ionized gas is locally enriched; neutral gas remains chemically unmixed.

3 CENTER: NO H I but BRIGHT Hα

M83 galactic center is lacks neutral hydrogen along the COS sightlines, yet shines brightly in Hα.

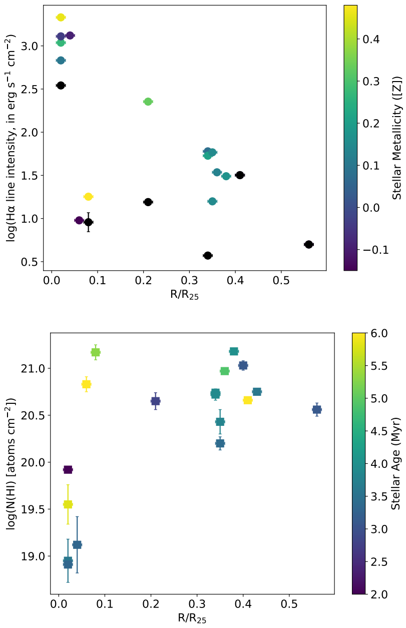

Hα intensity & H I column density versus galactocentric distance.

4 NITROGEN: SUPER-ENRICHED IN H II

Ionized gas (H II region) shows a strong nitrogen enhancement relative to the neutral gas.

ΔN/H ~ 1.5 dex

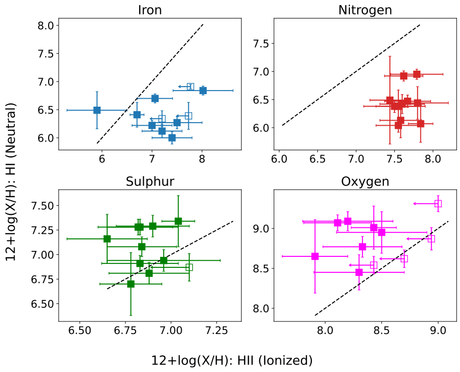

⋆ Nitrogen released by massive (O,B) stars.
⋆ Similar to metal-poor galaxies[4,5], but also seen here in metal-rich M83.
⋆ Iron: Appears enhanced because → strongly depleted on to dust in the neutral ISM.
⋆ α-elements: Slightly enhanced within neutral gas → previous generation of stars.

[4]James et. al. 2026(2026ApJ..1002...82J)
[5]Abril-melgarejo et. al. 2024(2024ApJ...973..173A)

5 STELLAR FEEDBACK→ENRICHMENT

Ionized-gas nitrogen excess (ΔN/H=(N/H)$_{HII}$ - (N/H)$_{HII}$) correlates strongly with young stellar bolometric luminosity & wind momentum, while neutral gas shows no strong trend.

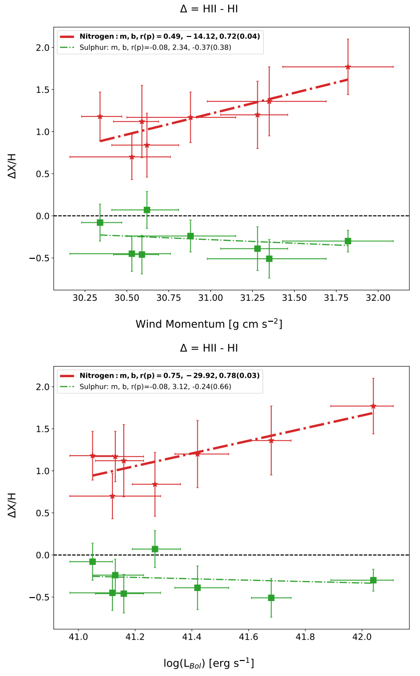

Nitrogen enrichment versus stellar feedback.

OBSERVATIONAL SUMMARY

- **Neutral gas:** UV absorption lines → HST/COS
- **Ionized gas:** optical emission lines → VLT/MUSE + LBT/MODS
- **Stellar properties:** UV continuum and winds → HST/COS
- **Elemental abundance:** O, S, N, and Fe → probe distinct nucleosynthetic pathways & mixing mechanisms across gas phases (H I ↔ *H ii*).

MAIN CONCLUSIONS

- Young massive stars rapidly enrich ionized gas in nitrogen on ~1-6 Myr timescales.
- Nitrogen enrichment is tightly linked to stellar luminosity & wind momentum.
- Surrounding neutral gas shows no corresponding enrichment trend.
- M83's deep gravitational potential likely limits nitrogen mixing into the larger neutral reservoir.
- Cross-phase mixing is inefficient on the timescales probed here.

---

[2]AURA for the European Space Agency, ESA Office, STScI [3]Astrophysics Division, Science Mission Directorate, NASA Headquarters, 300 E Street SW, Washington, DC, 20546, USA

Star formation in a metal-poor environment: The case of NGC 602

Jimena Rodriguez, Peter Zeidler, Anna McLeod, Antonella Nota, Elena Sabbi , Maria Jimenez Donaire

Contact: jrodriguez@stsci.edu

NGC 602

Young Stellar Cluster

- Location: SMC's wing
- Age: ~2-3 Myr
- Low metallicity 1/5 Z⊙
- M = 1.6 x 10^3M⊙
- Formation: interaction of 3 HI clouds

Data & Spectral Extraction

Data:

- **MUSE IFU** observations (3 pointings)
- Optical + Near IR photometry *HST+JWST*

Spectral extraction:

- PSF-fitting spectroscopy using *PampelMuse*
- spectra of **78** stars

Radial velocities:

- Stellar RVs from MUSEpack
- Precision: **~1-2 km s^{-1}**
- Ionized gas kinematics also derived

Cluster Membership Determination

- Multi-band CMDs (HST + JWST)
- Compared with isochrones:
  - Young cluster: ~ **2 Myr**
  - Field population: ~**4.2 Gyr**
- Adding Stellar kinematics information (RV)

✅ **54 cluster members identified** (P >0.5)

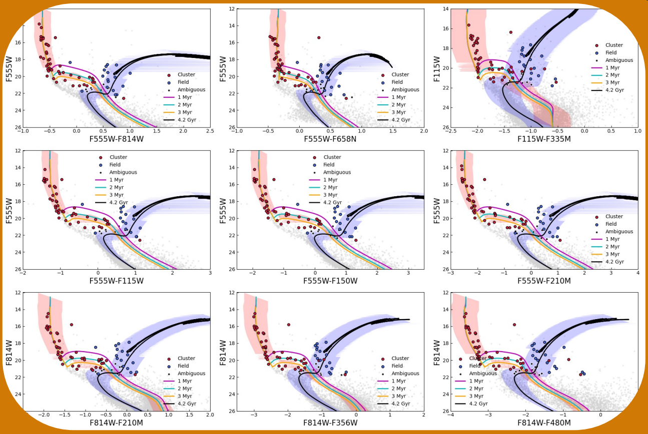

Radial Velocity Profile

Stellar RV Distribution

- Evidence for **multiple kinematic** components for stellar and ionized gas

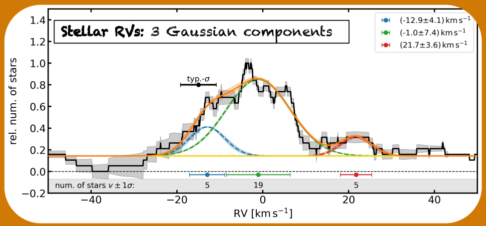

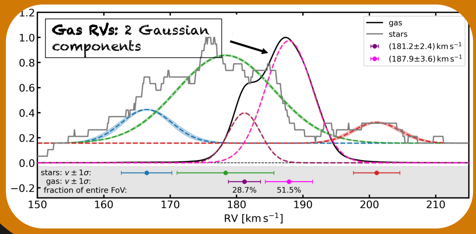

RV Map of the gas

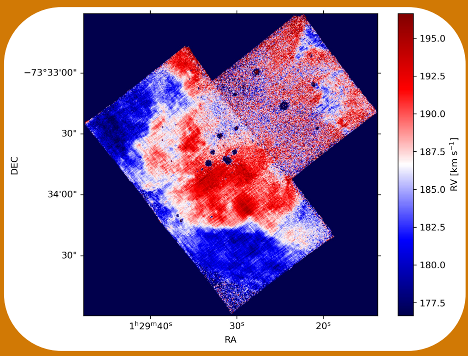

Key Results:

- ✓ 54 cluster members identified
- ✓ Systemic RV ~180 km s^{-1}
- ✓ **Multiple RV components**, likely **leftover imprints of the cluster formation process**
- ✓ With the current dataset, we find **no evidence for cluster rotation**
- ✓ High velocity dispersion, combined with the relatively low cluster mass, suggests **the cluster will disperse over time**

OLYMPIAN SYMPOSIUM

Université Paris Cité · université PARIS-SACLAY · cea irfu AIM · SPEXION

Disentangling Heating Mechanisms in the Interstellar Medium of Extremely Metal-Deficient Galaxies

Georgina Sampson Olalde[1]

[1] Université Paris-Saclay, Université Paris-Cité, CEA, CNRS, AIM, 91191 Gif-sur-Yvette, France

XMD GALAXIES

Extremely metal-deficient (XMD, < 10% solar metallicity) star-forming dwarf galaxies in the nearby Universe can be considered **analogous** to most “primitive” galaxies. They are **ideal laboratories** to probe feedback mechanisms and star formation in environments reminiscent of high-z galaxies (Izotov+2021).

Past studies have shown **peculiar properties** in nearby XMD galaxies:

- Molecular gas is predominantly CO-dark (Madden+2020; Ramambason+2024).
- Sub-linear dust-to-gas ratio (D/G) implying different dust production/destruction mechanisms and timescales (Galliano+2021)
- Relatively large escape fraction of ionizing photons (Ramambason+2022).

No comprehensive studies of feedback mechanisms on large sample of XMDs (multi-wavelength observations + intricate, multi-phase, models) result in **very limited knowledge** about feedback processes in quasi-primordial environments.

CONSTRAINING HEATING MECHANISMS

Radiative and mechanical feedback mechanisms **regulate the ability of gas to cool down, fragment, and collapse**. Direct access to the micro-physics of these ionizing and heating sources is difficult, still most of the energy is transferred to the ISM where it is redistributed. We can us UV, optical, and infrared emission lines to **indirectly constrain** the nature of excitation sources.

Studies will usually combine a few bright tracers to provide empirical diagnostics (BPT-like diagrams). However, these diagnostics are **not well calibrated for XMDs**, where energetic sources and ISM properties are expected to be different. In addition, they are **not good in disentangling more than ~2 mechanisms**. There is a need for a tool to infer potentially many mechanisms from potentially many lines.

SHOCKS

Shocks are among the least explored heating mechanisms in XMDs. A shock occurs when a strong dynamical event injects a large amount of mechanical energy in surrounding environments causing a **turbulent cascade** to develop.

Starting from the upstream supersonic state gas cell is: slowed down and compressed, heated up through compression, ion-neutral friction and viscosity, and cooled down through line emission.

Shocks can also be understood as a “machine” that reprocess **kinetic energy into magnetic and thermal energies, plus some radiative losses**.

MAJOR SCIENTIFIC QUESTIONS

- How can we **disentangle the main heating mechanisms** (photoionization from X-ray sources, cosmic rays, shocks) in extremely metal-deficient ISM ?
- What is the **relative importance of shocks** in heating the interstellar medium of metal-poor galaxies?
- What is their **role in diagnostic tools** often used to trace the cosmic evolution of galaxies?

METHODS

The project is split in two phases. The first one focuses on the creation of a **grid of shock models** (compatible with photoionization grids in XMDs created in our group (Varese+2024)) using the **Paris Durham shock code**. This grid will explore a wide range of physical parameters at different metallicities.

For the second phase, we will **apply the grid to a sample of low-z dwarf galaxies** (optical and IR lines). This will be done by integrating into the statistical galaxy modeling framework **MULTIGRIS** (Lebouteiller & Ramambason, 2022), which uses a Bayesian probabilistic approach.

Currently, we are working on phase one.

Shock velocity
Initial transverse magnetic field strength

Pre-shock proton density

Cosmic ray ionization rate

Radiation field intensity

Elemental abundances

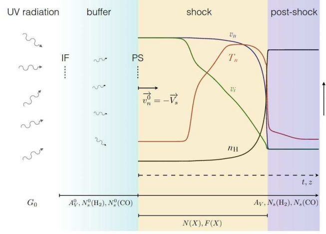

Fig. 1. Schematic view of the shock model geometrical assumptions in the shock frame. The positions of the ionization front and of the pre-shock are indicated as IF and PS.

Godard et al., 2019

Temperature

Fluid velocities

Abundances

Line intensities

… etc

PRELIMINARY RESULTS

Collaboration with Paris Durham Shock Code team (B. Goddard, A. Gusdorf, G. Pineau des Forêts – LPENS)

- Customization of species abundance files depending on **metallicity scaling parameter**.
- Exploratory grid of shocks at low $Z/Z_\odot$ (592 models)
- Metallicity has a strong impact on the type of shock that will develop. At lower metallicities, the magnetosonic speed increases, promoting the development of **C-type** shocks (where ions and neutrals decouple). At the same time, due to the sharp decrease of dust, the abundance of H_2 also decreases, hampering the cooling of the gas and promoting the development of **C*-type** and **CJ-type** shocks. All of this combined difficults the development at low metallicities of **J-type** shocks (where ions and neutrals are coupled and temperature, velocity, and density abruptly change).

nH [cm^{-3}]
1,10,100,1000,1000

$Z/Z_\odot$
1, 0.2, 0.1, 0.03, 0.01

Vs [km/s]
10,20,30,40

Bβ
0.3,1,3

RAD [Habing]
0,1

REFERENCES

Galliano, F., Nersesian, A., Bianchi, S., et al. 2021, A&A, 649, A18

Godard, B., Pineau des Forêts, G., Lesaffre, P., et al. 2019, A&A, 622, A100

Izotov, Y. I., Guseva, N. G., Fricke, K. J., et al. 2021, A&A, 646, A138

Lebouteiller, V. and Ramambason, L. 2022, A&A, 667, A34

Madden, S. C., Cormier, D., Hony, S., et al. 2020, A&A, 643, A141

Ramambason, L., Lebouteiller, V., Bik, A., et al. 2022, A&A, 667, A35

Ramambason, L., Lebouteiller, V., Madden, S. C., et al. 2024, A&A, 681, A14

Varese, M., Lebouteiller, V., Ramambason, L., et al. 2025, A&A, 693, A14

Mechanical and radiative feedback in high-mass cluster forming regions - an ALMAGAL study

Peter Schilke, Han-Tsung Lee, Beth Jones, Thomas Möller, Tatiana Rodriguez
Institute for Astrophysics, University of Cologne, Germany

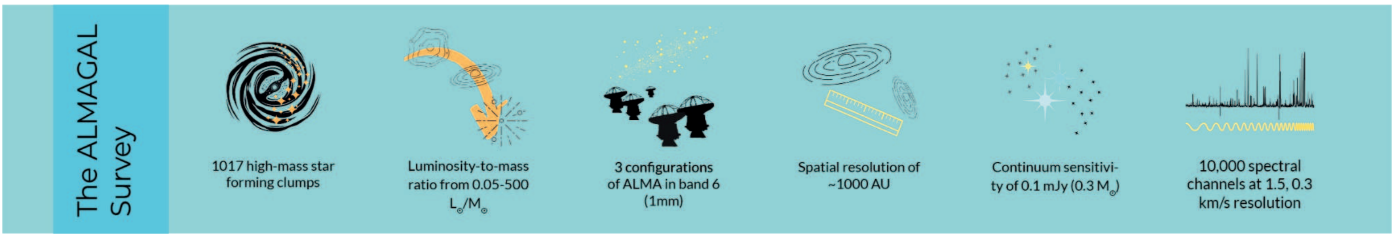

The ALMAGAL Survey

1017 high-mass star forming clumps

Luminosity-to-mass ratio from 0.05-500 $L_\odot/M_\odot$

3 configurations of ALMA in band 6 (1mm)

Spatial resolution of ~1000 AU

Continuum sensitivity of 0.1 mJy (0.3 $M_\odot$)

10,000 spectral channels at 1.5, 0.3 km/s resolution

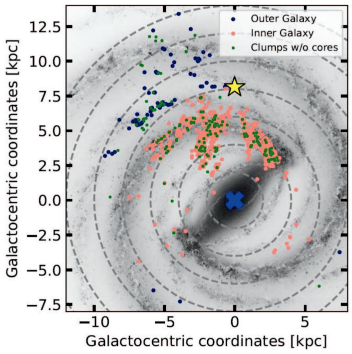

Fig. 1 Galactic distribution of ALMAGAL sources.

Feedback

One of the goals of ALMAGAL was to characterise the feedback, both mechanical and radiative, by measuring the temperature distribution. For this, a variety of tracers was observed, most notably $CH_3CN(J=12-11)$ and $H_2CO(J=3-2)$. While CH_3CN is centred on the cores, but has enough transitions to reliably determine temperatures up to 600 K, H_2CO is more extended. However, since the observed lines only originate from levels 21 and 68 K above ground, they can characterise only temperatures below approximately 150 K, and become unreliable above that.

We found (Han-Tsung Lee, in prep) that in many sources (419) there is extended warm or hot gas (Fig. 4, 5), more than one would naively expect from pure thermal heating. Some of this heating comes from outflows, some is thermal from protostars or from interfaces to HII regions.

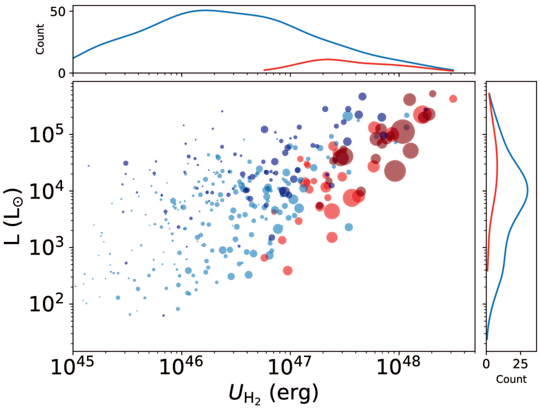

Fig. 6 Clump luminosity based on Herschel data vs. thermal energy based on our temperature maps. red = clump with extended hot region; size = fit area, darker colours show HII regions.

References: Coletta et al. 2025, A&A, 691, 151; Elia et al. 2022, ApJ, 941,162; Molinari et al. 2025, A&A, 691, 149; Sánchez-Monge et al. 2025, A&A, 691, 150

Context

ALMAGAL is a large ALMA project that observed 1013 high-mass star-forming regions in our Galaxy (Fig. 1) with a large range of clump masses and luminosities (Fig. 2) at 1.3 mm with a setup resulting in 1000-1500 au linear resolution. A large variety of source morphologies was found (Fig. 3). First results have been published in Molinari et al. 2025, Sánchez-Monge et al. 2025 and Coletta et al. 2025.

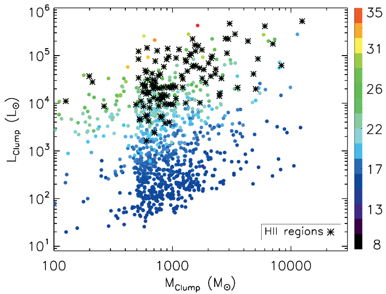

Fig. 2 Mass/Luminosity distribution of ALMAGAL sample.

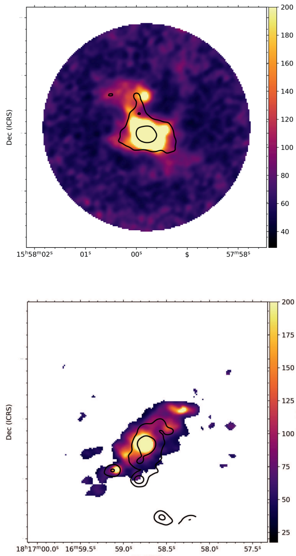

Fig. 4 Examples of temperature maps based on H_2CO LTE fitting.

(preliminary) Results

We calculated the total thermal energy based on our temperature maps (Fig. 6). As expected, this correlates with the clump luminosity (Elia et al. 2022), albeit with a large scatter. We can compare with the total clump kinetic energy based on the Herschel derived dust temperature and find an anticorrelation (Fig. 7), that we still have to interpret. One possibility for the difference is the different dependence on radiative thermal energy, which can heat both dust and gas, while the gas has mechanical energy as an additional heating source, i.e. by shocks and outflows.

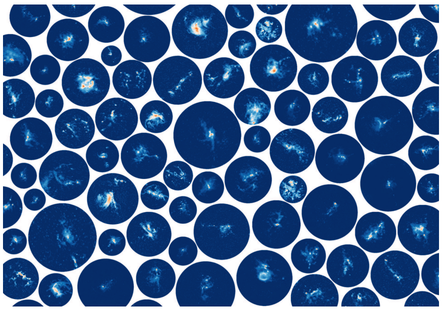

Fig. 3 Maps of representative ALMAGAL sources in 1.3 mm continuum, scaled by distance to show the same linear resolution.
Credit: Chiara Mininni.

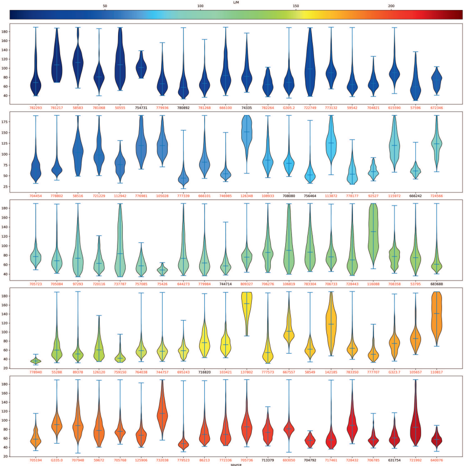

Fig. 5 Distribution of temperatures in 100 sources. Red labels mean outflow sources. The sources are sorted from blue to red by L/M~0.3-237 $L_\odot/M_\odot$

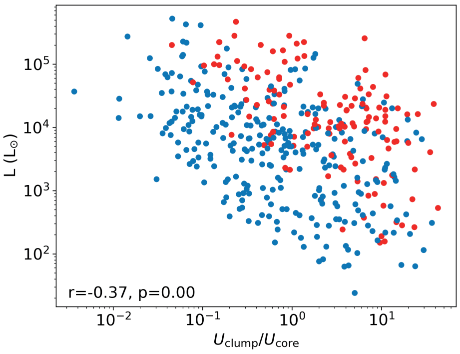

Fig. 7 Clump luminosity vs. ratio of clump thermal energy based on Herschel data and thermal energy based on H_2CO. Blue and red dots denote near and far sample, respectively.

Complex Aromatic Chemistry Detected at the Dawn of Star and Planet Formation:
An Update on GLUCOSE, the GBT L1544 Unbiased Complex Organics SurvEy

PI: Samantha Scibelli, Jansky Fellow, NRAO (sscibell@nrao.edu)
Co-Is: Paola Caselli (MPE), Ci Xue (NRAO), Silvia Spezzano (MPE), Judit Ferrer Asensio (RIKEN), Andrés Megías (CAB), Izaskun Jimenez-Serra (CAB), Beatrice Kulterer (UVa), Anna Punanova (Chalmers), Danna Qasim (SWRI), Giulia Perotti (NBI/MPIA), Laurie Chu (NOIRLab), Robin T. Garrod (UVa), Yancy Shirley (UA), Anton I. Vasyunin (Ural), Yvonne Pendleton (UFC), Anthony Remijan (NRAO), Brett McGuire (MIT/NRAO)

Background and motivation: *Why is L1544 our target of interest?*

- The prestellar core L1544 is the perfect 'laboratory' for investigating the initial chemical conditions at the onset of star and planet formation because:
  1. It is dynamically evolved and on its way to becoming a mature planetary system, due to its well characterized infall motions and high central density of ≥ 10^7 cm^{-3} at its cold (~6 K) dust peak (e.g., Crapsi et al. 2007, Caselli et al. 2019).
  2. The physical and chemical structure is already well-modeled (e.g., Keto et al., 2015, Chacón-Tanarro et al., 2019)
  3. Previous observations identify a rich complex (> 6 atom) molecular chemistry towards multiple positions around the core (e.g., Vastel et al. 2014; Jiménez-Serra et al. 2016, Lefloch et al. 2018, Bianchi et al. 2023)
- There is a need for detailed studies that can pinpoint whether this complex chemistry, now observed to be widespread in other cores and across all stages (e.g., Scibelli et al., 2024, Ferrer Asensio et al., 2026), can be directly incorporated into forming stars and planets from the earliest cloud stage.
- We use the 100m Green Bank Telescope to carry out the Large Legacy Program 'GLUCOSE' (PI: Scibelli), which observes complex molecular line transitions towards the central dust 'kernel' of L1544 across a wide bandwidth (~10 GHz) at incredibly high spatial (18 arcsec beam) and spectral resolution (Δv ~ 0.01 km/s).

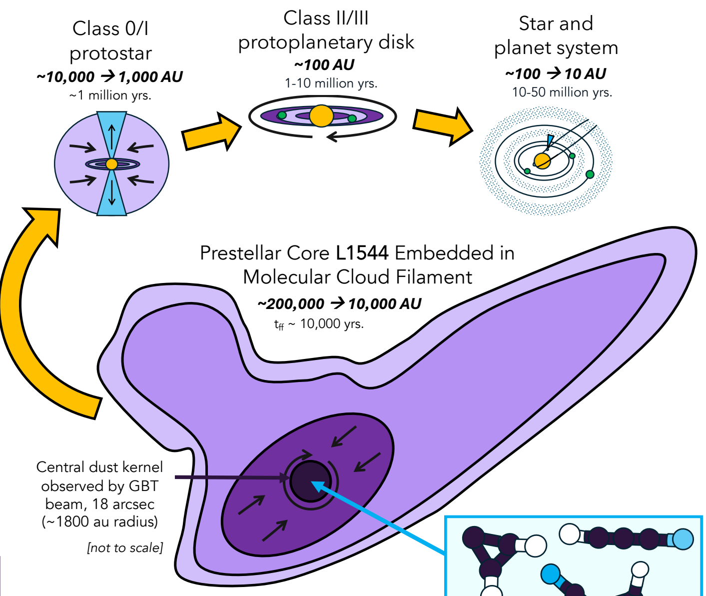

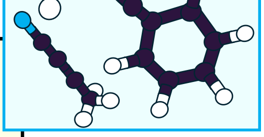

Many small and large aromatic species, as well as chemically related carbon-chains!

Survey progress: *Observations with the Green Bank Telescope*

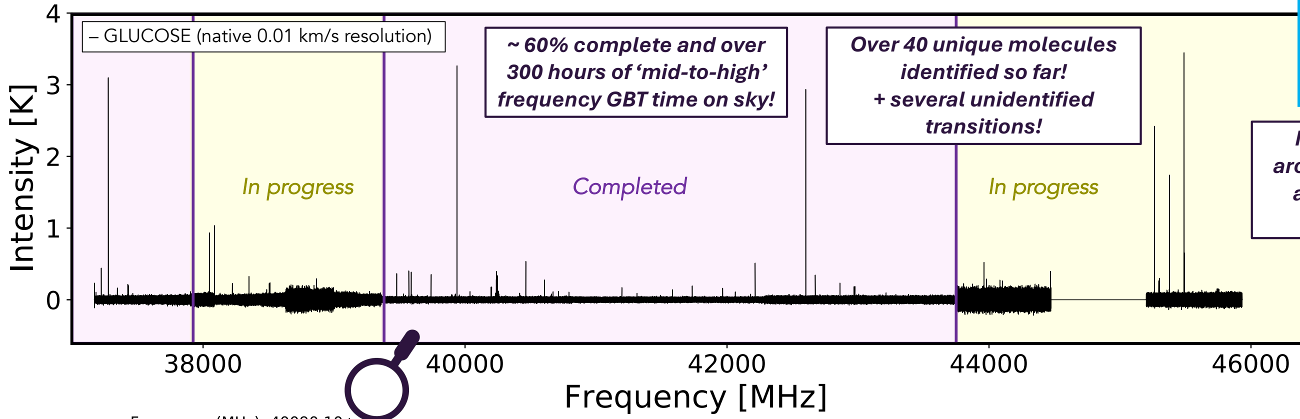

~ 60% complete and over 300 hours of 'mid-to-high' frequency GBT time on sky!

Over 40 unique molecules identified so far! + several unidentified transitions!

Spectra will be available to the public after the first data release (scheduled for 2027)

Exciting early results: *Discovery and kinematic analysis of benzonitrile, c-C_6H_5CN*

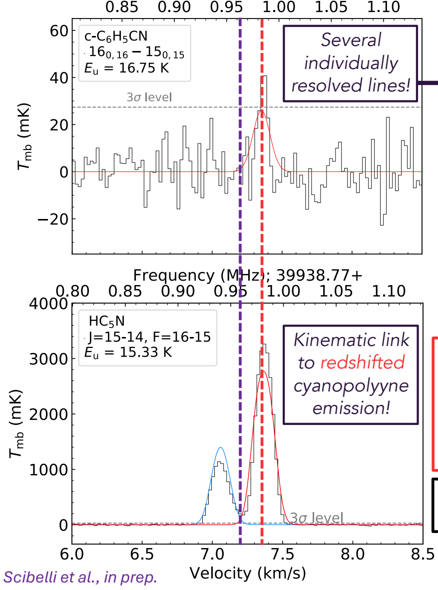

Several individually resolved lines!

Kinematic link to redshifted cyanopolyyne emission!

Scibelli et al., in prep.

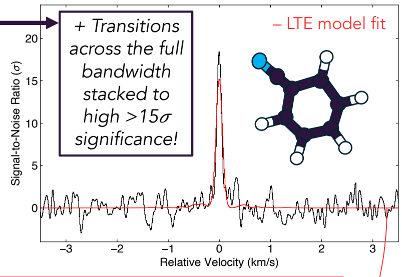

+ Transitions across the full bandwidth stacked to high >15σ significance!

Modeled line parameters:
Line-of-sight velocity: 7.350±0.002 km/s
Linewidth: 0.136±0.007 km/s
Column Density: 5.62±1.15 x 10^{11} cm^{-2}
Excitation Temperature: 7.81±0.5 K

– $v_{LSR,systemic}$ = 7.2 km/s
– $v_{LSR,red}$ = 7.35 km/s

- The molecule benzonitrile (c-C_6H_5CN) is a well-known tracer of benzene (C_6H_6) and thus is an **early building block to polycyclic aromatic hydrocarbons (PAHs)**, which are thought to account for 10-25 % of carbon in the ISM (Draine et al., 2007) and are currently being studied in high detail with JWST to trace, for example, extragalactic star formation rates (e.g., Sandstrom et al., 2023).
- We detect *and resolve* benzonitrile emission at the dust peak of L1544, finding it kinematically linked to the redshifted peak seen in cyanopolyynes (e.g., HC_3N, HC_5N and HC_7N; Bianchi et al., 2023) as well as other, denser, and similarly optically thin gas emission that has been modeled to be due to the contraction of the core itself (e.g., $HC^{17}O^+$ (1-0); Ferrer Asensio et al., 2022).
- Our analysis demonstrates that **benzonitrile is associated with contracting and accreting material along the line-of-sight**

Discussion: *What does this mean for the ISM and star formation?*

How are PAHs transported from cloud to planet and solar system scales?

- Primitive solar system bodies, such as the asteroid Ryugu (Zeichner et al., 2023), have a rich PAH inventory. Our study provides evidence that conditions of surrounding cloud material are important indicators of aromatic content, and that in order to incorporate this chemistry into forming planetary system, dynamical processes, such as accretion or infalling gas, may be needed.

References

Bianchi et al. 2023, ApJ, 944, 2, 208 · Caselli et al. 2019, ApJ, 874, 89 · Chacón-Tanarro et al., 2019, A&A, 622, A141 · Crapsi et al. 2007, A&A, 470, 1, 221-230 · Draine et al., 2007, ApJ, 663, 866 · Ferrer Asensio et al., 2022, A&A, 667, A119, 32 · Ferrer Asensio et al., 2026, A&A, 707, A28 · Jiménez-Serra et al. 2016, ApJL, 830, L6 · Keto et al., 2015, MNRAS, 446, 4, 3731 · Lefloch et al. 2018, MNRAS, 477, 4, 4792-4809 · Scibelli et al., 2024, MNRAS, 533, 4 · Sandstrom et al., 2023, ApJL, 944, 2 · Vastel et al. 2014, ApJL, 795, L2 · Zeichner et al., 2023, Science, 382, 6677, 1411-1416

Software: GOTHAM Spectral Pipeline: Xue et al., 2025, APJS, 281, 1, 9 (zendo.15678187); `molsim`: McGuire 2024 (zendo.12697227)

Interested in getting involved in the survey?
Opportunities for students and prospective students!
***Reach out!* sscibell@nrao.edu**

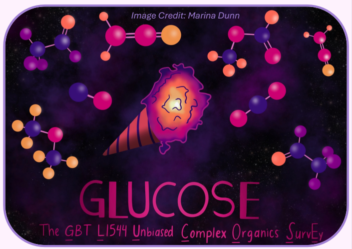

Dust polarisation in molecular clouds - Orientation and polarisation spectra

D. Seifried[1], S. Walch[1], T. Balduin[2], J. Soler[3]
[1]I. Physics Institute, University of Cologne, Germany
[2]Austrian Academy of Science, Space Research Institute, Graz, Austria
[3]Institute for Space Astrophysics and Planetology, Rome, Italy

Abstract

Part I: We present synthetic dust polarisation maps of simulated molecular clouds (MCs) [1,2]. The magnetic field becomes perpendicular to (column) density structures above N = $10^{21\text{-}21.5}$ cm^{-2} and n ~ 1000 cm^{-3}. This switch is related to **magnetic fields becoming subdominant** at higher densities (smaller scales), where gravity takes over.

Part II: We analyse the origin of the **V-shaped polarisation spectrum** in MCs [5]. It originates from regions where dust with different temperatures is present along the LOS. We find indications for **carbon grain destruction in feedback dominated regions**.

Part I: Magnetic field orientation

We use the galactic-scale **SILCC-Zoom** simulations to model MCs and create self-consistent **dust polarisation maps** [1,2]. We find that dust grains remain **aligned** up to densities of ~ 1000 cm^{-3} due to radiation from nearby stars.

We also investigate the magnetic field orientation with respect to (column) density structures. We find that

1. The magnetic field flips in 2D at N = $10^{21\text{-}21.5}$ cm^{-2} (Fig. 1, left panel).
2. Projection effects can disguise this flip (blue line, left panel).
3. The magnetic field flips in 3D at n = 100 - 1000 cm^{-3} (right panel).

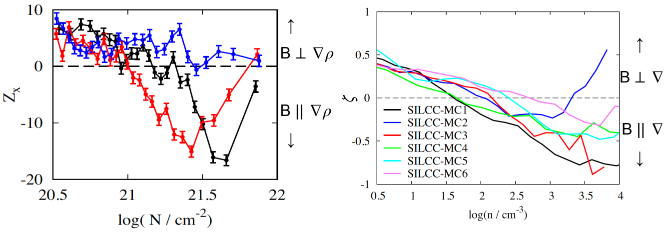

Fig. 1: Left: Projected Rayleigh Statistics showing the relative orientation of the magnetic field w.r.t. column density structures. Right: The orientation of the magnetic field in 3D as a function of the density.

Interpretation: B-fields vs. gravity

1. The flip in field orientation indicates the presence of an anisotropic, **converging** flow, which can be caused by gravitational infall.
2. The observed **amplification** of the magnetic fields [3] starts at the **same (column) densities** values where the flip occurs, which is only possible if velocities become superalfvenic.
3. **Energy analyses** show that the magnetic field energy drops below the gravitational energy above ~1000 cm^{-3} [4].

➡**All aspects independently point to the fact that magnetic fields become subdominant at densities above 1000 cm^{-3} (≙ scales below ~1 pc).**

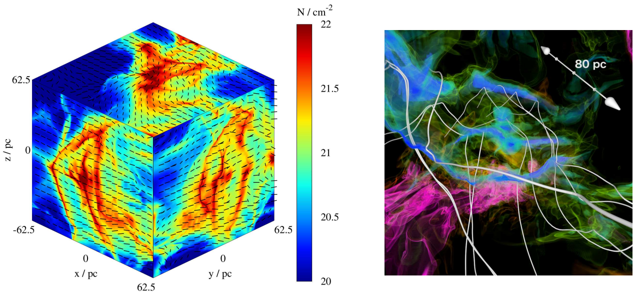

Fig. 2: Left: Synthetic dust polarisation map showing the column density and the synthetic dust polarisation vectors at 850 micron obtained with the POLARIS code. Right: 3D visualization of the same MC showing its filamentary structure (blue). The magnetic field lines (white) are **bend** towards the filaments by gravity.

Part II: Polarisation spectra

We use semi-analytical models to investigate the origin of **V-shaped polarisation spectra** (i.e. the polarisation degree showing a minimum around 350 μm) in MCs [5]. We show that for a single dust phase, the spectrum is a strictly monotonic function, thus not matching the V-shape.

Our further analysis shows:

1. The V-shape can only be obtained if **two dust phases**, (i) a dense and cold and (ii) a warm and dilute phase caused by **stellar radiation**, are present.
2. Comparison with observations indicates that **carbon grains are destroyed by radiative feedback of nearby massive stars** (Fig. 3, left and Fig. 4).
3. Reducing the alignment efficiency of silicate grains in the cold, dense phase has only a moderate effect (Fig. 3, right) and seems not to be necessary (Fig. 3).

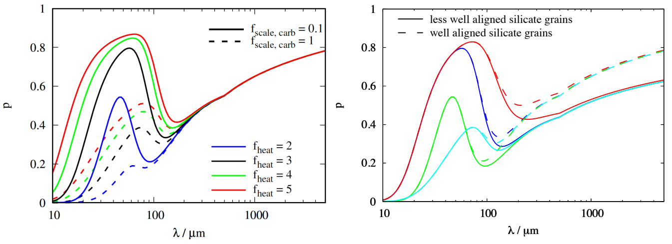

Fig. 3: Left: Carbon grain destruction (solid lines) increases the depth of the minimum in the polarisation spectrum (different colours indicated different temperatures in the warm dust phase due to radiative feedback). Right: A lower alignment efficiency of silicate grains only moderately affects the polarisation spectrum.

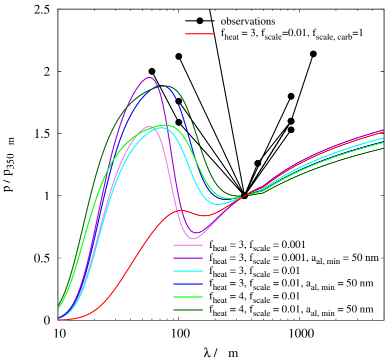

Scan me for the link to the paper

Fig. 4: Comparison with observational data from [6]. A good match is obtained when carbon grains are destroyed by UV radiation from massive stars in the warm phase.

Outlook

We extend the polarisation spectrum analysis to **3D, MHD simulations** from [1,2] including **radiative feedback from nearby stellar clusters**. The results are in good agreement with those of the semi-analytical model. This shows the potential to further study polarisation spectra with state-of-the art 3D, MHD simulations.

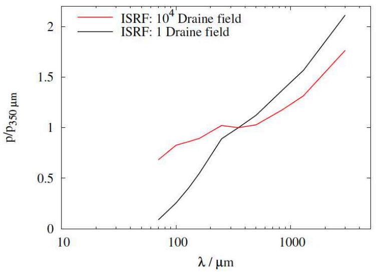

Fig. 5: First-ever synthetic polarisation spectrum obtained with POLARIS from a 3D, MHD simulation of an MC. The cloud is embedded into different radiation fields. For high UV fields, a weakly pronounced V-shape appears.

[1] Seifried, D., Walch, S., Reissl S., et al., 2019, MNRAS, 482, 2697
[2] Seifried, D., Walch, S., Weis, M., et al., 2020, MNRAS, 497, 4196
[3] Crutcher, R., 2012, ARA&A, 50, 29
[4] Ganguly, S., Walch, S., Clarke, S. D., Seifried, D., 2024, MNRAS, 528, 3630
[5] Seifried, D., Walch, S., Balduin, T., 2025, MNRAS, 542, 3302
[6]Vaillancourt, J. E. & Matthews, B. C. 2012, ApJS, 201, 13

Seeing Through the ISM: Recovering Intrinsic X-ray Emission in Metal-Poor Dwarf Galaxies

Dr. Dhrubojyoti Sengupta & SPEXION

CNRS, CEA Paris-Saclay, AIM, Université Paris-Saclay, Université Paris Cité, Gif-sur-Yvette, 91191, France

Introduction

- Extremely metal-deficient (XMD) dwarf galaxies are nearby analogs of primordial galaxies and are ideal laboratories for studying star formation, compact high-energy sources, and cosmic reionization [1,2]. Recent observations suggest that X-ray sources such as ultraluminous X-ray sources (ULXs), high-mass X-ray binaries (HMXBs), and potentially intermediate-mass black holes (IMBHs) may strongly influence the ionization, heating, and star-forming gas reservoir of these galaxies [3,4].
- In XMD galaxies, the low dust-to-gas ratio and porous ISM allow X-rays to propagate efficiently through both ionized and neutral gas phases. As a result, X-ray photoionization and heating can dominate over traditional heating mechanisms. These processes significantly affect emission-line diagnostics, molecular gas tracers, and star-formation indicators [4,5].
- High-ionization lines such as He II, [Ne V], and [O IV] suggest the presence of energetic compact sources like ULXs, HMXBs, and possible IMBHs [6,7].
- Previous studies have established that XMD galaxies host more luminous and numerous HMXBs and ULXs compared to metal-rich systems [9,10]. Observations with facilities such as *Chandra*, *XMM-Newton*, and infrared surveys have revealed signatures of compact objects and unusual ISM conditions in nearby dwarf galaxies. Particularly for the galaxy IZw18, showed that ISM tracers can successfully recover properties of embedded X-ray sources [4,8].
- However, no comprehensive study currently combines multi-wavelength observations, sophisticated ISM modeling, and statistical methods to systematically investigate the nature and impact of X-ray sources in XMD galaxies. Direct X-ray detections are limited by instrumental sensitivity and ISM absorption, especially in the soft X-ray regime. Consequently, the population, luminosity distribution, and physical nature of compact sources in XMD galaxies remain poorly constrained. The speXion project aims to address this for both nearby systems and high-*z* systems with future JWST observations.

Objectives

- Develop methods to recover the intrinsic X-ray spectrum and identify compact sources in XMD galaxies using ISM emission-line diagnostics.
- Investigate how X-ray sources influence the ionization, heating, and star-forming gas reservoir of XMD galaxies, and examine the relationship between X-ray absorption, ISM structure, and stellar environments using multi-wavelength observations from UV to radio wavelengths.
- Provide new observational diagnostics and predictive tools for interpreting primitive galaxies observed with the JWST and understanding their role in cosmic reionization.

Key Insight: The SpeXion project reveals how compact objects in XMD galaxies drive stellar and galactic evolution, providing a vital blueprint for understanding black hole growth, star formation and cosmic reionization in the early Universe.

Methodology

- Selected a sample of ~70 extremely XMD galaxies hosting XRBs/ULXs, including CLASSY galaxies, with available X-ray observations from ***Chandra*** **and** ***XMM-Newton***.
- Compile complementary FUV datasets, where ~50 galaxies possess **FUSE observations (90-120 nm)** and ~20 galaxies have **HST-COS observations (90-215 nm)**.
- Derive and compare N(H) values obtained from X-ray spectral fitting and N(HI) from FUV absorption measurements to investigate ISM absorption properties.
- Estimate FUV (N(HI)) using direct H I detections and UV absorption features from elemental tracers such as O I, P II, N I, C II, S II, and Si II, combined with metallicity and abundance measurements.
- Investigate the spatial correlation between X-ray emitting sources and COS/FUV sightlines to examine whether compact X-ray sources are physically associated with stellar clusters and absorbing ISM regions.

Correlation Plot on derived N(H)

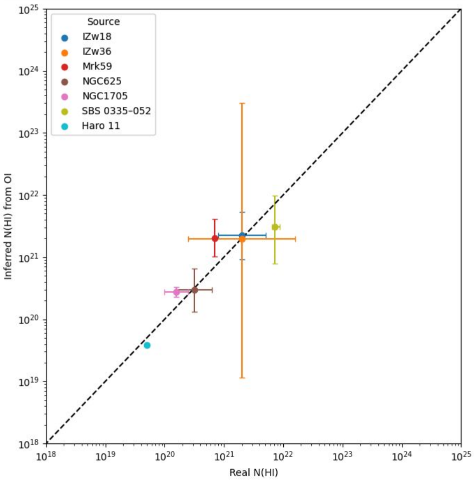

Fig. 1 - Hydrogen column density from OI abundance vs direct spectral measurement.

Expected Results with a Complete Sample

- It will allow us to test the physical association between XRBs/ULXs, OB stellar clusters, and the surrounding ISM, providing insight into whether compact sources preferentially form within dense star-forming environments.
- The comparison between FUV and X-ray column densities can be used to establish reliable N(H) priors for physical X-ray emission models, reducing degeneracies in X-ray spectral fitting.
- The complete sample will help map the potential distribution of N(H) toward XRBs within galaxies, revealing whether absorption primarily originates from local circum-source material, star-forming regions, or the diffuse galactic ISM.
- More XMD with improving spatial matching between COS/FUV and X-ray observations will likely reveal systematic trends between metallicity, ISM structure, and compact source populations, helping constrain the role of ULXs and possible IMBHs in low-metallicity systems.
- Ultimately, the study is expected to provide a predictive framework connecting ISM tracers and X-ray properties, enabling indirect identification of compact high-energy sources in high-*z* XMD galaxies observed with the JWST, where direct X-ray measurements may not be feasible.

Discussion on literature survey

- Figure 2 shows that several galaxies lie close to the equality relation, supporting the scenario in Figure 3 that compact X-ray sources are located near young OB stellar clusters.
- Sources significantly offset from the equality line likely indicate differences in geometry, intrinsic absorption, or source position within the galaxy.
- Figure 3 provides a diagnostic of the 3-D distribution of XRBs in dwarf galaxies: sources near the line may trace co-spatial XRB-OB cluster systems, while offsets may reflect foreground/background configurations or local intrinsic absorption.
- Even with the current sample, the scatter suggests diverse ISM environments and absorption properties among XMD galaxies.

Observed Hydrogen Column Density

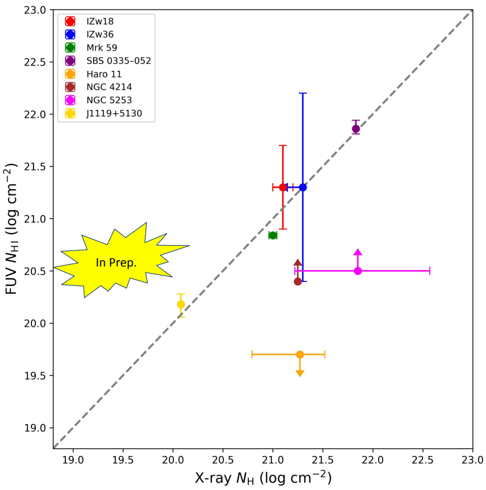

Fig. 2 - Observed N(HI) from Far-UV observations vs N(H) from X-ray spectral fitting, for each source.

Location of X-ray source near OB clusters

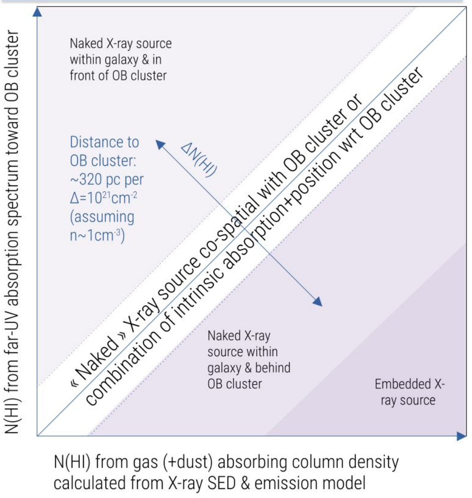

Fig. 3 - Comparison of foreground far-UV & X-ray absorbing column density towards same coordinates.

REFERENCES

[1] Benson, A., Venkatesan, A., & Shull, J. M. 2013, ApJ, 770, 76
[2] Izotov, Y. I., Thuan, T. X., Guseva, N. G., & Liss, S. E. 2018, MNRAS, 473, 1956
[3] Galliano, F., Hony, S., Bernard, J. P., et al. 2011, A&A, 536, A88
[4] Lebouteiller, V., Péquignot, D., Cormier, D., et al. 2017, A&A, 602, A45
[5] Bialy, S. & Sternberg, A. 2019, ApJ, 881, 160
[6] Schaerer, D., Fragos, T., & Izotov, Y. I. 2019, A&A, 622, L10
[7] Stanway, E. R. & Eldridge, J. J. 2019, A&A, 621, A105
[8] Lebouteiller, V. & Ramambason, L. 2022, A&A, 667, A34
[9] Mirabel, I. F., Dijkstra, M., Laurent, P., Loeb, A., & Pritchard, J. R. 2011, A&A, 528, A149
[10] King, A., Lasota, J.-P., & Middleton, M. 2023, , 96, 101672

Author's Contact

dhrubojyoti.sengupta@cea.fr

dhrubojyoti.sengupta@cnrs.fr

SIMULATING STAR FORMATION ON GALAXY SCALES

Recent highlights of our work investigating the connection between galactic enviroment and star formation using self-consistent high-resolution simulations and zooms.

Rowan Smith[1], Kamran Bogue[2], Ryan McDonald[1], Mairi Nonhebel[3,1], & Zoe Faes[1]
[1]University of St Andrews, [2]University of Manchester, [3]MPIA

1. Magnetic Fields alter the location of galaxies on the KS relation

In **Bogue et al. 2026** we present two AREPO simulations of an isolated star-forming galaxy with and without magnetic fields, using sink particles to model star formation.

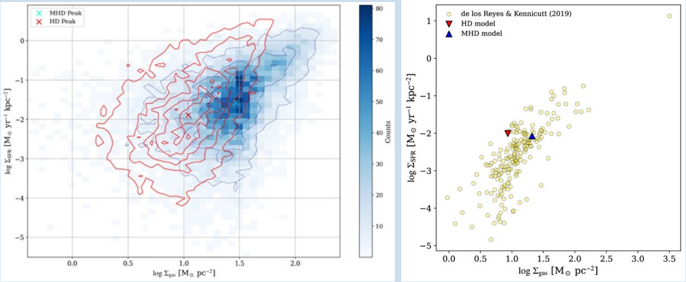

Fig. 1: *Left* Resolved KS relation inside the galaxy with a cross showing the peak value. *Right* Whole galaxy averaged KS relation including reference literature data.

We see a clear shift in the molecular gas Kennicutt Schmidt relation to higher gas surface densities in the MHD case, which is more consistent with observations. We find a more compact disc in the MHD case (radius ∼5.1 kpc, compared to ∼7.4 kpc), and the MHD simulation has a higher proportion of dense, gravitationally unbound gas than the HD case, but a lower star formation rate, an average between 125 and 150 Myr of $\sim 4.8\,\mathrm{M}_\odot\,\mathrm{yr}^{-1}$ compared to $\sim 8.4\,\mathrm{M}_\odot\,\mathrm{yr}^{-1}$.

3. The ISM density distribution dependence with Mach number varies

In **Nonhebel, Smith & Klessen *submitted*** we study the density PDFs of molecular cloud complexes in the Cloud Factory simulations (Smith et al. 2020); a suite of detailed zoom-in simulations that self-consistently generate a turbulent, multi-phase ISM.

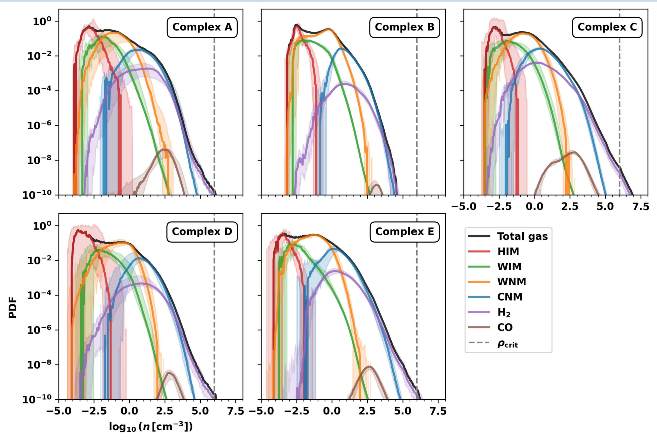

Fig. 2: Density distribution of gas in different phases from the cloud complexes drawn from the Cloud Factory simulations. The grey line shows the density above which sink particles form.

The density, Mach number ($\sigma_s^2 - \mathcal{M}$) relation varies between phases and with measurement method. The classical relation (e.g. Vazquez-Semadeni 1994) fails to capture the widths of the WNM and CNM density distributions. However it tentatively holds for the log-normal portion of the H_2 distribution, provided Mach number are calculated using the mean internal clump velocity dispersions instead of the full cloud complex value. The width of the CO density PDF is systematically overpredicted by the classical relation due to the selective nature of CO as a tracer.

2. Magnetic Fields are a bottleneck during the formation of cold gas

In **McGuiness, Smith & Whitworth 2026** using a high-resolution simulation of a dwarf galaxy, we quantify the energetic importance of magnetic fields within the different phases of its interstellar medium on parsec scales.

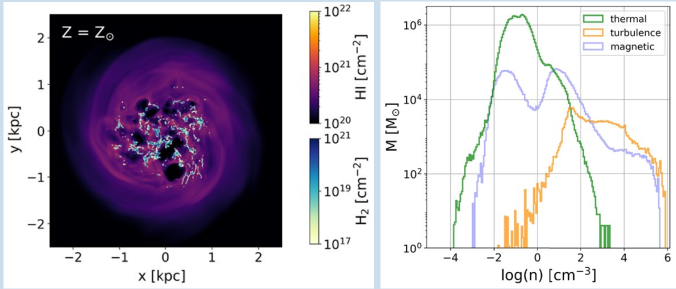

Fig. 3: *Left* Gas surface density in dwarf galaxy model. *Right* Density distribution of the the gas in which thermal, magnetic, and turbulent energy dominate. Gravity is not plotted as it is large-scale effect.

We show that, whilst overall the magnetic field is only energetically dominant for a small fraction of the ISM, it becomes important in the thermally unstable regime (45.2 per cent of the mass is magnetically dominant), and dominates in the cold neutral medium (66.1 per cent of the mass). In the molecular gas, the magnetic field dominates more of the total mass budget (39.8 per cent) than thermal energy, turbulent kinetic energy, or gas self-gravitating potential energy. This suggests that magnetic forces are non-negligible during the formation of cold dense gas, which will slow its collapse and lead to an increase in the fraction of cold atomic and molecular gas in the ISM.

4. The star formation efficiency depends on large-scale dynamics

In **Smith et al. *in prep*** we perform an analysis of the star formation efficiency per free fall time at fixed scales using a method inspired by the PHANGs survey (e.g. Leroy et al. 2025).

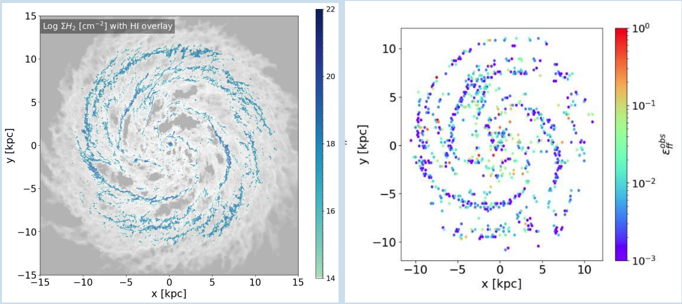

Fig. 4: *Left* The gas surface density in the galaxy model. *Right* The star formation efficiency per free fall calculated in 300 pc diameter hexagonal bins using molecular gas visible in CO emission.

Departures are seen from the expected 1% efficiency per free fall time. While the distribution peaks at 1% the range exceeds two orders of magnitude. These do not correlate well with features such as spiral arms, or with galactic radius, instead efficiency is raised when there are large scale streaming motions within the galaxy.

Email: rjs22@st-andrews.ac.uk

The neutral atomic shell of the extended Orion nebula

Juan D. Soler (University of Vienna) and the ODIN collaboration*

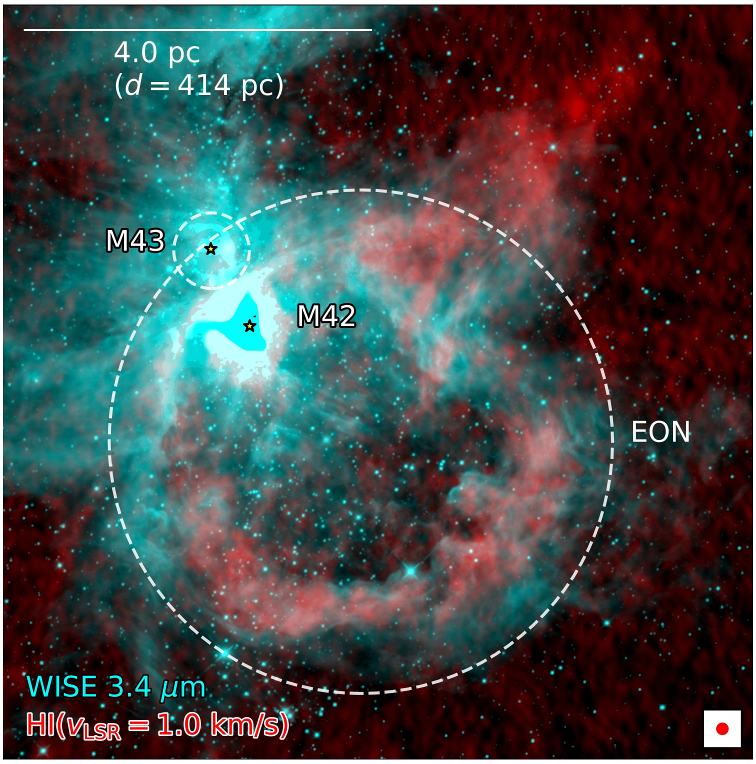

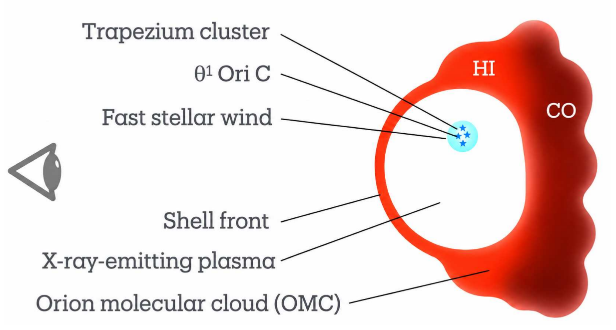

THE EON IN ATOMIC HYDROGEN

- Expansion velocity: ~13 km/s
- Shell front mass: ~100 solar masses.
- Mean column density: 3.8 x 10^{20} cm^{-2}
- Mean nucleon density: ~ 120 cm^{-3}

Position-velocity profiles

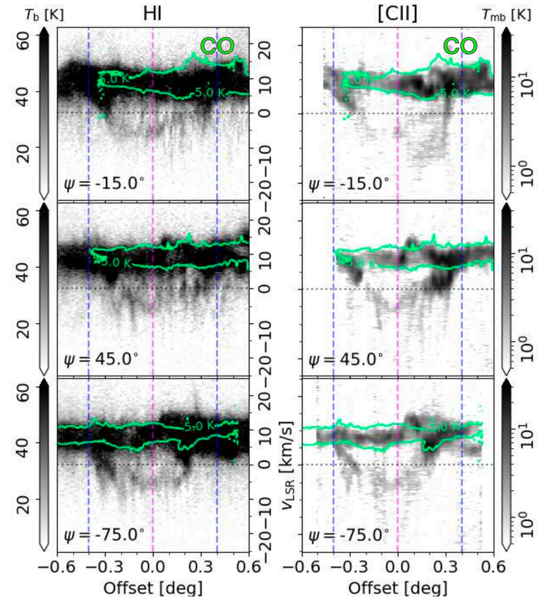

INTRODUCTION

- **Where:** The extended Orion nebula (EON), a wind-blown bubble around the nearest region of high-mass star formation (d = 414 pc).
- **What:** First arcminute-resolution map of the neutral atomic hydrogen (HI) line emission at 21-cm wavelength.
- **How:** combination of Jansky Very Large Array (VLA) D-configuration and Five-hundred-meter Aperture Spherical Telescope (FAST) observations.

HI and [CII] channel maps

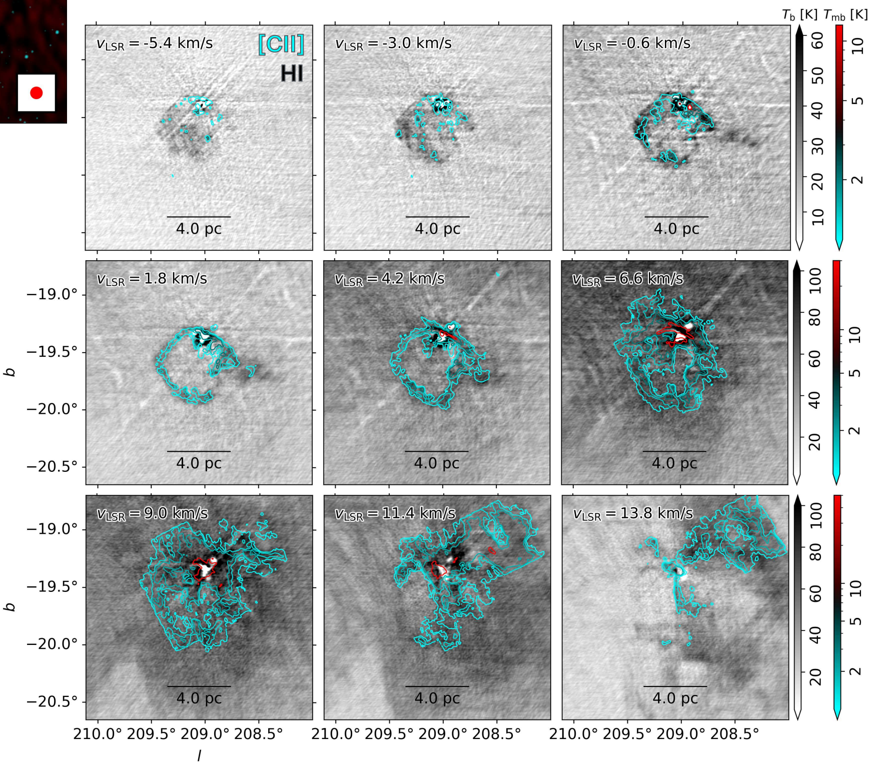

KEY RESULTS

- The shell is **lighter than expected**: HI measurements imply a shell mass of only ~100$M_\odot$; about ten times lower than [CII] estimates.
- The shell is **multiphase**: the frontal hemisphere shows negligible CO emission, but some material may be in the form of H_2.
- The EON is **more complex than a single wind-blown bubble**: HI reveals a possible secondary expanding cavity and a large protrusion.

---

*The Orion Diffuse Ionized and Neutral gas (ODIN) survey collaboration: J.D. Soler (PI), H. Beuther, S. C. O. Glover, R. S. Klessen, J. Ott,, M. Rugel, J. W. Teh, S. E. Clark, P. Goldsmith, A. Hacar, A. Socci, M. Heyer, M.-Y. Lee, C. E. Murray, D. Seifried, S. Walch, B. Godard and M.-A. Miville-Deschênes

NRAO National Radio Astronomy Observatory
FWF Austrian Science Fund

The Multi-Phase Magnetic Fields of the Dwarf Galaxy IC10

Physics and Astronomy
McCausland College of Arts and Sciences
UNIVERSITY OF SOUTH CAROLINA

Reagan Stanton[1], Enrique Lopez Rodriguez[1], and Sergio Martin Alvarez[2]
1. Department of Physics and Astronomy, University of South Carolina
2. Kavli Institute for Particle Astrophysics & Cosmology (KIPAC), Stanford University

Abstract

Dwarf galaxies provide unique insights into the processes that shape galaxies, due to their shallow potentials making them highly sensitive to galaxy-formation physics. However, the delicate interplay between star formation, feedback, turbulence, and magnetic fields (B-fields) in the interstellar medium (ISM) of dwarf galaxies is poorly understood. Here, we present the first far-infrared (FIR) polarimetric observations of a dwarf galaxy. Specifically, we study IC10, which is the nearest and brightest dwarf galaxy and therefore provides excellent spatial resolution (around 50 pc) and highly sensitive polarimetric data. We perform a comprehensive multi-wavelength analysis, combining observations and simulations, to identify the physical mechanism responsible for the multi-phase B-fields in IC10. Observationally, we compile SOFIA/FIR (155 um) and VLA/radio (3 cm) polarimetry, with Hα, HI, CO, X-ray data, dust temperature, and dust column density maps. Using our radiative transfer cosmic ray magnetohydrodynamical simulation, Pandora, we generate synthetic observations at all these wavelengths, matching the spatial resolution of IC10.

We find that the radio and FIR total intensities are spatially correlated with star-forming regions, inferred through Hα. However, radio and FIR polarized intensities are not spatially correlated. For the FIR polarized intensity, the inferred FIR B-field is spatially correlated with the star-forming regions and the CO. For the radio polarized intensity, the inferred radio B-field is spatially correlated with the X-ray emission in the southern region of IC10. Our synthetic observations confirm that the decrease in FIR polarization with increasing star formation activity is driven by turbulence induced by stellar feedback. We also use simulations to confirm that the spatial correlation between radio polarization and X-ray emission is driven by a shock front generated by a supernova bubble. Our work shows that B-fields in the dense and cold ISM co-regulate star formation in IC10, and supernova feedback drives B-field compression, modulating cosmic ray transport.

Introduction

- IC10 is the closest and brightest dwarf galaxy in the Local Group
- It has a high star-formation rate (0.05–0.2 $M_{\odot} yr^{-1}$) and a mass of $1.6 \: x \: 10^8 \: M_{\odot}$
- Our work builds on the previous radio polarization study by Basu et. al (2017) by adding FIR polarization data from SOFIA as well as our multiwavelength tracers
- The cosmological MHD simulation created by Martin Alvarez et. al (2023) involves the effects of dark matter, magnetic fields, turbulence, cosmic rays, stellar feedback, and radiative transfer
- Pandora, our simulated galaxy, is a similarly sized dwarf galaxy with comparable star formation rate (≈ 0.03 $M_{\odot} yr^{-1}$) and mass (≈ $10^7 \: M_{\odot}$)

Observational Results

The SOFIA observations are taken with HAWC+ instrument at a wavelength of 155 um and a resolution of 13.6 arcseconds (≈ 50 parsecs). All the images shown have been convolved and reprojected to the SOFIA reference.

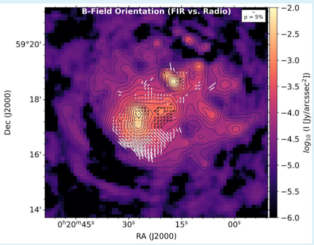

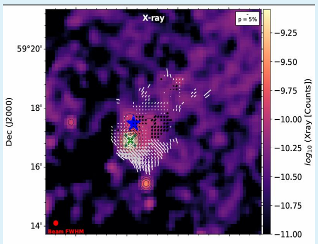

Figure 1(right): Overlaid comparison of the B-field orientation at 155 um (black lines) and 3 cm (white lines). The background is the radio total intensity (VLA and Effelsberg).

Figure 2 (left): Comparison of the B-field orientation at 155 um (black lines) and 3 cm (white lines) with the X-ray emission (Chandra).

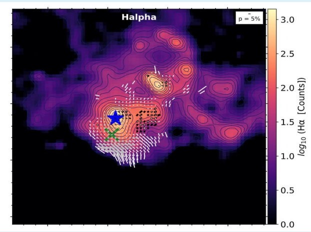

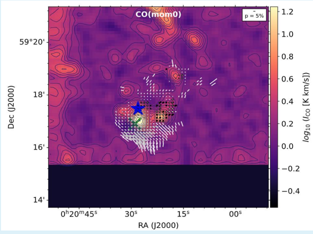

Figure 3 (left): Comparison of the B-field orientation at 155 um (black lines) and 3 cm (white lines) with the Hα emission (Palomar Observatory).

Figure 4 (right): Comparison of the B-field orientation at 155 um (black lines) and 3 cm (white lines) with the CO intensity (Combined Array from Research in Millimeter-wave Astronomy).

Simulation Results

We show the synthetic observations using our MHD simulations, where we smoothed and pixelated the original MHD simulations with a 10 parsec resolution to match the 50 parsec resolution of the SOFIA observations.

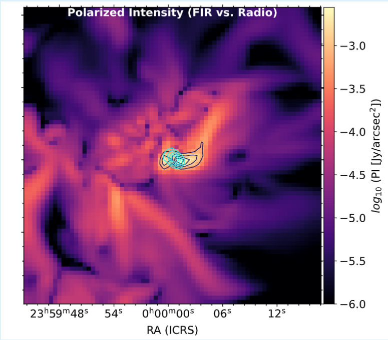

Figure 5: Overlaid comparison of the simulated polarized intensity at 155 um (cyan contours) and 3 cm (black contours). The background is the radio polarized intensity.

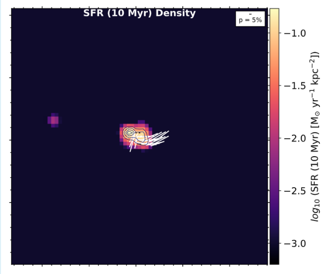

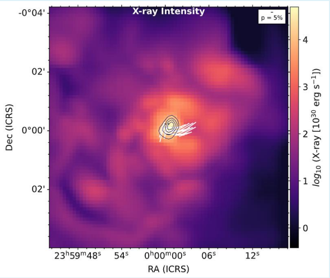

Figure 6 (left): Comparison of the simulated B-field orientation at 155 um (black lines) and 3 cm (white lines) with the SFR density.

Figure 7 (right): Comparison of the B-field orientation at 155 um (black lines) and 3 cm (white lines) with the X-ray emission.

Discussion and Conclusion

- We find that the inferred magnetic fields in radio and FIR are not spatially correlated, which indicates that they are formed by different processes.
- The FIR polarization is spatially correlated with the Hα emission and the CO intensity, which indicates that the magnetic field in the FIR is influenced by star formation and stellar feedback.
- In the FIR, we also find a polarization arc that may be a compressed and amplified B-field that is preventing the gravitational collapse of the CO molecular cloud shown in Figure 4.
- The radio polarization is spatially correlated with the X-ray emission, which indicates that the magnetic field in radio is influenced by a supernova shock.
- In the simulation, we see a similar split in the radio and FIR magnetic fields and correlations with SFR for FIR and X-ray for radio, which matches the observations.

References

[1] Lopez-Rodriguez, Enrique, et al. "Extragalactic Magnetism with Sofia (Salsa Legacy Program): The Magnetic Fields in the Multiphase Interstellar Medium of the Antennae Galaxies*." The Astrophysical Journal Letters, vol. 942, no. 1, Jan. 2023, p. L13. DOI.org (Crossref), https://doi.org/10.3847/2041-8213/acaaa2.

[2] Utomo, Dyas, et al. "The Resolved Distributions of Dust Mass and Temperature in Local Group Galaxies." The Astrophysical Journal, vol. 874, no. 2, Apr. 2019, p. 141. DOI.org (Crossref), https://doi.org/10.3847/1538-4357/ab05d3.

[3] Hubble Captures Elusive, Irregular Galaxy -NASA Science. 21 June 2019, https://science.nasa.gov/missions/hubble/hubble-captures-elusive-irregular-galaxy/.

[4] Basu, Aritra, et al. New Insights into the Interstellar Medium of the Dwarf Galaxy IC 10: Connection between Magnetic Fields, the Radio--Infrared Correlation and Star Formation. 2017. DOI.org (Datacite), https://doi.org/10.48550/ARXIV.1706.06426.

[5]Martin-Alvarez, S., Sijacki, D., Haehnelt, M. G., Farcy, M., Dubois, Y., Belokurov, V., Rosdahl, J., & Lopez-Rodriguez, E. (2023). The Pandora project—I. The impact of radiation, magnetic fields, and cosmic rays on the baryonic and dark matter properties of dwarf galaxies. *Monthly Notices of the Royal Astronomical Society*, *525*(3), 3806–3830. https://doi.org/10.1093/mnras/stad2559

Acknowledgements

We would like to thank Alejandro Serrano Borlaff, Nushkia Chamba, Pamela Marcum, Rainer Beck, and Adam Leroy for sharing their data.

Contact Information

Reagan Stanton- rstanton1200@gmail.com

Cosmic fireworks mark the 1st billion years: the extreme interstellar medium conditions of giant elliptical galaxies in formation

Nikolaus Sulzenauer et al. (2026) | Max Planck Institute for Radio Astronomy

Motivation

Local galaxy clusters host a distinct population of giant elliptical galaxies that co-evolve with their hot and metal-rich atmospheres. While cluster environments are well studied out to redshifts 1-2, the formation process in the first two billion years remain enshrouded in cosmic history. Contrary to a slow, continuous assembly over billions of years, the first giant elliptical galaxy must form rapidly – possibly in a spherical collapse. This is supported by observations of their z~5 precursors as interacting, compact groups of vigorously star-forming (SFR>300 M_o yr^{-1}), dust obscured galaxies (DSFGs).

Characterized by enormous molecular reservoirs, these protocluster cores show spatially correlated star-formation on the scales of the emerging cosmic web. These are the sites for early heating and metal enrichment of the intracluster medium around the brightest cluster galaxies, already in place by cosmic noon. Selected from the 25000 deg^2-large South Pole Telescope survey (SPT-SZ[10,11]), the sensitivity and angular resolution of ALMA and JWST enables detailed characterization of the physical conditions in the $[CII]_{158\mu m}$-bright, tidally disrupted, multi-phase molecular envelopes of 4<z<7 protocluster cores.[5]

SPT2349-56

at z = 4.3 or just 1.4 Gyr after the Big Bang, contains fifteen ULIRGs within only 100 kpc in projection[7,8] and a compact DSFG quartet at its center (see Fig. 1,2). With ultradeep, multi-cycle [CII] line observations, we discovered 12 more galaxies (40+ in total) surrounding the central merger and M_{gas} = 8.9x10^9 M_o of spatially resolved tidal debris, thus showing all properties expected for a galaxy cluster in formation.[1,4,12]

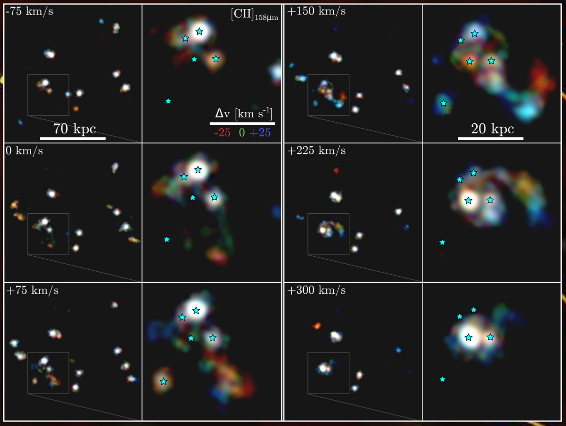

Figure 1. A beacon of this "mega merger" are bright, giant tidal arms or streamers, serendipitously discovered in our ultra-deep ALMA spectral cube. Surprisingly, these bridges are 10x brighter in $[CII]_{158\mu m}$ intensity than expected for typical ISM conditions, while occupying the same LOS velocity range as roughly half of the DSFGs in the protocluster. The most likely origin is tidal ejection from the massive HyLIRGs ($L_{IR}>10^{13}$ L_o) making up the central quartet (blue stars), both hosting radio AGNs.[2]

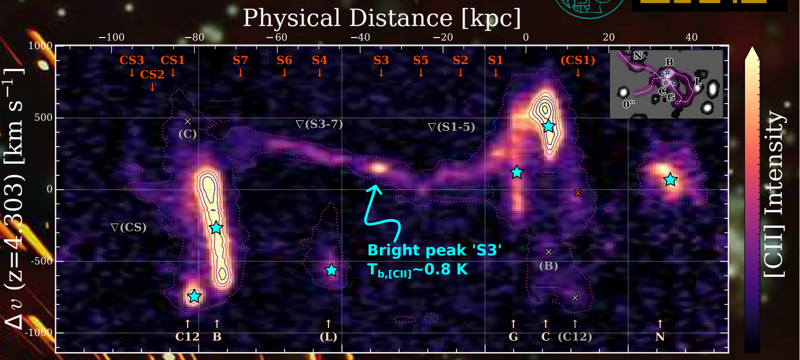

Figure 1. Clumpy ionized carbon arcs, bright in [CII] extend coherently over l_{3D}~60 kpc, and orbit the core. Cold stripped material, $L_{[CII]}$ = 3.0±0.2 x10^9 L_o, traces the ejected gas. The tidal debris fragments into a total of 10 clumps with narrow line emission along two separate tidal arms – resembling beads-on-a-string.

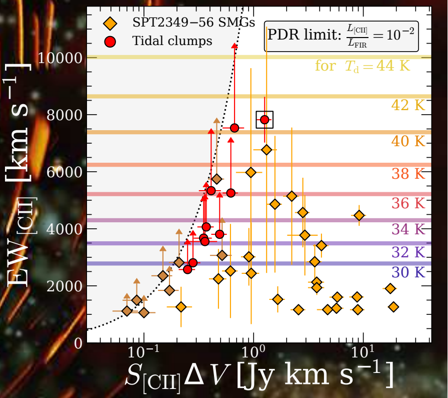

Figure 3. Typical dust temperatures of DSFGs at z>2 are 30-40 K, thus an $EW_{[CII]}$ of >7000 km s^{-1} requires either unusually warm dust (>40 K) or the [CII] line is brighter than expected from PDRs alone. Thus gas heating from turbulent energy dissipation is required to explain the Streamer clumps at T_d=30 K, with line excess at 2-3x over the PDR $L_{[CII]}/L_{FIR}$ limit at 1% of FIR-luminosity.

Physical properties of the CGM clumps

Despite bright [CII], only clump 'S1' is detected in dust continuum. Assuming T_d = 30 K, we estimate ~2.2x10^9 M_o in gas mass within R~5.3 kpc (GDR = 100) Importantly, we measure a ten times lower mass-to-light ratio ($\alpha_{[CII]}$ = 2.95 M_o/L_o; see Fig. 4). At the peak, this CGM clump shows Σ_{gas} = 59 M_o pc^{-2}, densities typical for spiral arm GMCs at kpc-resolution (see Fig. 6).

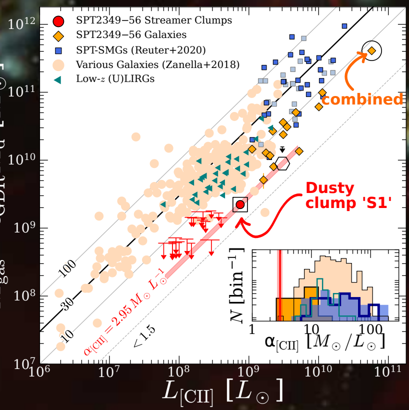

Figure 4. Comparing the canonical Zanella et al. (2018) mass-to-light ratio to massive DSFGs (blue) and protocluster galaxies (orange), we find that the Streamer clumps (red) and galaxies in SPT2349, show extremely lower values. CGM gas at z=4.3 might be metal-rich, predominantly molecular yet warm and highly turbulent. Although the gas is bright, it contains a small fraction of the gas mass.

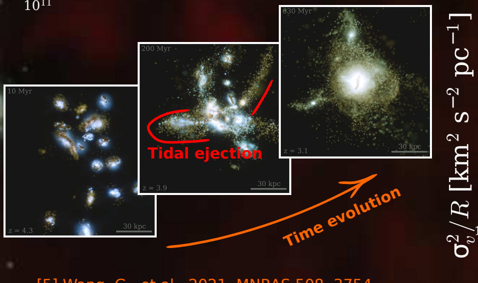

Figure 5. Isolated numerical hydro-simulations that draw initial conditions from the phase-space confirm that SPT2349 is undergoing a wet multiple major merger, dissipatively forming a giant elliptical galaxy only within ~300 Myr or by z<3[6,9], highlighting the importance of tidal ejection for SF quenching.

Figure 6. The high specific intensity (Fig. 3) of the Streamer clumps require warm (T_{kin}~300 K) and dense gas (n~2670 cm^{-3}) conditions at solar metallicity. Thus, in equilibrium, a pressure of P_{th}/k_B = 8.0x10^5 K cm^{-3} is expected, supporting kinetic energy dissipation from galax-scale, molecular shocks toward supersonic, small-scale turbulence at σ_v ≳ 30 km s^{-1} tens of kpc into the CGM.

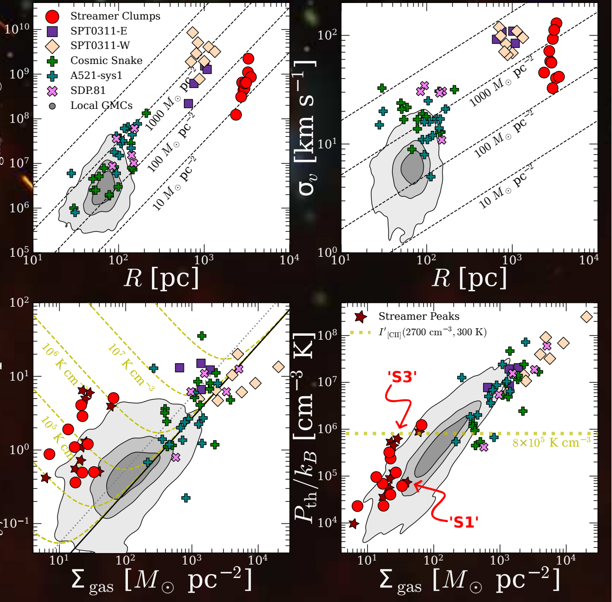

[1] Apostolovski, Y., et al., 2023, A&A, 683, A64
[2] Chapman, S.C. et al., 2026, ApJ, 1000, L10
[3] Hill, R., et al., 2022, MNRAS, 512, 4352
[4] Rotermund, K.M. et al. 2021, MNRAS, 502, 1797
[5] Wang, G., et al., 2021, MNRAS 508, 3754
[6] Rennehan, D., et al., 2020, MNRAS 493, 4607
[7] Hill, R., et al., 2020, MNRAS 495
[8] Miller, T.B., et al., 2018, Nature 556
[9] Sulzenauer, N., et al., 2026, ApJ 998, 191
[10] Vieira, J., et al., 2010, ApJ 719, 763
[11] Weiß, A., et al., 2013, ApJ 767, 88
[12] Zhou, D., 2026, Nature 649

Resolving the star formation relation of early starbursts with ALMA

Pablo Arriagada Torres[1],
Tom J. L. C. Bakx[1], Kirsten K. Knudsen[1], Toshiki Saito[2]
[1]*Chalmers University of Technology, Sweden;* [2]*Shizuoka University, Japan.*

Email me at *pablo.arriagadatorres@chalmers.se*; or meet me for a chat!

Background: Star formation is one of the main drivers of galaxy evolution. The *Schmidt-Kennicutt* relation (SK) is a fundamental tool to understand the conversion of gas into stars in galaxies, linking surface densities of star formation rate (Σ_{SFR}) and star-forming molecular gas (Σ_{H2}) via a power law. While widely studied in the local Universe, it remains largely unconstrained at high redshift.

For the first time, we study the resolved SK relation of high-z starbursts in a large sample; consisting of 23 *Herschel*-selected dusty star-forming galaxies (DSFGs) at z = 2—4.5. As the main contributors to SFR density at cosmic noon, DSFGs constitute a key population within galaxy evolution.

Reliable tracers with ALMA:

- SFR: Resolved (~0.1") Band 7 dust continuum, coupled with *Herschel* photometry.
- Molecular gas: Resolved (~0.5") CO(3-2, 4-3, 5-4) lines.

We measure beam-by-beam:

- Beam-like apertures probe Σ_{SFR} and Σ_{H2} in independent sightlines at ~3 kpc scales.
- Tessellation is relocated ~60 times per galaxy, for a better sampling of the ISM.

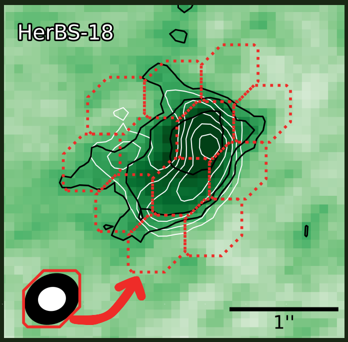

x 23 galaxies!

Robust statistics:

- Hamiltonian MCMC fit of a hierarchical Bayesian model.
- Upper limits included in likelihood with censored cumulative Gaussian.
- +200 independent data points from 23 galaxies!

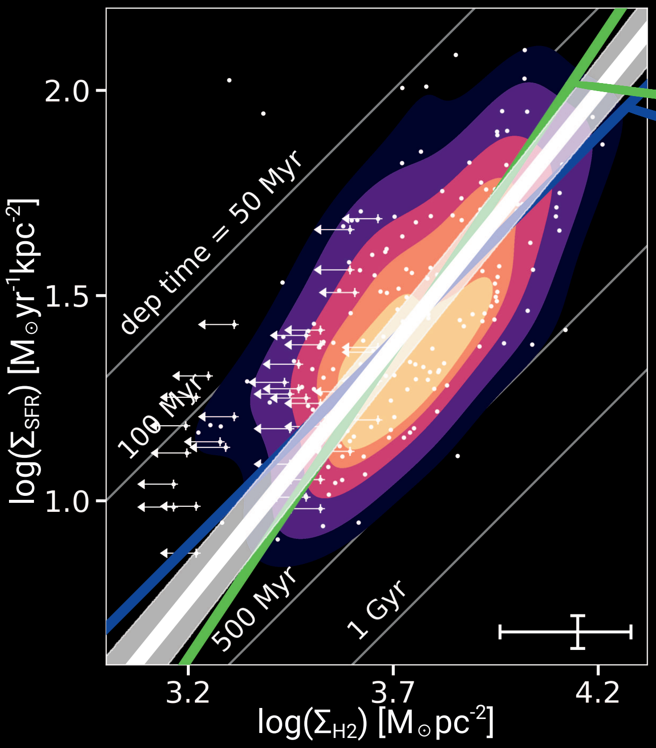

Resolved SK of early starbursts is **super-linear** (N = 1.23 ± 0.15): regions with more gas form stars more efficiently!

Models disagree about massive galaxies at z = 2—4:

Colibre	**NewHorizon**
Universal star formation [1]	Free-fall star formation [2]

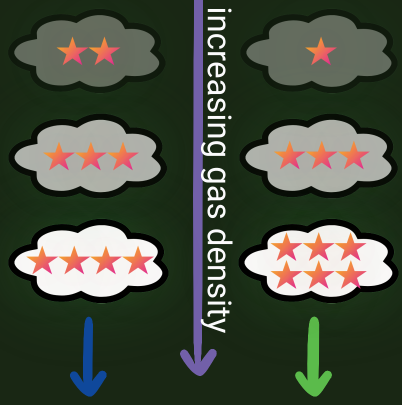

SK slope N = 1	SK slope N = 1.5

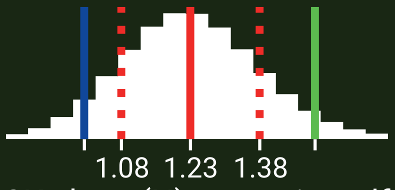

SK slope (N): posterior pdf

- DSFGs may **quench faster** than predicted by unresolved studies [3].
- N>1 claim is extended to a **sample**; beyond individual sources [e.g. 4-6].
- Scenario is consistent with **turbulence** dominating ISM regulation [2, 7].
- Compared to local galaxies, star formation resembles **merging LIRGs**, but differs from isolated LIRGs and main-sequence (N=1) [8-10].
- This is the first large sample to **benchmark** conflicting simulations.
- Exciting **opportunities** of improvement come from deeper observations of a single CO transition, as well as JWST-based metallicity constraints.

References: [1] Lagos et al. 2025, arXiv:2512.11309 ; [2] Kraljic et al. 2024, A&A, 682, A50 ; [3] Hagimoto et al. 2023, MNRAS, 521, 5508 ; [4] Hodge et al. 2015, ApJL, 798, L18 ; [5] Chen et al. 2017, ApJ, 846, 108 ; [6] Gómez et al. 2025, A&A, 704, A178 ; [7] Salim et al. 2015, ApJ, 806, L36 ; [8] Sánchez-García et al. 2026, A&A, 707, A144 ; [9] Pessa et al. 2021, A&A, 650, A134 ; [10] Sun et al. 2023, ApJL, 945, L19.

JWST MIRI-MRS Mapping of the Nucleus of the Nearby Starburst Galaxy NGC 253

Utsav Siwakoti[1], Elisabeth Mills[1], Ashley Lieber[1], Kaitlyn Sheriff[1] Rebecca Levy[2], Alberto Bolatto[3], Sara Duval[4]
[1]University of Kansas, [2]Space Telescope Science Institute, [3]University of Maryland, [4]University of Toledo

NGC 253 is a nearby (d=3.5 Mpc) nuclear starburst. Within the starburst, 14 massive (~10^5 to 10^6) $M_\odot$ candidate embedded clusters have been identified with ALMA. Using JWST MIRI-MRS, we map the central 250 pc of NGC 253 to study the gas kinematics, dust, and radiation field of the nuclear starburst.

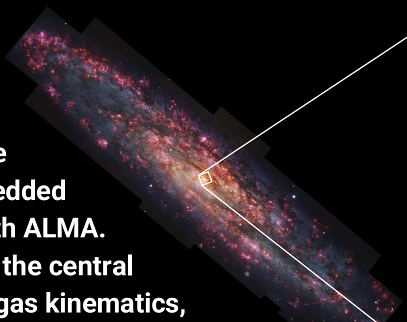

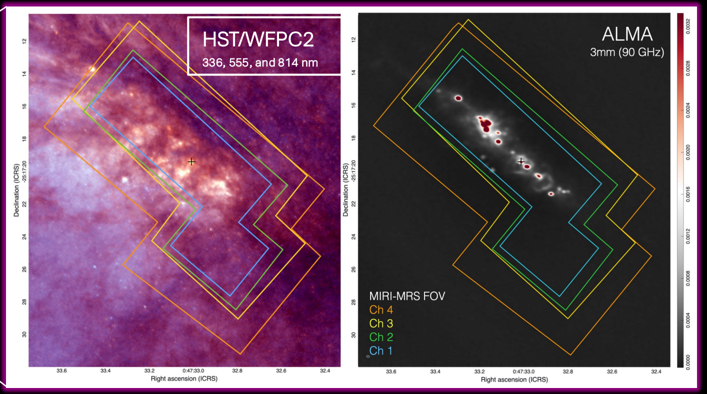

Only 5/14 embedded clusters seen with ALMA are detected with JWST MIRI-MRS

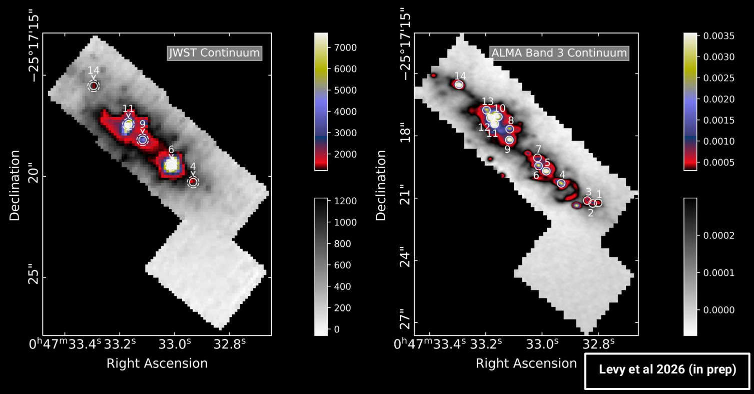

Levy et al 2026 (in prep)

Even with the sensitivity of JWST, mid-infrared observations are insufficient to see through the compact dense dust and gas clumps in which the youngest clusters are embedded. We estimate a total ionizing photon rate $Q_0 = 2.764 \times 10^{53}\ s^{-1}$ for the starburst using the emission from the H5α line. This is 82.5% of the total estimated ionizing photon rate measured from radio recombination lines by Bendo et al. (2015) that are insensitive to extinction. This indicates that even though many individual clusters are obscured, the majority of the starburst activity is still recovered by JWST.

Warm H2 is not detected toward any of the clusters

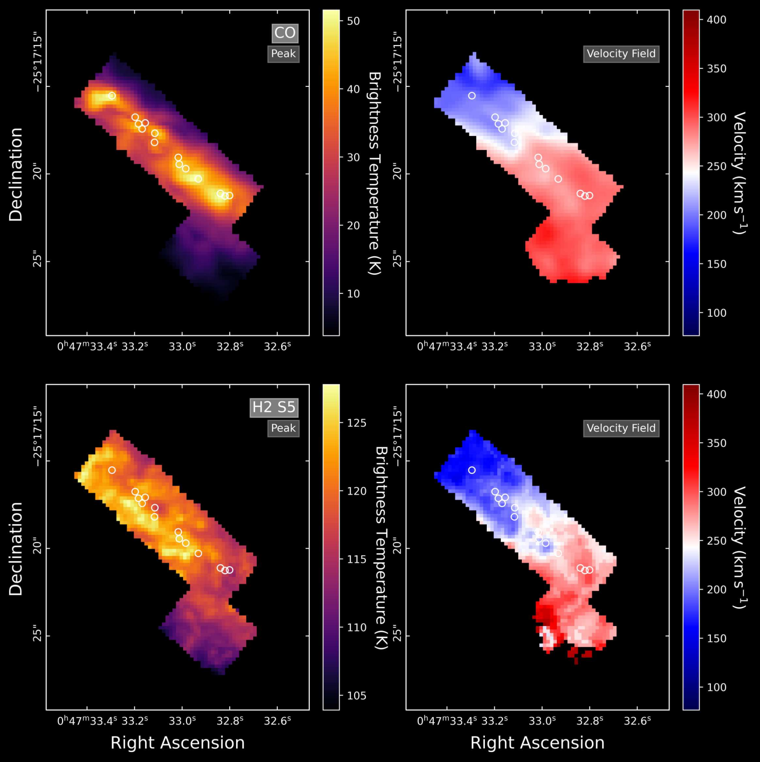

Compared to our ALMA CO observations, the H_2 emission primarily arises in the southern (lower) part of the central disk. H_2 is also not detected toward individual clusters, suggesting the difference between the appearance of these tracers is due to extinction.

Measured A_V values range from 12 to 240 magnitudes

Using PAHfit, we map extinction using the 9.7 micron silicate feature. Adopting an extinction law from Fritz et al. (2011), we measure a median A_V of 50 mag, with values ranging between 12-240 mag. However, as 9/14 clusters are not detected, the true extinctions are likely significantly higher toward the most embedded sources

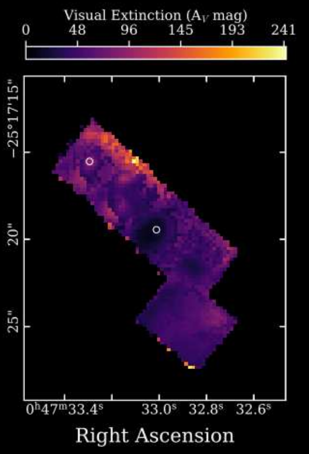

We find no evidence of AGN activity

Our measured mean [NeIII]/[NeII] ratio of 0.13 is consistent with a pure starburst origin for the ionized gas emission. AGN typically have ratios > 0.4, while the highest measured ratio in NGC 253 is <0.3. We thus are still unable to pinpoint the location of the central black hole.

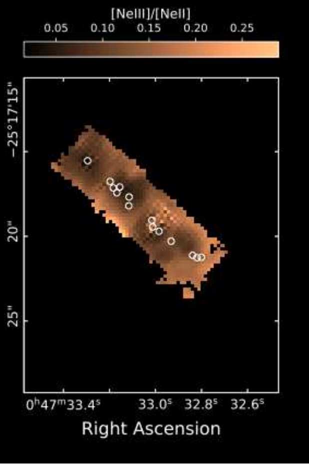

Unveiling the Magnetic Field Morphology in a bright, isolated region of HMSF

Analysis of the influence and importance of the B-field in AFGL961 using JCMT

Ben Wakefield, Kate Pattle, Janik Karoly
benjamin.wakefield.25@ucl.ac.uk

HMSF in AFGL961

- AFGL961 is a high-mass star forming clump in the Rosette Molecular Cloud[1].
- Consists of 5 YSOs.
- B type star drives a **compact HII region**.
- Class 0 protostar drives a **molecular outflow**.
- A **bright, compact and isolated** source, at a distance of ~1.6 kpc. An **ideal testbed** for probing B-field + stellar feedback influence on HMSF.

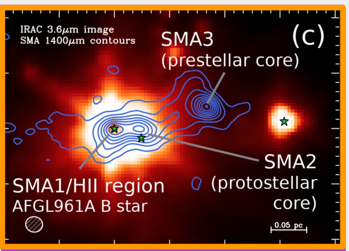

Figure 1: *IRAC image and SMA contours of AFGL961[2].*

A dynamically important B-field?

- Our JCMT observations show field structure at clump-scale (Fig. 2). Reveals **ordered B-field.**
  - Dispersion in position angle calculated via structure function[3] and unsharp masking[4]:

$$\sigma_\theta \sim 4.5 \pm 1.0\,°$$

  - Modified-classical DCF method used to calculate plane-of-sky B-field strength[5,6,7]:

$$B_{POS} \sim 370 \pm 190\ \mu G$$

  - λ relates B-field and gravity influence:

$$\lambda \sim 0.48 \pm 0.25$$

  - Approx. energies calculated for HMSF regulation contributors (10^{45} ergs):

E_B	E_G^{uni*}	$E_G^{gauss**}$	E_K^{th}	$E_K^{non\text{-}th}$
1.6	1.0	0.49	0.12	0.68

* Uniform density sphere ** Gaussian density sphere

Magnetically regulated HMSF: a nuanced perspective

- Magnetic field **energetically important** (but DCF can overestimate B-field strength).
- HMSF is underway—gravity dominates now, but B-field played **important evolutionary role.**
- Pillar-like streams align with the Planck cloud-scale field, but field threading SF clump is **strongly misaligned.**

Results expected? Partially...

- B-field and gravitational energy approx. balanced—**reasonable** for active SF regions.
- B-field low angular dispersion despite presence of turbulent HII region and outflow—**interesting...**

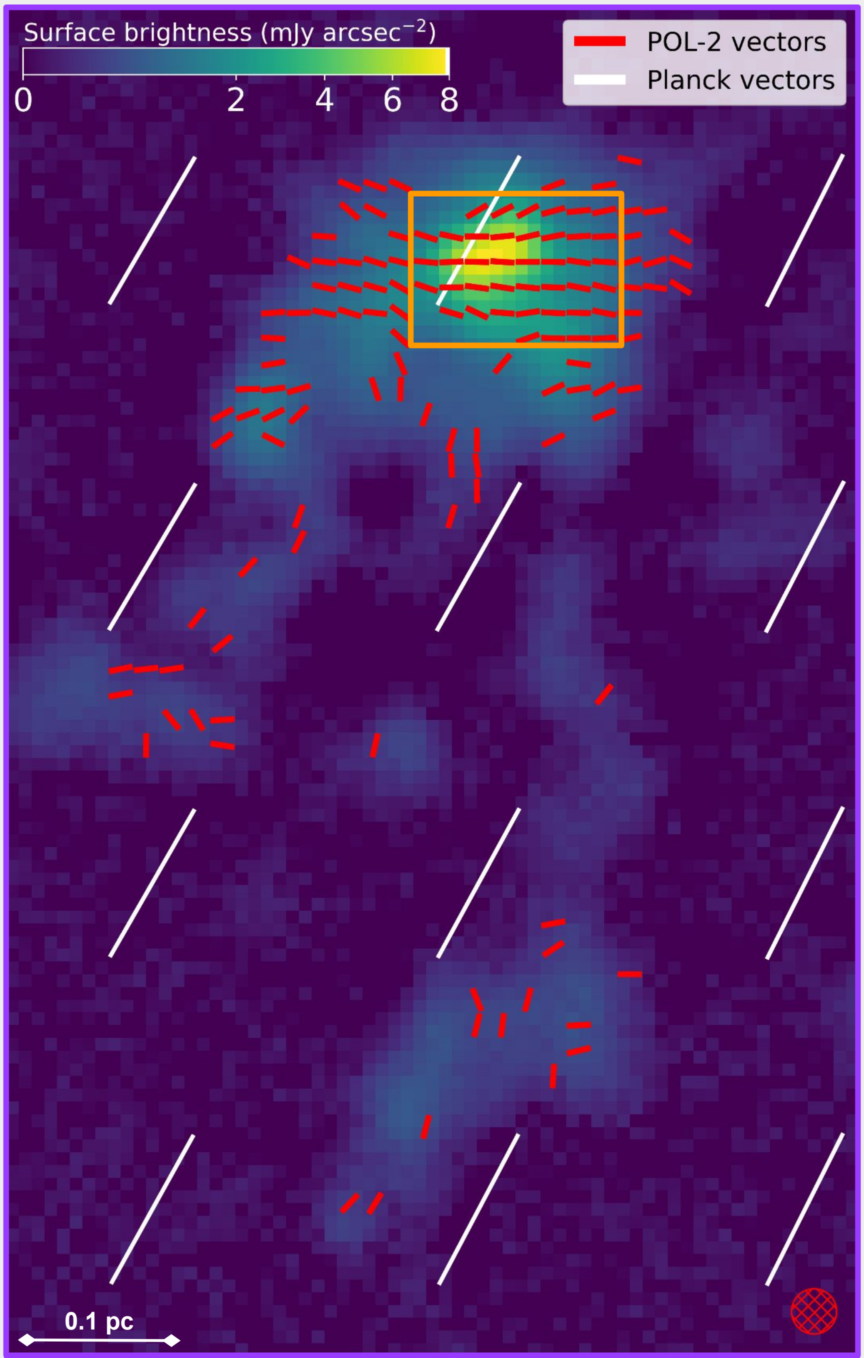

Figure 2: *POL-2 Stokes I map of AFGL961. Red vectors represent orientation of measured polarization vectors rotated by 90° to show B-field direction, binned to 8", and pass a S/N cut of I/δI > 5.0 and p/δp > 3.0 The JCMT beam size is displayed by the red hatched circle. Planck polarization vectors rotated by 90° are represented in white.*

Future work

- Full B-field morphological and energetic analysis (Wakefield et al., in prep).
- Kinematics analysis via JCMT HARP spectra of N2H+ (Fig 3), HCO+, H13CO+, and archival CO (Wakefield et al., in prep).

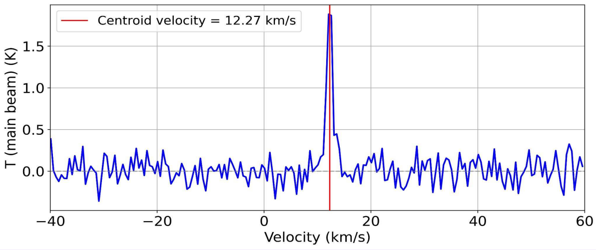

Figure 3: *N2H+ (4-3) spectrum at brightest pixel, via HARP.*

References

1. Cohen 1973. ApJ, 185, L75
2. Williams et al. 2009. ApJ, 699, 1300
3. Hildebrand et al. 2009. ApJ, 696, 567
4. Pattle et al. 2017. ApJ, 846, 122
5. Chandrasekhar & Fermi 1953. ApJ, 118, 1137
6. Ostriker et al. 2001. IOP, 546, 980
7. Cho & Yoo 2016. ApJ, 821, 21

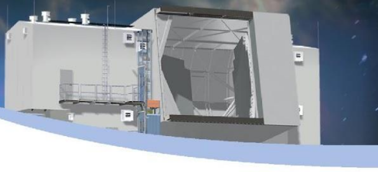

Hot core chemistry in the outer Galaxy: impact of metallicity on the formation of COMs

Youxin Wang[1], Arnaud Belloche[1], Robin T. Garrod[2] ([1]MPIfR, [2]University of Virginia)

I. Motivation

Complex organic molecules (COMs): with 6 atoms or more, many of them are believed to form on the surfaces of dust grains or in their ice mantles
Hot core: compact (<0.1 pc), high density (>10^6 cm^{-3}), high temperature (150-250 K), and rich spectrum with many COM lines, **perfect for studying interstellar chemistry**
Outer galaxy: low metallicity and dust-to-gas ratio

→has metallicity an impact on the growth of molecular complexity in the ISM?

II. Search for hot cores in the outer Galaxy

only two hot cores known in the outer Galaxy so far (WB89-789 & Sh 2-283-1a, Shimonishi et al. 2021, Ikeda et al. 2026). **Our strategy:**

- ☐ **Single-dish observations of 19 sources associated with H_2O or class II CH_3OH masers**
  ⇒ **4 hot core candidates identified**
- ☐ **Follow-up observations at high angular resolution with NOEMA of 3 sources**
  215.1-246.4 GHz; ~ 0.8" (5000 au); ~ 0.7 km s^{-1}
- ☐ **First results: G135.27-2.79** (D_{gc} = 13.1 kpc, $Z \sim 0.5\ Z_\odot$) , *accepted by A&A*

III. Continuum morphology

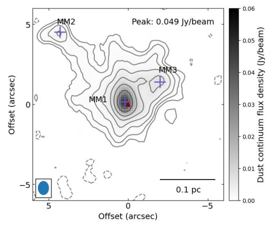

three dust continuum sources

IV. Outflows

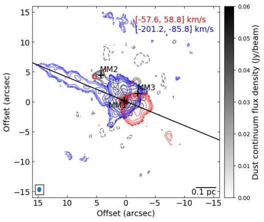

MM1 drives **a bipolar outflow** traced by ^{12}CO

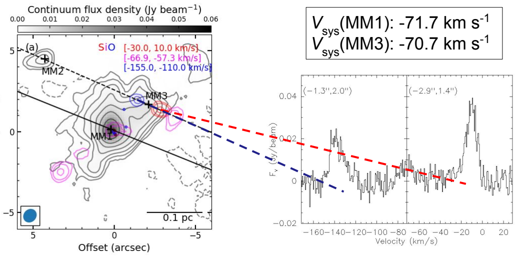

V_{sys}(MM1): -71.7 km s^{-1}
V_{sys}(MM3): -70.7 km s^{-1}

SiO extremely high-velocity (EHV) outflow, associated with MM3

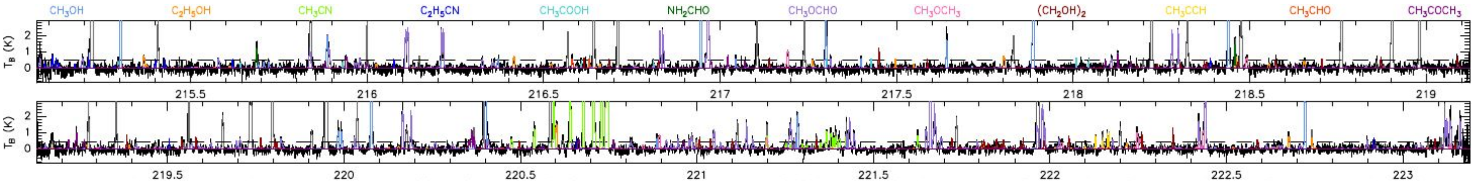

12 COMs identified, tracing high temperatures (T_{rot} > 100 K) → *a new hot core in the outer Galaxy*

Portion of the NOEMA spectrum of MM1, with LTE model overlaid

V. Comparison to astrochemical model predictions

Three-phase hot core chemical model **MAGIKCAL** (Garrod et al. 2022);
Predictions of the astrochemical model: ratios of the predicted abundances (relative to methanol) between low-Z and normal-Z conditions:

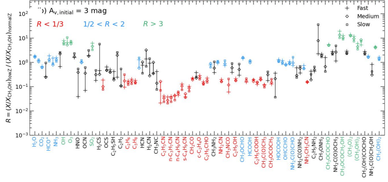

Blue: molecules with similar sensitivity to Z and dust-to-gas ratio as CH_3OH
Red: molecules more sensitive than CH_3OH
Green: molecules less sensitive than CH_3OH, or even enhanced

. Lower dust-to-gas ratio → slower adsorption onto grains → more efficient gas-phase conversion of available carbon to CO → reduced CH_4 abundance on the grains, further enhanced by lower C:O ratio
. Reduced CH_4 abundance → reduced abundance of hydrocarbon species as well as larger N-bearing species while CO and related O-bearing species are less affected
. Slower adsorption → lower CO ice coverage → favors conversion to COMs of increasing degrees of saturation

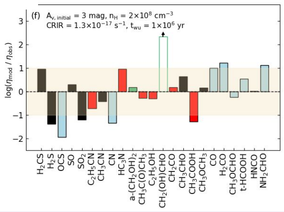

approximate agreement between composition of MM1 and predictions of model with reduced *Z* and dust-to-gas ratio

VI. Comparison to other galactic hot cores

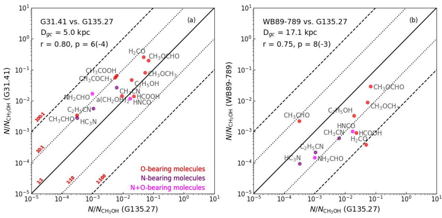

Good correlation of COM abundances (relative to CH_3OH) between G135.27 and both G31.41 and WB89-789;

COM abundances (relative to CH_3OH) of G135.27 **between** G135.27 and both inner-galaxy hot core G31.41 and far-outer-galaxy hot core WB89-789

VII. G135.27/G31.41 observational ratios vs. lower-Z/normal-Z model predictions

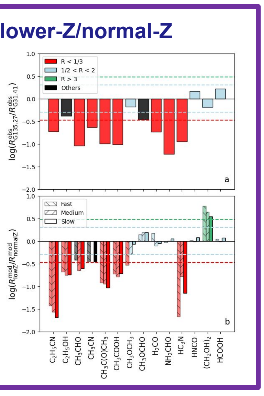

panel **a**: **observed ratios** between G135.27 and G31.41
panel **b**: **ratios of model predictions** under sub-solar (~0.5 $Z_\odot$) and solar metallicity conditions

→most COMs agree well with predictions, but some molecules ($CH_2(OH)CHO$, a-$(CH_2OH)_2$, CH_3OCHO, and NH_2CHO) show discrepancies, their chemical networks require more attention

Conclusion: G135.27 is a new hot core in the outer Galaxy. Comparisons to other galactic hot cores and astrochemical model predictions suggest that metallicity and dust-to-gas ratio have an impact on the formation of COMs.

Outlook: extension of analysis to sample of six sources (our 4 NOEMA sources + WB89-789 + Sh 2-283-1a) will yield more robust understanding of COM formation under low-metallicity conditions.

Universität zu Köln · ph1 Universität zu Köln · rrzk · UNIVERSITÄT BONN · Argelander-Institut für Astronomie · Max-Planck-Institut für Radioastronomie · JÜLICH Forschungszentrum

KATE WHITAKER · University of Massachusetts Amherst · Cosmic Dawn Center

Discovering *globular clusters*
when the Universe was a few billion years old.

Globular clusters are a fossil record of how their host galaxies formed. In already-quiescent galaxies, where star formation has shut off, they are the freshest, most direct probe of the formation epoch of the most massive systems. JWST now identifies individual GC candidates in two strongly-lensed quiescent galaxies at z = 1.95 and 2.53, opening the first direct view of cluster populations in the era when these galaxies were still being assembled and beginning to quench.

redshifts of 2 & 2.5
pushing individual detections into epoch of GC formation

~10 Myr – 2 Gyr ages
youngest caught at formation, oldest already evolved

up to 150× magnification
lensing magnification reaches down to 10 pc scales

NO. 01 · FORMATION

Uncovering the formation history of *the Relic*

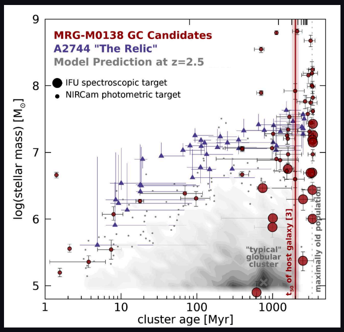

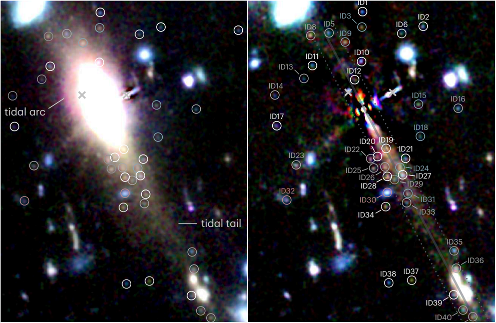

Distant globular clusters as probes of formation pathways and early properties.

The Relic hosts over a dozen nascent GC candidates, already gravitationally bound and consistent with the most massive clusters predicted by models, with NIRSpec/IFU spectra (JWST-GO-6405) catching one in formation at just 7 Myr. As an elliptical with high GC specific frequencies, it offers a key laboratory for early cluster formation.

Whitaker et al. (2026, ApJ,1001,107; left/middle), Cutler et al. (in prep, right)

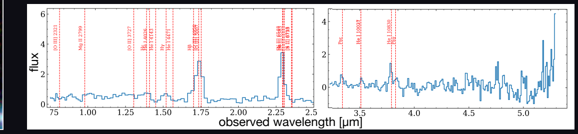

NO. 02 · DISCOVERY

Remarkable clusters in *MRG-M0138*

Globular cluster candidates up to 150× magnified in a quiescent galaxy at z = 1.95.

MRG-M0138 represents a truly exceptional system: its extreme magnification provides a unique window into the low-mass end of the GC population at cosmic noon, reaching regimes in mass, age, and spatial resolution that have been entirely inaccessible until now. It offers a rare, and likely singular, opportunity to obtain direct spectroscopic constraints on typical globular clusters at high redshift.

A photometric analysis of the GC population using archival 6-band JWST imaging is ongoing, and will be expanded through a JWST Cycle 5 program adding deep F090W/F360M imaging and an ultra-deep NIRSpec/IFU (prism) pointing (JWST-GO-11883, PI: Whitaker/Matthews; see Figure to right).

Matthews, Whitaker et al. (in prep)

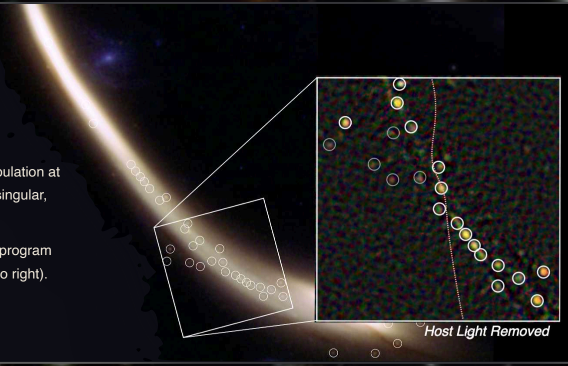

NO. 03 · SYNTHESIS

Towards a global picture of *quenching.*

Annual Review of Astronomy & Astrophysics:
The Quenching of Star Formation in Massive Galaxies
Whitaker & Bezanson (ARAA, 2026)

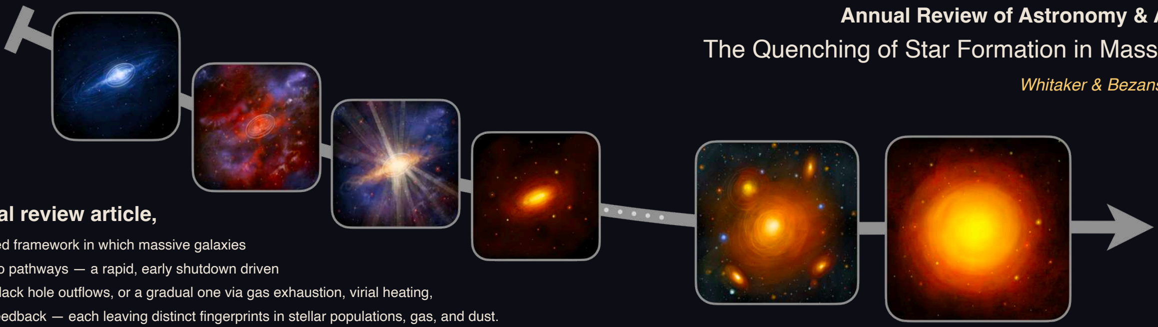

In this annual review article,

we develop a unified framework in which massive galaxies quench through two pathways — a rapid, early shutdown driven by supermassive black hole outflows, or a gradual one via gas exhaustion, virial heating, and preventative feedback — each leaving distinct fingerprints in stellar populations, gas, and dust.

kwhitaker@astro.umass.edu

ON THE RELATION BETWEEN MAGNETIC FIELD STRENGTH AND GAS DENSITY IN THE INTERSTELLAR MEDIUM. II. DENSITY UNCERTAINTIES AND DIFFUSE GAS CONSTRAINTS

David Whitworth, Amit Seta, Ralph E. Pudritz, Mordecai-Mark Mac Low, Juan D. Soler, Aina Palau, Ralf S. Klessen

The relationship between magnetic field strength and gas density is essential to understand the interstellar medium and star formation. Recently generalized as a two-part power-law with non-zero slopes. We have extended our previous hierarchical Bayesian framework by incorporating a large body of pulsar observations that probe the diffuse interstellar medium. Our results confirm a non-zero exponent in the diffuse gas as well as a broad transition density:

$\boldsymbol{\alpha_1 = 0.18^{+0.02-0.02}}$, $\boldsymbol{\alpha_2 = 0.63^{+0.08-0.05}}$, $\boldsymbol{n_0 = 1630^{+2560-1430}}$ **cm**$^{-3}$**, and** $\boldsymbol{B_0 = 7.60^{+2.00-3.47}}$ **μG**

Extended data sets: pulsars

- DS1: Original Zeeman data
- DS2: Original Zeeman data with outlier removed
- DS3: Expanded Zeeman (Hwang et al. 2024) and pulsar data (Seta & McClure-Griffiths 2025)
- DS4: Expanded Zeeman and pulsar data with out-lier removed

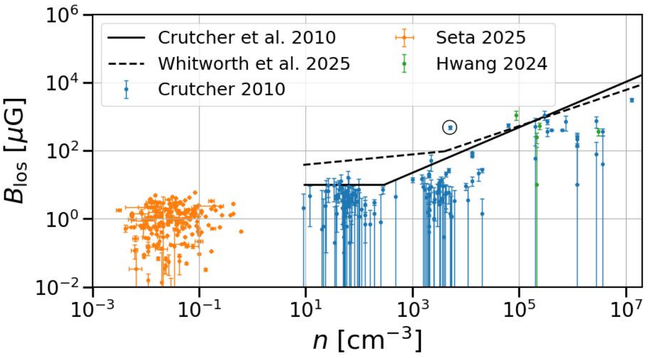

Distribution of observations

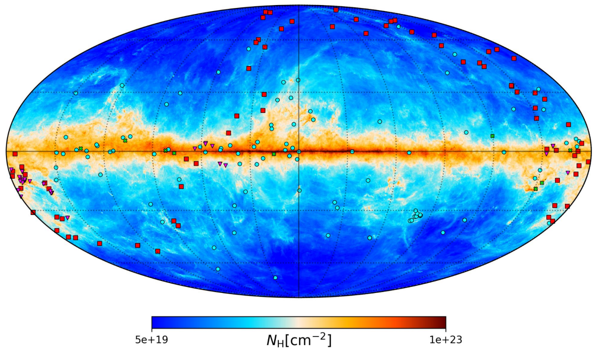

Observational positions overlaid on a Planck Map (Planck Collaboration et al. 2016, 2020). Pulsars (Seta & McClure-Griffiths (2025)) are cyan circles. OH Zeeman measurements (Troland & Crutcher (2008)) are magenta triangles. CN Zeeman measurements (Falgarone et al. (2008)) are cyan crosses. HI Zeeman measurements (Heiles & Troland (2004)) are red squares.

Hierarchical Bayesian Analysis

We developed four models, running each dataset on each model. Priors & hyperpriors are in log space. The parameters are: the two slopes (α_1, α_2), the break density (n_0) & field strength (B_0), the intrinsic scatter on n (R_n) & B (σ_B), and the envelope scaling factors (f_B, $f_{B,1}$, $f_{B,2}$)

- Model A - Free density error R_n
- Model B - Fixed density error R_n
- Model C - Two-envelope model with free density correction
- Model D - Two-envelope model with reported pulsar density errors

Zeeman Sensitivity

We removed 41 (~⅓ of all) Zeeman data below a S/N of 3μG (Troland & Crutcher 2008). The Bayesian produced bimodality in the corner plots even though the form of the relationship remained the same. A more complete examination requires a more detailed model.

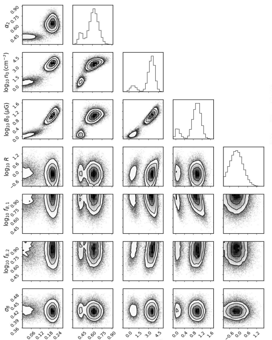

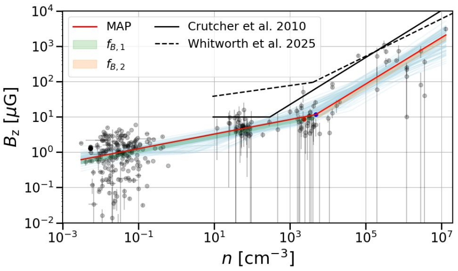

α_1	α_2	n_0 (10^3cm^{-3})	B_0(μG)	$f_{B,1}$	$f_{B,2}$	σ_B	R_n
$0.21^{+0.02}_{-0.03}$	$0.66^{+0.06}_{-0.12}$	$4.83^{+0.66}_{-4.83}$	$11.63^{+2.52}_{-6.81}$	$0.78^{+0.22}_{-0.05}$	$0.75^{+0.25}_{-0.02}$	$0.42^{+0.02}_{-0.02}$	$1.18^{+0.02}_{-1.08}$

Conclusions

- The inclusion of the pulsar data, **DS4**, in **Model D** yields the most robust B–n relation:

  $\boldsymbol{\alpha_1 = 0.18^{+0.02-0.02}}$, $\boldsymbol{\alpha_2 = 0.63^{+0.08-0.05}}$,
  $\boldsymbol{n_0 = 1630^{+2560-1430}}$ **cm**$^{-3}$, $\boldsymbol{B_0 = 7.60^{+2.00-3.47}}$ **μG**,
  $\boldsymbol{f_{B,1} = 0.80^{+0.20\,-0.02}}$, $\boldsymbol{f_{B,2} = 0.75^{+0.23-0.00}}$,
  $\boldsymbol{\sigma_B = 0.42^{+0.02\,-0.02}}$, $\boldsymbol{R_n = 0.55^{+0.59-0.45}}$

- The large variance in n_0 suggests that the transition between diffuse and dense gas likely occurs over a range of densities.
- Fixing the intrinsic scatter R_n leads to larger n_0 and B_0

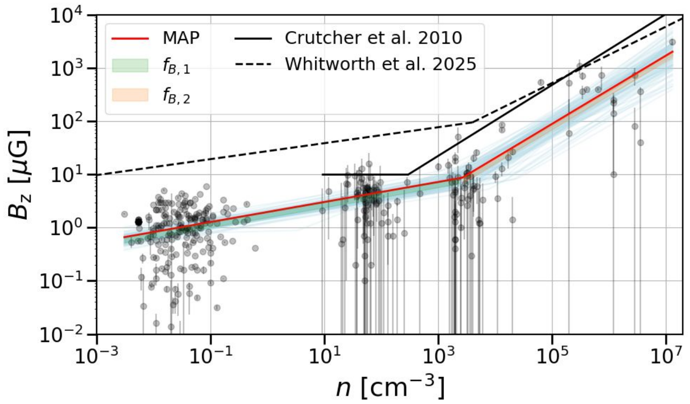

Fractal Dimension of the Eos Molecular Cloud

Victoria Williamson[1], Blakesley Burkhart[1,2]

[1]Department of Physics and Astronomy, Rutgers University

[2]Center for Computational Astrophysics, Flatiron Institute

Eos and its Tracers

At just 94 parsecs from the Sun, Eos is the closest dark molecular cloud [1]. It holds significant quantities of molecular gas but low CO abundance made it "dark" and hidden. Eos was the first molecular cloud ever to be identified using H_2 far-UV fluorescent line emission, which traces gas at the boundary layers of star-forming and supernova remnant regions. Although Eos likely does not form stars, its proximity makes it incredibly accessible for studying cloud evolution [2].

Due to its "dark" nature, we use a variety of tracers other than CO to identify structure and processes throughout the cloud. UV H_2, used to identify the cloud, is the primary tracer of Eos, highlighting the boundary of the cloud, where H_2 has been excited due to UV radiation from stars hitting the gas. Dust extinction and emission reveal the total column density of the cloud, with extinction tracing ISM dust where background starlight is blocked in lower density areas, while emission maps high-density, cold regions. Full HI, from both the GALFA and HI4PI surveys, traces the column density of HI only. The full HI HI4PI data has been decomposed into thermal phases, the Cold Neutral Medium (CNM) and the Warm Neutral Medium (WNM) [3]. CNM, at 100 K, is denser and tends to clump around boundaries, while WNM, at 8000 K, is more diffuse and space-filling around the denser cloud.

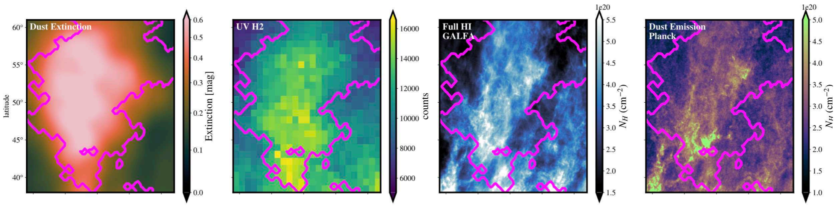

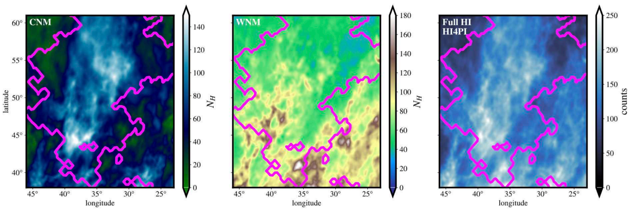

Results

The slopes reveal the measured fractal dimension to be approximately 3 for each tracer. CNM and UV H_2 sharing this dimension ~3 suggests they are tracing the same underlying field, consistent with a volume-filling geometry rather than shielded structure. This is expected for Eos with such little CO. Predictions for systems with lower Damköhler numbers, where chemical reactions occur faster than eddy turnover times, find the fractal dimension to be 8/3 [5]. We find that WNM has γ ~ 2.73, consistent to the predicted value, implying that the warmer, more diffuse medium of the WNM is less fractal than the CNM it surrounds because chemical processes dominate over turbulence. The tracers of full HI in Eos, the GALFA survey, at a resolution of 4 arcmin/pix, and the HI4PI survey, at a resolution of 6.9 arcmin/pix, have nearly identical fractal dimension, 3.02 and 3.03. This suggests that resolution does not have significant effects on the wavelet power spectrum, at least for smaller spectral resolution differences. PPV decomposition of GALFA full HI shows the slope converges to the integrated value at low velocity thickness, suggesting fractal dimension dominated by density rather than velocity fluctuations.

Fractal Dimension

Fractal dimension quantifies how "complex" or "space-filling" a structure is across all scales. To recover the true geometry of 3D clouds seen as 2D projected images, projection in a wavelet basis is the simplest approach [4]. Box-counting techniques fail to recover the fractal signal when projected and Fourier methods become contaminated by aliasing effects. The wavelet power spectrum of a projected γ-dimensional measure scales as $P_j \propto 2^{-j\gamma}$, which holds regardless of embedded dimension, N, or projected dimension, D. From this relation, the true fractal dimension is recovered directly from the slope of the wavelet power spectrum of a projected image. Dimensionality of a molecular cloud indicates the underlying physics, whether it be dominated by turbulent or chemical processes.

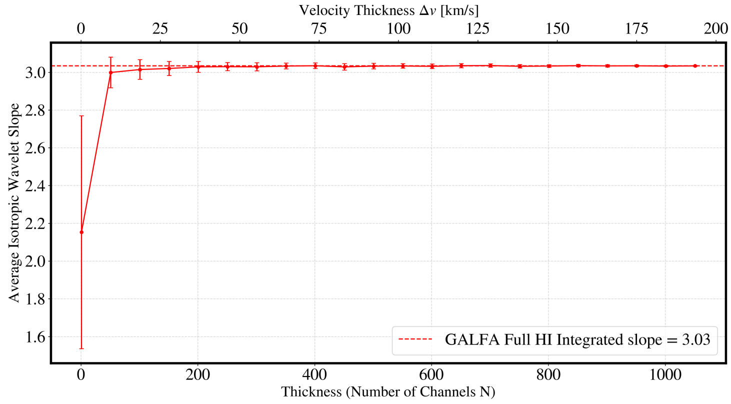

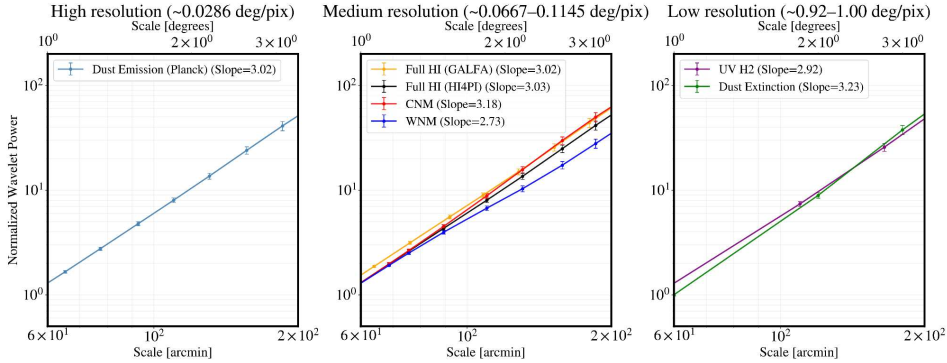

Future Works

To strengthen this work, the next step is to compare our results to high resolution simulation studies. We predict that thermal instability will steepen from 8/3 toward 3, as power is added at intermediate scales through isobaric condensation. Although there are several works on this using the power spectrum, there are none for wavelets thus far. The work presented has assumed isotropy, however, our preliminary studies have revealed different fractal dimensions in different directions. This could be due to MHD turbulence being anisotropic in the presence of a large scale magnetic field; further study is needed to confirm these trends and the underlying reasons.

References

1. Burkhart et al. *Nat. Astron.* **2025**, 9, 1064. https://doi.org/10.1038/s41550-025-02541-7
2. Saxena et al. *MNRAS Lett.* **2025**, 540, L109. https://doi.org/10.1093/mnrasl/slaf044
3. Marchal et al. *Astron. Astrophys.* **2019**, 626, A101. https://doi.org/10.1051/0004-6361/201935335
4. Mayboroda & Spergel. *ArXiv.* **2025**, 2503.23202. https://doi.org/10.48550/arXiv.2503.23202
5. Chatakonda et al. *Combust. Flame* **2013**, 160, 2422. https://doi.org/10.1016/j.combustflame.2013.05.007

Dust Extinction Properties in Nearby Galaxies

Petia Yanchulova Merica-Jones *
Institute of Astronomy, Bulgaria
National Astronomical Observatory Rozhen

Bulgarian Academy of Sciences

Fulbright Bulgaria

Publications

* A large portion of this work was performed at the Space Telescope Science Institute and also as a Fulbright U.S. Scholar at Sofia University *

Introduction

Photometric surveys of nearby galaxies are transforming our understanding of galactic properties on small scales through rich multi-band observations of spatially-resolved stars.

We complement these with **UV spectroscopic measurements** (HST STIS) to see what drives **dust extinction properties**.

We examine:

- **Extinction curve variations** in the Local Group with ISM environment.
- **Stellar**, **dust**, & **3D properties** for millions of stars at a time.
- **How the ISM influences dust grain properties and dust extinction**.

A wealth of data

- **HST UV Spectra: SMC, M31, M33** (PIs Yanchulova, G.Clayton, K.Gordon, E.Fitzpatrick, D. Massa, M. Decleir).
- **HST Multiband SMC+LMC Photometry** - **Scylla Survey** (PI C. Murray)
- **SMIDGE Survey** (PI K. Sandstrom) SMC (Yanchulova M-J+ '17, '21, '25)

Photometric and spectroscopic observations together probe a variety of ISM conditions

We fit the **photometric SED** of millions of stars with the BEAST tool (Gordon+ '16) to constrain:

Dust properties:

- A(V), R(V), f_A (MW+SMC mixture)

Stellar properties:

- Distance, Age, IMF, Metallicity

Credit: NASA/CXO/JPL-Caltech/STScI

The N13 nebula in the Small Magellanic Cloud SMIDGE SW Bar region:

- **Chandra X-ray** (purple)
- **HST** (red, green, blue), F336W, F475W, F814W.
- **Spitzer IRAC** (red)

Complex 3D geometry requires distance modeling

Scylla & SMIDGE **dust extinction maps**:
Some fields show a clear correlation with **dust mass surface density, Σ_{DUST}, the dust IR emission, and/or CO**. Others do not!

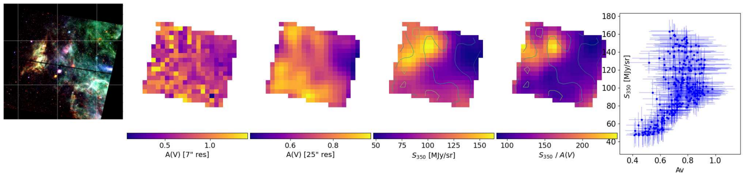

The **IR/A(V) ratio** traces **how much infrared dust emission** is produced **per unit stellar extinction**, combining dust column, dust heating, grain emissivity, and line-of-sight geometry.

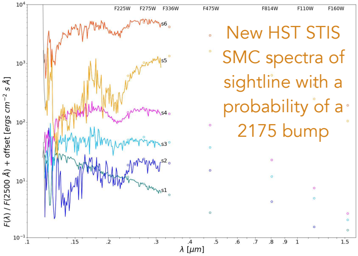

Work-in-progress:
The average SMC extinction curve does not show a 2175A bump.
We targeted with HST STIS **lines of sight with a high probability of a bump** to see what **ISM conditions** lead to the 2175A spectral feature.

We made the **first measurements of M33 extinction curves** & compiled the **most complete set of** SMC, M31 & M33 **extinction curves.**

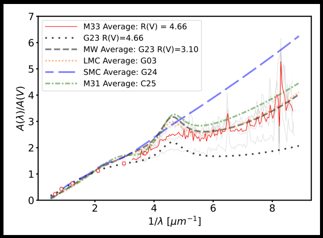

Gordon+ '26, Clayton+ '25

M31: **Wide sightline-to-sightline variation** and no clear radial metallicity trend. Therefore, **local conditions**, not global galaxy metallicity, mainly **shape dust properties**.

M33: **Large variations** in the **2175 Å bump** and **UV slope**, therefore **gas-to-dust ratio** and **local environment drive dust extinction** more than global metallicity.

Gordon+ '26, Clayton+ '25

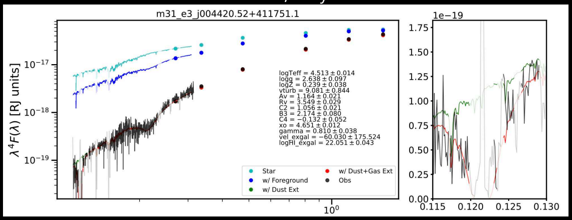

References:

Yanchulova M-J+'17, '21, '25; K. Gordon+26; G. Clayton+25; C.Murray+24; R. Cohen+24, C. Lindberg+25,26;Gordon+16; Clayton+15; Gordon+03; Fitzpatrick 99

Spectuner-D1: Spectral Line Fitting of Interstellar Molecules Using Deep Reinforcement Learning

Yisheng Qiu[1], Tianwei Zhang[1], Tie Liu[2], Fengyao Zhu[1], Dezhao Meng[2,3,4], Huaxi Chen[1], Thomas Möller[5], Peter Schilke[5], Donghui Quan[1,6]

[1]Zhejiang Lab, [2]Shanghai Observatory, [3]Xinjiang Observatory, [4]Uni. of Chinese Academy of Sciences, [5]Cologne Uni., [6]Xi'an Jiaotong-Liverpool Uni.

Abstract: We introduce a novel deep reinforcement learning framework to automate molecular line fitting in the massive (sub-) millimeter wavelength data. Using observational data from ALMA, we train a transformer-based neural network that maps both molecular spectroscopic data and observed spectra to physical parameters such as excitation temperature and column density. Our method achieves fitting results consistent with global optimization with multiple runs, while reducing the number of forward modeling runs by an order of magnitude. It is proved to be efficient and accurate in the pixel-level fitting of multiple molecules.

Peak-matching Loss Function

$$\mathcal{L}_{\mathrm{PM}} = \mathcal{L}_{\mathrm{MAE}} + \sum_{\mathrm{TPPs}} \mathcal{L}_{\mathrm{TP}} + \sum_{\mathrm{FPPs}} \mathcal{L}_{\mathrm{FP}}$$

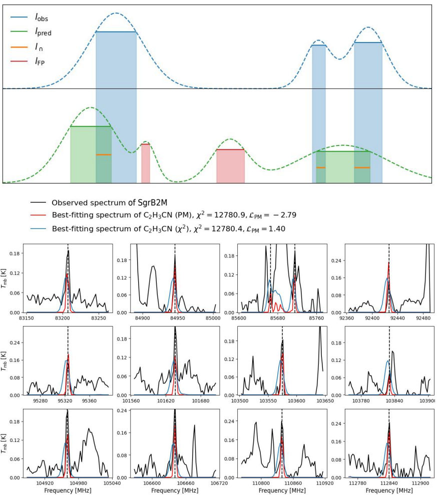

Fig. 1: Upper panel: Schematics of the true peak (TP) and false peak (FP) in our peak-matching loss funstion (L_{PM}). L_{MAE} is the linear absolute difference of the real spectrum (I_{obs}) and the predicted one (I_{pred}). L_{TP} measures the overlap of TP and I_{obs}. L_{FP} will add penalty to the loss function if there is no overlap of FP and I_{obs}. Lower panel: Comparison of the best-fitting spectra using different loss functions. Using χ^2 loss often results in overly broad linewidths with insufficient intensities. The PM loss can distinguish good and poor fits even when the χ^2 loss values are comparable.

(Qiu et al. 2025, ApJS, 277, 21)

Network Architecture

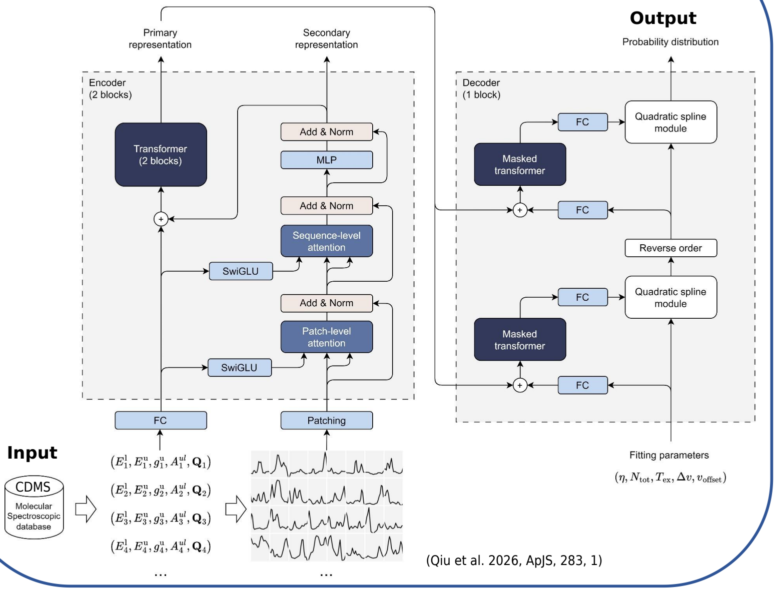

(Qiu et al. 2026, ApJS, 283, 1)

Training and Testing Data

Dataset	ALMA project ID	Beam ($''$)	Freq. range (GHz)	Freq. coverage[a] (GHz)	δf[b] (kHz)	$\langle\sigma^{\mathrm{global}}_{\mathrm{RMS}}\rangle$[c] (K)	N_{fit}[d]
Training							
ATOMS-80-band3-2as	2019.1.00685.S	1.3 - 2.7	97.57 - 101.39	3.74	488	0.129	67098
IRAS16293-A-band6-0.5as	2012.1.00712.S	0.5	231.01 - 250.72	1.81	122	0.250	5721
IRAS16293-B-band6-0.5as	2012.1.00712.S	0.5	231.01 - 250.72	1.81	122	0.250	9350
IRAS16293-A-band7-0.4as	2018.1.01496.S	0.4	281.68 - 283.88	0.94	244	1.652	5144
IRAS16293-B-band7-0.4as	2018.1.01496.S	0.4	281.68 - 283.88	0.94	244	1.652	4820
IRAS16293-A-band7-0.5as	2021.1.01164.S	0.5	232.05 - 240.80	8.74	122	1.024	9350
IRAS16293-B-band7-0.5as	2021.1.01164.S	0.5	232.05 - 240.80	8.74	122	1.024	13403
IRAS16293-band6-5.9as	2017.1.00108.S	5.9	232.06 - 233.93	1.87	488	0.011	5611
G327-band6-0.1as	2022.1.01354.S	0.1	216.70 - 236.07	7.50	977	1.864	11766
G327-band6-1.9as	2016.1.00168.S	1.9	215.56 - 231.32	5.12	488,977	0.048	5702
G327-band7-1.1as	2024.1.00653.S	1.1	279.44 - 294.37	5.84	122,977	0.327	9462
Testing							
ATOMS-20-band3-2as	2019.1.00685.S	1.3 - 2.7	97.57 - 101.39	3.74	488	0.129	16240
IRAS16293-A-band3-1.0as	2015.1.01193.S	1.0	86.58 - 101.57	1.64	244	0.399	3704
IRAS16293-B-band3-1.0as	2015.1.01193.S	1.0	86.58 - 101.57	1.64	244	0.399	4755
Orion KL-band6-4.9as	-	4.9	221.15 - 233.42	4.46	880,921	0.080	8044

NOTE—[a]The frequency coverage is derived by summing the bandwidth of all spectral windows.
[b]This is the resolution of frequency channels.
[c]The estimation of the global RMS noise is introduced in Section 2.4.1. The average is taken over all spectral windows.
[d]This is the number of fitting results for evaluation as described in Section 2.7.

Comparing Fitting Results

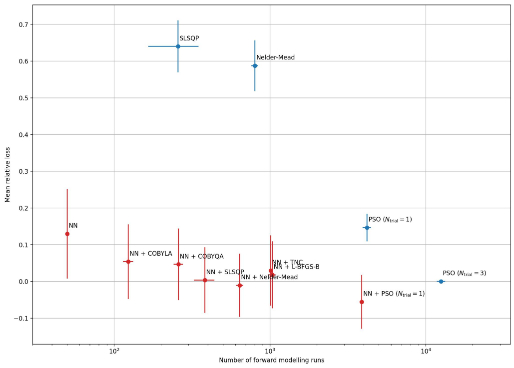

Fig. 2: Relation between the mean relative loss (smaller means better fit) and the number of forward runs (more runs lead to greater time-consumption) for different fitting methods. Blue dots: traditional global/local optimization methods. Red dots: a neural network generates the initial guess for the local optimizers. We recommend NN+SLSQP to balance the fitting quality and and time cost.

Single-pixel Line Survey

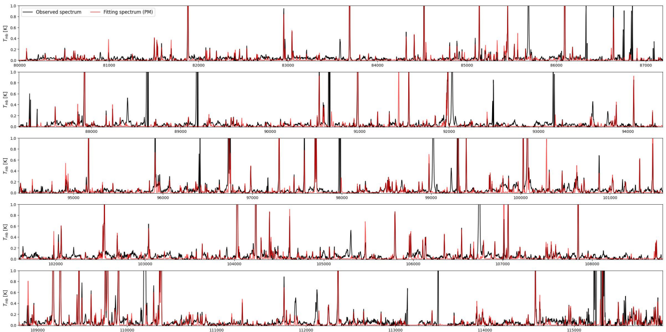

Fig. 3: Best-fitting results using PM loss for SgrB2M oberved by IRAM. Similar tests were run for five line surveys. The recall rates (number of matched lines / lines in referred paper) are 74%~93%, and the precision rates (number of matched lines / lines identified by PM loss) are 78%~92%.

Pixel-level Fitting Example

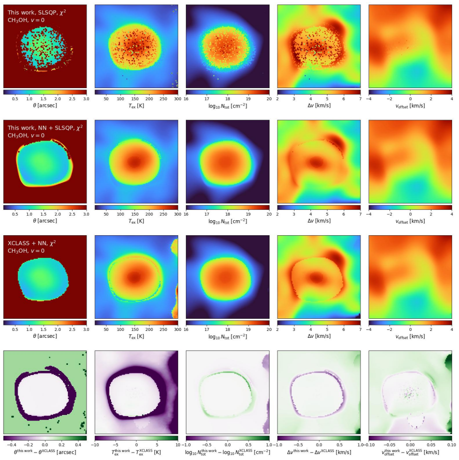

Fig. 4: Comparison of our pixel-level fitting results with XCLASS. The fitted region is from an ALMA observation of a typical hot core, G327.3-0.6, covering a total bandwidth of ~5 GHz. The fitted molecule is methanol (CH_3OH). From left to right, the columns show the fitting results for source size, excitation temperature, column density, velocity width, and velocity offset. The first row uses random initial guesses for SLSQP. The second row is NN+SLSQP. The third row is NN+ XCLASS. The fourth row shows the difference between our results and those based on XCLASS. In the central hot core, our results are consistent with XCLASS.

Linking simulations and observations

Masses and temperatures of ALMA(GAL)-like cores

Birka Zimmermann, A. Sanchez-Monge, S. Walch, G. Fuller

Methods:

We analyse radiation–hydrodynamic simulations of a collapsing clump of **1000 $M_\odot$** within a **radius 1 pc**, evolved with **FLASH** including self-gravity, non-equilibrium chemistry, radiative transfer, ionising radiation, and the associated radiation pressure. The evolution is followed until the formation of an ultracompact H II region. Two resolutions are studied (minimum cell sizes **400 au** and **50 au**) and post-processed with **RADMC-3D** to produce **1.36 mm** dust-continuum maps. These are then processed with CASA to generate synthetic **ALMA** Band 6 images matched to the **ALMAGAL** observations, including realistic interferometric spatial filtering and thermal noise. This enables a direct comparison between intrinsic and observationally inferred core properties (see Fig.1).

Cores are defined as fixed-aperture regions of radius **1500 au** centred on sink particles, allowing one-to-one comparisons of masses from the **3D simulation**, **2D projections**, idealised **RADMC-3D** maps, and synthetic **ALMA** images. We quantify how **resolution**, **projection** and **flux reconstruction** affect derived core properties, and evaluate three dust-temperature prescriptions for mass estimates: **L/M, L/M+F**, and a supervised **machine-learning** model. The mass can be estimated with:

$$M = F_\nu d^2 / (fd\, \kappa_\nu B_\nu(T_X))$$

> Individual ALMA continuum derived **core masses** may be **uncertain by a factor of ~3–5** up to 10 for extreme cases.

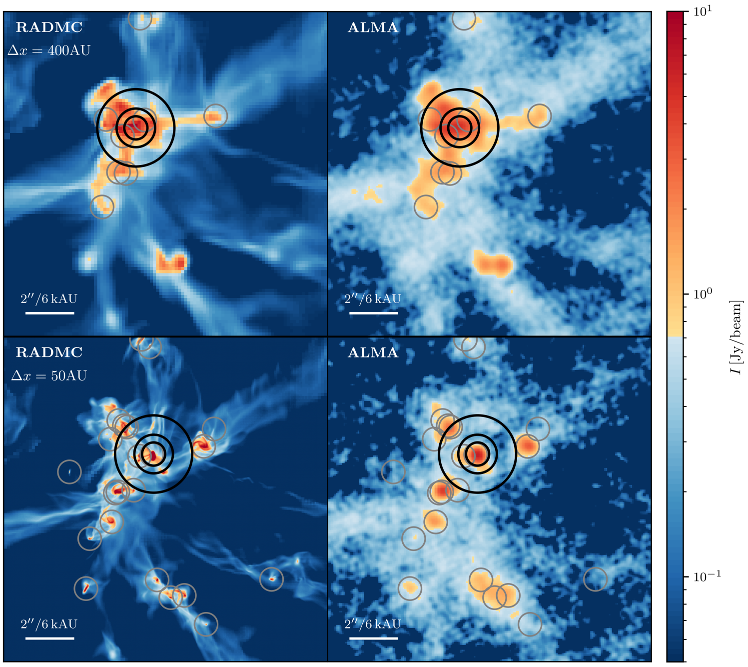

Figure 1: Synthetic flux distributions from RADMC (idealised) and ALMA for two different numerical resolutions. Grey circles denote Cores. Grey circles indicate cores (at sink location). Black circles mark physical radii of 1500au, 2500au, and 5000au, centred on the most massive sink particle. The intrinsic simulation resolution sets which features remain visible and how clear the cores are defined.

Results:

In the simulations, **projected** core masses are systematically larger than the corresponding spherical **3D masses** by a factor of ~2–3, mainly because of foreground and background contamination along the line of sight. For most cores, the ALMA fluxes remain broadly consistent with the corresponding RADMC-3D fluxes, indicating that the overall **flux scaling is largely preserved**. At low fluxes ($\lesssim$ 2 mJy), ALMA tends to slightly overestimate the emission, while at intermediate fluxes (~1.5–12 mJy) the scatter increases, likely due to noise, beam convolution, and partially resolved-out structure.

For both **RADMC-3D** and **synthetic ALMA** data, errors in the assumed dust temperature translate directly into biases in the derived core masses: **underestimated temperatures lead to overestimated masses**, and vice versa, (see Fig.2). Using only the luminosity to mass relation of the clump **(L/M)** produces the largest scatter, with the **most massive cores** tending to have **underestimated temperatures** (with R^2=0.43) and therefore **overestimated masses**. Adding the core flux **(L/M+F)** significantly tightens the relation and improves the recovery of both temperatures (with R^2=0.83) and masses, especially for the more massive cores.

A supervised **machine-learning** temperature estimator (based on gradient-boosted decision trees) further improves the core-temperature recovery by combining clump-scale and local observables. Using L/M, core flux, projected distance from the clump centre, and the empirical $T_{L/M}$ estimate as input features, the model gives the best agreement with the simulated temperatures, reaching R^2=0.96. It also provides the **most accurate mass estimates** in our tests: in the RADMC-3D maps, the derived masses lie close to the one-to-one relation, whereas in the synthetic ALMA data the higher-mass cores are recovered well, but the lower-mass cores remain systematically overestimated.

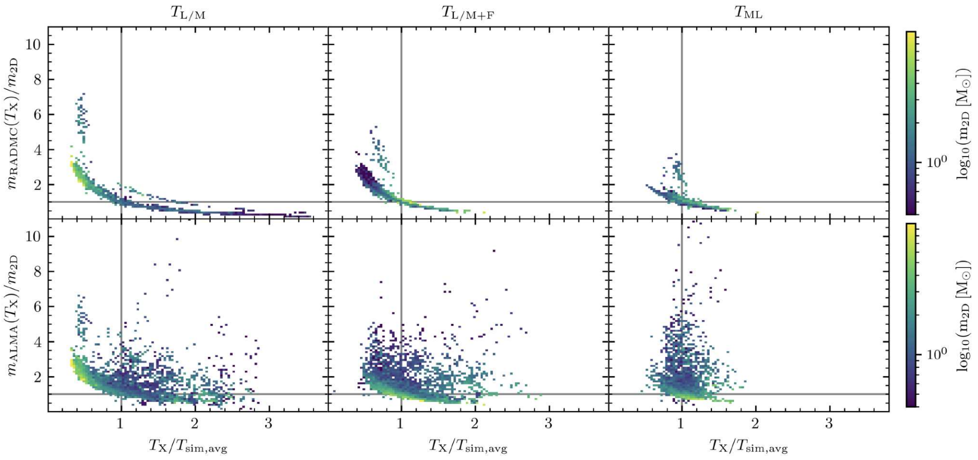

Figure 2: Comparison of the temperature and mass biases of core masses derived from RADMC-3D models (top row) and synthetic ALMA maps (bottom row). From left to right, the temperatures are estimated using **L/M**, **L/M + flux**, and a supervised **machine-learning model**. The temperature estimates improve from left to right. However, in the ALMA case, the lowest-mass cores remain systematically overestimated even when the temperature bias is small.

Conclusions:

- **projected** core masses exceed the corresponding 3D **spherical** masses by a factor of 2-3
- **Imperfect flux recovery** results into mass biases of a factor of 1-2
- $\mathbf{T_{L/M}}$ (used in observational works) captures global thermal evolution but fails the large core-to-core temperature scatter – mass bias of a factor of 2-5
- simple **L/M + flux model** improves core-temperature estimates
- supervised **machine-learning model** to predict core-temperatures performs best

Birka Zimmermann
zimmermann@ph1.uni-koeln.de

UNIVERSITY
OF COLOGNE

OLYMPUS riviera

PIERIA - GREECE

Natural environment
1. Mt. Olympus National Park
2. Pieria Mountain
3. Enipeas Canyon
4. Agia Kori Stream
5. Vrondou Caves
6. Orlias Stream

Wetlands:
1. Aliakmonas Delta
2. Wetland of Alikes Kitros
3. Wetland of Nei Pori

Traditional Villages:
1. Palios Panteleimonas
2. Palii Pori
3. Palia Skotina
4. Palia Leptokiaria
5. Skotina (Morna)
6. Kolindros

Monasteries:
1. St. Dionisios of Olympus Main (Old) Monastery Mt. Olympus
2. St. Dionisios of Olympus Recent Monastery Litochoro
3. Osios Efrem of Syria Monastery Kontariotisa
4. Monastery of Virgin Mary Makrirahi
5. St. George Monastery Korinos
6. St. George Church Kolindros
7. St. George Monastery Ritini
8. Monument of St. Payl Crossing Methoni
9. St. Athanasios Church Kitros

History & Culture:
1. Makrigialos
2. Pidna
3. Kitros- Louloudies
4. Dion Archeological Park
5. Dion Acheological Museum
7. Livithra
8. Mount Olympus Geological Museum
9. Mount Olympus Natural History Museum
10. Maritime Museum of Litohoro
11. Kolindros Folklore Museum

6. Platamona's Castle

Mountain Refuges:
Mt. Olympus
1. D. Boudolas 1100m
2. S.Agapitos 2100m
3. H.Kakalos 2650m
4. G.Apostolidis 2760m
Pieria Mountain
6. Ano Milia 1000m
7. Sarakatsana 1680m

Airport

Railway Station

Highway Exit

Port

1 HOTEL & SPA
MEDITERRANEAN
VILLAGE
★★★★★

2 HOTEL
MEDITERRANEAN
RESORT
★★★★

3 ADULT HOTEL
MEDITERRANEAN
PRINCESS
★★★★

4 HOTEL
OLYMPUS
MEDITERRANEAN
★★★★

OPEN WAYS
EVENTS & TRAVEL

openways.gr
17 Tsimiski Str. | Thessaloniki | 54624 | GREECE